DENSITY FUNCTIONAL THEORY INVESTIGATIONS ON UPGRADING OF PHENOLIC CATALOGUE OF UNPROCESSED BIO-OIL

Submitted in partial fulfilment of the requirements

for the degree of

DOCTOR OF PHILOSOPHY

By

ANAND MOHAN VERMA

DEPARTMENT OF CHEMICAL ENGINEERING

INDIAN INSTITUTE OF TECHNOLOGY GUWAHATI

GUWAHATI, ASSAM – 781039, INDIA

DECEMBER 2017

CERTIFICATE

It is certified that the work contained in the thesis entitled "**Density Functional Theory Investigations on Upgrading of Phenolic Catalogue of Unprocessed Bio-Oil**", by Anand Mohan Verma (Roll No. 136107042)**,** has been carried out under my supervision and that this work has not been submitted elsewhere for a degree.

Date: 1st December 2017

Dr. Nanda Kishore
Associate Professor
Department of Chemical Engineering
Indian Institute of Technology Guwahati
Guwahati, Assam
India - 781 039

ACKNOWLEDGEMENTS

This doctoral thesis is not only an ensemble of various research projects but a journey of almost four years of my life. It has not only polished me scholastically but personally too. Coming to IIT Guwahati turned out to be one of the best decisions of my life. I learned a lot from here and each individual who is and was part of my life here. Having forgotten any important person must not feel that they mean less to me. Acknowledging each individual would not be possible but I would like to extend my heartfelt regards to following persons.

First and foremost, I would like to express my sincere gratitude to the thesis advisor Dr. Nanda Kishore for his constant supervision and throughout support. His vision, patience, and motivation led me to successfully complete this thesis. I could not have imagined a better supervisor and I thank him for being there whenever I required his presence either on professional or personal front. Besides my thesis supervisor, I thank my doctoral committee members Dr. Anki K. Reddy, Dr. Aditya N. Panda, and Dr. Vairakannu Prabu for their insightful suggestions and comments in order to shape this thesis. Their strong questions and remarks widened my research perspectives.

I thank to the Indian Institute of Technology Guwahati for the accessibility of supercomputer *PARAM-ISHAN* without which the essence of this thesis may have not been possible. In this regard, I once again thank Dr. Aditya N. Panda for instructing me the technicalities of *PARAM-ISHAN* and *Gaussian* parallel version software and also for meeting me every time when I requested him.

I am grateful to my fellow labmates who were not only helpful on academic but on personal grounds as well. The group discussions with them led me to understand various research aspects. There are many to be thankful of but few of them are Dr. Rahul, Kushagra, Harshal, Satyendra, Abhipsit, Madhu, Malladi, and Vasu.

This thesis is dedicated to my family. To my father, who is one of the reasons behind my presence in higher academics. To my mother, whose unconditional love for me is indescribable. To my brother & sister-in-law and to my sisters & brother-in-laws for their love and all kinds of supports. To all the little ones in my family. And, to my departed *Dadi*, who is one of the top reasons behind my attentiveness in the education at elementary schooling.

Finally, I am thankful of the God for all the blessings and always showing me the right path.

Anand Mohan Verma

CONTENTS

List of Tables

List of Figures

ABSTRACT

In the era of renewable energy resources, biomass is the only renewable energy resource which holds the potential of providing sustainable carbon element useful for transportation vehicles and/or platform chemicals. However, unprocessed bio-oils derived from fast pyrolysis of lignocellulosic biomass exhibit various drawbacks, for instance, low pH, low heating value, low stability, and high viscosity, thus, it cannot be applied directly to transportation vehicles. The major reason behind these undesirable properties of unprocessed bio-oil is the presence of high number of oxygenated compounds (>400) classified in various oxy-functional groups such as acids, aldehydes, esters, sugars, phenols, furans, etc. On the other hand, due to such high number of oxygenated compounds, unprocessed bio-oils can be a great source of obtaining specialty or platform chemicals with appropriate conversion methods.

In this dissertation, phenolic oxygenated compounds of unprocessed bio-oils are considered as model compounds to investigate their decomposition mechanisms using density functional theory (DFT). Seven phenolic bio-oil model compounds, namely, vanillin, eugenol, ferulic acid, guaiacol, 2-hydroxybenzaldehyde, *p*-isopropenylphenol, and 2-hydroxy-6-methylbenzaldehyde are considered for vapour phase decomposition in the absence of catalyst. Further, guaiacol and 2-hydroxybenzaldehyde compounds are subjected to catalytic hydrodeoxygenation in the presence of Pd(111) catalyst. Moreover, five phenolic bio-oil species, i.e., phenol, 2-hydroxybenzaldehyde, anisole, vanillin, and guaiacol are represented as model compounds to investigate the adsorption phenomena over Pd- and Pt-doped graphene sheets acting as catalysts. Also, a thermochemical analysis is carried out to numerically understand the productions of long range liquid alkanes (C9, C12, and C15) using C6-glucose as representative compound.

During non-catalytic vapour phase decomposition of model compounds, it is found that direct cleavages of functional groups such as methoxy, hydroxyl, allyl, and formyl are not kinetically favourable because of corresponding very high bond dissociation energies. However, a single step hydrogenation reaction, at the carbon atom to which a functional group is attached, prior to the scission of functional group delivers a considerably less kinetic barrier. The catalytic hydrodeoxygenation of 2-hydroxybenzaldehyde over Pd(111) catalyst leads to the major production of phenol *via* dehydrogenation of formyl group of 2-hydroxybenzaldehyde followed by elimination of CO and association of hydrogen atom, respectively. The hydrodeoxygenation of guaiacol over Pd(111) catalyst proceeds through dehydrogenation of methoxy functional group followed by elimination and association of methylene radical and hydrogen atom, respectively, to produce catechol as major product. Further decompositions of phenol and catechol from 2-hydroxybenzaldehyde and guaiacol, respectively, are high kinetic demanding reaction steps. On the other hand, phenolic bio-oil model compounds bind strongly to Pd-doped graphene sheets compared to Pt-doped graphene sheets. Finally, the thermochemical analyses of the productions of liquid alkane chains report all participating reactions such as hydrogenation, dehydration and hydrodeoxygenation as favourable except aldol crossed- and self-condensation reactions.

INTRODUCTION

1.1. Background

The 'energy' has always been a hot topic among human being from a very beginning of urbanization of societies. Before the discovery of fossil fuel reserves, mankind's energy resource was solely dependent on biomass but due to the introduction of inexpensive liquid and gaseous fuels in 19th century, the society's living standard rose to an elevated level and industrial sector had been revolutionized [1]. However, currently fossil fuels are diminishing at very fast pace because of constantly increasing energy demands due to increased population and improvements in living standards. The population of the world in July 2015 was reported to be 7.2 billion people according to United Nations Population Division (2015); and it is expected to rise to 11.2 billion people by 2100 [2]. Figure 1.1 represents the energy demands by *Organization for Economic Co-operation and Development* (OECD) regions, non-OECD regions, and world total *vis-à-vis* years [3]. It can be seen from Figure 1.1 that non-OECD regions (i.e., most developing nations) entail a phenomenal increase in energy demand over the years while the same due to OECD regions remain almost same. Similarly, the world's total energy demand forecast almost linearly increasing from 2008 to 2035.

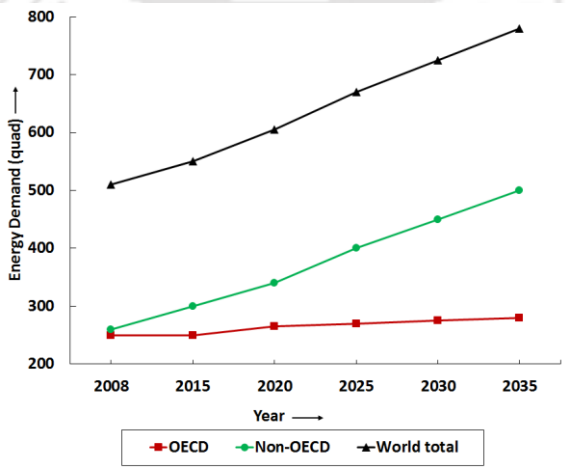

Figure 1.1: Regional energy perspective with respect to year [3].

On the other hand, increasing application of fossil fuels cause significant environmental impacts which affects the atmosphere in terms of pollution and thus health hazards to humans [1, 4]. Fossil fuels are the main reasons for growth in the pollution levels in urban and sub-urban regions across the world because they release the oxides of carbon (CO and CO_2), sulphur (SO_x), and nitrogen (NO_x) causing serious impacts on habitats [4, 5]. The declining fossil reserves (especially petroleum fuels) along with increasing energy demands and atmospheric pollution concerns have attracted researchers to develop a socio-economic green fuel technology to overcome these major obstacles. In this scenario, renewable energies are found to be the best possible alternative to diminish the environmental pollution and fossil fuel depletion concerns. The share of renewable energy resource (other than hydro power) in total primary energy supply, surveyed by World Energy Resources (2013) [6], has been documented as 11 % in 2011 which is further projected to reach 16 % of share in 2020. Renewable energy resources such as solar energy, tidal energy, hydro power, geothermal energy, biomass, etc. are serving to the nations as great green energy resources for electricity and heat sources [1, 7, 8]. However, specifically for transportation fuels and specialty chemicals, only biomass is a sustainable renewable energy resource that provides sustainable carbon element amongst all renewable energy resources [9–11]. This unique feature of biomass queues itself out from other potential renewable energy resources and has become a hot topic for research across the globe.

1.2. Biomass

Biomass is a generic term for the plant material derived from photosynthesis reaction between CO_2 and water in the presence of sunlight to produce various fractions or building blocks of biomass [12]. The stored energy in biomass is in the form of chemical bonds between carbon, oxygen, and hydrogen atoms; and it can be released back by combustion, digestion or decomposition processes [12]. Biomass is plentifully available in most countries inexpensively, therefore, in the recent past, a major fraction of research is devoted towards biomass.

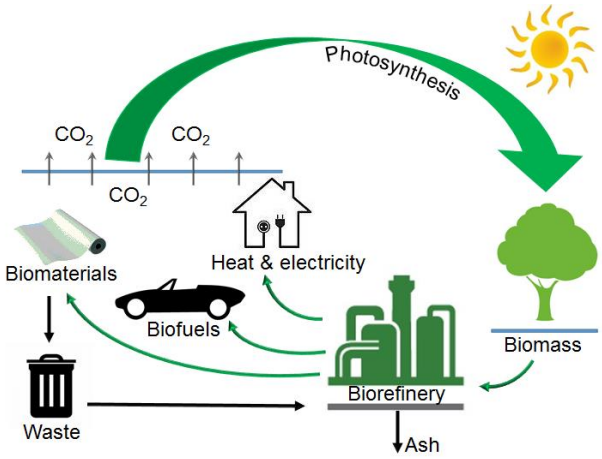

Figure 1.2: CO_2 cycle in the context of biomass [5].

Irrespective of its being the fourth highest energy source in the world, it is primarily used to generate the heat and power [13]. It is regarded as one of the most promising alternative energy resource to fossil fuel because of zero net rise in the atmospheric CO_2 level if exploited properly (see Figure 1.2) [14].

Lignocellulosic biomass belongs to the most abundant class of biomass and is a persuasive candidate for biofuel production because of no 'food or fuel' concern which is a major issue with first generation biofuels such as biodiesel or bioethanol, etc. It is abundantly available in the world with an annual production of ~170 billion metric tons [15]. In addition,

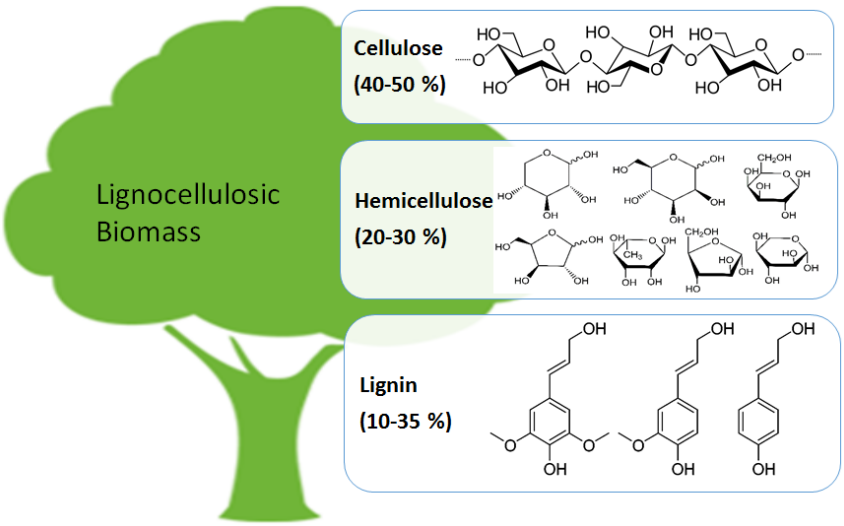

Figure 1.3: Building blocks of lignocellulosic biomass.

unlike other biomass feedstocks such as corn and starch, it does not raise any uncertainty between food or fuel concern because of inedibility to mankind. There are three main building blocks of lignocellulosic biomass as shown in Figure 1.3 *viz.* cellulose (40-50 %), hemicellulose (20-30 %), and lignin (10-35 %) [1, 12, 14, 16]. Cellulose is a crystalline polymer composed of D-glucose units linked *via* β-1,4-glycosidic bonds in the cell walls of wood fibres [4, 14]. Hemicellulose is an amorphous polymer of branched polysaccharides such as xylose, mannose, galactose, arabinose, rhamnose, and others [4, 14]. The hemicellulose fraction is surrounded by cellulose (inwards) and lignin (outwards) fractions. On the other hand, lignin is three dimensional polymer with very high structural complexity [4, 14]. It consists of different phenylpropane units linked *via* ether or C-C bonds. Generally, it is a polymer of three main units, i.e., coniferyl alcohol, sinapyl alcohol, and *p*-coumaryl alcohol.

The fractions of building blocks fluctuate with different types of biomass feedstocks [1, 12, 17, 18]. There are numerous lignocellulosic biomass feedstocks categorized in several sections such as wood biomass (cedar, pine, redwood, spruce, birch, oak, eucalyptus, etc.), agricultural wastes (shells of almond, ground nut, hazelnut, oil palm, etc.; husks of rice and olive; straws; non-edible seeds), other wastes (municipal, timber, households, etc.), and energy crops (bermuda grass, elephant grass, switch grass, etc.) [9, 19]. The fractional analyses of building blocks of these biomass feedstocks are carried out using several approaches such as proximate analysis, ultimate analysis, fiber analysis, thermal analysis, and kinetic analysis [19–22]. The proximate analysis is simplest and most common amongst others. It determines the four important fractions of any particular feedstock, i.e., moisture, volatile matter (except for water), fixed carbon (FC) content, and ash content. Ultimate analysis restricts itself to analyse the elemental compositions of carbon, hydrogen, oxygen, nitrogen, and sulphur. Fiber analysis is about the determination of building blocks of biomass, i.e., cellulose, hemicellulose, and lignin. Thermal analysis determines decomposition behaviour of biomass while the kinetic

analysis describes decomposition rates in the course of dissociation progress. Recently, Dhyani and Bhaskar [19] reviewed various biomass feedstocks in terms of proximate, ultimate, and fiber analyses along with their higher heating values (HHV).

Irrespective of a substantial share of lignin in lignocellulosic biomass, it has been underutilized in the past due to higher complexity in its molecular structure [16, 23]. However, apart from its ample fraction in the lignocellulosic biomass, it is highly abundant from other sources such as byproduct in the pulp and paper industries, residue from biomass-to-ethanol process, and agricultural products [23]. The isolation of lignin from lignocellulosic feedstocks is achieved by two main approaches using solubilizing processes [23]. First approach dissolves cellulose and hemicellulose fractions of lignocellulosic biomass and leaves lignin as residue (as byproduct of lignin in biorefinery) while second approach dissolves lignin only and leaves cellulose and hemicellulose fractions as residues (in kraft and sulfate pulping in pulp and paper industries) [9, 23]. Currently, most of biorefineries produce lignin as a waste stream and utilize it to produce inferior quality heat or power; however, according to the suggestions by several researchers [16, 23, 24], lignin fraction can play a vital role in the biorefineries because:

i) it accounts for ~40 % of stored energy in lignocellulosic biomass due to its highly carbonaceous nature,
ii) it is known to be most abundant aromatic resource in nature by far which presents it as a suitable candidate/feedstock for the production of platform chemicals,
iii) it is sustainable at high temperature thermal decomposition compared to cellulose and hemicellulose fractions, and
iv) it resembles highly to petroleum compared to cellulose and hemicellulose fractions.

Thus, lignin fraction holds exceptional potential as renewable energy resource and could be utilized very effectively in biorefineries to increase the productivities and yields. The effective

industrial utilization of lignin is not only productive and efficient but also mandatory in order to prevent the release of organic pollutants in the atmosphere due to its partial combustion [24, 25]. For instance, tenacious organic pollutants such as polycyclic aromatic hydrocarbons (PAHs), oxygenated PAHs, dioxins, and particulate matter emerge due to incomplete combustion of lignin which are very harmful to the atmosphere and thus human species [24, 25].

1.3. Chemistry of Lignin

Lignin (see Figure 1.4) is highly complex three dimensional copolymer of mainly three phenylpropane units, namely, *p*-coumaryl alcohol, sinapyl alcohol, and coniferyl alcohol. The association of propyl side chain with phenyl ring is common in all of these three monomer units and is the reason why lignin is often termed as phenylpropane units [23, 26, 27].

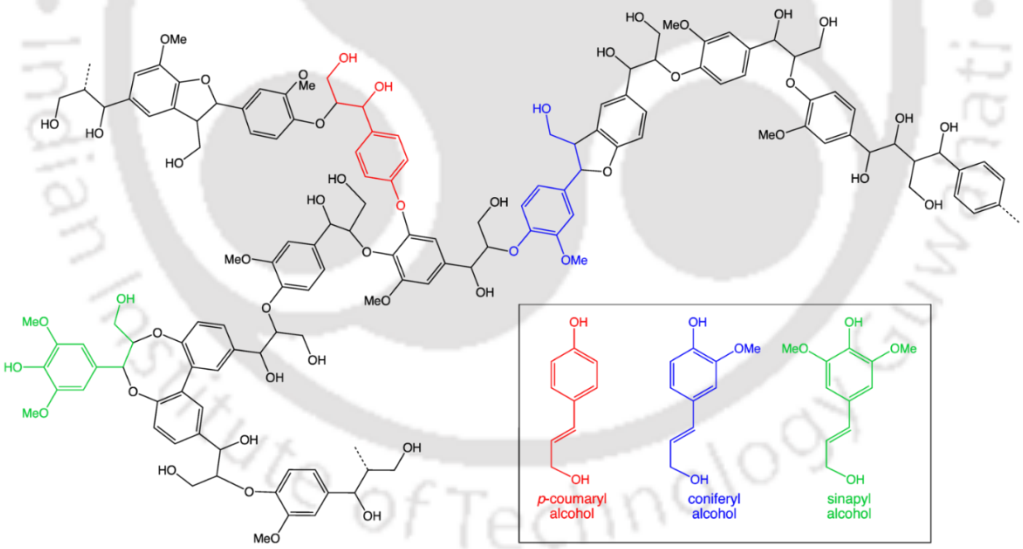

Figure 1.4: A schematic of lignin structure with depiction of all three lignin monomers [28].

The exact structure of lignin is still unclear because each wood species depict different linkages and the exact compositions of all phenylpropane units vary with different lignin feedstocks. For instance, softwood lignin is comprised of ~90 % of coniferyl alcohols while hardwood lignin is roughly equally composed of coniferyl alcohol and sinapyl alcohol [25].

Typical structures of (a) softwood and (b) hardwood lignins can be seen in Figure 1.5. Compared to the softwood, hardwood lignin is more linear due to methoxy group attachment to the aromatic rings which prevent to form 5-5 linkages [27].

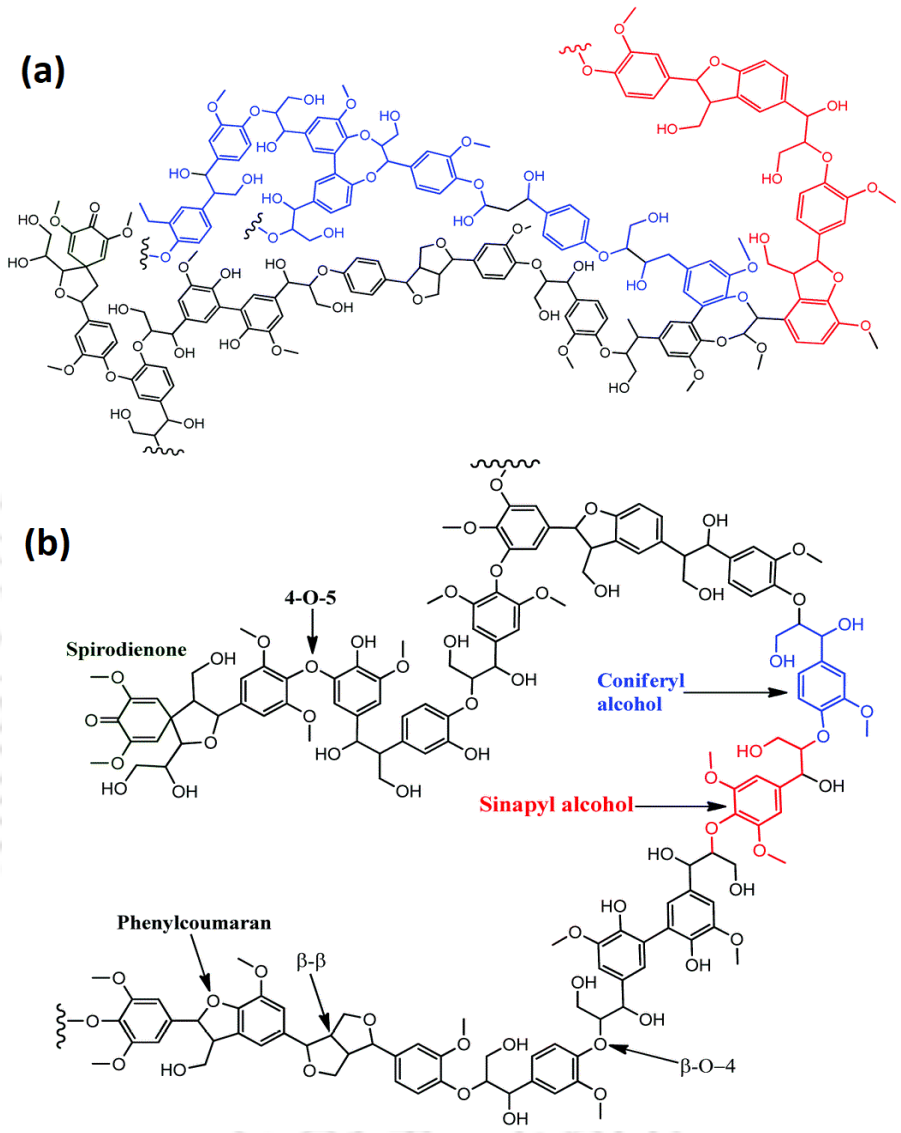

Figure 1.5: Structural representation of (a) softwood lignin and (b) hardwood lignin [25].

The elucidation of lignin structure suggests about 50 % of the aromatic content in it and majorly connected by bond linkages such as β-O-4 ether bonds, β-5 phenylcoumaran bonds, α-O-4 aryl ether bonds, β–β resinol, 4-O-5 diaryl ether, β-1 linkages, β-5 linkages, 5-5 linkages, and others as shown in Figure 1.6 [24, 26]. The compositions of all of these bond linkages are not uniform in any lignin feedstock and they differ with type of the samples (see Table 1.1).

Out of all these linkages, β-O-4-aryl ether linkage is found to be most frequent type of coupling linkage amongst other linkage types in both softwood and hardwood lignin samples [24, 26].

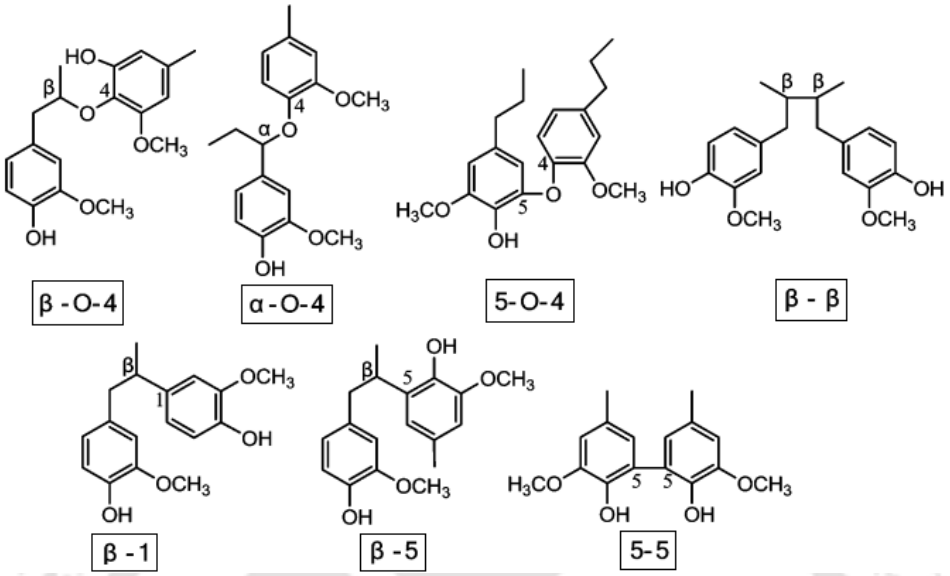

Figure 1.6: Bond linkages in lignin molecular structure [23, 24, 26, 27].

Table 1.1: Fractions of various bond linkages in softwood and hardwood lignin samples (ppu= phenylpropane units) [24, 26].

Linkage	Number/100 ppu	
	Softwood	**Hardwood**
β-O-4	43−50	50−65
β-5	9−12	4−6
α-O-4	6−8	4−8
β−β	2−4	3−7
5−5	10−25	4−10
4-O-5	4	6−7
β-1	3−7	5−7
Others	16	7−8

1.4. Conversion Processes of Lignin

The conversion of lignin generally occurs by oxidation, in neutral environment, and by reducing agents. Numerous lignin feedstocks can be targeted for their depolymerization using these three types of conversion processes of lignin (see Figure 1.7). Most lignin conversion

processes, whether in the presence or absence of catalysts, occur at the temperature range of 250-650°C that consequences a complex phenolic mixture comprising of alkylated and polyhydroxylated phenols along with volatile components and chars [24, 26]. Oxidation process of lignin occurs with the cleavages of C-C or C-O bond linkages using suitable oxidants. The conversion of lignin in neutral environment occurs by acid/base catalyzed depolymerization, liquid phase reforming, gasification, and pyrolysis. Finally, hydroprocessing of lignin occurs in the presence of suitable catalyst using hydrogen gas stream [24].

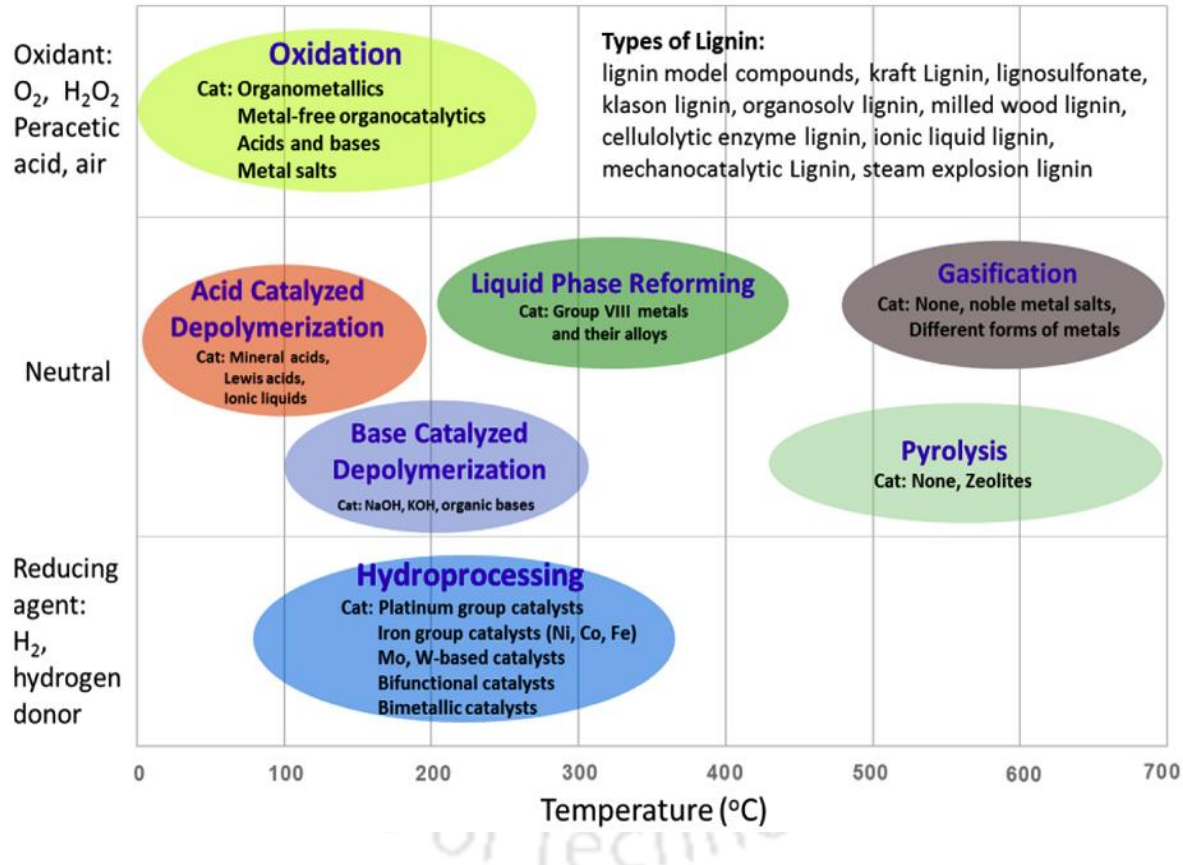

Figure 1.7: Various decomposition processes of lignin [24].

1.4.1. Oxidation

Lignin is a promising candidate for the oxidation process because of embracement of extensive hydroxyl groups. The oxidative cracking mechanism of lignin encompasses the cleavages of aryl ether bonds, carbon-carbon bonds, aromatic rings and other linkages [24]. The

depolymerization of lignin in oxidation process using popular oxidants such as O_2, H_2O_2, air, and peracetic acid focuses on the production of polyfunctional aromatic compounds ranging from aromatic aldehydes to carboxylic acids such as vanillin, syringaldehyde, 4-hydroxybenzaldehyde, and muconic acid [24, 26]. However, the products derived from oxidation of lignin depend on the severity of the reaction conditions. Various catalytic systems such as organometallic catalysts, metal-free organic catalysts, acid or base catalysts, metal salts catalysts, photocatalytic oxidation, and electrocatalytic oxidation have been employed in the past for the depolymerization of lignin. The catalytic oxidation of lignin is divided into two main categories, namely, heterogeneous and homogenous in which former is highly preferable because it allows for easy separation and catalyst recovery [24]. However, oxidative degradation of lignin does not necessarily require a catalyst but the reactions are less product selective without a suitable catalyst.

1.4.2. Hydroprocessing

Depolymerization of lignin using hydroprocessing associates the reducing agents such as hydrogen gas and/or hydrogen donor components to produce simple aromatic compounds, for instance, phenols, benzenes, toluene, and also alkane chains [1, 16, 24]. It is one of the most popular techniques for the degradation of lignin into smaller fractions and it occurs at the temperature range of 100-350^{o}C in the presence of hydrogen gas stream and preferably over catalytic systems such as monometallic, bimetallic and bifunctional catalysts [16, 29]. Hydroprocessing entails various reactions such as hydrogenation, hydrogenolysis, hydrodeoxygenation, and others [16]. Hydrogenation reaction usually saturates the double or triple bonds between carbon-carbon and/or carbon-hetero atoms such as C=C or C=O using hydrogen molecule(s), however, sometimes it employs the cleavage reactions as well. Hydrogenolysis reaction is about the cleavage of either C-C or C-hetero atom using hydrogen

molecule while hydrodeoxygenation reaction specifically restricts to the cleavage of C-O bonds producing water as side product. In the recent past, various types of catalysts have been employed for hydroprocessing of lignin, for instance, platinum group catalysts, iron group catalysts, bimetallic and bifunctional catalysts [8, 16, 24, 26].

1.4.3. Acid-Base Catalyzed Depolymerization

1.4.3.1. Acid Catalyzed Depolymerization (ACD)

Acid catalyzed depolymerization process of lignin produces small fragment products by breaking C-O and/or C-C bond linkages [24, 26]. The first acid catalysed depolymerization of lignin was reported by Hägglund and Björkman [30] in 1924. They carried out lignin depolymerization experiment with hydrochloric acid as the reagent to obtain thiobarbituric acid, phloroglucinol, and barbituric acid. However, in the recent past, various reagents have been examined for the hydrolysis of lignin and lignin derived model compounds such as mineral acids (HCl, H_2SO_4), Lewis acid ($FeCl_3$, $ZnCl_2$, BF_3, $AlCl_3$), zeolites, acidic ionic liquids ([Hmim]Cl, [Bmim]Cl, [Amim]Cl), and organic acids [24, 26]. The hydrolytic cleavages of α- and β-aryl ether bond linkages play a vital role in the ACD of lignin because of stable natures of aryl-aryl ether bonds, phenolic C-O bonds, and C-C bonds [24, 26]. The primary step in the ACD process is dehydration reaction which yields enol aryl ethers. Further, the enol aryl ethers can be frequently hydrolysed to guaiacol and α-ketocarbinol.

1.4.3.2. Base Catalyzed Depolymerization (BCD)

Depolymerization of lignin feedstock using base catalyzed mechanism is one of the unique way for the production of simple aromatic compounds at mild reaction conditions. Ether bond linkages such as aryl-alkyl ether bonds and β-O-4 ether bonds are reported to be the weakest bonds in the lignin structure, therefore, alkaline depolymerization processes generally target these bonds for the lignin breakdown [24, 26]. There are several inexpensive basic reagents

available in the commercial market for base catalysed depolymerization process such as LiOH, KOH, and NaOH; however, yield of product mixture strongly depends on the nature of base because of dependence of conversion rate on the strength of base material [24]. BCD process usually occurs in the temperature range of 100-300^{o}C. In addition to the temperature, selectivity and yield of products in base depolymerization of lignin depend on pressure, time, base concentration, and lignin to solvent ratio. Higher temperature and high reaction time favour the generation of monomers; however, repolymerization reactions favour the formation of solid residue and are major problem in the generation of monomers, therefore, deaccelerating the repolymerization rate could in fact enhance the product yield [23, 24].

1.4.4. Liquid Phase Reforming (LPR)

Liquid phase reforming process of lignin generally occurs at moderate temperature (250-400^{o}C) than those of thermochemical conversions of lignin such as gasification and pyrolysis. It employs various types of liquids to dissolve lignin, for instance, water, ethanol/water, supercritical ethanol, and liquid ammonia at low temperature and pressure. The dissolution of lignin is mostly preferable in ethanol and ammonia; however, water is most preferred solvent because of low cost and readily available but has a low solubility of lignin [23, 24]. In aqueous phase reforming, most abundant bond linkages such as β-O-4 and 5-5' are first targeted for depolymerization into various aromatic monomers followed by reformation of alkyl chains on these monomers to produce simple aromatics and hydrogen [23, 24, 27].

1.4.5. Thermochemical Methods

1.4.5.1. Gasification

Gasification process depolymerizes the lignin fraction into *syngas* (CO and H_2) upon reacting with air, steam and/or oxygen. A complex combination of chemical reactions occur at different stages of gasification tower during gasification process such as partial oxidation, water-gas

shift, pyrolysis, steam gasification, and methanation reactions [1]. Pyrolysis process decomposes the lignin feedstock into lower fractions and occurs in the absence of oxygen stream, whereas, partial oxidation requires less amount of oxygen for combustion compared to stoichiometric requirement. Steam gasification implicates the decomposition reaction with water to produce CO, H_2, and CO_2; and, in water-gas shift reaction, CO and water react to produce CO_2 and H_2. On the other hand, methanation is about the production of methane and water from reaction of CO and H_2. The product gases contain CO, H_2, CH_4, CO_2, and N_2 in different fractions. The composition of product gases is dependent of lignin feedstock, gasifier type, reaction parameters, and others. Nevertheless, the produced *syngas*, i.e., CO and H_2, can be employed in several ways [31], for instance, in the production of hydrogen by water-gas shift reactions, in the production of methanol by methanol synthesis, and in the production of alkanes by Fischer-Tropsch process. Furthermore, the utilization of *syngas* can be in the productions of isobutane by isosynthesis, ethanol by fermentation, aldehydes and alcohols by oxosynthesis, and others [31]. Methanol, on the other hand, which is produced during methanol synthesis from *syngas* can be utilized in the production of dimethyl ether (DME).

1.4.5.2. Pyrolysis

Pyrolysis is one of the promising and old thermochemical techniques for the decomposition of biomass feedstocks producing bio-oils directly either in the presence or absence of a catalyst. Bio-oils from pyrolysis process are produced by the rapid heating of lignocellulosic biomass in the absence of air/oxygen at elevated temperature of 450-600^oC [22]. It is an endothermic reaction; however, from energy point of view, pyrolysis process of cellulose is only observed as endothermic while hemicellulose and lignin fractions release energies upon depolymerization [19]. At such elevated temperature, the decomposition of lignocellulosic biomass produces vapour phase products which can subsequently be condensed into liquid

phase upon cooling, called bio-oil or pyrolysis oil. Along with vapour phase products, the pyrolysis process also generates non-condensable gases and chars. The non-condensable gases are often used as heating agent for the pyrolysis process in reaction system. The produced bio-oils from fast pyrolysis comprise high oxygen content, low carbon content, and high moisture content [4]. However, the product compositions, i.e., bio-oil, char, and non-condensable gases strongly depend on the pyrolysis conditions such as temperature, heating rate, residence time, pressure, environment, catalyst, and others. High temperature and low residence time is generally favourable in order to produce high amount of condensable products while high temperature and high residence time lead to favour the production of non-condensable gases due to secondary reactions [1, 14, 19]. On the other hand, low temperature condition could yield high amount of solid products. Based on the pyrolytic process conditions, pyrolysis process is classified in several categories such as fast pyrolysis, intermediate pyrolysis, slow pyrolysis, and hydropyrolysis [19].

1.5. Characteristics of Bio-oil

Bio-oils, having a distinctive odour, are free flowing liquid with appearance of dark brown colour. During the conversion of biomass in to bio-oil, various reactions take place such as dehydration, hydrolysis, isomerization, dehydrogenation, aromatization, condensation, coking, and others [1, 4, 14]. Branca et al. [32] in their experiment of biomass pyrolysis reported more than 400 oxy-compounds in unprocessed bio-oil which are classified into acids, esters, alcohols, aldehydes, sugars, miscellaneous oxygenates, furans, phenols, guaiacols, and others. However, pyrolysis of lignin feedstock produce CO, CO_2, H_2O, gaseous hydrocarbons, volatile liquids, monolignols, monophenols, polysubstituted phenols, char, and coke [24, 26]. The formations of CO and CO_2 are majorly due to the reformation reaction between C=O and COOH functional groups. Water is produced due to hydrogenolysis reaction. Gaseous hydrocarbons contain a variety of products such as CH_4, C_3H_6, C_2H_2, C_2H_4, etc. while volatile

liquids are a mixture of benzene, methanol, acetone, acetaldehyde, and alkyl substituted aromatics. Monolignols are generally the initial lignin components such as coniferyl alcohol, sinapyl alcohol, and *p*-coumaryl alcohol. Monophenols contain a wide range of products such as phenol, catechol, syringol, guaiacol, vanillin, and others. The exact composition of these pyrolytic products of lignin feedstock depends on following factor [1, 33]:

a) feedstock type
b) nitrogen and protein contents
c) heat transfer rate and final char temperature
d) water content of feedstock
e) storage issues, and others

Monophenol catalogue derived from pyrolysis of lignin is a complex category of phenolic compounds and there exists various subcategories such as:

- phenols (phenol, cresol, *p*-isopropenylphenol, etc.)
- guaiacols (guaiacol, alkylguaiacol, eugenol, etc.)
- anisoles (anisole, alkylanisole, etc.)
- catechols (catechol, alkylcatechol, methoxycatechol, etc.)
- syringols (syringol, alkylsyringols, etc.)
- others (vanillin, vanillic acid, sinapaldehyde, acetosyringone, salicylaldehyde, 2-hydroxy-6-methylbenzaldehyde, ferulic acid, etc.) [7].

Though, the number of oxygenated compounds in bio-oil may range in hundreds as referred by various literature investigations [1, 8, 14, 16, 32]; however, a few important phenolic bio-oil model compounds are shown in Figure 1.8.

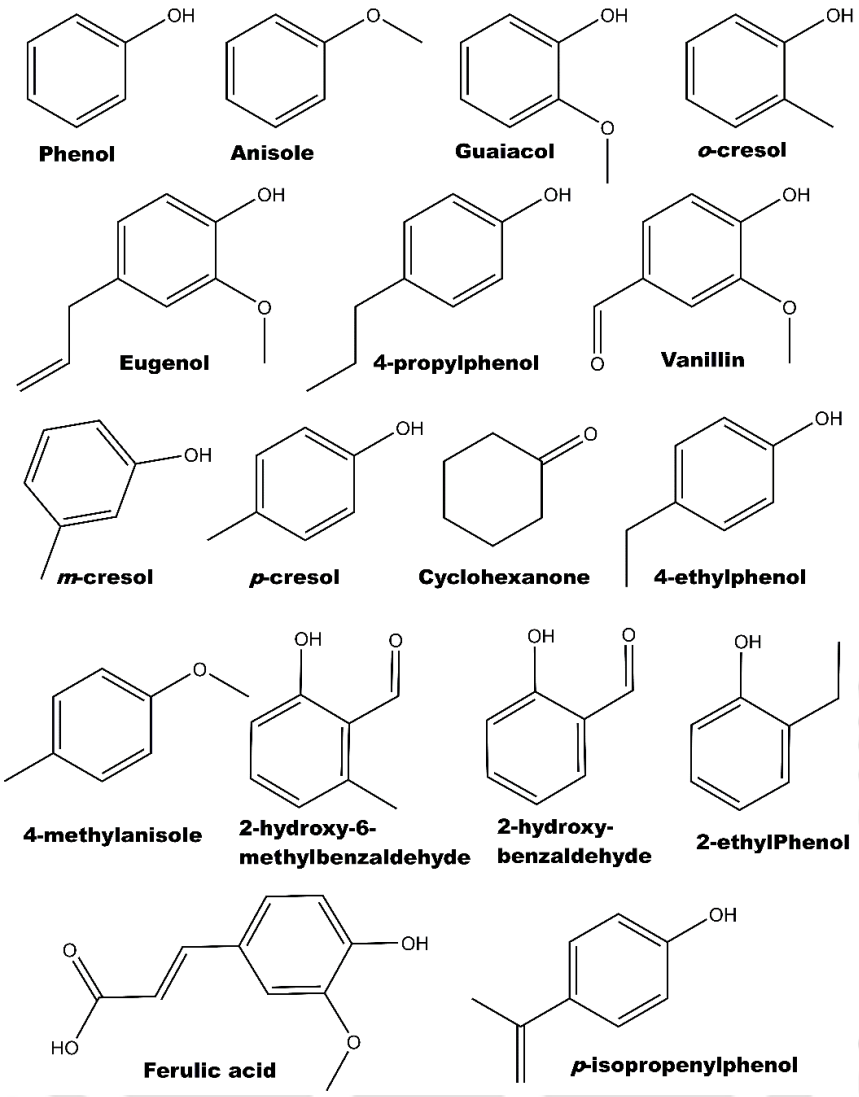

Figure 1.8: Lignin derived bio-oil compounds [8, 16, 34–36].

1.6. Snags to Raw Bio-oil and Its Upgrading

As it is aforementioned in the 'Characteristics of Bio-oil' subsection that raw bio-oil from pyrolysis contains hundreds of oxy-organic compounds, unprocessed bio-oil does not display desired characteristics of a good fuel. High amount of oxygenated compounds degrade the quality of bio-oil in terms of:

- low heating value
- low carbon content

- poor volatility
- low pH
- high viscosity
- less stability
- coking
- cold flow problems, etc. [1, 7, 8, 35].

The problem occurs with bio-oil subjected to diesel engine is that it is difficult to start ignition because of corrosiveness and coking. Therefore, bio-oil obtained from fast pyrolysis cannot be used in transportation fuel directly, hence, it has to be channelized through appropriate upgrading processes before being subjected as an alternative to transportation fuel such as diesel and gasoline. Primarily, bio-oils can be upgraded using numerous mechanisms, for instance, hydrotreating, hydro-cracking, supercritical fluids, solvent addition/esterification, emulsification, steam reforming, and others [8, 11, 16]. However, in the recent past, zeolite upgrading, forming emulsions with the diesel fuel, and hydrodeoxygenation process are extensively applied in the upgrading of unprocessed bio-oils [1, 7, 14, 16].

1.6.1. Zeolite Upgrading

Zeolites are widely used catalysts in the petroleum industries for oil refining, production of special or fine chemical, and for petrochemistry inside the petroleum fuel [37]. These are crystalline microporous materials with 5-10 Å pore structures and bio-oils can be upgraded using zeolite to reduce oxy-functional groups [37]. The products from zeolite upgrading contain hydrocarbons, water-soluble organics, gases, and coke. A number of reactions occur during zeolite upgrading such as dehydration, cracking, deoxygenation, aromatization, and polymerization. Advantages to zeolite upgrading are that it doesn't require additional hydrogen, operates at atmospheric pressure, and temperatures are also same as of bio-oil

production [1, 37]. But some disadvantages such as poor hydrocarbon yields and high yield of coking brand this process less suitable in bio-oil upgrading processes [1, 37].

1.6.2. Forming emulsions with the diesel fuel

Because of high water content in raw bio-oil derived from pyrolysis or liquefaction of lignocellulosic biomass, it is not solvable in petroleum derived fuel; however, it can be blended with diesel fuel employing the use of appropriate surfactants [38–40]. Bio-oil emulsion depicts constructive ignition characteristics, though, it becomes costly because of addition of surfactant in emulsification process. Nonetheless, corrosion process is still a challenging task in the engine upon the application of bio-oil emulsions [40].

1.6.3. Hydrodeoxygenation (HDO)

Hydrodeoxygenation is a chemical process of cleaving C-O bonds using hydrogen gas over appropriate catalytic system. Various types of catalysts have been used in HDO processes such as sulfided NiMo and CoMo based catalysts, mono metallic, bimetallic, noble metal catalyst and transition metal oxide catalysts [16]. Sulfided NiMo and CoMo based catalysts are very popular in the petroleum industries because these are used to remove sulphur, oxygen and nitrogen based functional groups from petroleum feedstocks. Due to less oxygen content in petroleum feedstocks, these do not involve with large water formation during refining. Sulfided NiMo and CoMo based catalysts show poisonous behaviour if the reaction encompasses water formation or reaction itself is in water phase [16]. Since bio-oil contains a large amount of oxy-compounds, the product stream during upgrading would contain a large amount of water, therefore, sulfided NiMo and CoMo based catalysts may not be appropriate. On the other hand, noble metal catalysts such as Pt, Pd, and others show exceptional characteristics of HDO in both cases but are very costly [16]. A major disadvantage to HDO process is that it requires a

Table 1.2: Analysis of properties of bio-oils and upgraded bio-oils [41].

Elemental analysis	High pressure liquefaction	Flash pyrolysis	Hydrodeoxygenated bio-oil
Carbon (wt %)	72.6	43.5	85.3-89.2
Hydrogen (wt %)	8.0	7.3	10.5-14.1
Oxygen (wt %)	16.3	49.2	0.0-0.7
Sulphur (ppm)	<45	29.0	50
H/C atom ratio	1.21	1.23	1.40-1.97
Density (g/mL)	1.15	24.8	0.796-0.926
Moisture (wt %)	5.1	24.8	0.001-0.008
HHV (MJ/kg)	35.7	22.6	42.3-45.3
Viscosity (cP)	15000 (61^{o}C)	59 (40^{o}C)	1.0-4.6 (23^{o}C)

large amount of hydrogen at high pressure. Table 1.2 depicts the properties and elemental analyses of raw bio-oil from liquefaction and pyrolysis and upgraded bio-oil from HDO [41]. It is seen from this table that wt % of carbon is increased to ~85-90 % when bio-oils were subjected to hydrodeoxygenation compared to the carbon content of unprocessed bio-oils due to pyrolysis (43.5%) and liquefaction (72.6%). Similarly, the oxygen content decreased to 0.0-0.7 wt % upon HDO of raw bio-oil and, therefore, the higher heating value (HHV) increased to 42.3-45.3 MJ/kg. Consequently, HDO process is able to upgrade the unprocessed bio-oil to a higher-end biofuel which can be useful in transportation.

1.7. Application of Density Functional Theory for Hydrodeoxygenation of Bio-oil Model Compounds

The density functional theory is based on electron density function unlike *ab initio* methods which are based on wavefunctions. The advantage with electron density function is that it remains a function of only three spatial variables no matter how big the molecule is, whereas, wavefunction methods also account for spin variable along with spatial variables for each

electron [42, 43]. Therefore, density functional theory methods have seen an astonishing rise in the popularity in the recent past. The application of density functional theory in chemistry and chemical research fields is vast including geometry optimization and their energetics, spectra of IR, UV, and NMR, chemical reactions and others. Recently, in the field of bio-oil upgrading, the application of DFT has increased enormously due to its ability to predict correct molecular structure and energy levels with high accuracy. It has been applied to investigate the favourable reaction mechanism amongst a vast reaction network of any particular bio-oil model compound to produce a specific product along with the prediction of activation energy, thermochemistry, kinetic parameters such as reaction rate constants, Arrhenius constants, and equilibrium rate constants.

There have been several numerical studies based on DFT to upgrade bio-oil model compounds, for instance, HDO of guaiacol [44–47], propanoic acid [48], furfural [49]; non-catalytic decompositions of guaiacol [50, 51], vanillin [52], glucose [53], fructose [54], and others. All of these numerical works carried out by numerous researchers showed an excellent correlation with their experimental counterparts. Therefore, the objectives of this thesis are considered under the framework of density functional theory.

1.8. Organization of Thesis

This dissertation deals with upgrading of phenolic catalogue of unprocessed bio-oil using vapour phase non-catalytic decomposition and catalytic hydrodeoxygenation of model compounds. The thesis is organized in following chapters:

- Chapter 1 presents the background of energy demands, types of renewable energy resources, biomass, conversion routes of lignocellulosic biomass, characteristics of bio-oil, problems to unprocessed bio-oil and upgrading techniques. Further, this chapter outlines

advantages and disadvantages of various upgrading techniques and the application of density functional theory in bio-oil upgrading process.

- Chapter 2 deals with the literature survey involving several experimental and numerical works dedicated to model compounds of cellulose, hemicellulose, and lignin fractions. Further, in lignin fraction, numerous phenolic model compounds such as guaiacol, vanillin, eugenol, salicylaldehyde and others are reviewed separately.
- Chapter 3 is about the objectives of this thesis based on the literature survey conducted in Chapter 2. There are eleven objectives dedicated to this thesis in which first seven objectives are about non-catalytic vapour phase decompositions of phenolic bio-oil model compounds; objectives 8 and 9 are about Pd catalytzed hydrodeoxygenation of salicylaldehdye and guaiacol, respectively; objective 10 carries out adsorption studies of phenolic bio-oil model compounds over Pd- and Pt-doped graphene sheets; and finally, objective 11 deals with the thermochemical analyses of transformation of glucose model compound into three long alkane chains (C9, C12, and C15).
- Chapter 4 is dedicated to compoutational methodology. It starts with the justification of selection of density functional theory (DFT) followed by mathematical explanation of DFT based on the works of Hohenberg & Kohn and Kohn & Sham to calculate the energy along with the algorithm. Thereafter, it describes various DFT functionals, basis set types, bond dissociation energy, adsorption energy, and kinetic modelling.
- Chapter 5 deals with the results and discussions of this thesis work. It is divided into eleven subchapters based on eleven objectives of this thesis.
- Chapter 6 is about conclusions and furture scopes. The individual conclusions of all subchapters of Chapter 5 are included under ‘Conclusions’ subsection. Thereafter, various future scopes are discussed in this chapter.

Chapter 2

LITERATURE REVIEW

In 1983, Furimsky [55] published a review paper on catalytic hydrodeoxygenation (HDO) process in the framework of crude oil upgrading. He discussed the details of chemistry, catalyst behaviour, mechanism, and kinetic study of hydrodeoxygenation process in crude oil upgrading. The main reason behind unfamed hydrodeoxygenation process earlier in 80s and 90s was due to intensifying appeal of crude petroleum oil. The oxygen content in crude petroleum oil is very less and sulphur content is high, therefore, the main hydrotreating process in petroleum refining industries was and is hydrodesulphurization (HDS) process. However, due to rapid declination of fossil fuels, increasing pollution and energy demand, researchers diverted their concerns towards biomass-to-bio-oil process but the case with raw bio-oil derived from pyrolysis or liquefaction of lignocellulosic biomass is quite reverse *vis-à-vis* petroleum fuel. In unprocessed bio-oil, oxygen content is quite high and sulphur appears as trace amounts, therefore, hydrodeoxygenation process is dominating in the bio-oil upgrading process. Following this trend, in the year 2000, Furimsky [56] reviewed another catalytic hydrodeoxygenation process with further extended range of investigations. This time, more detailed information was included about the compounds such as phenol, furan, ether, and other oxygenated compounds. In the recent past, numerous theoretical and experimental works were devoted to analyse the potential of all building blocks of biomass and compounds derived from these building blocks. As it is mentioned in the 'Introduction' section that cellulose and hemicellulose fractions were considered very often compared to lignin fraction, the advancements in former fractions are briefly discussed first followed by elaborated discussion on the lignin building block and major phenolic compounds derived from lignin fraction such as guaiacol, vanillin, eugenol, and others.

2.1. Cellulose and Hemicellulose Fractions

In the year 2005, Huber et al. [57] reported the production of liquid alkanes (ranging from C_7 to C_{15}) from biomass derived carbohydrates by aqueous phase processing over solid base catalysts. They reported three liquid alkane products *viz.* C_9, C_{12} and C_{15} produced from C_6-sugar feedstock over various base catalysts. Ragauskas et al. [5] reported reaction routes for producing bio-oils and special platform chemicals such as 5-hydroxymethyl furfural (5-HMF), levulinic acid, and others from biomass. They also discussed the implementation and link among biofuels, biopower, and biorefineries. Huber et al. [1] presented a thorough review on synthesis of transportation fuels from biomass. They reported the chemistry of biomass, transformation routes of biomass to bio-oil and catalysis in bio-oil transformation into special chemicals or upgraded biofuels. Schmidt et al. [58] reviewed hybrid routes to biofuels in which they reported the production of synthetic diesel, ethanol, 5-HMF and dimethylfuran (DMF) from the starch polymer. They reported three pathways: 1) conventional thermochemical route to biofuels, 2) conventional biological route to convert the starch to glucose followed by the production of ethanol, and 3) hybrid route that enzymatically converted starch into fructose. Kunkes et al. [59] carried out catalytic conversion of biomass to monofunctional hydrocarbons in which they targeted the productions of liquid fuel and chemical over various catalysts such as Pt-Re/C, Pd/CeZrOx, and others at various temperature ranges. Lin et al. [29] reviewed the role of heterogeneous catalysis in the conversion of lignocellulosic biomass into liquid fuels. They provided an insight of catalytic processing in biomass conversion using various routes such as *syngas* conversion, selective thermal processing, liquid phase catalytic processing, and integration with the petrochemical refinery. In continuation of this, Bond et al. [60] carried out a catalytic conversion experiment of γ-valerolactone (GVL) in to liquid alkenes for transportation fuels followed by the work of Lange et al. [61] about the production of valeric biofuels from cellulosic building block of biomass. Bond et al. [60] indicated the conversion

of GVL into butene upto 99 % over SiO_2/Al_2O_3 catalyst at 648 K and 36 bar pressure. Lange et al. [61] reported the selectivity and productivity of reaction progresses C_6-sugar → levulinic acid → γ-valerolactone → valeric acid → alkyl (mono/di)valerate esters. Stöcker [4] reviewed catalytic conversion processes of lignocellulosic biomass using porous material in which he pointed out the generations of biofuels, e.g., first generation bio-fuels such as methanol and ethanol from sugarcane; second generation biofuels obtained by gasification followed by the Fischer-Tropsch process to convert biomass to liquids (BTL). He also pointed out major reactions occurring in fluidized catalytic cracking, decarboxylation, hydrotreating, and hydrodeoxygenation. Assary et al. [53] carried out a numerical study to investigate the thermochemistry involved in the conversion of glucose to levulinic acid. They found that first two dehydration steps and glucose-to-fructose conversions were endothermic reactions but the rehydration reaction to form levulinic acid reported exothermicity. Alonso et al. [14] reviewed the catalytic conversion of biomass to biofuels and covered a vast work starting from lignocellulosic biomass structures to approaches for the conversion of lignocellulosic biomass to liquid fuels. They also revealed the selective transformations about platform chemicals such as furfural, 5-HMF, levulinic acid and γ-valerolactone. Assary et al. [62] further published a numerical study on thermochemical investigation for the dissociation of 5-HMF to C_9 alkanes with various intermediates using G4 theory and compared the results with other theories such as G4MP2, MP2, and others.

There have been numerous experimental and theoretical works performed over cellulose and hemicellulose fractions in which a few of them are discussed above. However, as it is pointed out earlier that lignin fraction recently engaged a substantial attention, it is elaborated intensively in various subsections below.

2.2. Lignin Fraction

The lignin fraction did not attract researchers' attentions at higher level because of its complex three dimensional structure due to which the lignin fractions were used to be either scrapped off or to produce low efficiency heat and electricity. Apart from numerous review works over cellulose and hemicellulose building blocks of biomass, recently, a few literature reviews were solely devoted to discuss the lignin fraction of lignocellulosic biomass [8, 16, 23, 24, 26, 27]. For instance, Pandey and Kim [23] reviewed thermochemical methods for the depolymerization of lignin and their conversion in to smaller fractions. They reported that conversion of lignin in to liquid fuels is favourable while treated thermally in hydrogen environment. Bu et al. [63] reviewed the upgrading of lignin derived phenol compounds such as phenol, *o*-, *m*-, and *p*-cresol over various catalytic systems. They concluded that various sections need improvements or whole attention, for instance,

i) synthesis of an improved catalyst for upgrading bio-oils

ii) investigation of an alternate hydrogen source for hydrotreating; iii)

iii) detailed kinetic analysis

iv) optimization of reaction conditions so that they could be employed in biorefineries.

Mu et al. [8] reviewed upgrading of lignin derived bio-oil compounds and they presented detailed phenomena of numerous catalysts and their deactivation along with the roles of supporters and promoters for the catalyst. They reported poor performance of sulfided metal catalysts in upgrading of bio-oil compared to that of noble metal catalysts. Similarly, Saidi et al. [16] reviewed upgrading of lignin derived bio-oil model compounds such as guaiacol, phenol, anisole, and others with corresponding reaction networks and mechanisms. They included several catalytic systems such as mono metallic, bimetallic, metal sulphides, metal phosphides, metal nitrides catalysts along with the promoters and supporters to the catalyst.

They also concluded that noble metal catalysts are advantageous over sulfided metal catalysts for hydrodeoxygenation reactions. Davis et al. [64] reviewed about the recovery mechanism of lignin and its thermochemical depolymerization for the production of liquid fuel. Furthermore, they reviewed biological and chemical pathways for upgrading mechanisms of lignin monomer compounds.

Further, there exists various important phenolic components in unprocessed bio-oil resulting from pyrolysis of lignin feedstocks or from phenolic catalogue of bio-oil such as guaiacol, anisole, vanillin, eugenol, and others (see Figure 1.8) which are not only a great source of obtaining the aromatic hydrocarbons for fuel but also can be utilized to obtain numerous specialty chemicals. Separate literature review for each major phenolic compound is carried out in following subsections.

2.2.1. Vanillin

Vanillin (3-methoxy-4-hydroxy-benzaldehyde) is one of the most key components in phenolic catalogue of bio-oil obtained from biomass pyrolysis/liquefaction because it contains one of the highest proportions of phenolic fractions of bio-oil [8, 34, 65–67]. Peng et al. [68] carried out the pyrolysis of rice husk and found vanillin as 2.37 area % in raw bio-oil. Vanillin comprises of three oxy-functional groups, namely, hydroxyl, methoxy, and aldehyde group; and thus it is one of the best representations of phenolic fractions present in bio-oil [66, 67, 69]. Shin et al. [70] carried out a pyrolysis experiment on vanillin and reported various products such as phenol, benzene, cyclopentadienyl, guaiacol, and dihydroxybenzaldehyde. Bindwal and Vaidya [67] carried out hydrogenation of vanillin over Ru/C heterogeneous catalyst experimentally and reported creosol as the end product with vanillin alcohol as an intermediate. They also reported reaction kinetics of their proposed reaction scheme. On the other hand, Liu et al. [71] carried out a combined experimental and computational study on vanillin pyrolysis

over various temperature values and reported guaiacol as major product. The other detected components from vanillin pyrolysis are phenol, hydroxybenzaldehyde, catechol, carbon mono oxide, and 5-formylsalicylaldehyde. Wang et al. [52] carried out computational study on vanillin pyrolysis and reported products such as benzene, phenol, dihydroxybenzaldehyde, and others. Further, they also reported thermochemistry over various temperature values.

It is found by this literature survey that the conversion of vanillin has not been studied extensively, however, there are a very few experimental [67, 70, 71] and computational studies [71, 52] on vanillin pyrolysis are available to the best of authors' knowledge.

2.2.2. Eugenol

Eugenol comprises of two oxy-functionals *viz.* hydroxyl and methoxy functional groups; and an alkenyl functional [72–74]. Eugenol component is observed as one of the product in many lignocellulosic biomass pyrolytic study [8, 65]. The number of carbon atoms in the eugenol ($C_{10}H_{12}O_2$) is more than other competitive model components of phenolic fraction of bio-oil, e.g., guaiacol ($C_7H_8O_2$) [44, 46, 75], catechol ($C_6H_6O_2$) [44, 47], phenol (C_6H_6O) [76, 45, 77], vanillin ($C_8H_8O_3$) [71, 52], etc. which can be significant in the production of many specialty or platform chemicals. There has been a few experimental studies [72–74, 78–80] on eugenol as the bio-oil model compound and only a single combined, i.e., both experimental and computational study [80] of eugenol as the bio-oil model compound is available in the literature to the best of authors' knowledge. For instance, Nimmanwudipong et al. [73] carried out conversion of eugenol in the presence of Pt/γ-Al_2O_3 and HY zeolite catalysts; and reported various products, e.g., phenol, guaiacol, veratrole, 4-propylguaiacol, 4-propylphenol, and *p*-cresol. They reported guaiacol and isoeugenol as major products using zeolite catalyst, whereas, 4-propyl-guaiacol as major product from Pt/γ-Al_2O_3 catalyst. On the other hand, Zhang et al. [74] carried out experiments of eugenol hydrogenation/deoxygenation over Pd/C

and HZSM-5 catalysts; and reported that eugenol first underwent allyl hydrogenation to produce 4-propyl-guaiacol followed by ring saturation to produce 2-methoxyl-4-propyl-cyclohexanol. Deepa and Dhepe [79] carried out hydrodeoxgenation experiments of eugenol in the presence of noble metal catalysts; and they schemed that eugenol first underwent saturation of allyl followed by ring saturation. Horácek et al. [72] also suggested that eugenol first underwent allyl hydrogenation over zeolite supported platinum catalyst. Chen et al. [78] carried out hydrodeoxygenation of eugenol over carbon nanotube (CNT) supported ruthenium catalyst and reported propylcyclohexane as final alkane product with 4-propyl-guaiacol and 4-propylcyclohexanol as intermediate products. A combined study of eugenol decomposition in vapour phase carried out by Ledesma et al. [80] and they reported methane, ethylene, acetylene, propylene, benzene, CO, and 1-butene as the major products.

Finally, it can be understood from the literature review that eugenol component has been studied by only a few experimental researchers and only one computational work due to Ledesma et al. [80]. Eugenol can be decomposed by various possible reaction mechanisms; however, Ledesma et al. [80] carried out only one reaction pathway which initiated from the dehydrogenation of hydroxyl functional.

2.2.3. Ferulic Acid

Ferulic acid ($C_{10}H_{10}O_4$) is a phenolic bio-oil model compound which comprises the representation of three oxy-functional groups *viz.* alcohol, ether, and carboxylic groups [81, 82]. The presence of ferulic acid in the lignin pyrolysis products is avowed by Jiang et al. [34] in their pyrolytic study of Alcell and Asian lignin samples. They carried out pyrolysis of Alcell and Asian lignin samples in the range of 400-800^{o}C and concluded ferulic acid as one of the pyrolytic product in pyrolysis GC-MS analyses. They stated that the temperature rise from 400^{o}C to 600^{o}C increases the fraction of ferulic acid in product compositions but beyond

600°C, a decline in the amount of ferulic acid is recorded. Various other literatures confirm the presence of ferulic acid in the product composition of pyrolysis of lignin or lignocellulosic biomass [8, 83–86]. Further reduction of ferulic acid has been carried out by a few researchers. For instance, Fiddler et al. [87] carried out the thermal decomposition of ferulic acid and observed various products such as guaiacol, methyl- and ethylguaiacol, *p*-vinylguaiacol, vanillin, *cis*-isoeugenol, and acetovanillone. The decomposition of ferulic acid by Fiddler et al. [87] was carried out in two stages; first stage reduced the ferulic acid into *p*-vinylguaiacol. In second stage, they found the presence of 4-methylguaiacol, 4-ethylguaiacol, and other aforementioned products on the expense of *p*-vinylguaiacol intermediate component. However, the productions of vanillin, vanillic acid, and acetovanillone were observed in the air environment. On the other hand, Wit et al. [88] carried out experiment of ferulic acid conversion in the presence of copper powder and they synthesized *p*-vinylguaiacol as primary product. The experimental work of Wit et al. [88] affirmed the formation of *p*-vinylguaiacol as also observed by Fiddler et al. [87]. Karmakar et al. [82] carried out the conversion of ferulic acid and they also reported the formation of *p*-vinylguaiacol as an intermediate using decarboxylation reaction of ferulic acid. Further, the component *p*-vinylguaiacol was synthesized to vanillin, vanillic acid, protocatechuic acid in their experiment. Mathew et al. [89] also performed the conversion of ferulic acid and they too observed the production of *p*-vinylguaiacol as an intermediate which further undergoes the formation of vanillin. Furthermore, the vanillin component undergoes oxidation and reduction processes to produce vanillic acid and vanillyl alcohol, respectively. Hasyierah et al. [86] presented a wide reaction network for degradation of ferulic acid enzymatically to yield vanillin with various intermediate products. They reported the formations of various intermediate value added products such as caffeic acid using demethylation of ferulic acid, *p*-vinylguaiacol using decarboxylation of ferulic acid, coniferyl alcohol using hydrogenation and hydrogenolysis, etc.

The intermediate *p*-vinylguaiacol directly underwent the formation of vanillin; however, the intermediate coniferyl alcohol first reduced to vanillic acid followed by the formation of vanillin.

It can be observed from the literature review that the thermal degradation of ferulic acid results into various products; however, the presence of *p*-vinylguaiacol and vanillin is often observed by most of the cited researchers. It is noticed from aforementioned literature survey that most experimental works regarding the decomposition of ferulic acid were carried out in the context of food chemistry with the objective of formation of vanillin which is a very important substance in food industry. The literature about ferulic acid in the context of biomass or bio-oil is very limited. Apart from a few experimental works regarding the thermal decomposition of ferulic acid, authors have not found any theoretical work which is devoted to the decomposition of ferulic acid.

2.2.4. Guaiacol

Out of many phenolic compounds present in unprocessed bio-oil, guaiacol is the most widely considered model compound which is abundantly available in lignin derived bio-oil. Guaiacol contains two oxy-functional groups, i.e., hydroxyl group and methoxy group attached to phenyl ring. Extensive research based on HDO of guaiacol model compound has been reported on the basis of experimental studies in the presence of various catalysts such as Pt/γ-Al_2O_3 [90, 91], Pt/MgO [90], Pt/C [92–94], Pd/C [92–96], Ru/C [92–95, 97], Rh/C [92, 94], Ru/Al_2O_3 [91, 97], Ni-Mo/TiO_2 [98], Mo/C [95, 99], Ni–Cu/SiO_2–ZrO_2–La_2O_3 [100], CoMo/ϒ-Al_2O_3 [101], Fe/SiO_2 [102], Ni-V/TiO_2 [98], etc. For instance, Nimmanwudipong et al. [90] carried out HDO of guaiacol in the presence of Pt/MgO and Pt/Al_2O_3 catalysts. They reported higher product selectivity using Pt/MgO catalyst compared to Pt/Al_2O_3. Primary products due to Pt/MgO catalyst were phenol, catechol, benzene, and anisole. However, they also found

considerable fractions of cyclohexanone and cyclopentanone in the product mixture. The production of cyclohexanone occurred due to HDO and ring hydrogenation of guaiacol while the cyclopentanone production from guaiacol involved ring opening, decarboxylation and ring closing reaction steps. The formations of cyclopentanone, catechol and phenol were also reported by Gao et al. [92, 103] who carried out HDO of guaiacol in the presence of Pt/C catalyst. Hurff and Klein [101] carried out hydrodeoxygenation of anisole and guaiacol compounds over pre-sulfided CoMo/ϒ-Al_2O_3 catalysts. They reported major products as phenol, benzene, and cyclohexane in HDO of anisole while catechol, phenol, benzene, and cyclohexane in HDO of guaiacol. Olcese et al. [102] performed experiments on gas phase hydrodeoxygenation of guaiacol in the presence of Fe/SiO_2 catalyst. According to their results, hydrogenation of guaiacol first underwent demethoxylation to produce phenol followed by the formation of benzene and finally hydrogenation of benzene gave rise to cyclohexane. Boonyasuwat et al. [97] performed HDO of guaiacol over C, TiO_2, SiO_2, and Al_2O_3 supported Ru catalysts. They reported better catalytic activity and stability for Ru/TiO_2 catalyst compared to others; and the primary products were phenol, cresol and benzene. Gao et al. [92] carried out HDO of guaiacol in the presence of activated carbon supported Pt, Pd, Ru, and Rh catalysts. For all catalytic systems, phenol was observed as most abundant product with various other significant fractions such as catechol, cresol, cyclopentanone and anisole. Sun et al. [93] carried out HDO of guaiacol over carbon-supported metal (Pd, Pt, Cu, Ru, etc.) catalysts. They reported phenol component as primary intermediate product; however, precious noble metals led to the formation of ring-saturated products such as cyclohexanone, cyclohexanol, etc. while the base metals produced benzene as end product.

A few theoretical approaches have also been performed for upgrading guaiacol. For instance, Lee et al. [46] performed HDO of guaiacol over Pt(111) catalyst and reported that the guaiacol underwent through dehydrogenation reactions of methoxy functional group instead of

direct functional cleavages such as dehydroxylation, demethylation, and demethoxylation; and catechol was major product. Lu et al. [45] over Pt(111) catalyst also reported catechol as major product in HDO of guaiacol. The dominating reaction pathway underwent through dehydrogenation of methoxy group of guaiacol followed by dissociation of CH_2 group of 2-methylene-oxy-phenol and a single step hydrogenation reaction of hydrogen-catecholate to produce catechol [45]. Chiu et al. [47] carried out HDO of guaiacol over Ru(0001) catalyst and their computations reported catechol component as major product while the phenol and benzene as intermediate and end products, respectively. They [47] reported that HDO of guaiacol favoured the pathway of dehydrogenation of hydroxyl group of guaiacol followed by dehydrogenation of guaiacolate to produce 2-methylene-oxy-phenolate. Further, 2-methylene-oxy-phenolate underwent a dehydrogenation reaction to produce 2-methylidyne-oxy-phenolate followed by CH removal reaction of 2-methylidyne-oxy-phenolate to produce catecholate [47]. Finally, a molecular hydrogenation reaction of catecholate produced catechol [47]. Lu et al. [44] also performed HDO of guaiacol over Ru(0001) catalyst in addition to Pt(111) catalyst [45] with full microkinetic modelling; however, unlike to the Pt(111) catalyst, they reported phenol as major product over Ru(0001) catalyst. Over Ru(0001) catalyst, Lu et al. [44] found the favourable reaction progress of HDO of guaiacol undergoing through dehydrogenation of hydroxyl group of guaiacol to produce guaiacolate followed by full dehydrogenation of methoxy fragment of guaiacolate to produce 2-carbide-oxy-phenolate. This trailed through the decarbonylation reaction of 2-carbide-oxy-phenolate to produce 2-oxyphenyl and CO species followed by molecular hydrogenation of 2-oxyphenyl that gave rise to phenol [44]. Liu et al. [50] carried out the vapour phase decomposition of guaiacol in the absence of catalyst using density functional theory and proposed five reaction schemes initiating from guaiacol as:

i) homolysis of methyl group

ii) homolysis of methoxy group

iii) hydrogenation at carbon atom of $C_{aromatic}$-OCH_3 bond followed by cleavage of methoxy group

iv) migration of hydrogen atom from hydroxyl group to the carbon atom of $C_{aromatic}$-OCH_3 bond followed by the cleavage of methoxy group, and

v) rearrangement of methoxy group which yields *o*-quinonemethide.

It can be seen from aforementioned literature review that theoretical works on HDO of guaiacol are a very few compared to their experimental counterparts. Further, to the best of authors' knowledge, theoretically only platinum [46, 45, 103] and ruthenium [44, 47] catalysts are employed for HDO of guaiacol though a few non-catalytic numerical pyrolytic studies of guaiacol are also available in the literature [50, 51]. Furthermore, experimentally it has been demonstrated that the noble metal catalysts are the best catalytic systems because of higher conversion, higher yield, low or no poisoning, less deactivation, advantageous in gas or aqueous phase, etc. [16] Amongst various noble metal catalysts, palladium is often utilized as catalyst in bio-oil upgrading because of low cost and abundance. In addition, Pd and supported Pd metal catalysts often offer better resistant towards C-O poisoning which is one of the major problem in bio-oil because of huge organic oxygenated compounds [16]. Therefore, palladium catalyst could be a better option for bio-oil upgrading.

2.2.5. Salicylaldehyde (2-Hydroxybenzaldehyde)

Amongst various oxy-functional compounds present in unprocessed bio-oil, salicylaldehyde (also called 2-hydroxybenzaldehyde) [8] component of raw bio-oil comprises two oxy-functional groups, namely, hydroxyl and formyl functionals attached to phenyl ring. However, a few researchers [104–107] have pointed out the formation of 2-hydroxybenzaldehyde from guaiacol component through hydrogen-migration reactions of methoxy substituent of guaiacol. For instance, Robichaud et al. [104] carried out thermal decomposition of *o*-, *m*-, and *p*-

dimethoxybenzene at high temperatures and reported guaiacolate as an intermediate which further underwent hydrogen-migration and 1,3-aryl shift reactions to produce 2-hydroxybenzaldehyde. Similarly, Huang et al. [105] carried out the pyrolysis processes of α-O-4 linkage lignin dimer model compound and they also reported the guaiacolate as an intermediate in the process of 2-hydroxybenzaldehyde production. On the other hand, Zhang et al. [106] carried out pyrolysis of a non-phenolic lignin dimer model compound with β-O-4 linkage aiming to produce 2-hydroxybenzaldehyde as the final product through guaiacolate as an intermediate. Custodis et al. [107] carried out pyrolysis of guaiacol and reported 2-hydroxybenzaldehyde component as one of their products. Similarly, Huang et al. [51] also reported the formation of 2-hydroxybenzaldehyde from guaiacol; which further converts to phenol by decarbonylation reaction.

It is found that researchers have only carried out their experiments till the production of 2-hydroxybenzaldehyde component which contains two oxygen atoms in the form of formyl and hydroxyl functionals attached to phenyl ring. As a result, 2-hydroxybenzaldehyde still needs to be converted till both oxygen atoms are removed.

2.2.6. *p*-Isopropenyl Phenol

p-Isopropenylphenol (*p*-IPP) [8] as a model compound represents phenolic fraction of bio-oil. It comprises of hydroxyl and isopropenyl groups attached to phenyl ring [8]. The presence of *p*-IPP component in unprocessed bio-oil is reported by various researchers [8, 34]. For instance, Jiang et al. [34] carried out pyrolysis of Asian lignin over various temperature and found that *p*-isopropenylphenol component was quantified in the pyrolysis GC-MS analyses at each temperature. Mu et al. [8] also reviewed the presence of *p*-isopropenylphenol component in pyrolytic products. McClymont et al. [108] carried out pyrolysis of eight various *Sphagnum* moss plant species and outlined the major presence of *p*-isopropenylphenol component along

with phenol and 4-ethylphenol. On the other hand, they did not find any trace of *p*-isopropenylphenol component in the pyrolysis processes of non-*Sphagnum* moss, sedge, and other peat forming plants. The production of *p*-isopropenylphenol can occur by two subsequent decarboxylation reactions of sphagnum acid [108]. In addition, it is to be noted that the synthesis of *p*-isopropenylphenol component has also been attempted by various researchers from the cleavage of bisphenol A [109–112].

The literature regarding decomposition of *p*-isopropenylphenol is not available as far as authors' knowledge. Since, the abundance of this component in *Sphagnum* moss pyrolytic bio-oil is already discussed, its further conversion into low molecular weight fractions or special chemicals should also be debated in order to fill the information gap.

2.2.7. 2-Hydroxy-6-methylbenzaldehyde (HMB)

2-Hydroxy-6-methylbenzaldehyde (HMB), comprising hydroxyl, aldehyde, and methyl groups attached to phenyl ring, is one of organic oxygenated compounds often found in the unprocessed bio-oil derived from pyrolysis of lignin feedstock [113–116]. The presence of HMB is frequently reported in pyrolysis of lignin feedstock, for instance, Nowakowski and Jones [115] performed pyrolysis of chlorogenic acid, a lignin feedstock, in uncatalyzed and potassium catalyzed environments and found HMB component as one of the important product from both environments along with phenol, catechol, 4-ethylcatechol, benzoic acid, etc. The formation of HMB component from uncatalysed decomposition of chlorogenic acid occurred *via* an intermediate component 1,3,4,5-tetrahydroxycyclohexane-1-carboxylic acid; however, potassium catalysed environment did not show its formation as an intermediate. Djokic et al. [116] carried out analyses of crude bio-oil derived from pine wood and Ru/C hydrotreated bio-oil analytically. They also affirmed the presence of HMB component in unprocessed bio-oil; however, after hydrotreatment of bio-oil over Ru/C catalyst, the presence of HMB component

vanished because of its reduction into lower fractions. Similarly, several other literature studies have reported its presence in unprocessed bio-oil [8, 34, 113] but to the best of authors' knowledge, further decomposition of HMB has not been reported in the literature.

Finally, it can be seen from the above literature survey that lignin fraction of lignocellulosic biomass needs a proper attention irrespective of its complex structure because it offers numerous advantages compared to other two fractions of lignocellulosic biomass. The experimental works based on phenolic catalogue of unprocessed bio-oil are available in considerable number; however, the same is not true with their computational counterparts. A very few computational investigations are carried out using phenolic model compounds as representative compounds of unprocessed bio-oil. Since computational investigations can be very beneficial and expressive in finding out the prevailing or rate determining reaction step, kinetics, thermodynamics, and others, here in this dissertation, numerous phenolic model compounds are considered to elucidate their decomposition mechanisms in to corresponding lower fraction products. Furthermore, two model compounds, namely, guaiacol and 2-hydroxybenzaldehyde, are considered to investigate their catalytic hydrodeoxygenation over Pd(111) catalyst. Further details can be found in the next chapter called "Objectives of Thesis".

OBJECTIVES OF THESIS

It is evident from numerous literature that bio-oil, collectively, is comprised of hundreds of oxy-organic compounds in various oxy-catalogues but, in particular to phenolic fraction, only guaiacol compound is studied extensively either using experiments or computations. However, a few other compounds such as vanillin and eugenol are also considered as model representations but there exists a huge information gap regarding their upgrading mechanisms. Further, there are numerous phenolic or aromatic oxygenated compounds present in phenolic catalogue of bio-oil which have not yet drawn any attention for their upgrading into smaller fractions such as ferulic acid, *p*-isopropenylphenol, 2-hydroxybenzaldehyde, 2-hydroxy-6-methylbenzaldehyde, and others. Therefore, such aromatic oxygenated compounds are considered here in this work for their vapour phase decomposition into various smaller fraction aromatic compounds under the framework of density functional theory (DFT). It is also seen from literature review that various high non-volatile compounds such as vanillin, ferulic acid, eugenol, etc. produce a common major product, i.e., guaiacol, therefore, a catalytic hydrodeoxygenation study is performed using palladium catalyst to investigate its upgrading mechanism. In addition, salicylaldehyde is also considered for catalytic hydrodeoxygenation study similar to that of guaiacol. Furthermore, five phenolic compounds, i.e., phenol, anisole, guaiacol, salicylaldehyde, and vanillin are considered as model representations to understand the surface phenomena of Pd- and Pt-doped graphene sheets.

As it is discussed that cellulose fraction is a polymer of C_6-glucose compounds, here, in this study, we have considered C_6-glucose as model compound of cellulose building block and numerically generated three long chain carbon products, namely, C_9H_{20}, $C_{12}H_{26}$, and

$C_{15}H_{32}$ alkanes. The reaction mechanisms for this work are adapted from Huber et al. [57] with proper permission. Therefore, the objectives of this thesis are as follows:

1) Molecular modelling approach to elucidate the thermal decomposition routes of vanillin

2) Gas phase conversion of eugenol into various hydrocarbons and platform chemicals

3) Unravelling the dissociation mechanism of ferulic acid under density functional theory framework

4) DFT analyses of reaction pathways of various guaiacol conversion reactions in gas phase environment

5) Production of benzene from 2-hydroxybenzaldehyde by various reaction paths using IRC calculations within density functional theory framework

6) Quantum chemical study on gas phase pyrolysis of *p*-isopropenylphenol

7) DFT study on the production of toluene from decomposition reactions of 2-hydroxy-6-methylbenzaldehyde

8) Molecular simulations of palladium catalyzed hydrodeoxygenation of 2-hydroxybenzaldehyde using density functional theory

9) Elucidation of Gas Phase Hydrodeoxygenation Mechanism of Guaiacol over Pd(111) Catalyst Surface: The DFT Framework

10) Pt- and Pd-doped graphene sheets as catalysts for upgrading bio-oil model compounds: chemisorption study by density functional theory

11) Thermochemistry analyses for transformation of C_6 glucose compound into C_9, C_{12} and C_{15} alkanes using density functional theory

COMPUTATIONAL INSIGHTS

Molecular modelling is a set of methods to explore various chemistry problems on a computer platform such as molecular geometries and their energetics, chemical reactivity, spectra of IR, UV and NMR, substrate-enzyme interaction, physical and chemical properties of substances. To investigate these chemical problems, there are several computational chemistry tools available such as molecular mechanics, ab initio methods, semi-empirical methods, and density functional theory methods. Molecular mechanics (MM) model of any particular molecule acts as a collection of balls held together by springs where balls and springs represent atoms and chemical bonds, respectively [42]. The calculation of minimum-energy geometry in molecular mechanics corresponding to optimum bond lengths, angles, and dihedrals of a molecule is based on energy equation which is a function of the resistance towards bond bending, bond stretching, and atom crowding. The atoms and molecules, with few exceptions, can be described using classical mechanics but the electronic structure calculations can solely be described using quantum mechanical approach because electrons are much lighter than nuclei. Molecular mechanics is computationally inexpensive, however, it ignores electrons which limits its application in chemical reaction based system where electron flow is a major assignment. On the other hand, ab initio methods are based on the Schrodinger equation which is a fundamental equation of modern physics and explains the behaviour of electrons in a molecule. Upon solving the Schrodinger equation for a particular molecule, ab initio methods yield energy and wavefunction. For more than one electron system, the Schrodinger equation cannot be solved exactly, thus, various approximations require to be included [42]. Similarly, semi-empirical methods are also based on Schrodinger equation but utilizes a large number of approximations. The complicated integrals in semi-empirical methods are parameterized to in-

house best fitting experimental values in the program [42]. Hence, semi-empirical methods are much faster compared to ab initio methods but much slower to molecular mechanics methods. Similar to ab initio and semi-empirical methods, density functional theory (DFT) is another computational chemistry tool and also based on Schrodinger's equation; however, unlike to both methods, it does not derive conventional wavefunction rather it directly derives the electron density distribution to calculate physical properties [117–119]. DFT is relatively faster than ab initio methods but much slower compared to semi-empirical methods. Density functional theory methods are based on the electron density which is a function of three spatial parameters (x, y, and z) no matter how big the molecule is. On the other hand, wavefunction of a molecule containing *n* number of electrons is a function of 4*n* (three spatial coordinates and one spin coordinate) variables for each electron, thus, a 10 electron molecule will have 40 variables [42]. But, irrespective of how big the molecule is, electron density remains a function of three variables only and this is one of the major reasons why DFT method is widely hailed.

4.1. Density functional theory (DFT)

Prior to proceed to the details of DFT theory, it is beneficial to understand the concepts of function and functional. A function is a rule which transforms a number into another number and a functional is a rule which transforms a function into a number. For instance, for a variable x, the function $f(x)$ and functional $F[f(x)]$ are:

$$f(x)=x^2 \Rightarrow F[f(x)]=\int_0^3 f(x)dx=\left.\frac{x^3}{3}\right|_0^3=9 \qquad (4.1)$$

Therefore, a functional $\int_0^3 f(x)dx$ transforms the function x^2 into a number nine. A functional is usually designated as:

$$\int_0^3 f(x)dx = F[f(x)] \tag{4.2}$$

Similar to a function, the electron density function can be designated as $\rho(x, y, z)$.

4.1.1. Electron density

Density functional theory calculates all atomic and molecular properties from the electron density (also known as electron probability density or electron density function). The electron density is advantageous over wavefunction by several ways, for instance, i) it is a measurable entity, e.g. by X-ray diffraction or electron diffraction, ii) it is mathematically more traceable compare to wavefunction, and iii) it is intuitively comprehensible [43]. The electron density for a one-electron system is the square of wavefunction ψ at any point X; however, for a multi-electron system, it is more complicated and defined by the number of electrons in the molecule times the sum over all their spins of the integral of the square of the molecular wavefunction integrated over the coordinates of all but one of the electrons [42, 117, 43, 120].

$$\rho(\mathbf{r}) = N \sum_{s_1} \ldots \sum_{S_N} \int d\mathbf{r}_2 \ldots \int d\mathbf{r}_N \left|\Psi(\mathbf{r}_1, s_1, \mathbf{r}_2, s_2, \ldots \mathbf{r}_N, S_N)\right|^2 = \left\langle \Psi \middle| \hat{\rho}(\mathbf{r}) \middle| \Psi \right\rangle \tag{4.3}$$

The idea of calculating atomic or molecular properties from electron density appears from the independent works on an ideal electron gas by E. Fermi and P.A.M. Dirac in 1920s (currently known as Fermi-Dirac Statistics). According to Fermi [121] and Thomas [122], atoms were demonstrated as a system with positive potential, i.e., the nucleus, in a uniform homogeneous electron gas. This is called Thomas-Fermi model [43, 121, 122]; however, further developments by Dirac led to introduce the Thomas-Fermi-Dirac model [43, 121, 122]. This model presented decent outcomes for atoms but failed entirely for molecules. Nowadays, all DFT calculations for molecules are based on Kohn-Sham method [117, 118, 123]; however, its foundation was created by Hohenberg and Kohn [118].

4.1.2. The Hohenberg–Kohn (H-K) Theorems

The *first Hohenberg-Kohn theorem* states that all properties of any specific molecule in a ground electronic state are determined by the ground state electron density function, i.e., $\rho_0(x, y, z)$ [118, 43]. For instance, the ground state energy E_0 can, in principle, be determined by the ground state electron density function:

$$\rho_0(x, y, z) \rightarrow E_0 \tag{4.4}$$

In other words, according to the *first Hohenberg–Kohn theorem*, any ground state property of a molecule is a functional of the ground state electron density function. For instance, if ground state energy is a functional of electron density:

$$E_0 = F[\rho_0] = E[\rho_0] \tag{4.5}$$

The major concern with the *first H-K theorem* is that, though it assures about the existence of functional *F* in principle but does not recommend on how to find it. Nevertheless, the *second Hohenberg–Kohn theorem* states that any trial electron density function will provide an energy higher than (or equal to, if it were exactly the true electron density function) the true ground state energy [118, 43], i.e.,

$$E_v[\rho_t] \geq E_0[\rho_0] \tag{4.6}$$

where E_v is trial energy; ρ_t is a trial electronic density; and $E_0[\rho_0]$ is the true ground state energy corresponding to the true ground state electron density ρ_0. Further, the trial electron density ρ_t must satisfy two conditions that are:

$$\int \rho_t(\mathbf{r}) d\mathbf{r} = n \tag{4.7}$$

$$\rho_t(\mathbf{r}) \geq 0 \tag{4.8}$$

The eq. (4.7) is analogous to wavefunction normalization condition where the number of electrons '*n*' in all infinitesimal volumes must be equal to total number in molecule. Eq. (4.8) which states that the number of electrons per unit volume must not be negative.

According to eq. (4.6), any calculated energy with trial electron density will be upper bound to the true energy; however, the exact functional is still unknown, therefore, actual DFT calculations employ approximate functionals and thus are not variational which means that they may give an energy lower to the true energy also.

4.1.3. The Kohn–Sham (K-S) Energy and K-S Equations

The *first Kohn-Sham theorem* states that it is worth looking for a way to calculate ground state property of any molecule from electron density. The *second Kohn-Sham theorem* states that a variational approach might yield a way to calculate the energy and electron density which could be utilised to calculate other molecular properties [42, 43, 123]. Two basic ideas behind K-S approach are: (1) to express the molecular energy as a sum of different terms with one of which, relatively small term (because even if large error occurs in this term, there would not be significant change in total energy), carries the 'unknown' functional. (2) To use an initial guess of electron density ρ in K-S equations to calculate the initial guess of K-S orbitals and energy levels; this initial guess is then used to iteratively refine the initial guessed orbitals and energy levels [42, 43].

4.1.3.1. The Kohn–Sham (K-S) Energy

In Kohn-Sham energy, it is strategized to separate the electronic energy into various fractions which can be calculated accurately without the use of DFT and a relatively small term that require a vague functional. The concept of a fictitious non-interacting reference system is the key idea in this approach and defined as the one in which the electrons do not interact and the

ground state electron density ρ_r is same as real ground state system, i.e., $\rho_r = \rho_0$. Therefore, the ground state electronic energy of a molecule is sum of the electron kinetic energies (T), the nucleus-electron attraction potential energies (V_{Ne}), and the electron–electron repulsion potential energies (V_{ee}), respectively in eq. (4.9):

$$E_0 = \langle T[\rho_0] \rangle + \langle V_{Ne}[\rho_0] \rangle + \langle V_{ee}[\rho_0] \rangle \tag{4.9}$$

The angle brackets $\langle\ \rangle$ are quantum-mechanical average values or "expectation values" and can be explained by:

$$\langle Q \rangle = \langle \psi | \hat{Q} | \psi \rangle = \int \psi \sum_{i=1}^{2n} Q(\mathbf{r}_i) \psi d\tau = \int \rho(\mathbf{r}) Q(\mathbf{r}) d\mathbf{r} \tag{4.10}$$

The term V_{Ne} for all $2n$ electrons can be written as:

$$\langle V_{Ne} \rangle = \sum_{i=1}^{2n} \sum_{nucleiA} -\frac{Z_A}{\mathbf{r}_{iA}} = \sum_{i=1}^{2n} v(\mathbf{r}_i) \tag{4.11}$$

where $Z_A/\mathbf{r}_{iA}$ is the potential energy due to attraction of nucleus and electron at varying distance $\mathbf{r}$; $v(\mathbf{r}_i)$ is external potential for the attraction of electron 'i' to all the nuclei. Expanding the expectation value of V_{Ne} [43], we get:

$$\langle V_{Ne} \rangle = \langle \psi | \hat{V}_{Ne} | \psi \rangle = \int \psi \sum_{i=1}^{2n} v(\mathbf{r}_i) \psi d\tau = \int \rho(\mathbf{r}) v(\mathbf{r}) d\mathbf{r} \tag{4.12}$$

Therefore, eq. (4.9) becomes

$$E_0 = \langle T[\rho_0] \rangle + \int \rho(\mathbf{r}) v(\mathbf{r}) d\mathbf{r} + \langle V_{ee}[\rho_0] \rangle \tag{4.13}$$

Now, the middle term is classical electrostatic attraction potential. Since, we do not know the functionals of kinetic $\langle T[\rho_0] \rangle$ and potential energies $\langle V_{ee}[\rho_0] \rangle$, therefore, Kohn and Sham

[123] introduced the idea of fictitious non-interacting reference system of electrons. Considering the electronic kinetic energy, a quantity $\Delta\langle T[\rho_0]\rangle$ is defined as the deviation of the real electronic KE from that of the reference system:

$$\Delta\langle T[\rho_0]\rangle \equiv \langle T[\rho_0]\rangle_{rea} - \langle T[\rho_0]\rangle_{ref} = \langle T[\rho_0]\rangle - \langle T[\rho_0]\rangle_{ref} \tag{4.14}$$

Similarly, a quantity $\Delta\langle V_{ee}[\rho_0]\rangle$ as the deviation of the real electron-electron repulsion energy from a classical charge-cloud coulomb repulsion energy:

$$\Delta\langle V_{ee}[\rho_0]\rangle \equiv \langle V_{ee}[\rho_0]\rangle_{rea} - \frac{1}{2}\int\int \frac{\rho_0(\mathbf{r}_1)\rho_0(\mathbf{r}_2)}{r_{12}} d\mathbf{r}_1 d\mathbf{r}_2 \tag{4.15}$$

Thus, the term E_0 can be written as:

$$E_0 = \int \rho_0(\mathbf{r}) v(\mathbf{r}) d\mathbf{r} + \langle T[\rho_0]\rangle_{ref} + \frac{1}{2}\int\int \frac{\rho_0(\mathbf{r}_1)\rho_0(\mathbf{r}_2)}{r_{12}} d\mathbf{r}_1 d\mathbf{r}_2 + E_{XC}[\rho_0] \tag{4.16}$$

where $E_{XC}[\rho_0]$ is the exchange-correlation energy, a functional of the electron density function, and defined by:

$$E_{XC}[\rho_0] = \Delta\langle T[\rho_0]\rangle + \Delta\langle V_{ee}[\rho_0]\rangle \tag{4.17}$$

Solving the terms in eq. (4.16) separately, the first term is:

$$\int \rho_0(\mathbf{r}) v(\mathbf{r}) d\mathbf{r} = \int \left[\rho_0(\mathbf{r}_1) \sum_{nuclei A} -\frac{Z_A}{\mathbf{r}_{1A}} \right] d\mathbf{r}_1 = -\sum_{nuclei A} Z_A \int \frac{\rho_0(\mathbf{r}_1)}{\mathbf{r}_{1A}} d\mathbf{r}_1 \tag{4.18}$$

The second term:

$$\langle T[\rho_0]\rangle_{ref} = \left\langle \psi_r \left| \sum_{i=1}^{2n} -\frac{1}{2}\nabla_i^2 \right| \psi_r \right\rangle \tag{4.19}$$

ψ_r can be written exactly as a single Slater determinant [42, 43]. For a four electron system:

$$\psi_r = \frac{1}{\sqrt{4!}} \begin{vmatrix} \psi_1^{KS}(1)\alpha(1) & \psi_1^{KS}(1)\beta(1) & \psi_2^{KS}(1)\alpha(1) & \psi_2^{KS}(1)\beta(1) \\ \psi_1^{KS}(2)\alpha(2) & \psi_1^{KS}(2)\beta(2) & \psi_2^{KS}(2)\alpha(2) & \psi_2^{KS}(2)\beta(2) \\ \psi_1^{KS}(3)\alpha(3) & \psi_1^{KS}(3)\beta(3) & \psi_2^{KS}(3)\alpha(3) & \psi_2^{KS}(3)\beta(3) \\ \psi_1^{KS}(4)\alpha(4) & \psi_1^{KS}(4)\beta(4) & \psi_2^{KS}(4)\alpha(4) & \psi_2^{KS}(4)\beta(4) \end{vmatrix} \tag{4.20}$$

The 16 spin orbitals in the above determinant are the K-S spin orbitals of the reference system and each is the product of a K-S spatial orbital ψ_i^{KS} with a spin function α or β [43]. The eq. (4.19) can be simplified by invoking a set of rules as:

$$\langle T[\rho_0] \rangle_{\text{ref}} = -\frac{1}{2} \sum_{i=1}^{2n} \left\langle \psi_1^{KS}(1) \middle| \nabla_i^2 \middle| \psi_1^{KS}(1) \right\rangle \tag{4.21}$$

The third and fourth terms remain as they are. Now, putting eq. (4.18) and eq. (4.21) into equation (4.16):

$$E_0 = -\sum_{nuclei A} Z_A \int \frac{\rho_0(\mathbf{r}_1)}{\mathbf{r}_{1A}} d\mathbf{r}_1 - \frac{1}{2} \sum_{i=1}^{2n} \left\langle \psi_1^{KS}(1) \middle| \nabla_i^2 \middle| \psi_1^{KS}(1) \right\rangle + \frac{1}{2} \int\int \frac{\rho_0(\mathbf{r}_1)\rho_0(\mathbf{r}_2)}{r_{12}} d\mathbf{r}_1 d\mathbf{r}_2 + E_{XC}[\rho_0] \tag{4.22}$$

4.1.3.2. The Kohn–Sham (K-S) Equations

The equation of electron density distribution is given by:

$$\rho_0 = \rho_r = \sum_{i=1}^{2n} \left| \psi_i^{KS}(1) \right|^2 \tag{4.23}$$

where ψ_i^{KS} are the K-S spatial orbitals.

The Kohn-Sham equations are obtained by differentiating the energy E_0 (eq. 4.22) with respect to the ψ_i^{KS} while constraining the orthonormal condition, hence, the KS equation becomes [117, 43]:

$$\left[-\frac{1}{2}\nabla_i^2-\sum_{nuclei\,A}\frac{Z_A}{\mathbf{r}_{1A}}+\int\frac{\rho(\mathbf{r}_2)}{r_{12}}d\mathbf{r}_2+\nu_{XC}(1)\right]\psi_i^{KS}(1)=\varepsilon_i^{KS}(1)\psi_i^{KS}(1) \tag{4.24}$$

where ε_i^{KS} are the K-S energy levels and $\nu_{XC}(\mathbf{r})$ is a functional derivative of the exchange-correlation energy $E_{XC}[\rho(\mathbf{r})]$ that can be described as:

$$\nu_{XC}(\mathbf{r})=\frac{\delta E_{XC}[\rho(\mathbf{r})]}{\delta\rho(\mathbf{r})} \tag{4.25}$$

The KS equations (eq. 4.24) can also be written as:

$$\hat{h}_i^{KS}(1)\psi_i^{KS}(1)=\varepsilon_i^{KS}(1)\,\psi_i^{KS}(1) \tag{4.26}$$

The K-S operator $\hat{h}^{KS}$ can be defined by eq. 4.24.

4.1.3.3. Procedure for Solving the K-S Equations

The procedure of solving the K-S eigenvalue equations starts with the expansion of K-S orbitals in terms of basis functions ϕ with *m* functions in the set [43]:

$$\psi_i^{KS}=\sum_{s=1}^{m}c_{si}\phi_s\;;\;i=1,2,3,...,m \tag{4.27}$$

Putting eq. (4.27) in eq. (4.26), we get:

$$\begin{aligned}
&\sum_{s=1}^{m}c_{s1}\hat{h}^{KS}\phi_s=\varepsilon_1^{KS}\sum_{s=1}^{m}c_{s1}\phi_s\\
&\sum_{s=1}^{m}c_{s2}\hat{h}^{KS}\phi_s=\varepsilon_2^{KS}\sum_{s=1}^{m}c_{s2}\phi_s\\
&\qquad\text{M}\\
&\sum_{s=1}^{m}c_{sm}\hat{h}^{KS}\phi_s=\varepsilon_m^{KS}\sum_{s=1}^{m}c_{sm}\phi_s
\end{aligned} \tag{4.28}$$

Multiplying each of these m equations by ϕ_1, ϕ_2,..., ϕ_m (or complex conjugate ϕ_1^* and others), we get:

$$\begin{aligned}
\sum_{s=1}^{m} c_{s1} h_{1s}^{KS} &= \varepsilon_1^{KS} \sum_{s=1}^{m} c_{s1} S_{1s} \\
\sum_{s=1}^{m} c_{s2} h_{1s}^{KS} &= \varepsilon_2^{KS} \sum_{s=1}^{m} c_{s2} S_{1s} \\
&\text{M} \\
\sum_{s=1}^{m} c_{sm} h_{1s}^{KS} &= \varepsilon_m^{KS} \sum_{s=1}^{m} c_{sm} S_{1s}
\end{aligned} \tag{4.29}$$

where $h_{rs}^{KS} = \int \phi_r \hat{h}^{KS} \phi_s dv$ and $S_{rs} = \int \phi_r \phi_s dv$. Writing eq. (4.29), in general, for r = 1, 2, 3,…, m; and for each i = 1, 2, 3,…., m:

$$\sum_{s=1}^{m} h_{rs}^{KS} c_{si} = \sum_{s=1}^{m} S_{rs} c_{si} \varepsilon_i^{KS} \tag{4.30}$$

Subsuming the general eq. (4.30) into one matrix equation, we get:

$$\mathbf{HC} = \mathbf{SC\varepsilon} \tag{4.31}$$

Here, **H**, **C**, and **S** are m × m matrices; and $\boldsymbol{\varepsilon}$ is an m × m diagonal matrix with the non-zero elements $\boldsymbol{\varepsilon}_1$, $\boldsymbol{\varepsilon}_2$,..., $\boldsymbol{\varepsilon}_m$.

$$\mathbf{HC} = \begin{pmatrix} H_{11} & H_{12} & H_{13} & \Lambda & H_{1m} \\ H_{21} & H_{22} & H_{23} & \Lambda & H_{2m} \\ \text{M} & \text{M} & \text{M} & \text{O} & \text{M} \\ H_{m1} & H_{m2} & H_{m3} & \Lambda & H_{mm} \end{pmatrix} \begin{pmatrix} c_{11} & c_{12} & c_{13} & \Lambda & c_{1m} \\ c_{21} & c_{22} & c_{23} & \Lambda & c_{2m} \\ \text{M} & \text{M} & \text{M} & \text{O} & \text{M} \\ c_{m1} & c_{m2} & c_{m3} & \Lambda & c_{mm} \end{pmatrix} \tag{4.32}$$

$$\mathbf{SC\varepsilon} = \begin{pmatrix} S_{11} & S_{12} & \Lambda & S_{1m} \\ S_{21} & S_{22} & \Lambda & S_{2m} \\ \text{M} & \text{M} & \text{O} & \text{M} \\ S_{m1} & S_{m2} & \Lambda & S_{mm} \end{pmatrix} \begin{pmatrix} c_{11} & c_{12} & \Lambda & c_{1m} \\ c_{21} & c_{22} & \Lambda & c_{2m} \\ \text{M} & \text{M} & \text{O} & \text{M} \\ c_{m1} & c_{m2} & \Lambda & c_{mm} \end{pmatrix} \begin{pmatrix} \varepsilon_{11} & 0 & \Lambda & 0 \\ 0 & \varepsilon_{22} & \Lambda & 0 \\ \text{M} & \text{M} & \text{O} & \text{M} \\ 0 & 0 & \Lambda & \varepsilon_{mm} \end{pmatrix} \tag{4.33}$$

4.1.3.4. Algorithm

The algorithm to evaluate the energy from Kohn-Sham equation is shown in Figure 4.1 which describes the procedure as:

1) Specify a geometry (charge and mulitiplicity)
2) Specify a basis set (ϕ)
3) Make an initial guess of ρ
4) Calculate an initial guess of v_{XC} using ρ (using eq. 4.25)
5) Calculate KS operator $\hat{h}^{KS}$ by initial guesses of v_{XC} and ρ (using $\hat{h}^{KS}$ expression in eq. 4.24)
6) Calculate KS matrix elements (h_{rs}) using $\hat{h}^{KS}$ and basis function ϕ
7) Orthogonalize KS matrix; diagonalize it to get coefficients matrix **C′** and an energy level ε; and transform **C′** to **C.** This provides the first iteration value of ε and KS molecular orbital (MO) ψ_i (since $\psi_i = \sum c\phi_{basis}$)
8) Use the first iteration value of KS MO to get an improved ρ
9) Go back to step (4) with improved ρ and get the subsequent iterations
10) When the iterations are converged then calculate the energy E_0 (using eq. 4.22)
11) If required, go for geometry optimization.

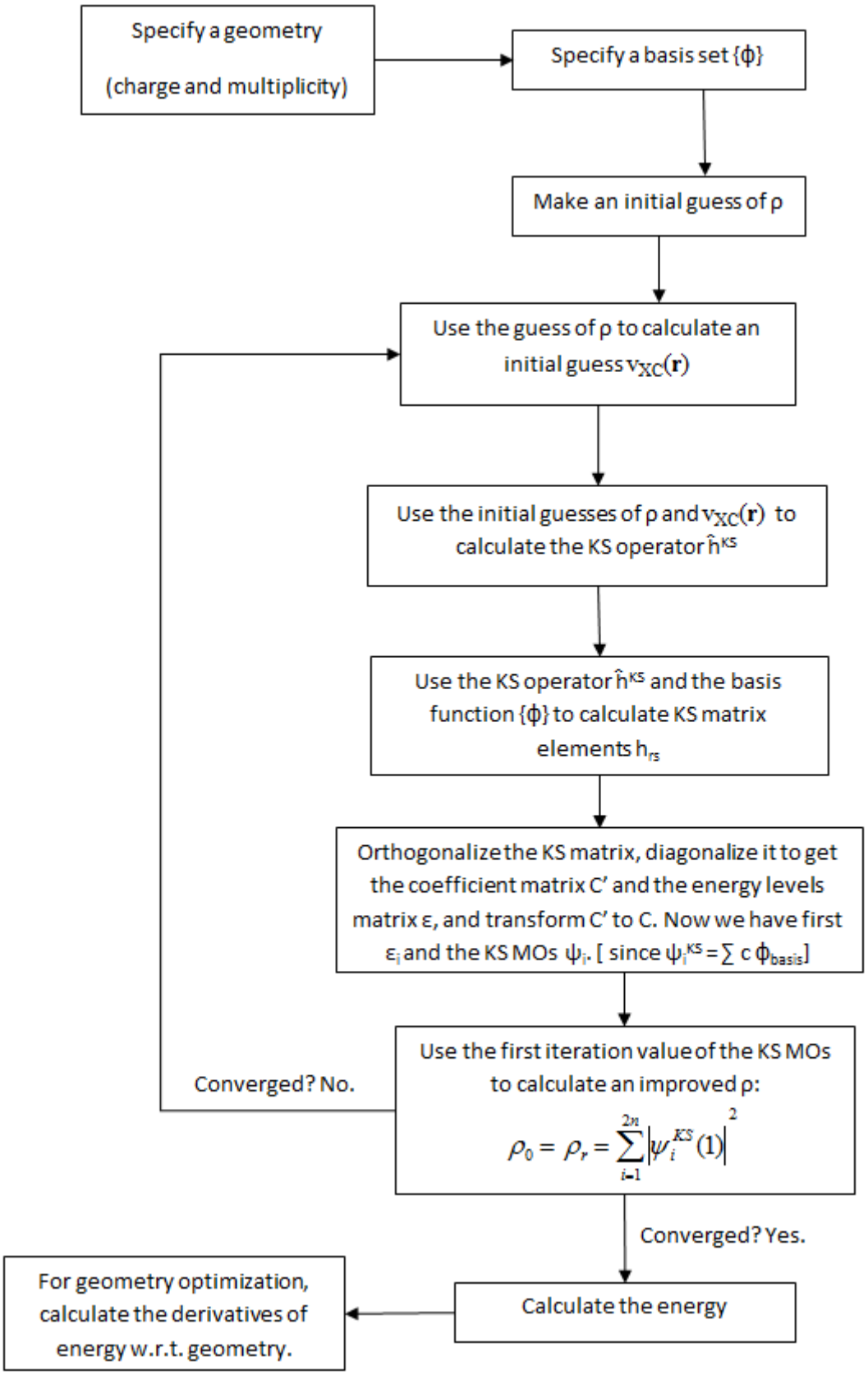

Figure 4.1: Algorithm to calculate the energy using density functional theory.

4.2. The Exchange-Correlation Energy Functional

The exchange correlation energy $E_{XC}[\rho(\mathbf{r})]$ is a quantity that depends on the electron density function $\rho(\mathbf{r})$ and the exchange-correlation potential $v_{XC}(\mathbf{r})$ is a functional derivative of $E_{XC}[\rho(\mathbf{r})]$ which is a function of the variable **r**, i.e., x, y, and z. The calculation of E_{XC} is proposed by various approaches which are described in following subsections [42, 43]:

4.2.1. The Local Density Approximation (LDA)

The simplest approximation to $E_{XC}[\rho(\mathbf{r})]$ is due to the local density approximation (LDA). The local density approximation is based on the assumption that at every point in a molecule the energy density has a value that would be given by a homogeneous electron gas which held the same electron density ρ at that point.

$$E_{XC}^{LDA}[\rho] = \int \rho(\mathbf{r})\varepsilon_{XC}[\rho]d\mathbf{r} \tag{4.34}$$

where $\varepsilon_{XC}[\rho]=\varepsilon_X[\rho]+\varepsilon_C[\rho]$

4.2.2. The Local Spin Density Approximation (LSDA)

The introduction of "spin" in LDA approximation is schemed in such a way that electrons holding opposite spins are positioned in different KS orbitals. A popular LSDA functional, i.e., the SVWN (Slater exchange plus Vosko, Wilk, Nusair) functional is given as:

$$\varepsilon_X[\rho_\alpha,\rho_\beta]=-2^{1/3}\frac{3}{4}\left(\frac{3}{\pi}\right)^{1/3}\left(\rho_\alpha^{1/3}+\rho_\beta^{1/3}\right) \tag{4.35}$$

4.2.3. The Generalized Gradient Approximation (GGA)

Currently, most DFT calculations employ exchange-correlation energy functionals E_{XC} which utilizes both the electron density and its gradient ($\nabla\rho$). These functionals are gradient

corrected functionals, hence, supposed to use the generalized-gradient approximation (GGA). Examples of gradient-corrected correlation-energy functionals are the LYP (Lee-Yang-Parr) and the P86 (Perdew 1986) functionals.

$$E_{XC}[\rho] = \int \rho(\mathbf{r})\varepsilon_{XC}[\rho]d\mathbf{r} + \int F_{XC}(\rho,\nabla\rho)d\mathbf{r} \tag{4.36}$$

4.2.4. Meta-Generalized Gradient Approximation Functionals (meta-GGA, MGGA)

The first derivatives of the electron density function (GGA functionals) are generally an improvement over ones depending only on ρ itself, therefore, a further improvement could also be obtained by introducing the second derivative of ρ, i.e., $\nabla^2\rho$. These functionals are called meta-gradient corrected (meta-GGA, MGGA) functionals, e.g., τ-HCTH (Hamprecht, Cohen, Tozer, Handy) and the B98 (Becke1998).

$$E_{XC}^{meta-GGA}[\rho] = \int \rho(\mathbf{r})\varepsilon_{XC}(\rho,\nabla\rho,\tau)d\mathbf{r} \tag{4.37}$$

where $\tau = \frac{1}{2}\sum_{i_\sigma}^{occupied}\left|\nabla\phi_i^{KS}\right|^2$

4.2.5. Hybrid GGA (HGGA) Functionals

Hybrid functionals comprise of HF exchange as well and they are advancements to the GGA functionals:

$$E_{XC}[\rho] = \int_0^1 \langle\psi(\lambda)|V_{ee}(\lambda)|\psi(\lambda)\rangle - \frac{1}{2}\int\int \frac{\rho(\mathbf{r}_1)\rho(\mathbf{r}_2)}{r_{12}}d\mathbf{r}_1 d\mathbf{r}_2 \tag{4.38}$$

The first popular, successful hybrid method was B3LYP [117, 120] which is given as:

$$E_{XC}^{B3LYP} = 0.20E_X^{H-F} + 0.80E_X^{LDA} + 0.72\Delta E_X^{B88} + 0.81E_C^{LYP} + 0.19E_C^{LDA} \tag{4.38}$$

The accuracy and reliability of B3LYP functional has been demonstrated by Simón and Goodman [124] by carrying out 19 different organic reactions using different DFT functionals and Hartree-Fock theory; and they reported that B3LYP is a better option for organic reactions. However, for metals, B3LYP functional does not report excellently, hence recently, a similar functional called B3PW91 [125, 126] is widely hailed to counter the interaction between metal atoms.

4.3. Basis Sets

A basis set is a set of mathematical functions, also known as basis functions, which in linear combinations yield molecular orbitals. Usually, the functions are centred on atomic nuclei; however, not consistently. The approximation of molecular orbitals in linear combinations of basis functions is known as linear combination of atomic orbitals (LCAO). A simple representation of linear combination of basis functions is as follows:

$$\psi = a_1\phi_1 + a_2\phi_2 + \mathrm{K} + a_k\phi_k \tag{4.39}$$

where *k* is size of the basis set; ϕ_1, ϕ_2,…, ϕ_k are the basis functions; and a_1, a_2,…, a_k are normalisation constants. The general expression for a basis function (BF) is given by:

$$BF = N \times e^{(-\alpha r)} \tag{4.40}$$

where N is the normalisation constant, α is the orbital exponent and *r* is the radius in angstroms.

4.3.1. Slater Type Orbitals (STO)

Slater type orbitals represent the real situation for the electron density in the valence region and beyond but are not effective nearer to the nucleus.

$$\phi_1(\alpha, n, l, m; r, \theta, \phi) = N r^{n-1} e^{-\alpha r} Y_{l,m}(\theta, \phi) \tag{4.41}$$

where r, θ, and ϕ are spherical coordinates; n, l, and m are quantum numbers; and $Y_{l,m}$ are angular momentum parts.

4.3.2. Gaussian Type Orbitals (GTO)

Gaussian type functions comprise of exponential $e^{-\beta r^2}$ rather than $e^{-\alpha r}$ of the STOs. These functions are very easy to evaluate. A Cartesian Gaussian function centred on an atom can be represented as:

$$G_{i,j,k} = N x_a^i y_a^j z_a^k e^{-\alpha r_a^2} \tag{4.42}$$

4.3.3. Types of Basis Sets

4.3.3.1. Minimal Basis Sets

A common naming convention for minimal basis sets is STO-XG; where X is an integer that represents the number of Gaussian primitive functions comprising a single basis function, e.g., STO-2G, STO-3G, STO-6G, STO-3G*, etc.

4.3.3.2. Valence Basis Sets

During most molecular bonding, it is the valence electrons which principally take part in the bonding. In recognition of this fact, it is common to represent valence orbitals by more than one basis function. The notation for these split-valence basis sets is typically X-YZg. In this case, X represents the number primitive Gaussians comprising each core atomic orbital basis function. The Y and Z indicate that the valence orbitals are composed of two basis functions each. A list of commonly used split-valence basis sets:

3-21g, 3-21g*, 3-21+g, 3-21+g*, 6-31g, 6-31g*, 6-311+g(d,p), etc.

4.3.3.3. Dunning Basis Sets

Basis sets in which there are multiple basis functions corresponding to each atomic orbital, including both valence orbitals and core orbitals or just the valence orbitals, are called

double, triple, or quadruple-zeta basis sets. Commonly used multiple zeta basis sets: cc-pVDZ - Double-zeta, cc-pVTZ - Triple-zeta, cc-pVQZ - Quadruple-zeta

4.3.3.4. Mixed Basis Sets

Sometimes, the valence basis sets do not work efficiently for transition or noble metal atoms because of inability to consider the relativistic phenomena. In this case, a mixed basis set can be applied for different atoms. For instance, LANL2DZ and LANL2MB are very famous basis sets that consider the relativistic phenomena of such metal atom, e.g., Pt, Pd, and others [127]. Further, other general atoms, e.g., C, H, O, and others may be defined efficiently with either of aforementioned basis sets.

4.4. Bond Dissociation Energy (BDE)

The transition state structures of many organic homolysis reactions are very tedious to find and thus the evaluation of corresponding activation barrier is difficult; however, bond dissociation energy (BDE) is a good approximation to the activation energy in such cases [52, 50]. Therefore, for such organic homolysis reactions, BDE calculations are carried out which is given by:

$$BDE_{298}(R - A) = H_{298}(R^{\bullet}) + H_{298}(A^{\bullet}) - H_{298}(R - A) \quad (4.43)$$

where H_{298} is the enthalpy of formation of the molecule (R-A) and radical species ($R^{\bullet}$, $A^{\bullet}$).

4.5. Kinetic Analysis

The thermodynamic parameters, e.g., internal energy (U), entropy (S), etc. are calculated using partition function (q_{tot}) which is the product of four individual partition functions due to translation (q_t), vibration (q_v), rotation (q_r), and electronic (q_e) degree of freedoms as given below and are necessary entities in the calculation of Gibbs free energies [42, 128]:

$$q_{tot} = q_t q_r q_v q_e \tag{4.44}$$

$$\left.\begin{aligned} q_t = \left(\frac{2\pi MkT}{h^2}\right)V \;;\; q_r = \frac{\sqrt{\pi}}{\sigma}\left(\frac{8\pi^2 kT}{h^2}\right)^{3/2}\sqrt{I_1 I_2 I_3} \;;\; q_v = \prod_{i=1}^{3N_{atom}-6(7)} \frac{e^{-h\nu_i/2kT}}{1-e^{-h\nu_i/kT}} \;;\; q_e = g_0 \end{aligned}\right\} \tag{4.45}$$

Total electronic energy (E_{tot}) is the summation of four electronic energy components, namely, translational (E_t), vibrational (E_v), rotational (E_r), and electronic (E_e):

$$E_{tot} = E_t + E_r + E_v + E_e \tag{4.46}$$

$$\left.\begin{aligned} E_t = \frac{3}{2}RT \;;\quad E_r = RT \;;\quad E_e = 0; \quad E_v = R\sum_{i}^{3N_{atom}-6(7)} h\nu_i / k\left(\frac{1}{2} + \frac{1}{e^{h\nu_i/k}-1}\right) \end{aligned}\right\} \tag{4.47}$$

Similarly, total entropy (S_{tot}) is the summation of the four individual entropy components, namely, translational (S_t), vibrational (S_v), rotational (S_r), and electronic (S_e):

$$S_{tot} = S_t + S_r + S_v + S_e \tag{4.48}$$

$$\left.\begin{aligned} S_t = R\left(\ln q_t + \frac{5}{2}\right);\; S_r = R(\ln q_r + 1); \\ S_v = R\sum_{i}^{3N_{atom}-6(7)}\left(\frac{e^{h\nu_i/k}}{e^{h\nu_i/k}-1} - \ln\left(1-e^{h\nu_i/k}\right)\right);\; S_e = R(\ln q_e) \end{aligned}\right\} \tag{4.49}$$

where k, M, T, and h are Boltzmann's constant, molecular mass, temperature, and Planck's constant, respectively; σ, g_o, υ_i, and R are symmetry number, degeneracy of energy level, vibrational frequency, and universal gas constant, respectively; and I_1, I_2, and I_3 are three principal moments of inertia. In the terms q_v, E_v, and S_v, i varies from 1 to 3N-7 and 3N-6 for transition state and minimum structures, respectively.

Then enthalpy and free energy are calculated by:

$$H_{corr} = E_{tot} + kT \tag{4.50}$$

$$G_{corr} = H_{corr} - TS_{tot} \tag{4.51}$$

The activation free energy ($\Delta^{\ddagger}G$) and forward rate constant (k_f) [129] are calculated by:

$$\Delta^{\ddagger}G = (G_{corr})_{TS} - (G_{corr})_{reac} \tag{4.52}$$

$$k_f = \frac{k_B T}{h} \exp\left(\frac{-\Delta^{\ddagger}G}{RT}\right) \tag{4.53}$$

Similarly, the equilibrium rate constant K_{eq} is calculated by:

$$K_{eq} = \frac{k_f}{k_r} \tag{4.54}$$

where k_f and k_r are rate constants of forward and backward reactions, respectively.

4.6. Catalyst Cluster and Adsorption Energy

The catalyst cluster used in this study is designed using 12 palladium atoms in monolayer surface with fixed Pd-Pd bond lengths as 2.751 Å (Figure 4.2) [130]. The bond lengths between Pd-Pd are fixed to perfectly emulate bulk palladium crystal structure. The spin state analyses of present Pd(111) model is performed by single point energy calculations at various spin multiplicities (SM = 2S + 1, where S is total spin of the system).

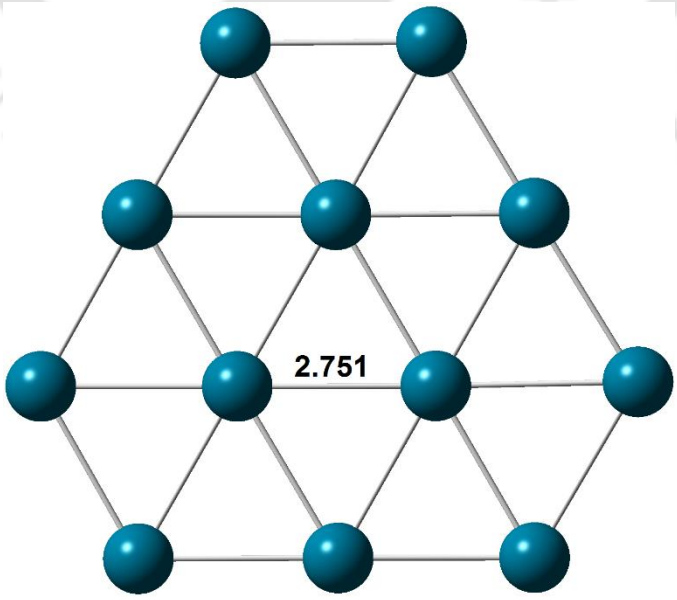

Figure 4.2: Pd(111) catalyst model with fixed Pd-Pd bond distance of 2.751 Å.

Table 4.1: Spin multiplicities (SM) and relative energies (E_{Rel}) of Pd(111) monolayer.

SM	1	3	5	7	9
E_{Rel} (kcal/mol)	22.4	3.3	7.3	0.0	18.1

The relative energies of cluster model at various spin multiplicities are presented in Table 4.1 and it is reported that ground state of designed catalyst cluster lies in septet spin multiplicity. The adsorption energies (E_{ads}) [47, 45, 103] of species in their favourable modes of adsorption and spin multiplicities are carried out by employing the following equation:

$$E_{ads} = E_{cluster+adsorbate} - E_{cluster} - E_{adsorbate} \quad (4.55)$$

where $E_{cluster+adsorbate}$ is the total energy of the adsorbed species over catalyst cluster; $E_{adsorbate}$ is total energy of the gas phase species; and $E_{cluster}$ is total energy of bare catalyst cluster alone.

RESULTS AND DISCUSSION

5.1. Molecular modelling approach to elucidate the thermal decomposition routes of vanillin

5.1.1. Reaction Schemes

The notations in reaction schemes are shown as, in general, **X_Y**, where **X** and **Y** denote the reaction scheme number and structure number in that particular reaction scheme, respectively. For instance, in **5_g**, **g** is the structure of reaction scheme 5. Similarly, the transition state structures have been designated as **TSX_Y**, where **X** is reaction scheme number and **Y** is the transition state number in a given reaction scheme, for instance, **TS7_2** is the second transition state structure in reaction scheme 7.

All reaction schemes considered in this study are briefly discussed here. The reaction scheme 1 (RS 1) is demethylation of vanillin followed by an atomic hydrogenation to produce 3,4-dihydroxybenzaldehyde which further undergoes dehydroxylation reaction to produce *p*-hydroxybenzaldehyde. The RS 2 is about the demethoxylation of vanillin followed by a single step hydrogenation reaction to produce *p*-hydroxybenzaldehyde. RS 3 describes the production of guaiacol using an atomic hydrogen addition to the aromatic carbon of $C_{aromatic}$-CHO bond followed by formyl removal reaction. RS 4 is about the cleavage of hydroxyl group of vanillin followed by a single step hydrogenation reaction to form *m*-anisaldehyde. RS 5 starts from the production of an intermediate *p*-hydroxybenzaldehyde by vanillin demethoxylation. Further, *p*-hydroxybenzaldehyde converts into the phenol structure using deformylation reaction followed by the production of benzene using dehydroxylation. RS 5 comprises of a secondary reaction scheme 5a which starts from the structure *p*-hydroxybenzaldehyde and produces

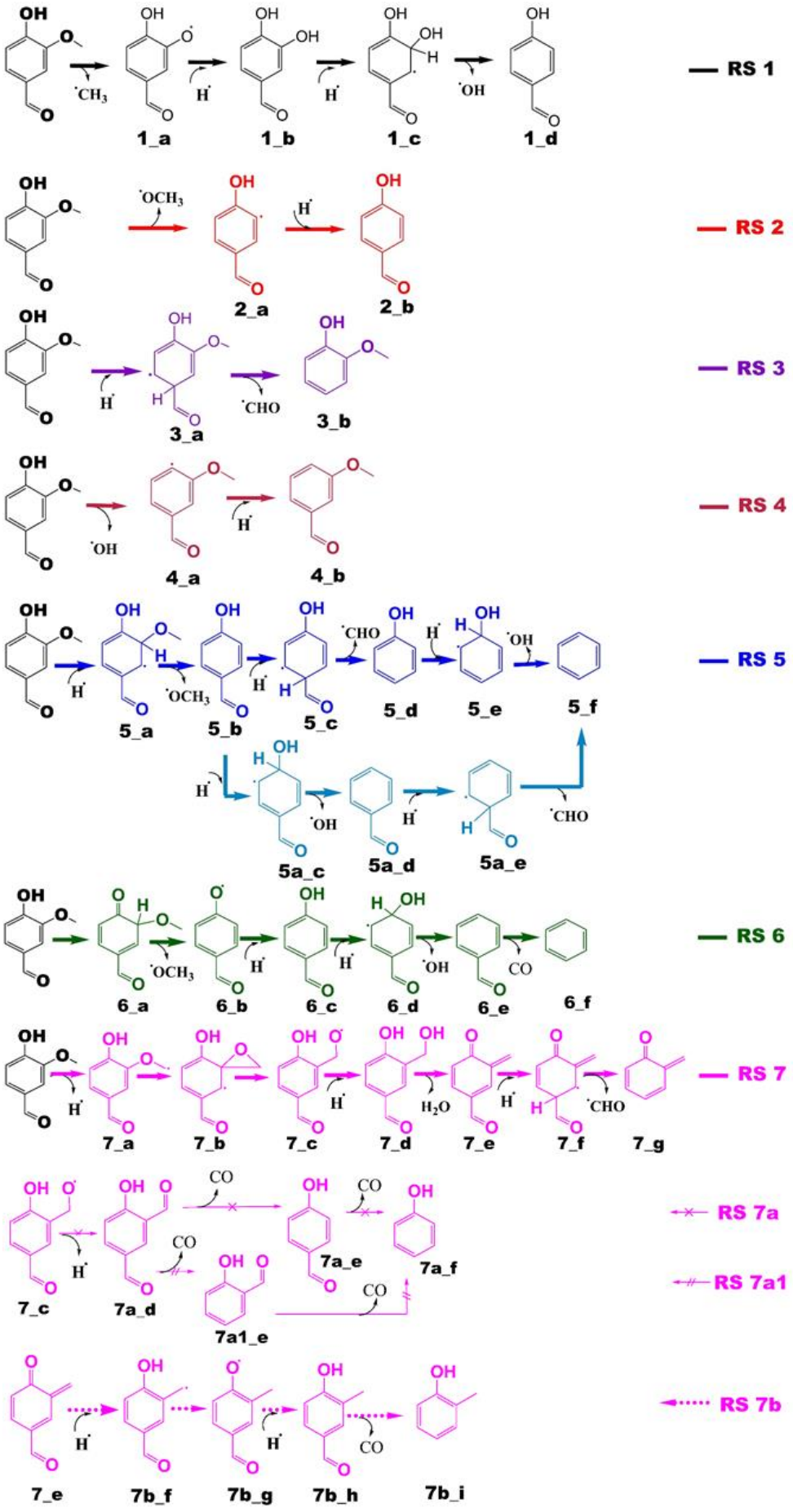
RS 1
1_a
1_b
1_c
1_d
RS 2
2_a
2_b
RS 3
3_a
3_b
RS 4
4_a
4_b
RS 5
5_a
5_b
5_c
5_d
5_e
5_f
5a_c
5a_d
5a_e
RS 6
6_a
6_b
6_c
6_d
6_e
6_f
RS 7
7_a
7_b
7_c
7_d
7_e
7_f
7_g
RS 7a
RS 7a1
7a_e
7a_f
7a_d
7a1_e
RS 7b
7_e
7b_f
7b_g
7b_h
7b_i

benzene. Under secondary reaction scheme of RS 5, *p*-hydroxybenzaldehyde converts to benzaldehyde component using dehydroxylation reaction followed by the production of benzene using deformylation reaction. RS 6 is also about the production of benzene but *via* keto-enol tautomerization reaction as the first step followed by a single step hydrogenation reaction to produce *p*-hydroxybenzaldehyde. Further, *p*-hydroxybenzaldehyde converts to benzaldehyde using dehydroxylation reaction followed by the decarbonylation reaction of benzaldehyde to produce benzene. Benzaldehyde is also found as the intermediate in pathway 5a along with pathway 6 but reaction approaches are different. RS 7 produces *o*-quinonemethide using methoxy group rearrangement and eliminations of water and formyl group. Reaction schemes 7a and 7a1 undergo for the production of phenol *via* the intermediate 5-formylsalicylaldehyde using decarbonylation reactions. On the other hand, RS 7b undergoes for an atomic hydrogen addition reaction of **7_e** followed by hydrogen migration and another atomic hydrogenation reaction to produce **7b_h**; and a decarbonylation reaction of **7b_h** produces *o*-cresol.

In this study, all proposed reaction schemes are carried out computationally in gas phase using B3LYP/6-311+g(d,p) level of theory under density functional theory (DFT) framework. Further, the reaction thermochemistry of each reaction is reported over a wide range of temperature, i.e., 598-898 K in gas phase at a fixed pressure of 1 atm.

The vanillin component can be represented by various conformers [131]; however, two conformers, *conformer 1* and *conformer 2*, are very competitive in stability and are shown in Table 5.1 along with their energetics including zero point vibrational energy (ZPVE) at B3LYP/6-311+g(d,p) level of theory. It can be seen from Table 5.1 that *conformer 1* of vanillin is more stable than the *conformer 2*. The energy difference between *conformer 2* and *conformer 1* is found to be 1.18 kcal/mol which is in excellent agreement with the observations of Egawa et al. [132] and Velcheva et al. [131]. They [131, 132] have reported this difference as 1.19

Table 5.1: ZPVE added electronic energetics of vanillin conformers.

Energy (hartree) with ZPVE correction	
Conformer 1	***Conformer 2***
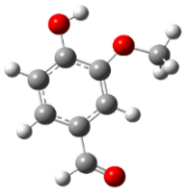	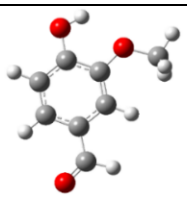
-535.3328	-535.3309

kcal/mol by MP2/6-31g(d,p) theory and 1.11 kcal/mol by B3LYP/6-31g(d) theory, respectively.

5.1.2. Bond Dissociation Energy (BDE)

The bond dissociation energy (BDE) calculations of vanillin structure have been performed for *Conformer 1* and these BDEs are discussed prior to discuss reaction pathways because these can be very helpful in determining required energy for cleavage of bonds so that reaction pathways can be prioritized [80, 50]. The BDEs of vanillin are carried out using B3LYP/6-311+g(d,p) theory and the equation of BDE is given in eq. (4.43). The bond cleavage sites of vanillin can be seen in the figure presented in Table 5.2 along with their BDEs**.** In this table, BDEs are also compared with their literature counterparts due to Shin et al. [70] who applied B3LYP/cc-pVDZ level of theory to track the trend. Briefly, this table presents the energy required for cleaving certain bonds involved in vanillin molecule; and further a comparison of the present values of BDE of each bond breaking are found to be in order of D1 < D2 < D6 < D3 < D5 < D8 < D4 < D7 < D10 < D9 according to their energetics. Further, it can be seen by comparing present and literature [70] BDE values that except D1 and D3, all BDEs are in good agreement with each other. The deviations in BDE values of D1 and D3 can be ascribed to different vanillin structure adopted by Shin et al. [70], which does not seem to be most stable conformer because Velcheva et al. [131] have calculated this geometry as 5.77 kcal/mol unstable than the most stable vanillin conformer, i.e., *Conformer 1* [131, 133].

Table 5.2: The bond dissociation energy (BDE) of vanillin of Conformer 1.

Bond		BDE (kcal/mol)	
		Shin et al.[70]	**Present**
D1	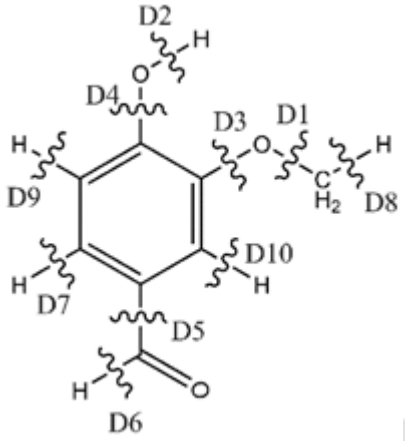	65	52.55
D2		87	85.77
D3		102	93.76
D4		112	110.11
D5		91	96.34
D6		88	89.80
D7		112	113.03
D8		94	97.19
D9		--	114.27
D10		--	113.84

5.1.3. Reaction Schemes 1-4

The reaction scheme 1 (RS 1) describes the production of *p*-hydroxybenzaldehyde by demethylation reaction of vanillin. The reaction schemes 2-4 describe the formation of *p*-hydroxybenzaldehyde, guaiacol, and *m*-anisaldehyde by the demethoxylation, deformylation, and dehydroxylation reactions of vanillin, respectively. The potential energy surfaces of these schemes, i.e., reaction schemes 1-4, are shown in Figure 5.1. The molecular structures of reactants, intermediates, transition states and products involved in reaction schemes 1–4 are presented in Figure 5.2. The structure **1_d** is same as the structure **2_b**, hence it is not repeated in Figure 5.2. The interatomic distances in transition state structures are in angstroms units (Å). The energies in Figure 5.1 are in kcal/mol included with zero point vibrational energy (ZPVE).

Shen et al. [69] in their study have suggested the production of catechol-type compounds from guaiacol-type components. In addition, according to BDE of various types of cleavages (see Table 5.2), the demethylation of vanillin is favourable scission, therefore, the vanillin demethylation reaction followed by an atomic hydrogenation reaction to produce 3,4-dihydroxybenzaldehyde component is designated as reaction pathway 1. The reaction further follows hydrogen attachment to the aromatic carbon of $C_{aromatic}$-OH bond at *meta* position of

the formyl group, and hydroxyl removal reaction. Further decomposition of the produced component, i.e., *p*-hydroxybenzaldehyde, into benzene is discussed in reaction scheme 5. The BDEs of first and second reaction steps of pathway 1 are 52.55 kcal/mol and 79.41 kcal/mol, respectively. Wang et al. [52] carried out the methyl radical removal from vanillin theoretically and reported BDE of 57.4 kcal/mol using M06-2X/6-31+g(d,p) level of theory.

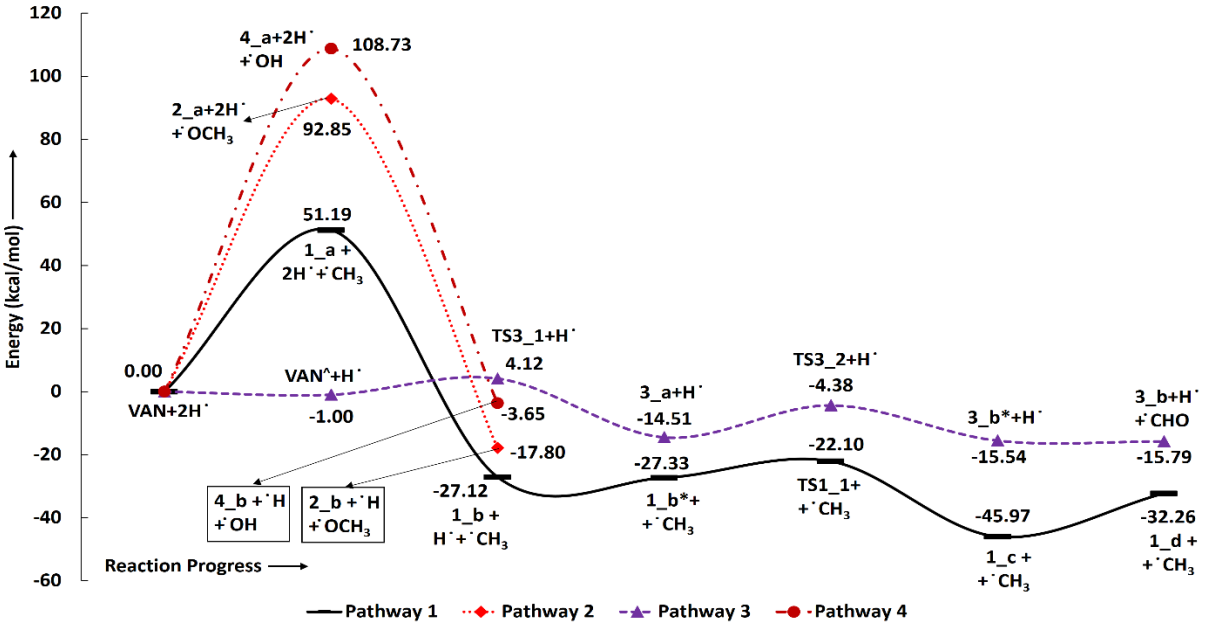

Figure 5.1: The potential energy surfaces of electronic energies of reaction schemes 1-4.

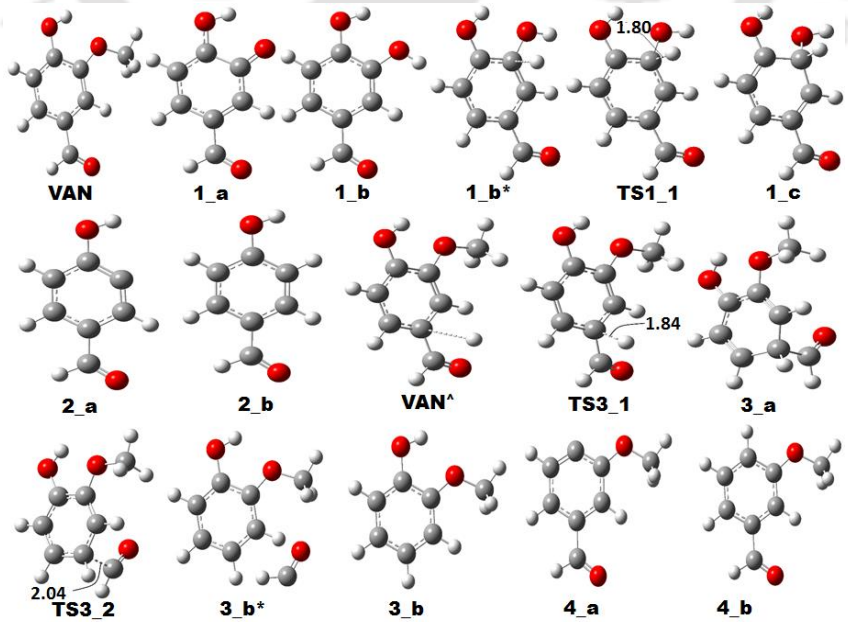

Figure 5.2: The optimized molecular structures involved in reaction schemes 1-4.

Table 5.3: The BDE and/or activation energy of each step of every reaction pathway.

Pathways	BDE/Activation Energy (kcal/mol)								
	Step 1	**Step 2**	**Step 3**	**Step 4**	**Step 5**	**Step 6**	**Step 7**	**Step 8**	**Step 9**
1	52.55	79.41	5.23	12.64	-	-	-	-	-
2	93.76	112.11	-	-	-	-	-	-	-
3	5.12	10.13	-	-	-	-	-	-	-
4	110.11	113.86	-	-	-	-	-	-	-
5	5.54	9.51	5.48	12.04	6.77	12.04	-	-	-
5a			6.60	14.20	5.50	11.31	-	-	-
6	66.34	35.41	86.46	-	-	-	-	-	-
7	97.20	15.73	0.04	103.83	32.06	2.38	19.73	-	-
7a	same as pathway 7			10.46	91.00	86.85	-	-	-
7a1					86.31	92.22	-	-	-
7b	same as pathway 7					58.19	28.34	84.01	87.79

The barrier height for hydrogen attachment to 3,4-dihydroxybenzaldehyde and BDE of dehydroxylation reaction are calculated as 5.23 kcal/mol and 12.64 kcal/mol, respectively. It can be seen that the vanillin demethylation requires comparatively less activation energy than the hydrogenation of **1_a** structure; however, latter two steps require very less activation energies compared to first two reaction steps. Therefore, this pathway doesn't seem to be very favourable.

Second reaction scheme is about the cleavage of methoxy radical from vanillin followed by single step hydrogenation reaction to produce 4-hydroxybenzaldehyde component. Experiments have suggested the production of phenol-type component from guaiacol-type component by removing methoxy radical and subsequent hydrogenation of 2-hydroxy-5-formylphenyl using hydrogen radical [69]. The methoxy radical removal possesses a BDE of 93.76 kcal/mol and single step hydrogenation to **2_a** component requires BDE of 112.1 kcal/mol to produce **2_b** component.

The reaction scheme 3 is about the production of guaiacol using single step hydrogenation reaction at aromatic carbon of $C_{aromatic}$-CHO sigma bond followed by the

removal of formyl group. The guaiacol component was found to be one of the major product from vanillin pyrolysis [71]. Liu et al. [71] reported the formation of guaiacol as 61.93 area % and 26.51 area % at 500^{o}C and 600^{o}C, respectively, whereas, no guaiacol formation has been reported at 400^{o}C. The production of guaiacol from vanillin is carried out by Wang et al. [52] and Liu et al. [71] using decarbonylation reaction of vanillin with activation energies of 99.5 kcal/mol and 87.89 kcal/mol, respectively. However, the study of Liu et al. [71] also mentioned the formation of guaiacol using radical-induced approach with activation energy of 115.36 kcal/mol. It can be seen that all three activation energies are quite high which cannot be possible without the use of a suitable catalyst. The demonstrated approach for production of guaiacol in Figure 5.1 as RS 3 carries out a single step hydrogenation reaction at the aromatic carbon of $C_{aromatic}$-CHO bond prior to the removal of formyl group with activation energies of 5.12 kcal/mol and 10.13 kcal/mol, respectively. Therefore, the activation energy for the production of guaiacol using this approach, i.e., 10.13 kcal/mol, requires considerably less activation energy compared to the activation energies of decarbonylation reaction of vanillin by Liu et al. [71], i.e., 99.5 kcal/mol, and Wang et al. [52], i.e., 87.89 kcal/mol.

The conversion of guaiacol component has been discussed by several researchers using experimental [75, 76, 92, 102, 134, 135] and computational [46, 47, 45, 50] studies, therefore, its decomposition has not been discussed further in this study.

The reaction scheme 4 produces *m*-anisaldehyde using direct cleavage of hydroxyl group followed by a single step hydrogenation reaction. The BDEs for cleavage of hydroxyl group from vanillin and single step hydrogenation of structure **4_a** under pathway 4 are 110.11 kcal/mol and 113.86 kcal/mol, respectively. It can be seen that this reaction is not possible without the application of any proper catalyst; however, the solution phase reactions may considerably lower the activation energies.

5.1.4. Reaction Scheme 5

The reaction scheme 5 is about the production of benzene as the final product along with several other intermediates, e.g., *p*-hydoxybenzaldehyde, phenol, and benzaldehyde. The structure of *p*-hydroxybenzaldehyde suggests the possibility of a secondary reaction pathway as 5a. Primary reaction scheme 5 carries out the formyl group removal of *p*-hydoxybenzaldehyde followed by dehydroxylation reaction to produce benzene, whereas, pathway 5a is about the dehydroxylation reaction of *p*-hydoxybenzaldehyde followed by formyl group removal process to produce benzene. The corresponding potential energy surfaces are shown in Figure 5.3 and the corresponding molecular structures of reactants, intermediates, transition states and products appearing in pathways 5 and 5a are shown in Figure 5.4. The interatomic distances in the transition state structures are shown in angstroms unit (Å).

The non-oxy aromatic components, within the context of bio-oil upgrading, are found to be desirable products because of no oxy-functionals attached to them which is the prime aim of bio-oil upgrading process [1, 16, 44, 47]. The reaction scheme 5 starts with hydrogen attachment to the aromatic carbon of $C_{aromatic}$-OCH_3 bond site (structure **5_a** in Figure 5.4) followed by the methoxy removal to produce 4-hydroxybenzaldehyde component, **5_b**. The reaction steps **VAN*** → **5_a** and **5_a** → **5_b** require the energy barrier heights of 5.54 kcal/mol and 9.51 kcal/mol, respectively. The asterisk corresponds to an intermediate component with an equilibrium hydrogen atom attacking at any specific atom of component. For instance, **VAN*** is an intermediate of vanillin and a hydrogen atom at aromatic carbon atom of $C_{aromatic}$-OCH_3 bond site. The imaginary frequencies corresponding to **TS5_1** and **TS5_2** under pathway 5 are 837.87*i* cm^{-1} and 452.61*i* cm^{-1}, respectively. The term '*i*' here demonstrates the frequency as an imaginary or negative frequency which affirms the structure as an actual transition state structure. Further decomposition of 4-hydroxybenzaldehyde carries out another reaction scheme possibility which is depicted as secondary reaction scheme 5a in Figure 5.3. Under RS

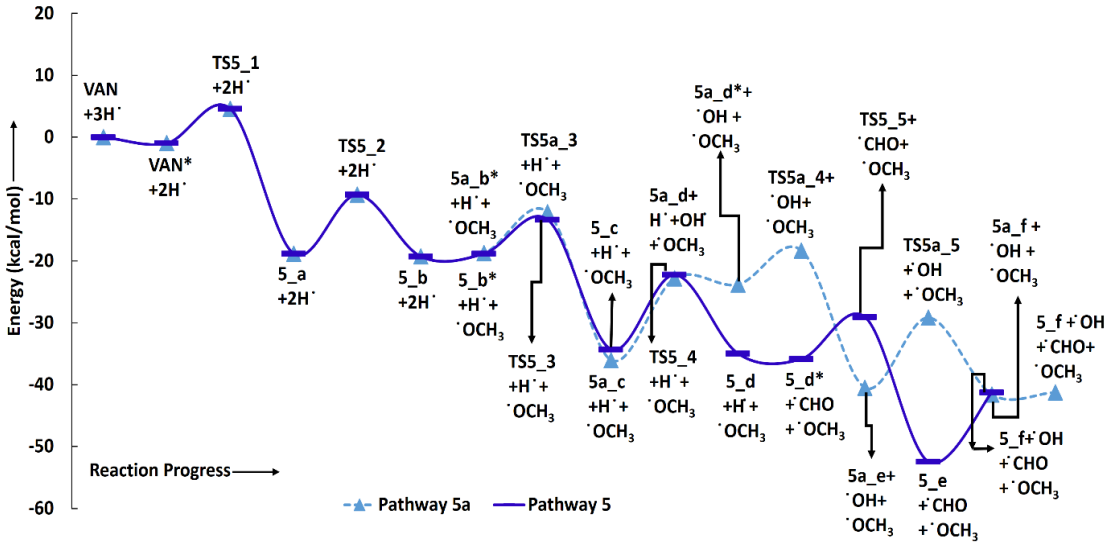

Figure 5.3: The potential energy surfaces of reaction schemes 5 and 5a.

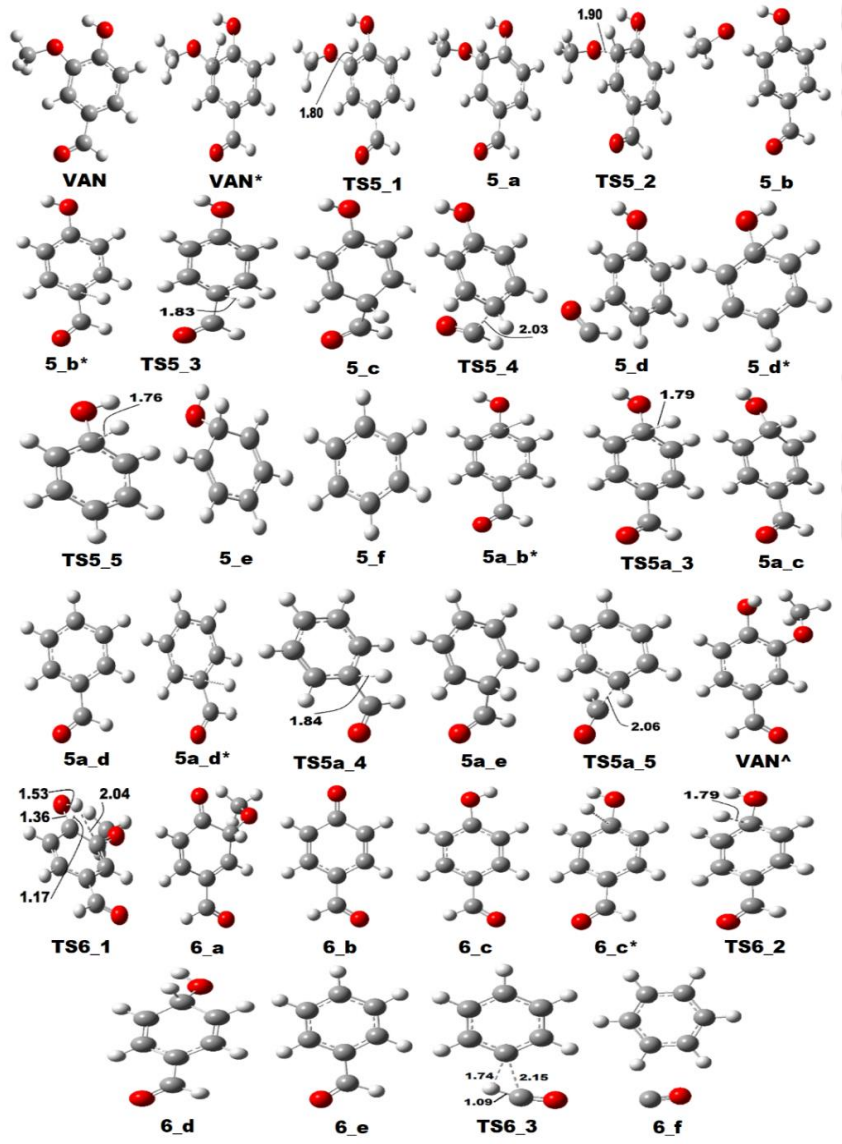

Figure 5.4: The optimized molecular structures involved in reaction schemes 5 and 6.

5, hydrogen atom forms a sigma bond with aromatic carbon atom of $C_{aromatic}$-CHO bond followed by the removal of formyl group to produce phenol component; with barrier heights as 5.48 kcal/mol and 12.04 kcal/mol, respectively. The frequencies corresponding to **TS5_3** and **TS5_4** are evaluated as 830.18*i* cm^{-1} and 529.18*i* cm^{-1}, respectively. Phenol is found as the tertiary component under vanillin pyrolysis study carried out by Shin et al. [70] in their experiment. Further, to produce the benzene component from phenol, a hydrogen atom is attached to aromatic carbon of $C_{aromatic}$-OH bond site of phenol under RS 5 with barrier height of 6.77 kcal/mol and the imaginary frequency, corresponding to **TS5_5**, as 954.81*i* cm^{-1}. Since, the transition state for OH removal reaction from **5_e** (see Figure 5.4) is very tedious to calculate [50, 51], BDE study has been carried out for this particular step and this suggests 12.04 kcal/mol energy requirement to produce benzene. The formation of benzene from phenol is studied by many researchers, for instance, Lu et al. [44] carried out the computations for production of benzene from phenol using hydroxyl cleavage of phenol followed by a single step hydrogenation over ruthenium catalyst; and they reported an activation energy of 26.52 kcal/mol. However, the mechanism is different compared to the present study but reactant and product are same. Further, the $C_{aromatic}$-CHO bond of 4-hydroxybenzaldehyde component is first cleaved under RS 5 followed by hydroxyl group removal reaction to form benzene, whereas, in secondary RS 5 (i.e., RS 5a), the $C_{aromatic}$-OH bond site is first cleaved followed by formyl group removal process to produce benzene component. Under secondary RS 5 (i.e., RS 5a), the hydrogen atom forms a sigma bond with aromatic carbon of $C_{aromatic}$-OH bond of 4-hydroxybenzaldehyde component followed by hydroxyl removal reaction. The barrier height of former reaction step (**5_b** → **5a_c**) and BDE of latter reaction step (**5a_c** → **5a_d**) are 6.60 kcal/mol and 14.21 kcal/mol, respectively. The produced component, i.e., benzaldehyde (**5a_d**) goes through hydrogenation at aromatic carbon atom of $C_{aromatic}$-CHO bond followed by formyl group removal process causing the barrier heights of 5.50 kcal/mol and 11.31 kcal/mol,

respectively. The imaginary frequencies corresponding to **TS5a_3**, **TS5a_4**, and **TS5a_5** are 959.61*i* cm^{-1}, 837.52*i* cm^{-1}, and 528*i* cm^{-1}, respectively.

Thus, it is found that both pathways are very competitive to each other in energetics. The rate determining steps are found to be the formyl group removal reaction step, i.e., **5_c** → **5_d**, for reaction pathway 5 and OH radical removal process for pathway 5a, respectively. The activation energies of pathways 5 and 5a are 12.04 kcal/mol and 14.21 kcal/mol, respectively, however, the activation energy difference between both pathways is only 2.07 kcal/mol. The reaction pathway 5 is favourable compared to pathway 5a for the production of benzene from vanillin component. As reported in BDE study that D5 (formyl group removal) requires less energy than D6 (dehydrogenation of formyl group), therefore, irrespective of the lowest activation energy required reaction pathways, i.e., 5 and 5a, these may or may not be possible unless a further dehydrogenation of CHO is possible to produce CO instead of hydrogenation reaction of CHO to produce HCHO component. Liu et al. [71] carried out vanillin pyrolysis and they reported no trace of formaldehyde at 400-600^{o}C but they did report the formation of CO which, in turn, must have been produced through vanillin decarbonylation reaction. The dehydrogenation of CHO group to produce CO molecule and H atom requires a BDE of 38.5 kcal/mol.

In reaction pathways 5 and 5a, aldehyde group is removed using single step hydrogenation of the structures **5_a** (under pathway 5) and **5a_d** (under pathway 5a) followed by formyl group removal. However, to compare the barrier height differences between decarbonylation and deformylation reactions of *p*-hydroxybenzaldehyde, a decarbonylation reaction of *p*-hydroxybenzaldehyde (as the reaction step **7a_e** → **7a_f**) is carried out in reaction scheme 7 to produce phenol which further can form benzene as per pathway 5. On the other hand, the decarbonylation of benzaldehyde is carried out in reaction scheme 6 as the reaction step **6_e** → **6_f**.

5.1.5. Reaction Scheme 6

The potential energy surface of RS 6 is depicted in Figure 5.5 and all structures associated with this pathway are shown in Figure 5.4 which are optimized structures at B3LYP/6-311+g(d,p) level of theory. The energetics including ZPVE presented in Figure 5.5 are shown in kcal/mol. The distances in transition state structures presented in Figure 5.4 are in angstroms units (Å).

To produce 4-hydroxybenzaldeyde, the demethylation and demethoxylation reactions of vanillin are carried out as the first reaction steps under RS 1 and RS 5, respectively. Another possibility is designated to produce 4-hydroxybenzaldehyde under RS 6 to compare the reaction favourability in terms of energies. The reaction scheme 6 starts with dihedral change of hydrogen of hydroxyl group to initiate keto-enol tautomerization reaction. This drives through the methoxy radical removal and a single step hydrogenation to oxygen radical of **6_b** structure. The **VAN*** structure in Figure 5.5 is found to be less stable than the *Conformer 1* of vanillin by 10.91 kcal/mol. The barrier height for keto-enol tautomerization reaction of vanillin is 66.34 kcal/mol, whereas, BDEs for the methoxy removal and single step hydrogenation are 35.41 kcal/mol and 86.46 kcal/mol, respectively. Further, the decomposition of 4-hydroxy benzaldehyde to form benzaldehyde is according to the pathway 5a. However, the decarbonylation reaction of benzaldehyde is carried out in pathway 6 to compare the barrier height differences between the approaches of pathways 5a and 6 to produce benzene. It can be seen that the barrier height of benzaldehyde decarbonylation reaction (RS 6) is 86.25 kcal/mol which is high energy demanding than the deformylation reaction of pathway 5a. Therefore, it can be concluded that the barrier height requirement for the production of benzene from benzaldehyde according to pathway 6 is not favourable compared to pathway 5a; however, it can be competitive compared to pathway 1 because the rate determining step in pathway 1 requires 79.41 kcal/mol barrier height. The imaginary frequencies for **TS6_1**, **TS6_2**, and **TS6_3** are calculated as 1212.51*i* cm^{-1}, 959.9*i* cm^{-1}, and 1678.08*i* cm^{-1}, respectively.

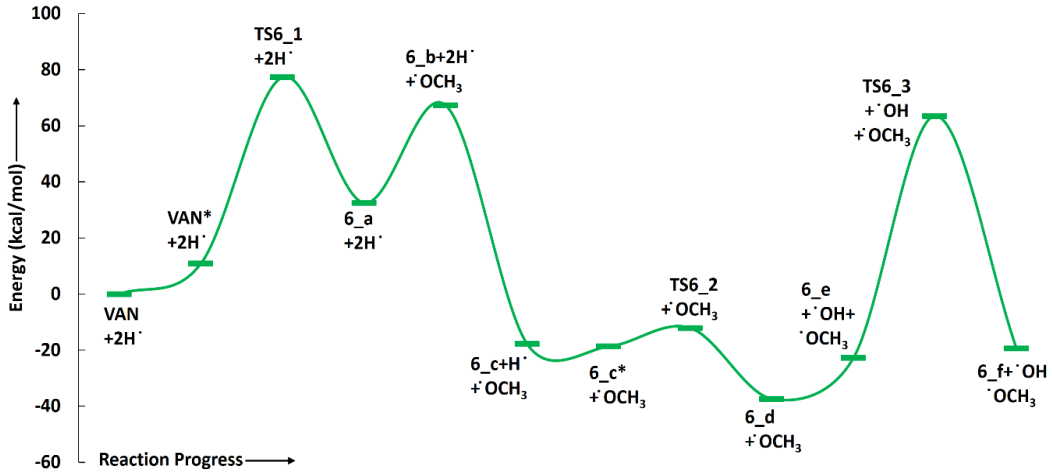

Figure 5.5: The potential energy surface of reaction scheme 6.

5.1.6. Reaction Scheme 7

The reaction scheme 7 presents the production of *o*-quinonemethide component which is a key polymerization component in the char formation [50]. The PES of reaction scheme 7 is shown in Figure 5.6. The reaction scheme 7 comprises of a secondary scheme under which the structure **7_c** undergoes the formation of 5-formylsalicylaldehyde followed by decarbonylation reaction to produce 4-hydroxybenzaldehyde; and further decarbonylation reaction of 4-hydroxybenzaldehyde produces phenol (see Figure 5.8 for PESs). Similarly, RS 7a1 starts from the decarbonylation reaction of 5-formylsalicylaldehyde to produce 2-hydroxybenzaldehyde;

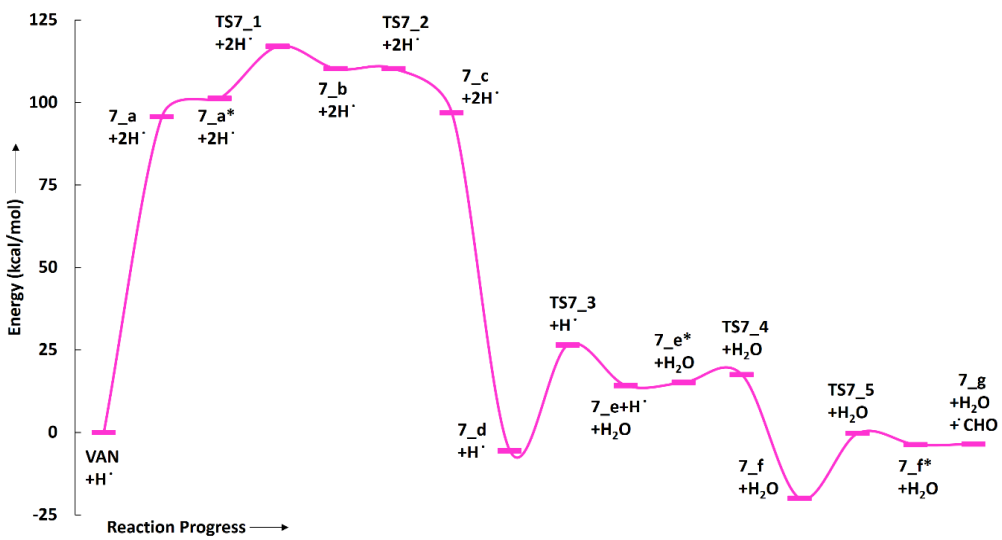

Figure 5.6: The potential energy surface of reaction scheme 7.

and further decarbonylation reaction of 2-hydroxybenzaldehyde produces phenol (see Figure 5.8 for PESs). On the other hand, RS 7 presents another secondary reaction scheme as pathway 7b starting from the structure **7_e** for the production of *o*-cresol (see RS 7b for reaction scheme and Figure 5.8 for PESs). The molecular structures associated with RSs 7, 7a, 7a1, and 7b are depicted in Figure 5.7.

The lignin pyrolysis studies have suggested the formation of *o*-quinonemethide; however, no particular vanillin pyrolysis experiment [69–71] has suggested its formation. On the other hand, a computational guaiacol pyrolysis study [50] has indicated the formation of *o*-quinonemethide, therefore, to accommodate this possibility as well, the formation of *o*-quinonemethide has been reported under RS 7. The reaction pathway 7 (see Figure 5.6 for PES) starts with the dehydrogenation of methyl group and as per BDE study, this step requires 97.20 kcal/mol; and it is third most favourable dissociation site (see Table 5.2). However, this pathway further goes through the production of **7_b** and **7_c** with barrier heights of 15.73 and 0.04 kcal/mol, respectively. Further, a hydrogenation reaction is carried out to saturate the oxygen radical of **7_c** structure with BDE of 103.83 kcal/mol followed by the water compound removal process requiring barrier height of 32.06 kcal/mol. The produced component **7_e** (1, 5-Cyclohexadiene-1-carboxaldehyde, 3-methylene-4-oxo-) undergoes formyl group removal process to produce *o*-quinonemethide component which requires two reaction steps with barrier heights 2.38 kcal/mol and 19.73 kcal/mol, respectively. The imaginary frequencies corresponding to **TS7_1**, **TS7_2**, **TS7_3**, **TS7_4**, and **TS7_5** in Figure 5.7 are calculated as 656.15*i* cm^{-1}, 352.18*i* cm^{-1}, 446.89*i* cm^{-1}, 585.85*i* cm^{-1}, and 303.51*i* cm^{-1}, respectively.

The formations of 2-hydroxybenzaldehyde, 4-hydroxy-3-methylbenzaldehyde, *o*-cresol, phenol, and 5-formylsalicylaldehyde (2,4-diformylphenol) components using the

pyrolysis of vanillin component has been reported by several experimental researchers [69–71, 52]. Liu et al. [71] have reported 3.76 area % production of 2-hydroxybenzaldehyde at 600^{o}C and no major trace of 4-hydroxybenzaldehyde between 400-600^{o}C. The vanillin pyrolysis experiment [71] reported the formation of 5-formylsalicylaldehyde (2,4-diformylphenol) component as 18.34 area % and 34.81 area % at the temperatures of 500^{o}C and 600^{o}C, respectively; however, no 5-formylsalicylaldehyde was traced at 400^{o}C. The *o*-cresol component is reported as 2.58 area % in vanillin pyrolysis experiment [71] at 600^{o}C, however, they have reported 4-hydroxy-3- methylbenzaldehyde (which is an intermediate in the process of production of *o*-cresol in this study) as 13.91 area % at 600^{o}C. Similarly, carbon mono oxide and phenol were found as one of the major products in vanillin pyrolysis [71]. Therefore, these reactions are also carried out and reported as reaction schemes 7a, 7a1, and 7b. According to the reaction scheme 7a, structure **7_c** (see Figure 5.7 for its structure) undergoes the dehydrogenation of CH_2 group to produce 2,4-diformylphenol which further undergoes the decarbonylation reaction of *ortho* positioned formyl group to form 4-hydroxybenzaldehyde; and finally produces phenol after another decarbonylation reaction step. The 2,4-diformylphenol is also decomposed into phenol according to pathway 7a1 which suggests the decarbonylation of 2,4-diformylphenol of *para* positioned formyl group to produce 2-hydroxybenzaldehyde which again undergoes the decarbonylation to produce phenol.

The BDE for the production of **7a_d** component from **7_c** is 10.46 kcal/mol. The barrier heights of the first reaction steps of pathways 7a and 7a1 in Figure 5.8 are 91.0 and 86.31 kcal/mol, respectively. Further decomposition reactions of 4-hydroxybenzaldehyde and 2-hydroxybenzaldehyde into phenol under pathways 7a and 7a1 require barrier heights of 86.85 kcal/mol and 92.22 kcal/mol, respectively. The imaginary frequencies corresponding to **TS7a_1**, **TS7a_2**, **TS7a1_1**, and **TS7a1_2** in Figure 5.7 are calculated as 1645.33*i* cm^{-1}, 1691.65*i* cm^{-1}, 1664.19*i* cm^{-1}, and 1706.63*i* cm^{-1}, respectively.

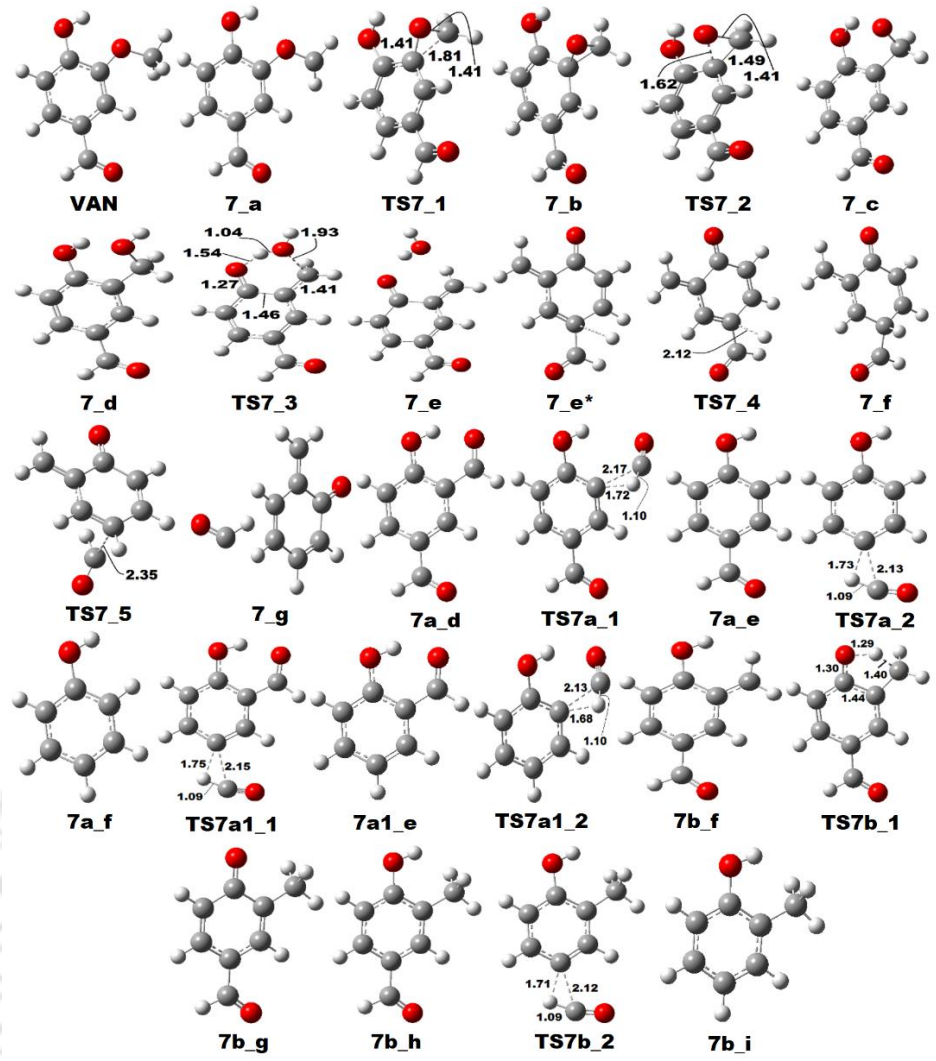

Figure 5.7: The optimized molecular structures involved in reaction scheme 7.

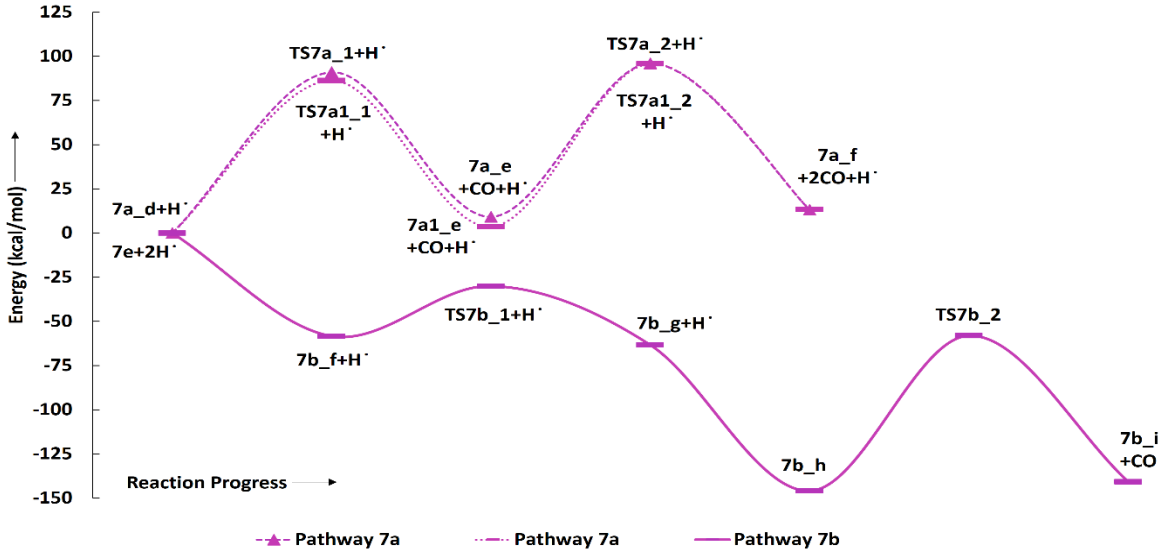

Figure 5.8: The potential energy surfaces of reaction schemes 7a, 7a1, and 7b.

The reaction pathway 7b originates from the single step hydrogenation reaction to the oxygen atom, which is para positioned to the formyl group of **7_e** structure (see Figure 5.7) with BDE of 58.19 kcal/mol followed by the hydrogen migration reaction from hydroxyl group to saturate the methylene into methyl group with barrier height of 28.34 kcal/mol. Further, the radical generated on oxygen atom of structure **7b_g** (see Figure 5.7), due to hydrogen migration, is saturated again and produces **7b_h** (see Figure 5.7) with BDE of 84.01 kcal/mol. Finally, the decarbonylation reaction of structure **7b_h** requires a barrier height of 87.79 kcal/mol to produce *o*-cresol. The imaginary frequencies corresponding to **TS7b_1** and **TS7b_2** are 2143.22*i* cm^{-1} and 1705.68*i* cm^{-1}, respectively.

The dissociation of H radicals from O-H bond is often found; though, there are various other possibilities as well, e.g., dissociation of H from formyl group ($^{\bullet}CHO \rightarrow CO + H^{\bullet}$) and dissociation of $H^{\bullet}$ from $^{\bullet}OCH_3$ group ($^{\bullet}OCH_3 \rightarrow OCH_2 + H^{\bullet}$). The BDEs for dissociation of hydrogen from formyl and methoxy radicals are of 38.5 kcal/mol and 43.7 kcal/mol, respectively. The dissociation energies can easily be obtained when pyrolysis temperature is very high, i.e., in the range of 698 K-898 K. Since, the production of formaldehyde (OCH_2) is not found in the vanillin pyrolysis experiment carried out by Liu et al. [71], further decomposition of formaldehyde to CO and two H radicals is a valid reason to proceed. Further, Shen et al. [69] have carried out similar experiment in which they proposed the decomposition of formaldehyde to CO and two H radicals. The dissociation of H radicals from $^{\bullet}OCH_3$ by Shen et al. [69] in their vanillin pyrolysis experiment is given as $^{\bullet}OCH_3 \rightarrow OCH_2 + H^{\bullet}$, $OCH_2 \rightarrow {}^{\bullet}CHO + H^{\bullet}$, and $^{\bullet}CHO \rightarrow CO + H^{\bullet}$. Similarly, the abstraction of $H^{\bullet}$ from $^{\bullet}CH_3$ group using reaction steps as $^{\bullet}CH_3 \rightarrow :CH_2 + H^{\bullet}$, $:CH_2 \rightarrow :\dot{C}H + H^{\bullet}$, and $:\dot{C}H + :O \rightarrow CO + H^{\bullet}$ is also given by Shen et al. [69]. In the similar way, the abstraction of $H^{\bullet}$ from $^{\bullet}RH$ is indicated by Liu et al. [71] as well using $^{\bullet}RH \rightarrow R^{\bullet} + H^{\bullet}$. Furthermore, the formation of CO from reaction steps such as $^{\bullet}CHO \rightarrow CO + H^{\bullet}$ (directly from formyl group and using methoxy group, i.e., $^{\bullet}OCH_3 \rightarrow$

$OCH_2 + H^{\bullet}$, $OCH_2 \rightarrow {}^{\bullet}CHO + H^{\bullet}$), and $:\dot{C}H + :O \rightarrow CO + H^{\bullet}$ (from methyldiene and oxygen atom) evidences the significant fraction of CO in product mixture of vanillin pyrolysis experiment carried out by Liu et al. [71]. In addition, Shen et al. [69] have also found the fractions of leftover hydrogen in pyrolytic product compositions which increases as the temperature increases. Therefore, it would be feasible to say that there are enough hydrogen radicals present in the system to utilize various proposed hydrogenation reactions.

5.1.7. Thermochemistry

The thermodynamic properties are very important parameters for any reaction to find out its spontaneity, exothermicity, degree of disorder, etc. The thermochemistry calculations in the terms of reaction free energies and reaction enthalpies are carried out at 598-898 K in gas phase because of high boiling point of vanillin (558 K) using B3LYP/6-311+g(d,p) level of theory. The reaction free energies (ΔG) and reaction enthalpies (ΔH) are presented in Table 5.4. The reaction pathways which are producing same products, ΔG and ΔH for those reactions are same, for instance, pathways 5 and 5a are producing benzene, therefore, for pathways 5 and 5a, ΔG and ΔH are same. Similarly, the same is true for pathways 7a and 7a1. For thermodynamic properties of pathways 7a and 7a1, the reactant and product are assumed as vanillin and phenol, respectively. Similarly, for pathway 7b, the reactant and product are assumed as vanillin and *o*-cresol, respectively. The reaction pathways 1 and 2 both produce same end product but pathway 1 deals with vanillin demethylation, whereas, pathway 2 deals with vanillin demethoxylation, therefore, both pathways produce different side products and hence both pathways give different ΔG and ΔH.

The RS 1 which produces 4-hydroxybenzaldehyde using methyl group cleavage of vanillin is favourable reaction at each temperature. The reaction enthalpy of RS 1 has not a major effect of temperature but the reaction spontaneity increases by almost 6 kcal/mol due to

Table 5.4: The thermochemistry parameters (ΔM) at 598-898 K in gas phase.

Pathways	ΔM	Temperature (K)			
		598	**698**	**798**	**898**
1	ΔG	-45.66	-47.66	-49.58	-51.43
	ΔH	-33.41	-33.97	-34.58	-35.22
2	ΔG	-27.91	-29.27	-30.58	-31.83
	ΔH	-19.57	-19.98	-20.38	-20.78
3	ΔG	-25.32	-26.63	-27.89	-29.09
	ΔH	-17.26	-17.68	-18.10	-18.53
4	ΔG	-9.43	-10.21	-10.95	-11.64
	ΔH	-4.60	-4.91	-5.23	-5.55
5 and 5a	ΔG	-66.16	-69.50	-72.67	-75.70
	ΔH	-45.61	-46.79	-47.97	-49.14
6	ΔG	-56.59	-62.27	-67.82	-73.24
	ΔH	-22.16	-23.10	-24.07	-25.05
7	ΔG	-34.40	-39.53	-44.57	-49.54
	ΔH	-3.46	-4.01	-4.63	-5.30
7a and 7a1	ΔG	47.07	34.06	21.04	8.04
	ΔH	124.86	124.95	124.91	124.77
7b	ΔG	-140.25	-142.09	-143.81	-145.44
	ΔH	-128.93	-129.67	-130.45	-131.24

temperature rise from 598 K to 898 K. The reaction schemes 2 and 3 which produce 4-hydroxybenzaldehyde and guaiacol, respectively show similar behaviour compared to RS 1, i.e., both schemes are endorsed by temperature increment. On the other hand, the reaction scheme 4, i.e., production of 3-methoxybenzaldehyde from vanillin, is least favourable compared to reaction schemes 1, 2, and 3. Though, it improves upon increment in temperature but even at 898 K, it does not reach to the values to that of reaction schemes 1, 2, and 3 at 598 K. The reaction scheme 3 which produces guaiacol from vanillin is more favourable compared to RS 4 which, in turn, affirms the experiment of Liu et al. [71] who reported guaiacol as one of the major product. The reaction schemes 5 and 6 produce benzene but with different byproducts, therefore, both reactions demonstrate different thermodynamic parameters. Both reaction schemes 5 and 5a are thermochemically approving; however, reaction scheme 5 is favourable reaction compared to RS 5a from activation barrier point of view. The reaction

schemes 6 and 7 produce benzene and *o*-quinonemethide, respectively. The reaction free energies of both reactions show exceptional behaviour because of improvements by ~17 kcal/mol (RS 6) and ~15 kcal/mol (RS 7) with temperature rising from 598 K to 898 K. The formation of *o*-quinonemethide can be responsible for coke formation, therefore, this should be suppressed down. The reaction pathway 7 shows exothermicity and spontaneity at each temperature. On the other hand, the pathways 7a and 7a1 are neither exothermic nor spontaneous at any temperature; however, the reaction free energies drastically decrease with increasing temperature but never become spontaneous even at 898 K. This, in fact, verifies the experimental analyses of vanillin pyrolysis from 698 K - 898 K by Liu et al. [71] because they did not report the formation of phenol. But, they reported the formation of *o*-cresol which is found to be most favourable reaction amongst all reaction schemes.

5.2. Gas Phase Conversion of Eugenol into Various Hydrocarbons and Platform Chemicals

5.2.1. Reaction Schemes

The notations in reaction schemes (RSs) and Figures 5.9-5.17 are shown as, in general, **X_Y**, where **X** and **Y** denote the reaction pathway number and structure number in that particular reaction pathway, respectively. For instance, in **4_b**, **b** is the structure of reaction pathway 4. Similarly, the transition state structures have been designated as **TSX_Y** in all potential energy surface figures, where **X** is reaction pathway number and **Y** is the transition state number in a given reaction pathway, e.g., **TS3_1** is the first transition state structure in reaction pathway 3.

The reaction scheme 1 presents the demethylation of eugenol followed by single step hydrogenation reaction to produce 4-allylcatechol. Further, 4-allylcatechol undergoes a single step hydrogenation reaction followed by dehydroxylation reaction to produce 4-allylphenol; followed by the similar reactions to produce 4-allylbenzene. Finally, two step hydrogenation reactions to the double bond of allyl are performed to produce 4-propylbenzene (see RS 1). The reaction scheme 2 describes a secondary reaction scheme as well. Under primary reaction scheme 2, a hydrogen atom is associated on the aromatic carbon of $C_{aromatic}$-allyl followed by removal of allyl group to produce guaiacol, whereas, the secondary reaction scheme is about the cleavage of allyl group of eugenol followed by a single step hydrogenation to produce guaiacol. Third reaction scheme is about the removal of vinyl group from eugenol followed by an atomic hydrogen addition to produce 4-methylguaiacol. Further, 4-methylguaiacol follows two schemes. Under primary reaction scheme 3 (bold blue lines in RS 3), a single step hydrogenation reaction is carried out at the aromatic carbon of $C_{aromatic}$-OCH_3 sigma bond followed by demethoxylation reaction to produce 4-methylphenol. The secondary reaction

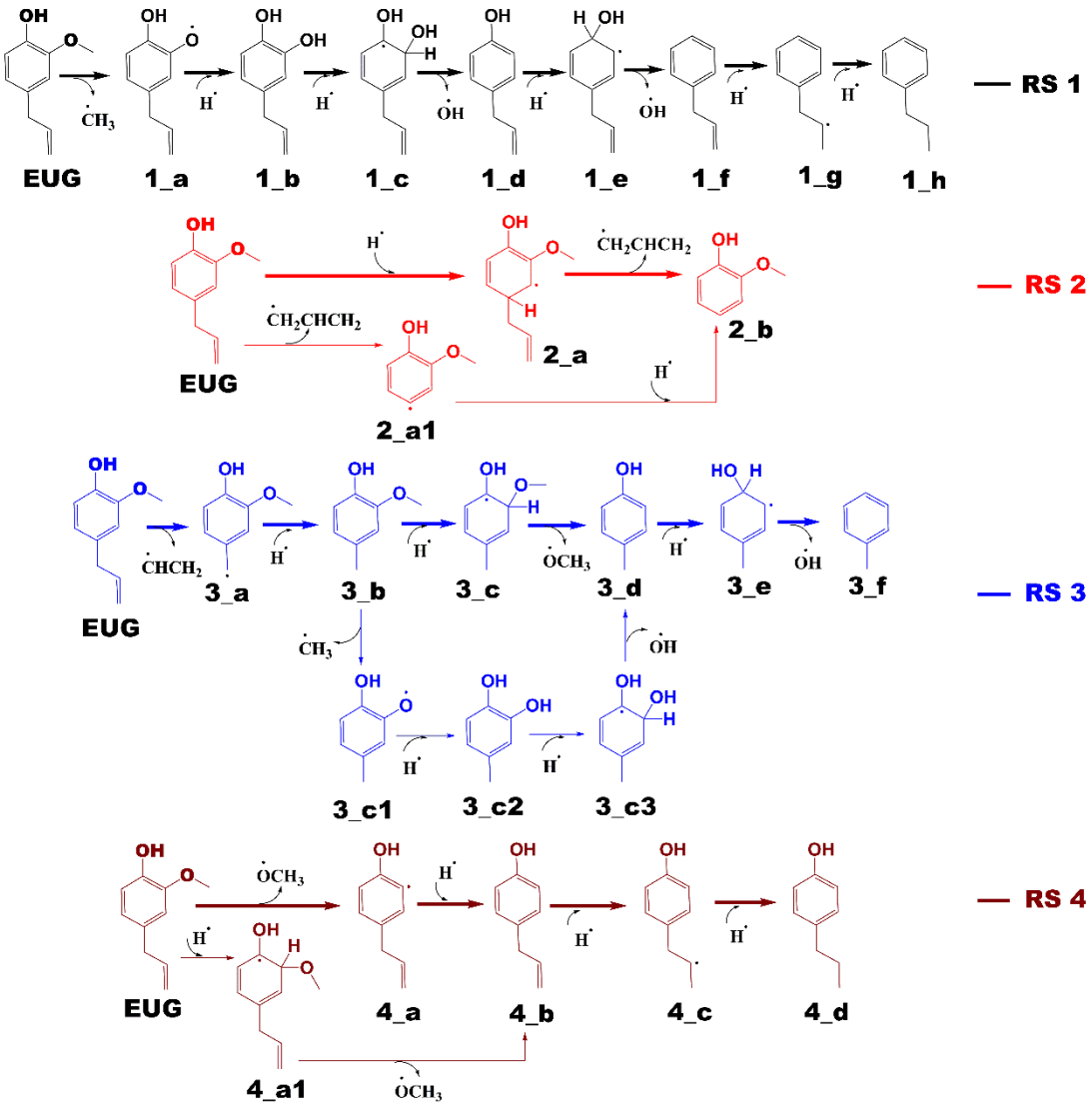

scheme 3 (regular blue lines in RS 3) is the demethylation reaction of O-CH_3 bond of 4-methylguaiacol followed by an atomic hydrogenation to produce 4-methylcatechol; and a single step hydrogenation reaction at the aromatic carbon of $C_{aromatic}$-OH bond, *meta* positioned to the methyl group, is carried out followed by dehydroxylation reaction to produce 4-methylphenol. The 4-methylphenol, an intermediate where secondary reaction scheme 3 merges, is further hydrogenated to remove the hydroxyl functional to produce 4-methylbenzene. Similar to the reaction scheme 3, the reaction scheme 4 also has a secondary reaction scheme. Under primary reaction scheme 4 (bold brown lines in RS 4), the eugenol undergoes methoxy group cleavage followed by a single step hydrogenation reaction to

produce 4-allylphenol; and two step hydrogenation reactions to the double bond of allyl to produce 4-propylphenol. On the other hand, the secondary reaction scheme 4 (regular brown

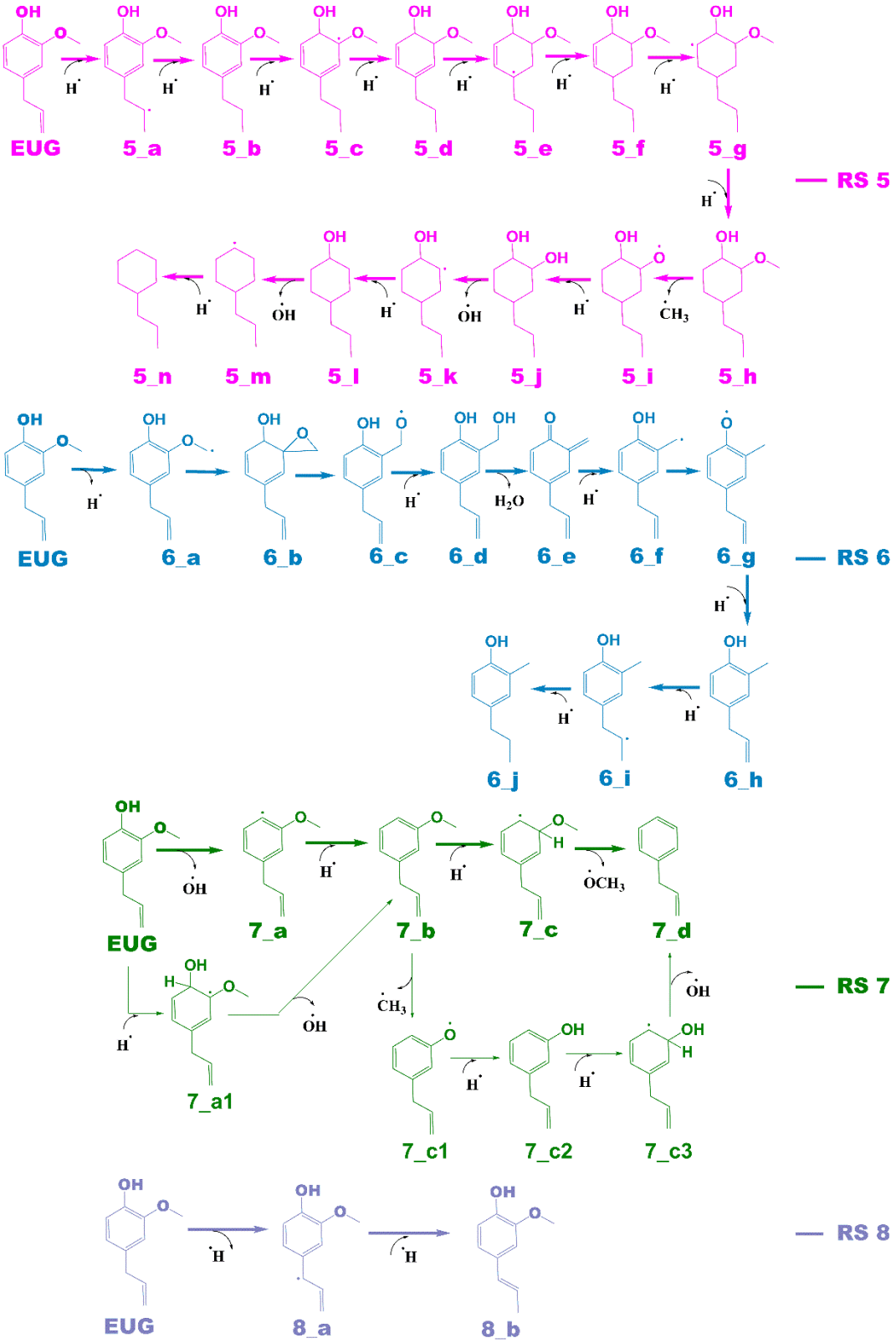

lines in RS 4) presents a single step hydrogenation reaction to the aromatic carbon of $C_{aromatic}$-OCH_3 bond followed by methoxy group removal and merges to 4-allylphenol. The reaction scheme 5 first carries out allyl hydrogenation reactions to produce 4-propylguaiacol followed by ring saturation reactions. The produced component after ring saturation, 2-methoxy-4-propylcyclohexanol, undergoes demethylation reaction followed by a single step hydrogenation reaction to produce 4-propyl-1,2-cyclohexanediol. This further undergoes hydroxyl cleavage and a single step hydrogenation reaction to produce 4-propyl-cyclohexanol. Similarly, another hydroxyl cleavage of 4-propyl-cyclohexanol is carried out followed by an atomic hydrogenation reaction to produce propylcyclohexane. The reaction scheme 6 is about the methoxy group rearrangement to produce 4-allyl-2-(hydroxymethyl)phenol. Further, the produced component undergoes water compound removal followed by two atomic hydrogen addition reactions to yield 4-allyl-2-methylphenol. Finally, the hydrogenation reactions to allyl produce 4-propyl-2-methylphenol. The reaction scheme 7 describes hydroxyl group cleavage and a single step hydrogenation reaction to produce 3-allylanisole which further undergoes an atomic hydrogen addition to $C_{aromatic}$-OCH_3 bond followed by demethoxylation reaction to produce allylbenzene. Similar to reaction schemes 3 and 4, the reaction scheme 7 also includes a secondary reaction scheme in which eugenol undergoes a single step hydrogenation followed by hydroxyl removal to produce 3-allylanisole; which further undergoes demethylation reaction and an atomic hydrogenation reaction to produce 3-allylphenol. Finally, a single step hydrogenation to 3-allylphenol followed by hydroxyl cleavage produces allylbenzene. The reaction scheme 8 is about the dissociation of benzylic hydrogen (see RS 8) followed by an atomic hydrogen addition reaction to the terminal carbon (methylene group) to produce isoeugenol. All above reaction pathways are carried out theoretically in gas phase milieu at B3LYP/6-311+g(d,p) level of theory under density functional theory (DFT).

Table 5.5: Competitive molecular structures of eugenol with relative energies in kcal/mol.

Structures	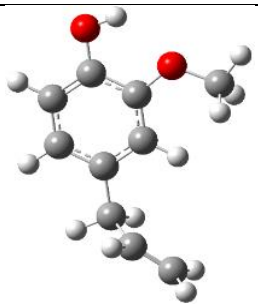	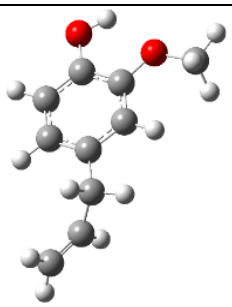
	Config. 1	**Config. 2**
Relative Energy	0	0.39

Eugenol component can be represented by various conformers of competitive energetics; however, two eugenol conformers are very close in their energetics and are presented in Table 5.5. The eugenol structure of **config. 1** is 0.39 kcal/mol more stable than the eugenol structure of **config. 2**. The present conformational analysis is under excellent agreement with Majkut et al. [136] because they also reported **config. 1** structure as the ground state conformer and according to their simulations, eugenol structure of **config. 2** (see Table 5.5) is 0.39 kcal/mol less stable than the **config. 1**. Therefore, all calculations, e.g., BDEs, reaction pathways, etc. are carried out using eugenol structure of **config. 1**.

5.2.2. Bond Dissociation Energy (BDE)

The bond dissociation energies (kcal/mol) of eugenol based on **config. 1** of eugenol are shown in Table 5.6. As it can be seen from Table 5.6 that the methyl cleavage (D1) from eugenol structure is found to be the least energy demanding but it slightly varies with the BDE given by Ledesma et al. [80]. However, the energetics of D1 given by Ledesma et al. [80] at B3LYP/6-311+g(d,p) level of theory is also the least energy demanding compared to other cleavages. The variation can be explained by the ground state conformer of eugenol but there is no molecular structure of eugenol reported by Ledesma et al. [80] based on which it could have been verified. However, the ground state eugenol structure, in this study, is validated with Majkut et al. [136] and it is in excellent agreement with them. The second most favourable

Table 5.6: The bond dissociation energies (in kcal/mol) of eugenol with considered bond cleavages.

Bond		BDE (kcal/mol)		% error
		Ledesma et al. [80]	Present (6-311+g(d,p))	
D1	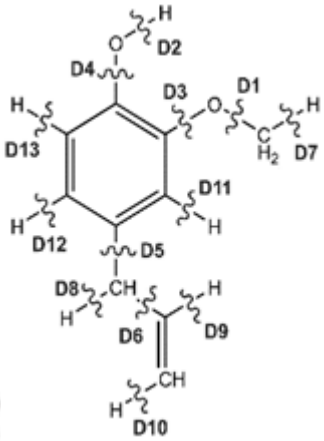	52.2	47.85	9.10
D2		87.8	82.59	6.31
D3		97.2	92.39	5.21
D4		112	108.02	3.68
D5		82.1	78.14	5.07
D6		83.2	78.17	6.44
D7		102	96.23	6.00
D8		79.1	73.68	7.35
D9		112	106.15	5.51
D10		116	110.36	5.11
D11		117	111.49	4.94
D12		118	112.13	5.23
D13		119	113.71	4.65

bond cleavage is reported as D8. The bond cleavages D5 and D6 are very competitive to each other in energetics; which are the allyl and vinyl group cleavages from eugenol, respectively. It can be seen that many bond cleavages are in ~5 % error with the literature values but the average deviation between the literature values [80] and present values is calculated to be 5.74 %. The bond dissociation energies in ascending order of their energetics are laid as D1 < D8 < D5 < D6 < D2 < D3 < D7 < D9 < D4 < D10 < D11 < D12 < D13, respectively.

5.2.3. Potential Energy Surfaces

5.2.3.1. Reaction Pathways 1, 2 and 2a

The potential energy surfaces of reaction schemes 1 and 2 are shown in Figure 5.9; the energies in Figure 5.9 are added with zero point vibrational energies (ZPVEs) and reported in kcal/mol. The molecular structures associated with reaction schemes 1 and 2 are depicted in Figure 5.10. The inter-atomic distances in transition state structures of Figure 5.10 are shown in angstrom

(Å) units. The BDEs and/or barrier heights (in kcal/mol) corresponding to each reaction step of all discussed reaction schemes are shown in Table 5.7.

The reaction scheme 1 produces propylbenzene from eugenol. As the BDE study suggests that the methyl group cleavage is most favourable compared to other bond cleavages, therefore, the reaction pathway 1 starts from methyl group cleavage. The produced component after methyl cleavage undergoes a single step hydrogenation reaction to produce 4-allylcatechol. The BDEs of these two reaction steps are 47.85 kcal/mol and 75.22 kcal/mol, respectively. Further, a hydrogen atom is adsorbed on the aromatic carbon of $C_{aromatic}$-OH sigma bond, the one which is *meta* positioned to allyl group, followed by the hydroxyl group removal reaction to produce 4-allylphenol. The barrier height of the hydrogen addition over aromatic carbon is 3.81 kcal/mol and since, the transition state for hydroxyl removal from **1_c** structure is hard to find, BDE calculation is carried out for this reaction step which is 16.51 kcal/mol. The produced component is recognized as 4-allylphenol. Further, to produce allylbenzene from 4-allylphenol, the similar reaction steps as of **1_b → 1_c → 1_d** are carried out as **1_d → 1_e → 1_f**.

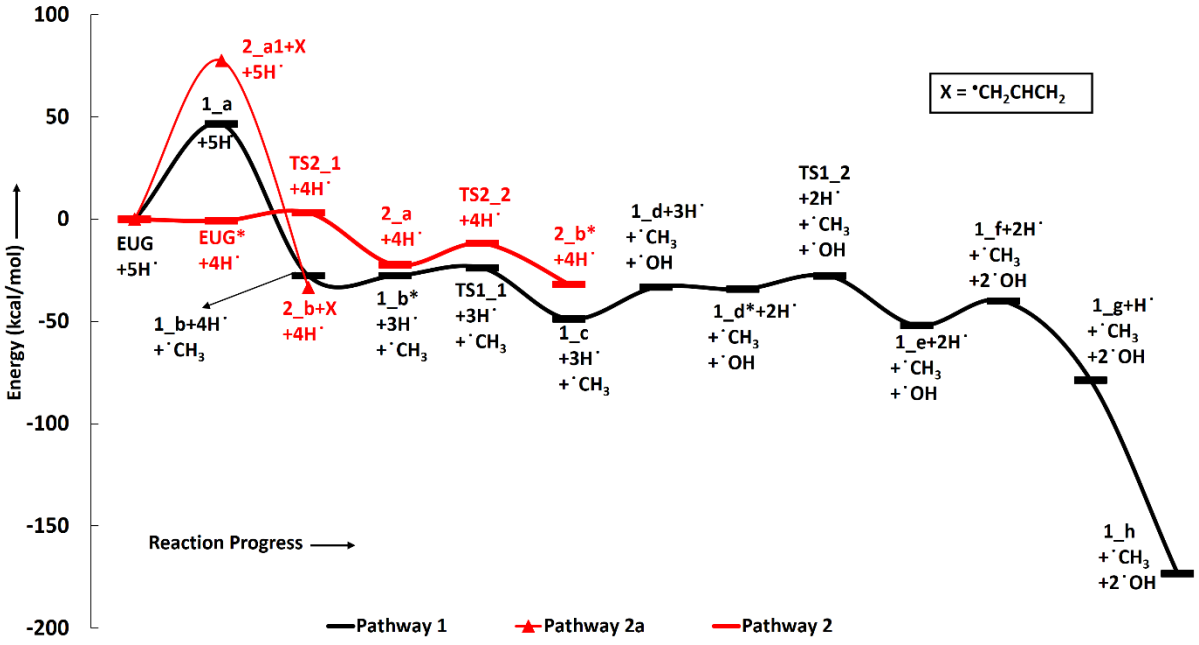

Figure 5.9: Potential energy surfaces of reaction pathways 1, 2 and 2a.

The barrier height of the reaction step **1_d** → **1_e** is 6.38 kcal/mol and BDE of the reaction step **1_e** → **1_f** is 5.65 kcal/mol. The production of allylbenzene is also carried out in the reaction scheme 7 with different mechanism compared to the reaction scheme 1 to compare activation energy. Nevertheless, allylbenzene does not contain any oxy-functional which is prime motive of bio-oil upgrading but it does contain a double bond in allyl group other than the ones in phenyl ring. Therefore, it is further hydrogenated to saturate the double bond of allyl into single bond by two single step hydrogenation reactions. Nimmanwudipong et al. [73] in their experiment suggested to hydrogenate the terminal carbon group first followed by the middle one, therefore, a single step hydrogenation is carried out at the terminal carbon (methylene) of allyl followed by another single step hydrogenation to saturate the radical on second carbon. These two steps require BDEs of 39.60 kcal/mol and 96.33 kcal/mol, respectively. The imaginary frequencies corresponding to **TS1_1** and **TS1_2** are 762.50*i* cm^{-1} and 933.63*i* cm^{-1}, respectively.

Second reaction scheme is about the production of guaiacol by deallylation of eugenol. The formation of guaiacol, as major product, has been suggested by Nimmanwudipong et al. [73] in their experiment of eugenol conversion over HY zeolite catalyst. Zhang et al.[74] also found guaiacol as one of the product in their experiment of eugenol over Pd/C and HZSM-5 catalysts. As it has been pointed out that the guaiacol production, in this study, is carried out by two reaction pathways, i.e., reaction pathways 2 and 2a. It can be seen in RS 2, under primary reaction pathway 2, that hydrogen atom is adsorbed on the aromatic carbon of $C_{aromatic}$-allyl bond prior to the removal of allyl group to produce guaiacol, whereas, under secondary reaction pathway 2a, eugenol first undergoes allyl group cleavage followed by a single step hydrogenation reaction to produce guaiacol. The barrier heights of the hydrogen adsorption on the aromatic carbon of $C_{aromatic}$-allyl bond and the deallylation reaction under reaction pathway 2 are 3.95 kcal/mol and 10.53 kcal/mol, respectively. On the other hand, the BDEs of direct

cleavage of the allyl group and a single step hydrogenation to the carbon radical under reaction pathway 2a are 78.14 kcal/mol and 112.46 kcal/mol, respectively. It can be seen that the direct cleavage of allyl group is not favourable at all; however, if the hydrogen atom is added on the aromatic carbon of $C_{aromatic}$-allyl bond prior to allyl cleavage then it is favourable. Thus, activation energies of both reaction pathways 2 and 2a are 10.53 kcal/mol and 112.46 kcal/mol, respectively. Therefore, it can be believed that the allyl group cleavage occurs after the hydrogen atom addition. The imaginary frequencies corresponding to **TS2_1** and **TS2_2** are 749.74*i* cm^{-1} and 585.99*i* cm^{-1}, respectively.

5.2.3.2. Reaction Pathways 3 and 3a

The reaction scheme 3 is about the production of toluene, an important product in the industries, from eugenol. Both reaction pathways, i.e., 3 and 3a, share the reaction till the production of 4-methylguaiacol (see RS 3). The potential energy surfaces are depicted in Figure 5.11; the energies are added with ZPVEs and are in kcal/mol. The corresponding molecular structures are shown in Figures 5.10 and 5.12. The inter-atomic distances are presented in angstrom units.

The reaction starts from vinyl group cleavage of eugenol followed by a single step hydrogenation reaction to produce 4-methylguaiacol. The production of 4-methylguaiacol is carried out by Deepa and Dhepe [79] and they reported that eugenol first undergoes allyl group saturation followed by methyl group cleavage from propyl group and addition of a hydrogen atom. Similar to the experiment of Deepa and Dhepe [79], Nimmanwudipong et al. [73] also suggested the same for the formation of 4-methylguaiacol. Here in reaction scheme 3, another approach has been considered, i.e., the methylene group is cleaved from allyl group of eugenol followed by a single step hydrogenation reaction to produce 4-methylguaiacol; however, the production of 4-methylguaiacol according to Nimmanwudipong et al. [73] and Deepa and

Dhepe [79] will be discussed in the sub-section of reaction scheme 5 as reaction steps **EUG → 5_a → 5_b → 3_a → 3_b**.

According to the reaction pathway 3, BDEs of the reaction steps **EUG → 3_a → 3_b** are 78.17 kcal/mol and 86.55 kcal/mol, respectively. The produced component, i.e., 4-methylguaiacol, follows two pathways as reaction pathways 3 and 3a. As it has been observed in the subsection of 'Bond Dissociation Energies' that the direct cleavages of methoxy, hydroxyl, and allyl of eugenol require a high BDEs, therefore, the direct cleavages of functional groups may not be favourable. To avoid such cases, other approaches are carried out in reaction pathways 3 and 3a. Under reaction pathway 3, a hydrogen atom is adsorbed on the aromatic carbon of $C_{aromatic}$-OCH_3 sigma bond followed by methoxy group removal. The barrier heights of reaction steps **3_b → 3_c → 3_d** are 4.11 kcal/mol and 9.30 kcal/mol, respectively. On the other hand, the reaction pathway 3a undergoes demethylation of 4-methylguaiacol followed by a single step hydrogenation reaction requiring bond dissociation energies of 46.81 kcal/mol and 74.22 kcal/mol, respectively, to produce 4-methylcatechol. The 4-methylcatechol further undergoes a hydrogen atom adsorption on aromatic carbon of $C_{aromatic}$-OH bond, the one which is *meta* positioned to methyl group, followed by hydroxyl group removal requiring barrier height and BDE of 4.60 kcal/mol and 17.04 kcal/mol, respectively, to produce 4-methylphenol. The secondary reaction pathway merges to the structure of *p*-cresol, i.e., **3_d**, from which the main reaction pathway 3 carries on. Although, *p*-cresol is an important compound in the industries but, for study purpose, further oxygen removal of *p*-cresol is carried out to produce toluene which is also a great industrial chemical. The single step hydrogenation reaction is carried out to the aromatic carbon of $C_{aromatic}$-OH sigma bond which requires a barrier height of 6.31 kcal/mol followed by the hydroxyl group removal and BDE of reaction step **3_e → 3_f** is 13.37 kcal/mol. The imaginary frequencies corresponding to **TS3_1**, **TS3_2**, **TS3_3**, and **TS3a_1** are 750.33*i* cm^{-1}, 403.66*i* cm^{-1}, 927.32*i* cm^{-1}, and 722.18*i* cm^{-1}, respectively.

Table 5.7: The bond dissociation energies and/or the activation energies of each reaction step of all reaction schemes.

Pathways	Bond Dissociation Energies/Barrier Heights (kcal/mol)													
	Step 1	**Step 2**	**Step 3**	**Step 4**	**Step 5**	**Step 6**	**Step 7**	**Step 8**	**Step 9**	**Step 10**	**Step 11**	**Step 12**	**Step 13**	**Step 14**
1	47.85	75.22	3.81	16.51	6.38	5.65	39.60	96.33	---	---	---	---	---	---
2	3.95	10.53	---	---	---	---	---	---	---	---	---	---	---	---
2a	78.14	112.46	---	---	---	---	---	---	---	---	---	---	---	---
3	78.17	86.55	4.11	9.30	6.31	13.37	---	---	---	---	---	---	---	---
3a	same as path 3		46.81	74.22	4.60	17.04	---	---	---	---	---	---	---	---
4	92.39	111.76	35.97	99.86	---	---	---	---	---	---	---	---	---	---
4a	4.48	9.40	same as path 4		---	---	---	---	---	---	---	---	---	---
5	39.37	96.11	22.75	67.99	52.51	76.67	36.79	97.49	73.28	100.31	89.76	97.72	87.32	96.44
6	96.23	14.71	0.03	102.76	32.26	58.54	27.74	80.30	39.46	96.32	---	---	---	---
7	108.02	113.91	6.23	10.07	---	---	---	---	---	---	---	---	---	---
7a	5.17	16.70	56.41	84.29	6.73	11.98	---	---	---	---	---	---	---	---
8	73.68	79.64	---	---	---	---	---	---	---	---	---	---	---	---

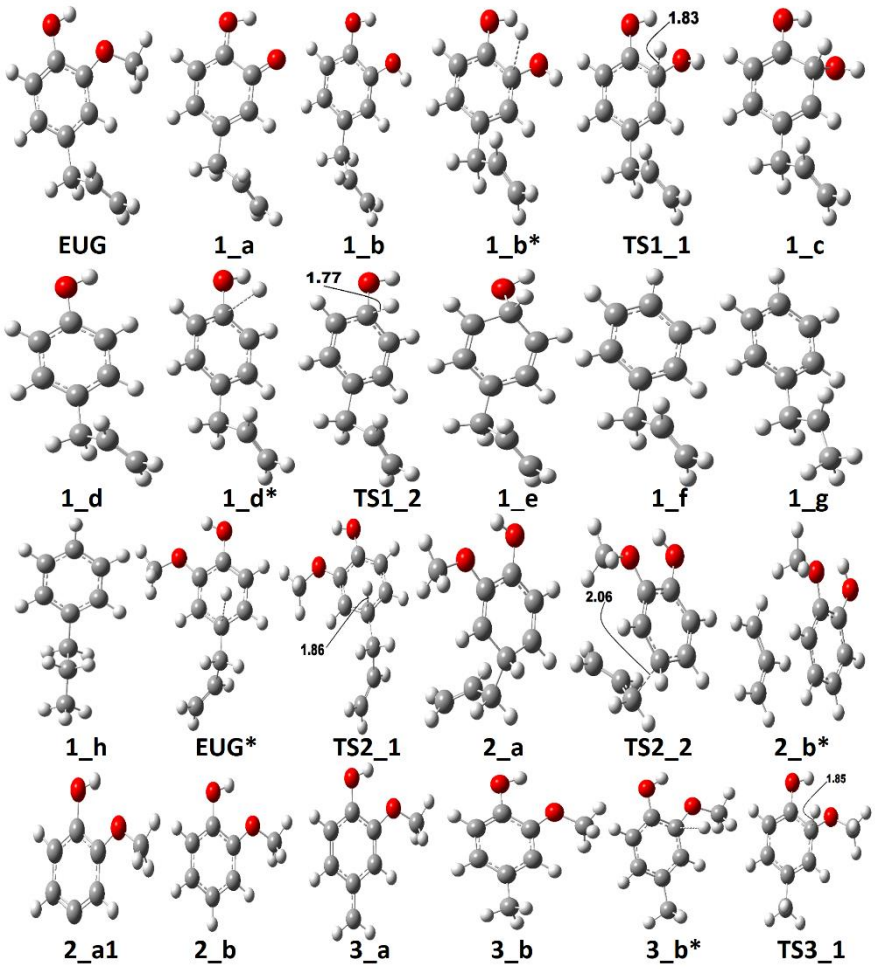

Figure 5.10: Optimized molecular structures corresponding to pathways 1, 2, 2a, and 3.

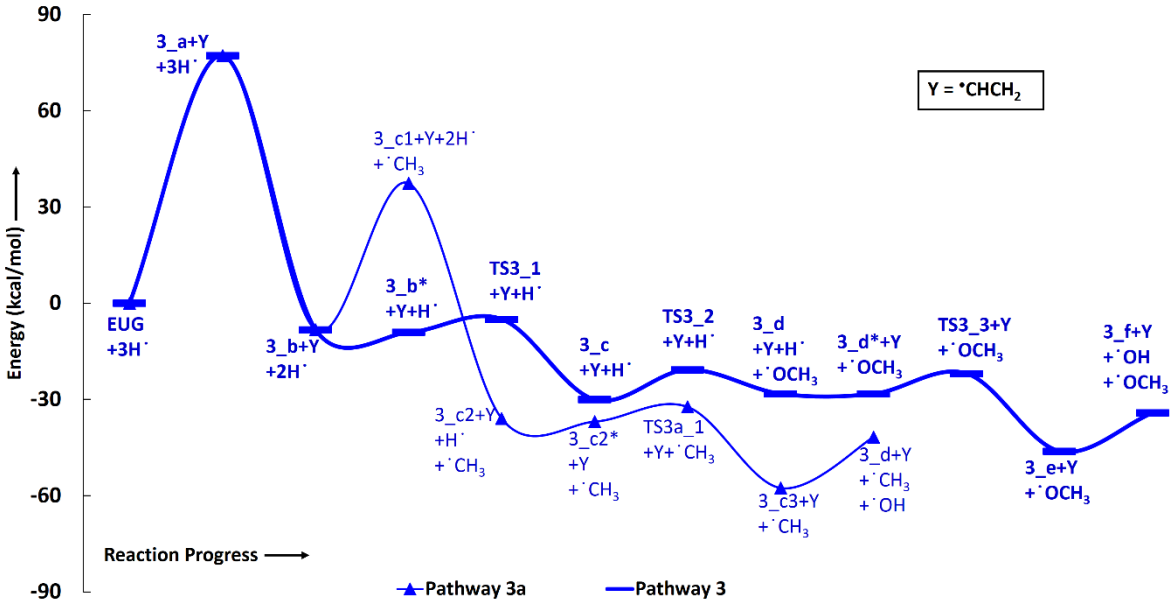

Figure 5.11: Potential energy surfaces of reaction pathways 3 and 3a.

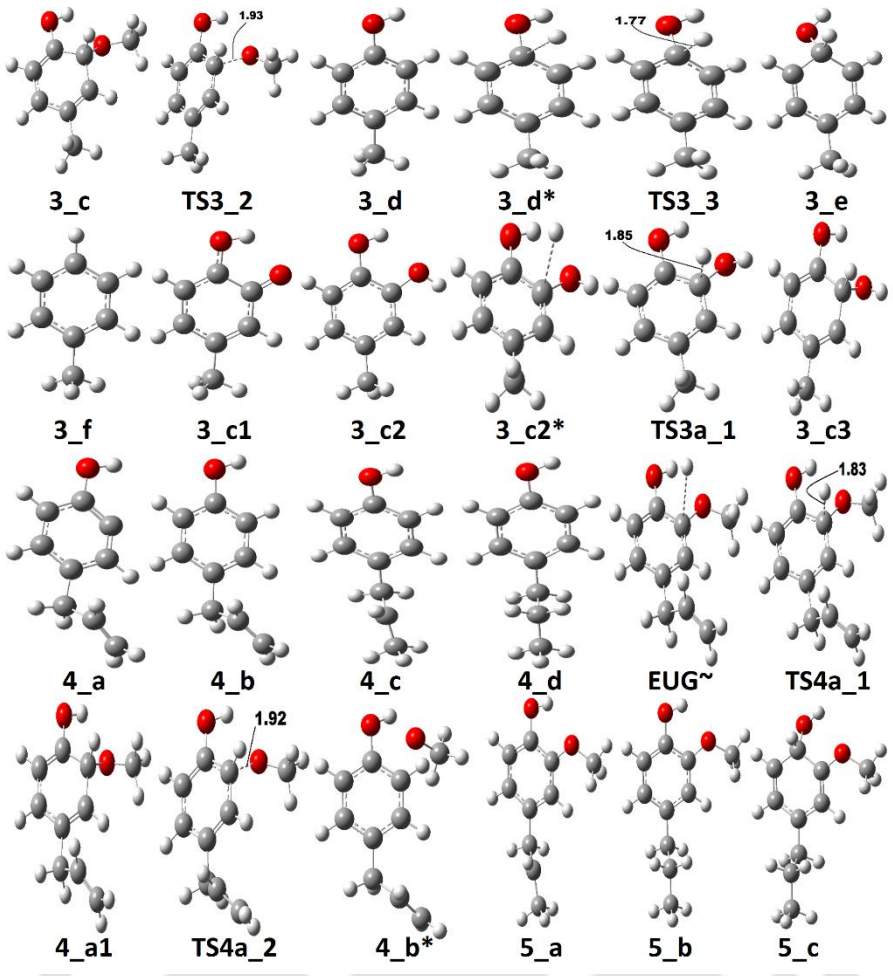

Figure 5.12: Optimized molecular structures corresponding to pathways 3, 3a, 4, 4a, and 5.

The rate determining step of reaction pathway 3 is the single step hydrogenation reaction which produces 4-methylguaiacol, i.e., **3_a → 3_b**, therefore, the activation energy is 86.55 kcal/mol. The production of 4-methylphenol from 4-methylguaiacol under reaction pathway 3 seems favourable because of less barrier height compared to that of reaction pathway 3a. Therefore, the production of toluene favours reaction pathway 3 compared to pathway 3a, however, the production of 4-methylguaiacol from eugenol requires a high amount of energy. Nevertheless, another approach will be discussed in the subsection of 'Reaction Pathways 5 and 6' for the production of 4-methylguaiacol from eugenol according to the mechanism provided by Nimmanwudipong et al. [73] and Deepa and Dhepe [79].

5.2.3.3. Reaction Pathways 4 and 4a

The reaction pathway 4 is about the production of 4-propylphenol. The production of 4-propylphenol from eugenol is reported in the experiments of eugenol conversion over supported Pd catalyst [79] and also in the presence of alumina supported Pt catalyst [73]. It is observed in the experiment carried out by Nimmanwudipong et al. [73] that the 4-propylphenol is produced *via* hydrogenation reactions to the allyl of 4-allylphenol thus the production of 4-allylphenol as an intermediate in the course of the production of 4-propylphenol from eugenol becomes mandatory. Therefore, under reaction pathway 4, eugenol has been subjected for the production of 4-propylphenol with an intermediate product 4-allylphenol. Similar to the reaction pathways 2 and 3, reaction pathway 4 also comprises a secondary reaction pathway as 4a. The potential energy surfaces of reaction pathway 4 and 4a are shown in Figure 5.13 and the corresponding molecular structures are depicted in Figure 5.12. Energies in Figure 5.13 are added with ZPVEs and are in kcal/mol.

The reaction pathway 4 presents the methoxy group cleavage of eugenol followed by a single step hydrogenation reaction to produce 4- allylphenol. BDE of the direct cleavage of

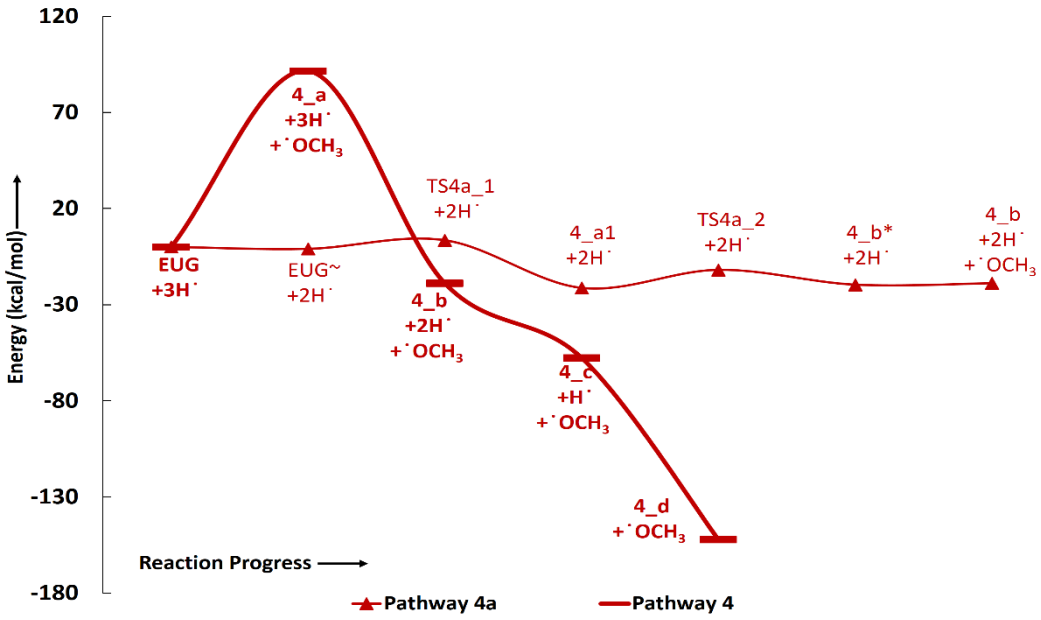

Figure 5.13: Potential energy surfaces of reaction pathways 4 and 4a.

methoxy group is given in Table 5.6, however, that is high energetics, 92.39 kcal/mol, and cannot be achieved without appropriate catalyst. Further, the BDE of atomic hydrogen addition requires an even higher BDE, i.e., 111.76 kcal/mol. Therefore, it is observed earlier and here too that the direct cleavages are not favourable. On the other hand, the reaction pathway 4a carries out an atomic hydrogenation at the aromatic carbon of $C_{aromatic}$-OCH_3 sigma bond prior to the methoxy group removal; and the barrier heights of these two steps are 4.48 kcal/mol and 9.40 kcal/mol, respectively. It can be seen that the direct cleavage of methoxy group from eugenol is not favourable; but, a single step hydrogenation reaction followed by methoxy group removal requires considerably less amount of barrier heights. The imaginary frequencies corresponding to **TS4_1** and **TS4_2** are 767.66*i* cm^{-1} and 410.44*i* cm^{-1}, respectively.

It should be noted that the reaction pathway 1 also produces 4-allylphenol (**1_d**) from eugenol and requires an activation energy of 75.22 kcal/mol considering 4-allylphenol as product and eugenol as reactant. This activation energy, i.e., 75.22 kcal/mol, is less compared to the activation energy demanded by reaction pathway 4 considering 4-allylphenol as product, but is considerably higher than the activation energy required by reaction pathway 4a for the same reactant and product. Furthermore, the saturation of double bond which is present in the allyl group is saturated *via* two atomic hydrogenation reactions which requires BDEs of 35.97 kcal/mol and 99.86 kcal/mol, respectively. The reaction pathway 4a merges to the structure of 4-allylphenol (see structure **4_b** in RS 4) and follows similar pathway as of RS 4, therefore, the saturation of double bond of allyl group will follow the same energetics as of RS 4.

5.2.3.4. Reaction Pathways 5 and 6

The reaction scheme 5 is about the production of propylcyclohexane from the eugenol and reaction scheme 6 produces 2-methyl-4-propylphenol. The reaction mechanisms can be seen in RS 5 and RS 6 and explanations are given in the 'Reaction Schemes' subsection. The

potential energy surfaces of reaction schemes 5 and 6 are shown in Figure 5.14; and the corresponding molecular structures are depicted in Figures 5.12, 5.15 and 5.17.

Zhang et al. [74] suggested the formation of 2-methoxy-4-propylcyclohexanol from eugenol in the presence of Pd/C catalyst with an intermediate called 2-methoxy-4-propylphenol. Similar phenomena have also been observed by Deepa and Dhepe [79] in the presence of Pd catalyst and Chen et al. [78] over Ru catalyst. Therefore, in this study, the reaction pathway 5 starts with the saturation of allyl group of eugenol which produces 2-methoxy-4-propylphenol. The first single step hydrogenation reaction is carried out at the terminal carbon of allyl according to the reaction mechanism suggested by Nimmanwudipong et al. [73]; followed by the second atomic hydrogen addition to saturate the radical produced due to the first atomic hydrogen addition. First hydrogen addition reaction requires an energy of 39.37 kcal/mol according to the BDE, whereas, the BDE of second step is 96.11 kcal/mol. This leads to the saturation of aromatic ring which requires six single step hydrogenation reactions to produce 2-methoxy-4-propylcyclohexanol. Though, the ring saturation reactions during decomposition mechanisms are not recommended but to understand the potential energy surface, it has been considered in this study. The formation of 2-methoxy-4-propylcyclohexanol from 4-propylguaiacol progresses through the productions of two intermediates, i.e., 6-methoxy-4-propylcyclohexa-2,4-dien-1-ol and 6-methoxy-4-propylcyclohex-2-en-1-ol. The bond dissociation energies of six single step hydrogenation reactions for ring saturation are calculated as 22.75 kcal/mol, 67.99 kcal/mol, 52.51 kcal/mol, 76.67 kcal/mol, 36.79 kcal/mol, and 97.49 kcal/mol, respectively (see Table 5.7). The produced component after the ring saturation is identified as 2-methoxy-4-propylcyclohexanol which further undergoes the demethylation reaction and a single step hydrogenation reaction to produce 4-propylcyclohexane-1,2-diol. The production of 4-propylcyclohexane-1,2-diol from 2-methoxy-4-propylcyclohexanol is carried out by Zhang et al. [74] using hydrolysis over Pd/C

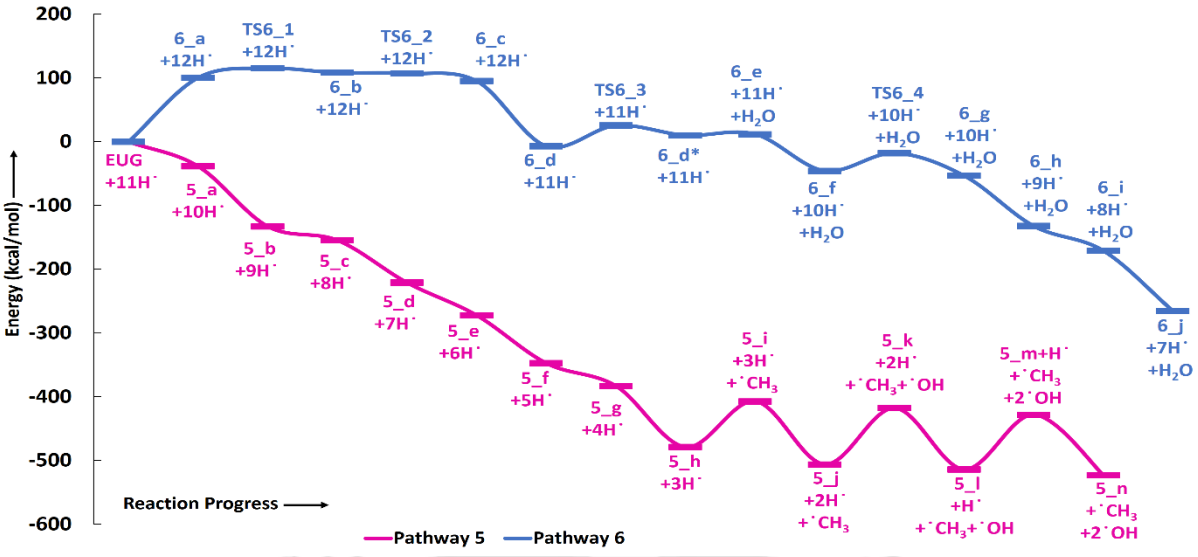

Figure 5.14: Potential energy surfaces of reaction pathways 5 and 6.

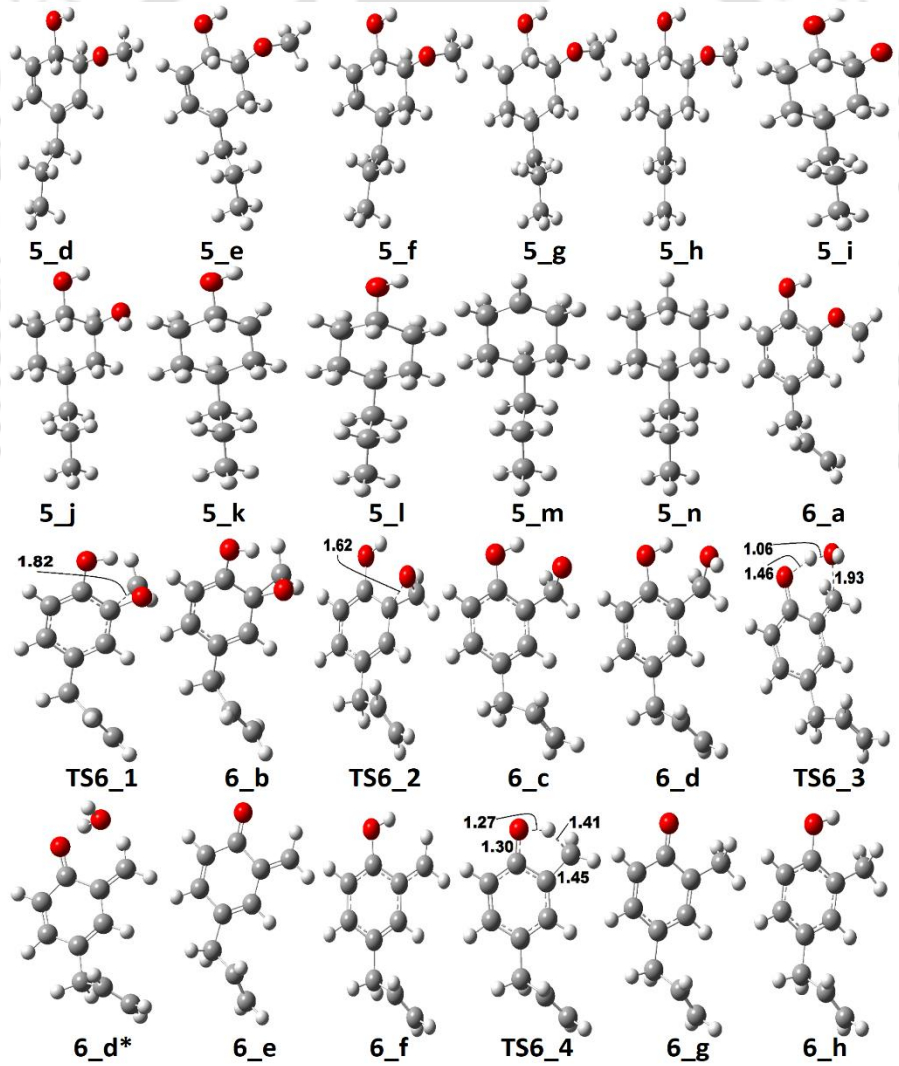

Figure 5.15: The optimized molecular structures corresponding to pathways 5 and 6.

in the aqueous phase environment, however, the present study represents the gas phase milieu. Nevertheless, a demethylation reaction is carried out at 2-methoxy-4-propylcyclohexanol followed by an atomic hydrogen addition reaction to produce 4-propylcyclohexane-1,2-diol. The BDEs of these two steps are 73.28 kcal/mol and 100.31 kcal/mol, respectively. Further, the production of propylcyclohexane involves the formation of an important intermediate called 4-propylcyclohexanol which is formed during the dehydroxylation reaction, the hydroxyl group which is *meta* positioned to propyl group, of 4-propylcyclohexane-1,2-diol followed by an atomic hydrogen addition reaction. The BDEs of hydroxyl cleavage and atomic hydrogenation reactions are 89.76 kcal/mol and 97.72 kcal/mol, respectively. The 4-propylcyclohexanol component can be a very good candidate to produce 4-propylcyclohexanone, an important component used as an intermediate of liquid crystals, by dehydrogenation reactions. However, in this study, the production of propylcyclohexane is also carried out. The production of propylcyclohexane requires the hydroxyl cleavage and a single step hydrogenation reactions similar to the production of 4-propylcyclohexanol from 4-propylcyclohexane-1,2-diol. The bond dissociation energies of these two steps to produce propylcyclohexane are 87.32 kcal/mol and 96.44 kcal/mol, respectively.

As mentioned in section of 'Reaction Schemes', the production of 4-methylguaiacol from eugenol in pathways 3 and 3a is carried out using the vinyl group removal followed by an atomic hydrogen addition reaction. However, the literature reviews [73, 74, 79] suggest the formation of 4-methylguaiacol through ethyl group removal of 4-propylguaiacol which is produced *via* allyl group saturation of eugenol followed by an atomic hydrogen addition reaction. Thus, the reaction steps for the production of 4-methylguaiacol according to the literature [73, 74, 79] can be laid as **EUG → 5_a → 5_b → 3_a → 3_b**. The bond dissociation energies of reaction steps **EUG → 5_a → 5_b** are 39.37 kcal/mol and 96.11 kcal/mol, respectively. The BDE of reaction step **5_b → 3_a** is 65.14 kcal/mol and BDE of single step

hydrogen reaction to structure **3_a** to produce **3_b** is 86.55 kcal/mol. Therefore, the activation energies for the production of 4-methylguaiacol according to the literature experiments [73, 74, 79] and reaction pathway 3 are 96.11 kcal/mol and 86.55 kcal/mol. Thus, it can be concluded that the production of 4-methylguaiacol under reaction pathway 3 is more favourable than the mechanisms given in literature experiments [73, 74, 79]. However, it entirely depends on catalyst, support, temperature-pressure conditions, etc. which promote the reaction in specific way; nevertheless, the study for production of 4-methylguaiacol from eugenol in the presence of various catalysis conditions is still limited and needs to be unravelled to finally understand the true mechanism.

The reaction pathway 6 is about the production of 2-methyl-4-propylphenol from eugenol. The reaction starts from the dehydrogenation reaction of methyl group for which BDE is 96.23 kcal/mol. The dehydrogenation of methyl group leads the methylene group to attach with one of the aromatic carbon (see Figure 5.15 for corresponding molecular structures) which completes *via* a transition state structure, **TS6_1**. Further, the detachment of oxygen is carried out using **TS6_2** in order to remove the C-O bond from the aromatic ring. The barrier heights corresponding to both transition state structures are 14.71 kcal/mol and 0.03 kcal/mol, respectively. The detachment of oxygen atom from phenyl ring generates a radical which is saturated using an atomic hydrogen addition to the oxygen atom. BDE of reaction step **6_c** → **6_d** is 102.76 kcal/mol. Further, the removal of water compound from structure **6_d** cause a barrier height of 32.26 kcal/mol with transition structure identified as **TS6_3**. The produced component after water removal is recognized as 4-allyl-6-methylenecyclohexa-2,4-dien-1-one. An atomic hydrogenation reaction to the oxygen atom is carried out, with BDE of 58.54 kcal/mol, to convert the keto group into an enol group; however, this reaction generates a radical on the carbon group (*meta* positioned to allyl group). The hydrogen atom of hydroxyl group is migrated to convert the methylene group into methyl group; and the barrier height for

the same is 27.74 kcal/mol. In addition, another single step hydrogenation to the oxygen atom is carried out to produce 2-methyl-4-allylphenol with calculated BDE of 80.30 kcal/mol. The produced component 2-methyl-4-allylphenol further undergoes two single step hydrogenation reactions to convert the double bond of allyl to single bond thus producing 2-methyl-4-propylphenol. The BDEs of allyl saturation are 39.46 kcal/mol and 96.32 kcal/mol, respectively. The imaginary frequencies corresponding to **TS6_1**, **TS6_2**, **TS6_3**, and **TS6_4** are calculated to be 660.0*i* cm^{-1}, 328.11*i* cm^{-1}, 558.04*i* cm^{-1}, and 2178.67*i* cm^{-1}, respectively.

5.2.3.5. Reaction Pathways 7, 7a, and 8

The reaction pathway 7 produces allylbenzene which is also an intermediate product in the RS 1. The reaction pathway 1 first carries out demethylation of eugenol to produce allylbenzene as an intermediate, whereas, the reaction pathway 7 first carries out the hydroxyl group cleavage. The reaction pathway 7 also possess a secondary reaction pathway as 7a which first carries out an atomic hydrogen addition reaction to the aromatic carbon of $C_{aromatic}$-OH sigma bond. The potential energy surfaces of reaction pathways 7, 7a, and 8 are shown in Figure 5.16. The molecular structures corresponding to the potential energy surfaces 7, 7a, and 8 are depicted in Figure 5.17.

The reaction pathway 7 starts from the cleavage of hydroxyl group followed by an atomic hydrogenation reaction to produce 3-methoxy-allylbenzene. The BDEs of the first two steps of pathway 7 are 108.02 kcal/mol and 113.91 kcal/mol, respectively. These energetics are quite high and are not possible without the use of any appropriate catalyst; however, the reaction pathway 7a finds a way to reduce the energetics. The reaction pathway 7a first carries out an atomic hydrogenation reaction to the aromatic carbon of $C_{aromatic}$-OH sigma bond by a transition state structure **TS7a_1** followed by hydroxyl group removal to produce 3-methoxy-allylbenzene. The barrier height and BDE of first and second reaction steps of reaction pathway

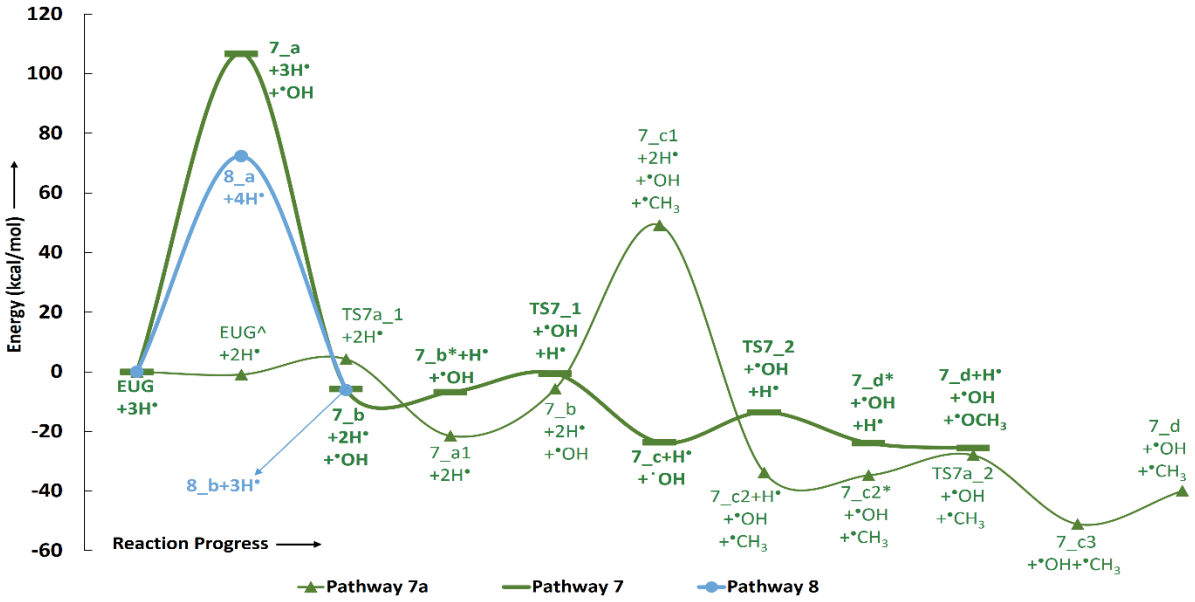

Figure 5.16: Potential energy surfaces of reaction pathways 7, 7a, and 8.

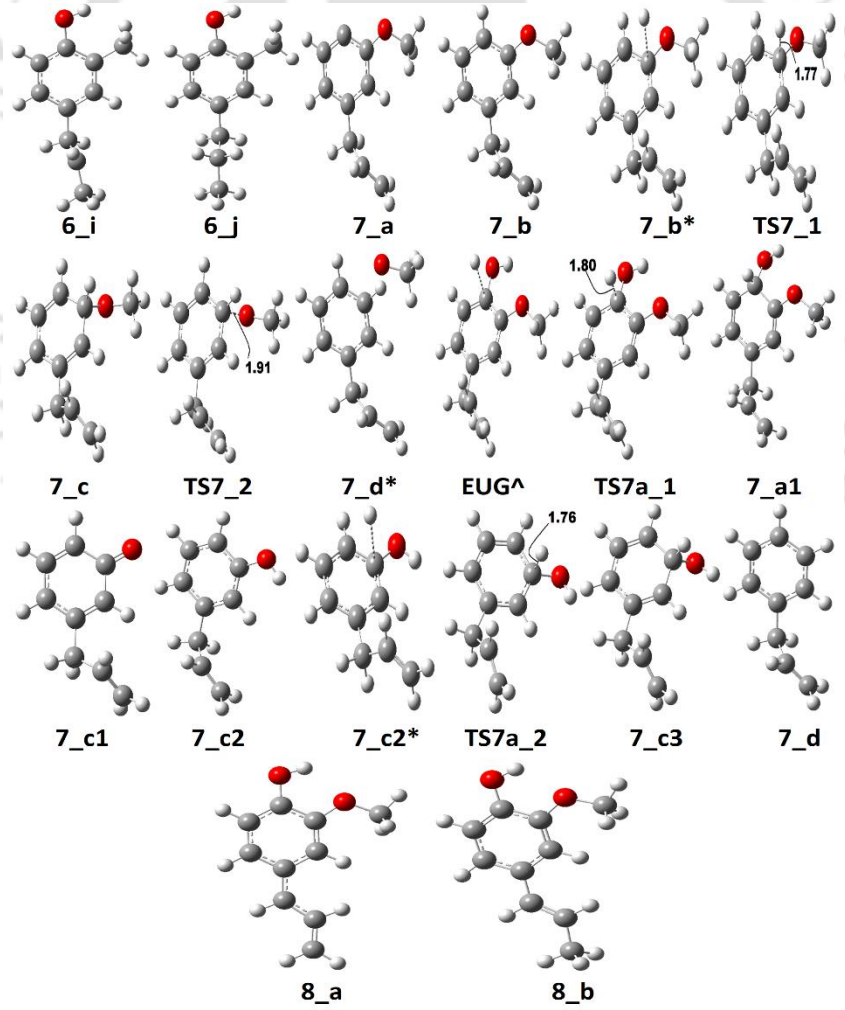

Figure 5.17: Optimized molecular structures corresponding to pathways 6, 7, 7a, 8, and 7a.

7a are 5.17 kcal/mol and 16.70 kcal/mol, respectively. Therefore, pathway 7a becomes favourable if the product and reactant are considered as 3-methoxy-allylbenzene and eugenol, respectively. Since, the direct cleavage of oxy-functionals is not favourable, referring to reaction pathways 2, 4 and 7, the adsorption of hydrogen atom is carried out on the aromatic carbon of $C_{aromatic}$-OCH_3 sigma bond under primary reaction pathway 7 followed by the removal of methoxy group to produce allylbenzene. The barrier heights corresponding to **TS7_1** and **TS7_2** are calculated to be 6.23 kcal/mol and 10.07 kcal/mol, respectively. On the other hand, the secondary reaction pathway 7a carries out demethylation reaction of structure **7_b** followed by an atomic hydrogen addition to produce 3-hydroxy-4-allylbenzene. The BDEs of these two steps are 56.41 kcal/mol and 84.29 kcal/mol, respectively. Further, 3-hydroxy-4-allylbenzene undergoes an atomic hydrogen addition to the aromatic carbon of $C_{aromatic}$-OH sigma bond followed by the removal of hydroxyl functional to produce allylbenzene. The barrier height corresponding to **TS7a_2** and BDE of the reaction step **7_c3** → **7_d** are 6.73 kcal/mol and 11.98 kcal/mol, respectively. The imaginary frequencies corresponding to **TS7_1**, **TS7_2**, **TS7a_1**, and **TS7a_2** are 908.09*i* cm^{-1}, 487.08*i* cm^{-1}, 855.78*i* cm^{-1}, and 957.67*i* cm^{-1}, respectively. It can be seen that the optimum reaction pathway for the production of allylbenzene from both reaction pathways 7 and 7a follows as **EUG** → **7_a1** → **7_b** → **7_c** → **7_d**. Therefore, the rate determining step of the optimum reaction steps can be identified as the reaction step **7_a1** → **7_b** which provides an activation energy of 16.70 kcal/mol. On the other hand, the activation energy for the production of allylbenzene from eugenol under RS 1 is 75.22 kcal/mol which is much higher than the activation energy given by optimum reaction pathway of allylbenzene. Thus, the production of allylbenzene should occur according to the optimum reaction pathway of allylbenzene, i.e., **EUG** → **7_a1** → **7_b** → **7_c** → **7_d**. However, the production of propylbenzene from allylbenzene follows the same pathway as of the reaction steps given in RS 1.

The reaction pathway 8 is about the production of *trans*-isoeugenol by dissociation of benzylic hydrogen followed by the atomic hydrogen addition to the terminal carbon (see **8_b** in Figure 5.17). As it is established in the subsection of 'Bond Dissociation Energies' that the dissociation of benzylic hydrogen (see D8 in Table 5.6) is second most favourable bond cleavage, therefore, the reaction based on the dissociation of benzylic hydrogen is considered in reaction pathway 8. Deepa and Dhepe [79] reported the formation of *trans*-isoeugenol as an intermediate product in their experiment of eugenol conversion over supported Pd catalyst. Furthermore, the production of isoeugenol is also studied by Nimmanwudipong et al. [73] in their experimental study on conversion of eugenol in the presence of HY zeolite catalyst; they reported this component as major product. Therefore, reaction pathway 8 incorporates the possibility of formation isoeugenol. The BDE of dissociation of the benzylic hydrogen is 73.68 kcal/mol and the BDE due to the atomic hydrogen addition to produce *trans*-isoeugenol is 79.64 kcal/mol. Further dissociation of *trans*-isoeugenol is not considered in the present study because experimental evidences due to Nimmanwudipong et al. [73] do not recommend. However, *trans*-isoeugenol can be hydrogenated at the C=C double bond present in the chain to produce 4-propylguaiacol which can follow the reaction forward as schemed in RS 5.

Finally, summarizing all reaction schemes, the activation energy for the production of guaiacol from eugenol under reaction scheme 2 is 10.53 kcal/mol only which is the least activation energy required amongst all activation energies corresponding to each reaction scheme. This verifies the experiment of eugenol conversion carried out by Nimmanwudipong et al. [73] who reported guaiacol as one of the major product in the presence of HY zeolite catalyst. However, they witnessed that deallylation of eugenol, i.e., formation of guaiacol from eugenol over zeolite catalyst, is relatively slower than the isomerization reaction of eugenol. It can be observed that some of the reaction schemes require a high amount of activation energies especially atomic hydrogen addition reactions after direct cleavages of functional groups. The

activation energies of reactions can be reduced using various ways such as application of appropriate catalysts, solution phase reactions, etc. Similarly, the variation of temperature and pressure conditions can also affect the rates of reactions.

5.2.4. Thermochemistry

The thermochemistry study for conversion of eugenol into various products using all reaction schemes is presented here at wide range of temperature of 498-898 K with an interval temperature of 100 K. The pressure is constant as 1 atm for each temperature variation. The reactions whose reactants and products are same, the thermodynamic parameters (ΔG and ΔH) are also identical, e.g., reaction pathways 2, 2a, 4, and 4a. On the other hand, the reactions whose reactants and products are different, the thermodynamic parameters (ΔG and ΔH) are different, e.g., reaction pathways 3, 3a, 7, and 7a. The thermodynamic parameters, ΔG and ΔH, are enlisted in Table 5.8.

It can be seen from Table 5.8 that all reaction schemes are spontaneous at each temperature condition except reaction pathway 8. The reaction scheme 1, i.e., the production of propylbenzene from eugenol, shows high spontaneity and exothermicity at all temperature conditions; however, it shows decrement in spontaneity as the temperature is increasing but it shows incremental behaviour in the case of exothermicity with increasing temperature. On the contrary, the reaction schemes 2 and 2a, i.e., the production of guaiacol from eugenol, show increment in spontaneity and exothermicity with increasing temperature. The reaction schemes 3 and 3a, i.e., the production of methylbenzene from eugenol, also show similar behaviour as of reaction schemes 2 and 2a, i.e., they become more favourable with increasing temperature, though, both reactions are reported to be favourable at each temperature. It should be noted that both thermodynamic parameters are different for reaction schemes 3 and 3a unlike the reaction schemes 2 and 2a (see Table 5.8).

Table 5.8: The thermochemistry parameters, ΔG and ΔH, of each reaction scheme in kcal/mol.

Pathways	Parameters	Temperature (K)				
		498	**598**	**698**	**798**	**898**
1	**ΔG**	-165.33	-162.48	-159.39	-156.10	-152.64
	ΔH	-178.86	-180.28	-181.69	-183.07	-184.41
2 & 2a	**ΔG**	-41.31	-42.52	-43.66	-44.75	-45.79
	ΔH	-35.09	-35.48	-35.87	-36.28	-36.69
3	**ΔG**	-56.16	-60.79	-65.33	-69.78	-74.16
	ΔH	-32.81	-33.37	-33.96	-34.56	-35.15
3a	**ΔG**	-73.25	-78.54	-83.72	-88.79	-93.76
	ΔH	-46.57	-47.21	-47.95	-48.75	-49.58
4 & 4a	**ΔG**	-136.74	-132.48	-128.06	-123.52	-118.88
	ΔH	-157.47	-158.47	-159.38	-160.21	-160.97
5	**ΔG**	-414.36	-395.88	-377.15	-358.26	-339.29
	ΔH	-505.46	-507.25	-508.57	-509.46	-509.96
6	**ΔG**	-207.96	-202.32	-196.74	-191.25	-185.86
	ΔH	-236.13	-235.91	-235.42	-234.69	-233.74
7	**ΔG**	-11.53	-15.45	-19.48	-23.65	-27.94
	ΔH	7.72	8.33	9.13	10.09	11.20
7a	**ΔG**	-28.62	-33.20	-37.87	-42.65	-47.53
	ΔH	-6.04	-5.51	-4.86	-4.10	-3.23
8	**ΔG**	20.45	18.49	16.30	13.87	11.21
	ΔH	29.55	30.92	32.47	34.18	36.03

The reaction schemes 4 and 4a, i.e., the production of 4-propylphenol from eugenol, show similar behaviour as of reaction scheme 1, i.e., reaction schemes 4 and 4a are spontaneous at each temperature but become less spontaneous with increasing temperature. On the other hand, increase in exothermicity is reported for both reaction schemes 4 and 4a with increasing temperature. The reaction scheme 5, i.e., the production of propylcyclohexane from eugenol, is reported to be highest exothermic and spontaneous amongst all reaction schemes but it becomes significantly less spontaneous with increasing temperature because the difference between ΔG_{898} and ΔG_{498} is calculated to be 75.07 kcal/mol. However, reaction scheme 5

becomes slightly more exothermic with increasing temperature as the difference between ΔH_{898} and ΔH_{498} is -4.50 kcal/mol. Thus, it can be observed that reaction scheme 5 is most favourable at 498 K. Hence, the highest exothermicity and spontaneity of reaction scheme 5 validate the work done by Deepa and Dhepe [79] for one of the major production of propylcyclohexane from eugenol in the presence of supported Pd catalysts. The reaction scheme 6, i.e., the production of 2-methyl-4-propylphenol from eugenol, is second most favourable reaction with similar observation of reaction free energy as of reaction scheme 5, however, the difference between ΔG_{898} and ΔG_{498} is only 22.10 kcal/mol. But, unlike reaction scheme 5, reaction scheme 6 becomes slightly less exothermic with increasing temperature. The reaction schemes 7 and 7a, i.e., the production of allylbenzene from eugenol, show opposite behaviour compared to reaction scheme 1. The ΔG of reaction schemes 7 and 7a decreases with increasing temperature or in other words it becomes more spontaneous with increasing temperature but the ΔH of reaction schemes 7 and 7a increases with increasing temperature. However, it should be noted that the ΔH values are positive for reaction scheme 7 and negative for reaction scheme 7a at all temperatures. Moreover, ΔG values of reaction scheme 7a are lower compared to reaction scheme 7. Therefore, reaction scheme 7a is more favourable compared to reaction scheme 7 at all temperature variations. The reaction pathway 8, i.e., the formation of *trans*-isoeugenol is neither spontaneous nor exothermic at any given temperature condition. The ΔG values for the formation of *trans*-isoeugenol decrease as the temperature increases but do not reach to negative values so that the reaction could become spontaneous. On the other hand, ΔH values of reaction pathway 8 increase as the temperature increases.

The reaction pathways 1, 4, 4a, 5, and 6 show decrement in spontaneity with increasing temperature, therefore, these reactions are most spontaneous at 498 K only (boiling point of eugenol is 527 K). Out of all reaction schemes, only reaction schemes 6 and 7a are the ones which report a reduction in exothermicity; however, reaction pathways 7 and 8 are the ones

which are endothermic at 498 K and become further endothermic with increasing temperature. On the other hand, reaction schemes 2, 2a, 3 and 3a are the only reactions which show an increment in both spontaneity and exothermicity with increasing temperatures.

5.3. Unravelling the Dissociation Mechanism of Ferulic Acid under Density Functional Theory Framework

5.3.1. Reaction Schemes

General notations for considered reaction schemes in this study are given as **X_Y** where **Y** is the molecular structure number in reaction scheme **X**. For example, the structure **3_i** implies i^{th} structure of 3^{rd} reaction scheme. Similarly, the structure **4_c3a** is **c3a** structure in reaction scheme 4. For transition state structures, a general notation is considered as **TSX_Y** where **Y** is the transition structure number in reaction scheme **X**, e.g., **TS4_3** is the 3^{rd} transition structure of 4^{th} reaction scheme.

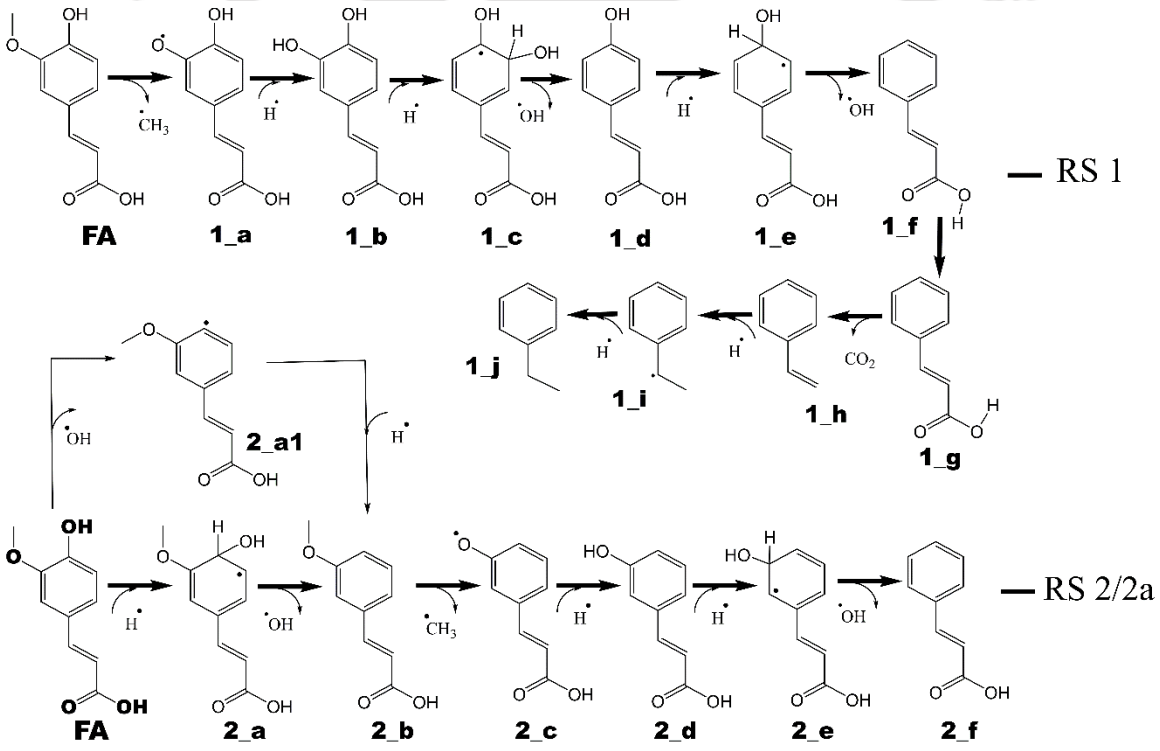

The first reaction scheme (see RS 1) is about the conversion of ferulic acid (FA) into ethylbenzene. The reaction starts from demethylation of ferulic acid followed by an atomic hydrogenation to form caffeic acid. Further, an atomic hydrogenation reaction to the caffeic acid is carried out followed by hydroxyl group elimination to yield 4-hydroxycinnamic acid. Similar reaction steps are again performed for dehydroxylation of 4-hydroxycinnamic acid to

form cinnamic acid followed by the production of styrene *via* decarboxylation reaction of cinnamic acid; and hydrogenation reactions to styrene gives rise to ethylbenzene. Reaction scheme 2 (see RS 2) produces cinnamic acid from FA. FA is first reduced to 3-(3-methoxyphenyl)acrylic acid (see structure **2_b** in RS 2) via two reaction possibilities. Then, structure **2_b** undergoes demethylation reaction to produce 3-(3-hydroxyphenyl)acrylic acid followed by dehydroxylation reaction of 3-(3-hydroxyphenyl)acrylic acid to produce cinnamic acid. Further reduction of cinnamic acid may follow the reaction route specified in RS 1 or it can follow the reaction route according to RS 3. In reaction scheme 3, ferulic acid is again converted into ethylbenzene, similar to RS 1, but with different reaction approach. The ferulic acid, under RS 3, first forms an intermediate 3-(4-hydroxyphenyl)acrylic acid *via* demethoxylation reaction of FA using two reaction routes followed by dehydroxylation reaction to produce cinnamic acid. Further, unlike to RS 1, cinnamic acid undergoes saturation of C=C chain double bond to produce 3-phenylpropanoic acid followed by the decarboxylation reaction to produce ethylbenzene and CO_2 molecules. In the reaction scheme 4, ferulic acid is converted into various end products such as eugenol, *cis*-isoeugenol, 4-ethylguaiacol, vanillin, and acetovanillone (see RS 4). The ferulic acid first undergoes decarboxylation reaction to produce 4-vinylguaiacol which is common intermediate product for all end products in RS 4. Further, 4-vinylguaiacol undergoes methyl group addition to the terminal carbon of vinyl group and hydrogen atom removal reaction to form eugenol and *cis*-isoeugenol, whereas, 4-ethylguaiacol is produced *via* saturation of vinyl group of 4-vinylguaiacol. On the other hand, 4-vinylguaiacol undergoes hydroxyl group addition to form structure **4_c2** followed by hydrogen migration to form **4_c3** which further reduces to vanillin and acetovanillone upon methyl group and hydrogen atom reductions, respectively. The reaction scheme 5 is about the production of guaiacol *via* a single step hydrogenation at the aromatic carbon of $C_{aromatic}$-CHCHCOOH followed by elimination of $^{\bullet}$CHCHCOOH group (see RS 5).

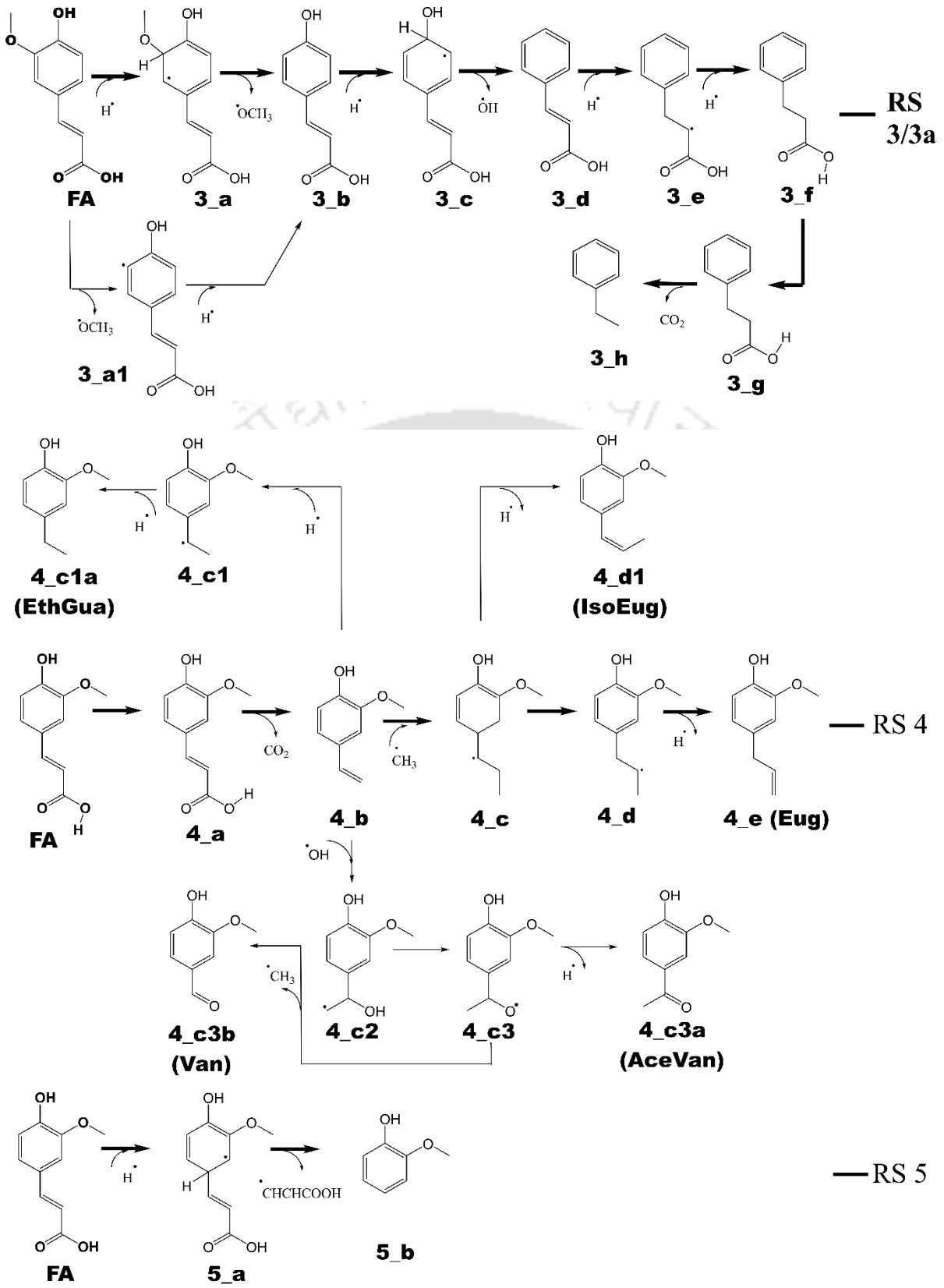

All reaction schemes are simulated using B3LYP/6-311+g(d,p) level of theory under density functional theory (DFT) framework.

Table 5.9: Various ferulic acid conformers with competitive energetics optimized at B3LYP/6-311+g(d,p) level of theory.

Conformers	**1**	**2**	**3**	**4**
Molecular Structures	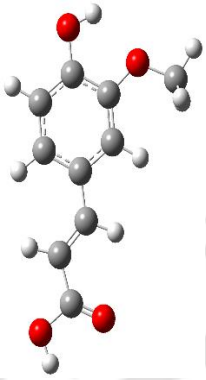	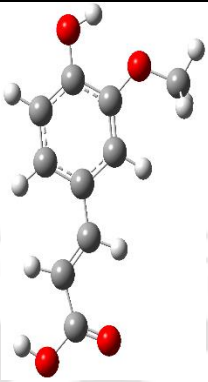	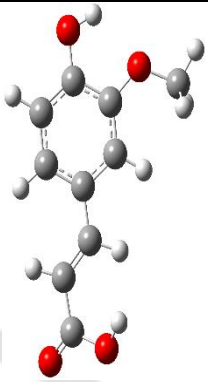	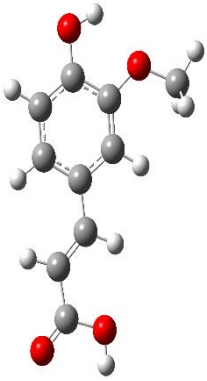
Relative Energy (kcal/mol)	0	6.0	7.59	0.64

To pursue the decomposition study of ferulic acid (FA), it is beneficial to locate its ground state minimum structure to accurately predict its molecular properties. FA can have several conformations, i.e., local minima; and, in this study, four such conformers of ferulic acid are investigated which can be energetically competitive to each other (see Table 5.9). The relative electronic energies added with zero point vibrational energies (ZPVE) of each structure are shown in Table 5.9. The conformer 1 is found to have ground state structure because of lowest electronic energy compared to other conformers. However, conformer 4 is very competitive to conformer 1 in the terms of its ZPVE added electronic energies. Otherwise, conformers 2 and 3 are unstable compared to conformer 1 by 6.0 kcal/mol and 7.59 kcal/mol, respectively. Therefore, all further calculations such as bond dissociation energies, reaction mechanisms, etc. are performed employing conformer 1 of ferulic acid.

5.3.2. Bond Dissociation Energy (BDE)

The bond dissociation energy calculation predicts the energy requirement for any organic homolytic bond scission in a particular molecule. It reflects the free radical stability and

presents a preliminary idea about the favourable bond scission to carry forward the reaction. It is also favourable in predicting the approximate activation energies for bond scissions of organic molecule for which the location of first order saddle point on potential energy surface is difficult. Therefore, ferulic acid has been subjected for the study of bond dissociation energies using 14 bond cleavage sites (see Table 5.10). The methyl group cleavage from FA requires least bond dissociation energy because of sp^3 hybridization; and, on the other hand, D2 bond scission requires slightly higher BDE to cleave $C_{aromatic}O$-H bond which consequently means that it undergoes the formation of less stable radical compared to D1. Similarly, D3 which cleaves methoxy group from FA requires even higher BDE than D2 bond scission. On the other hand, D8 and D7 bond scissions are very competitive to each other in their energy requirements to cleave OH group from carboxylic group of FA and hydrogen from methyl group of FA, respectively. Nevertheless, the bond scissions from FA can be laid as D1 < D2 < D3 < D8 < D7 < D6 < D11 < D9 < D4 < D10 < D13 < D12 < D5 < D14 according to their bond dissociation energies.

Table 5.10: Bond dissociation energies of various ferulic acid bond scissions.

Bond cleavages		BDE (kcal/mol)
D1	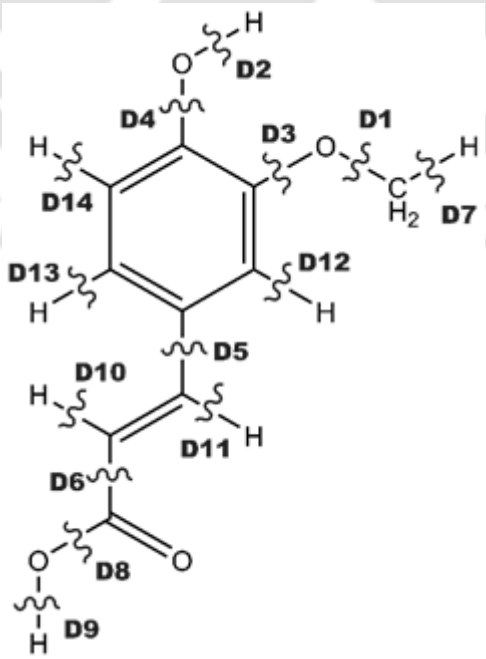	49.56
D2		82.07
D3		93.09
D4		109.49
D5		113.85
D6		103.11
D7		96.72
D8		96.47
D9		104.72
D10		110.57
D11		103.21
D12		112.11
D13		112.03
D14		114.08

5.3.3. Formation of Cinnamic Acid

The formation of cinnamic acid is achieved in reaction schemes 1 (structure **1_f** in RS 1), 2 (structure **2_f** in RS 2) and 3 (structure **3_d** in RS 3) using different reaction approaches. The potential energy surfaces of reaction schemes 1 and 2, and 3 are shown in Figures 5.18 and 5.20, respectively; and optimized molecular structures of reaction schemes 1-3 are depicted in Figures 5.19 and 5.21.

Under reaction scheme 1, the ferulic acid is first converted to caffeic acid using cleavage of methyl group and addition of an atomic hydrogen (**FA → 1_a → 1_b**). The cleavage of methyl group from FA requires a BDE of 49.56 kcal/mol which is already discussed in the subsection of 'Bond Dissociation Energy'. The structure **1_a** is a stable radical compared to other bond scissions because of least BDE demanding scission. Also, as it has been discussed that BDE can be a very good approximation to the activation energy for organic homolysis reactions, therefore, the scission of methyl group from FA will require approximately 49.56 kcal/mol of activation barrier. Though, this activation barrier is higher but during pyrolysis at high temperature, it can easily be achieved. However, the atomic hydrogenation reaction to saturate the oxygen atom of **1_a** structure requires even higher activation barrier, i.e., 76.63 kcal/mol, compared to the first elementary reaction step of methyl group cleavage (see Table 5.11 for activation barriers). Further, caffeic acid undergoes for OH group removal (*meta* positioned to the •CHCHCOOH group) using atomic hydrogenation at the aromatic carbon of $C_{aromatic}$-OH bond first (**1_b → 1_c → 1_d**), to produce *p*-coumaric acid. The structure **1_b** in Figures 5.18 and 5.19 is caffeic acid, however, the structure **1_b*** in Figures 5.18 and 5.19 is equilibrium structure of caffeic acid and hydrogen atom. The hydrogen atom at the aromatic carbon of caffeic acid is at equilibrium position which presents the structure **1_b*** as a minimum structure on PES. However, the equilibrium distance between hydrogen and aromatic carbon gets lessened to 1.83 Å when it reaches to first order saddle point on PES.

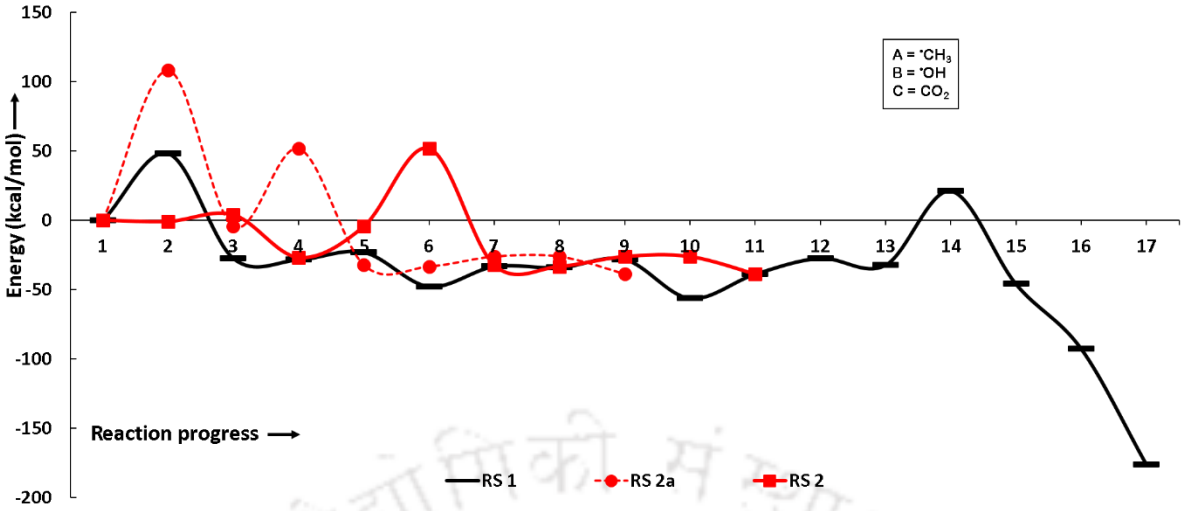

X-axis	1	2	3	4	5	6	7	8	9	10	11	12	13	14	15	16	17
RS 1	FA+5 H•	1_a+5 H•+A	1_b+4 H•+A	1_b*+ 3H•+A	TS1_1 +3H•+ A	1_c+3 H•+A	1_d+3 H•+A+ B	1_d*+ 2H•+A +B	TS1_2 +2H•+ A+B	1_e+2 H•+A+ B	1_f+2 H•+A+ 2B	TS1_3 +2H•+ A+2B	1_g+2 H•+A+ 2B	TS1_4 +2H•+ A+2B	1_h+2 H•+A+ 2B	1_i+H• +A+2 B+C	1_j+A +2B+ C
RS 2	FA+3 H•	FA2*+ 2H•	TS2_1 +2H•	2_a+2 H•	2_b+2 H•+B	2_c+2 H•+B+ A	2_d+H •+B+A	2_d*+ B+A	TS2_2 +B+A	2_e+B +A	2_f+2 B+A	--	--	--	--	--	--
RS 2a	FA+3 H•	2_a1+ 3H•+B	2_b+2 H•+B	2_c+2 H•+B+ A	2_d+H •+B+A	2_d*+ B+A	TS2_2 +B+A	2_e+B +A	2_f+2 B+A	--	--	--	--	--	--	--	--

Figure 5.18: Potential energy surfaces of reaction schemes 1, 2 and 2a.

The activation barrier for this reaction step is very low, i.e., 5.44 kcal/mol, compared to previous reaction steps. Further, the OH group removal from structure **1_c** to produce *p*-coumaric acid requires activation barrier of 15.47 kcal/mol. Similar reaction steps as of **1_b** → **1_c** → **1_d** is carried out for other hydroxyl group removal from *p*-coumaric acid to produce cinnamic acid in the form of **1_d** → **1_e** → **1_f**. The activation barriers for both reaction steps, i.e., **1_d** → **1_e** and **1_e** → **1_f** require activation barriers of 5.93 kcal/mol and 18.35 kcal/mol, respectively. The imaginary frequency values corresponding to **TS1_1** and **TS1_2** are calculated as 786.12*i* cm^{-1} and 932.79*i* cm^{-1}, respectively.

The rate controlling reaction step in the formation of cinnamic acid using reaction scheme 1 is reported as the atomic hydrogen addition reaction to structure **1_a** which requires activation barrier of 76.63 kcal/mol. This is undoubtedly a very high activation energy requirement and can only occur at very high temperature. Therefore, other reaction possibilities need to be searched.

Table 5.11: Activation barriers of each reaction step of all reaction schemes.

Schemes	Bond Dissociation Energies/Barrier Heights									
	Step 1	**Step 2**	**Step 3**	**Step 4**	**Step 5**	**Step 6**	**Step 7**	**Step 8**	**Step 9**	**Step 10**
1	49.56	76.63	5.44	15.47	5.93	18.35	11.55	53.48	48.23	85.02
2	4.82	23.44	57.66	85.33	7.13	11.73	---	---	---	---
2a	109.49	114.11	57.66	85.33	7.13	11.73	---	---	---	---
3	4.99	9.31	5.93	18.35	37.36	90.96	11.51	63.37	---	---
3a	93.09	112.46	same as above						---	---
4	11.41	52.53	30.02	44.26	37.71	---	---	---	---	---
FA - EthGua	same as above		48.51	83.20	---	---	---	---	---	---
FA-IsoEug	same as above		30.02	47.72	---	---	---	---	---	---
FA-Van	same as above		22.23	0.22	1.45	---	---	---	---	---
FA-AceVan	same as above				11.76	---	---	---	---	---
5	6.43	24.69	---	---	---	---	---	---	---	---

The formation of cinnamic acid is also discussed in reaction scheme 2 which progresses through the atomic hydrogenation at carbon atom of $C_{aromatic}$-OH bond followed by elimination of OH functional group. However, the direct elimination of OH group from FA followed by atomic hydrogenation is also carried out (see secondary reaction scheme 2 in RS 2) to analyse the activation barrier differences. The direct elimination of OH group from FA is reported to require the activation barrier of 109.49 kcal/mol and, atomic hydrogenation to structure **2a_1** requires 114.11 kcal/mol of activation barrier. Therefore, this reaction approach is clearly not the favourable approach. However, the atomic hydrogenation at the aromatic carbon of $C_{aromatic}$-OH bond followed by OH group removal requires activation barriers of 4.82 kcal/mol and 23.44 kcal/mol, respectively. This reaction approach require considerably less activation barrier compared to direct elimination of OH group from FA. However, further elimination of methyl group from structure **2_b** is again not a favourable reaction step because of high activation barrier demanding elementary reaction step, 57.66 kcal/mol. Further, the saturation of oxygen atom of structure **2_c** requires even higher energy which is calculated as 85.33 kcal/mol. Therefore, this reaction approach cannot be the favourable pathway as well because of very high energy demanding elementary reaction steps. However, the OH group elimination from structure **2_d** (**2_d** → **2_e** and **2_e** → **2_f**) follows the reaction approach similar to the first two reaction steps of reaction scheme 2; and presents barrier heights as 7.13 kcal/mol and 11.73 kcal/mol, respectively. Nevertheless, the rate controlling reaction step of reaction scheme 2 for the formation of cinnamic acid from FA, i.e., **2_c** → **2_d** which is the hydrogenation reaction step to the radical present at oxygen of **2_c**, requires activation energy of 85.33 kcal/mol. This reaction approach is even unfavourable compared to the reaction scheme 1 which required activation energy of 76.63 kcal/mol for the formation of cinnamic acid from FA. Two transition state structures are found in reaction scheme 2 for which the imaginary frequencies are reported as 846.08*i* cm^{-1} (**TS2_1**) and 973.25*i* cm^{-1} (**TS2_2**).

Another reaction possibility for the formation of cinnamic acid from FA is considered in reaction scheme 3. Similar to the reaction scheme 2, reaction scheme 3 also comprises of a secondary pathway which directly cleaves the methoxy functional group from FA with activation barrier of 93.09 kcal/mol. Though, the direct cleavage of methoxy from FA is less energy demanding than direct cleavage of hydroxyl group FA but still direct cleavage of methoxy is not encouraging reaction step to pursue because of high activation barrier. Further, the atomic hydrogen addition to structure **3_a1** is also required to have high barrier height, i.e., 112.46 kcal/mol. However, following the primary reaction scheme 3, ferulic acid structure is first hydrogenated at the aromatic carbon of $C_{aromatic}$-OCH_3 bond with calculated barrier height of 4.99 kcal/mol. Further, the cleavage of methoxy functional group from structure **3_a** requires barrier height of only 9.31 kcal/mol. Both of these two reaction steps involved transition state structures as **TS3_1** (802.28*i* cm^{-1}) and **TS3_2** (436.07*i* cm^{-1}) in their minimum energy path (see Figure 5.20). Further, elimination of hydroxyl group from caffeic acid to produce cinnamic acid proceeds through the reaction steps **3_b** → **3_c** → **3_d** which are same as the reaction steps **1_d** → **1_e** → **1_f**, therefore, both reaction steps require similar energetics and due to this, it is not explained further to avoid the repetitions.

It can be seen that the secondary reaction scheme 3 is obviously not favourable reaction approach for the formation of cinnamic acid; however, the reaction approach utilised in reaction scheme 3 appears advantageous. The cleavage of OH group from structure **3_c**, i.e., the reaction step **3_c** → **3_d** controls the overall reaction rate for the formation of cinnamic acid from ferulic acid which requires the activation energy of only 18.35 kcal/mol only. On the other hand, reaction schemes 1 and 2 require activation energies of 76.63 kcal/mol and 85.33 kcal/mol, respectively for the formation of cinnamic acid from FA, therefore, the conversion of ferulic acid to cinnamic acid favours the reaction route defined under primary reaction scheme 3.

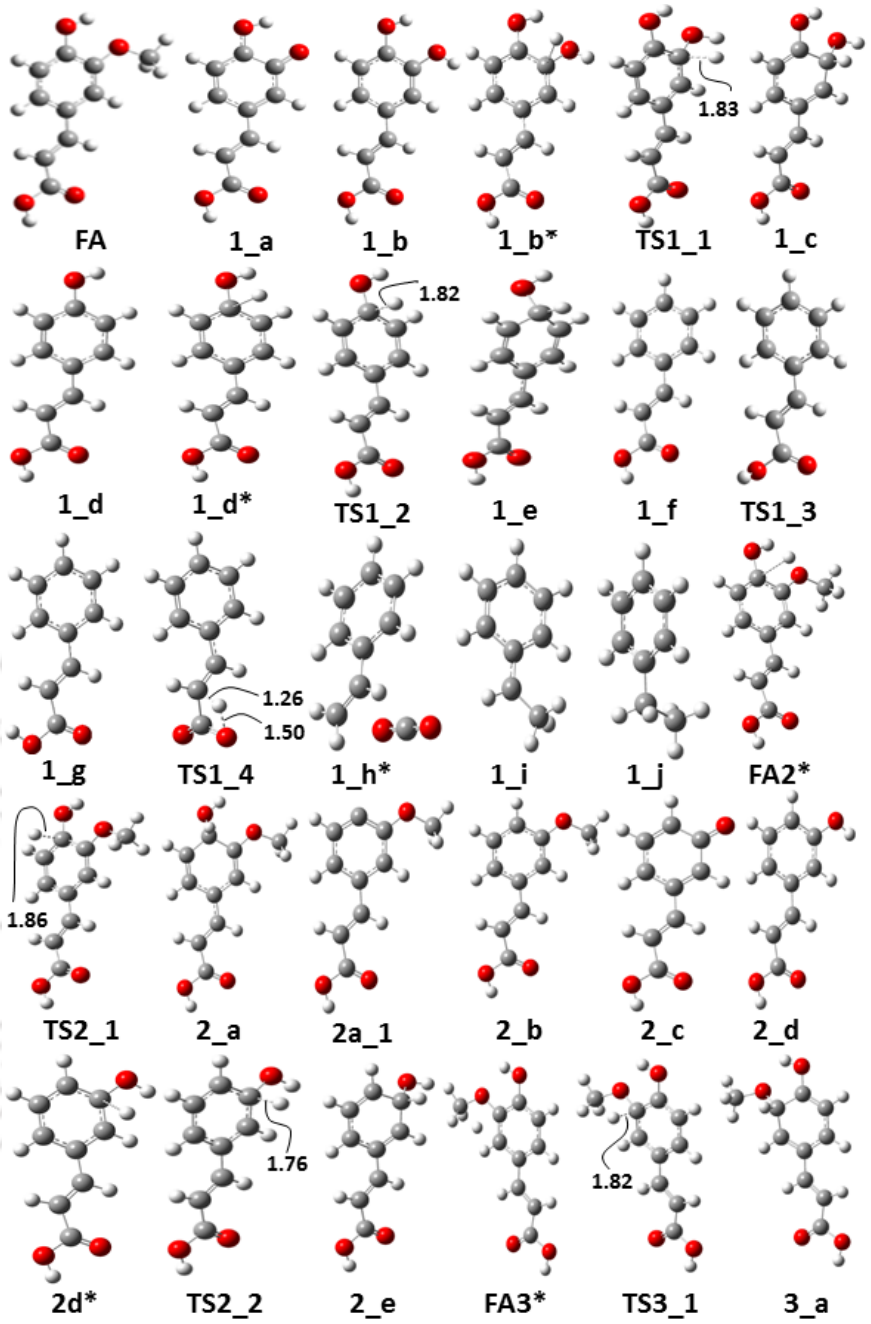

Figure 5.19: Optimized molecular structures involved in reaction schemes 1-3.

5.3.4. Conversion of Cinnamic Acid

Further conversion of cinnamic acid into ethylbenzene is discussed in reaction schemes 1 and 3. The potential energy surfaces of both reaction schemes 1 and 3 are shown in Figures 5.18 and 5.20, respectively; and optimized molecular structures corresponding to these reaction schemes are depicted in Figures 5.19 and 5.21.

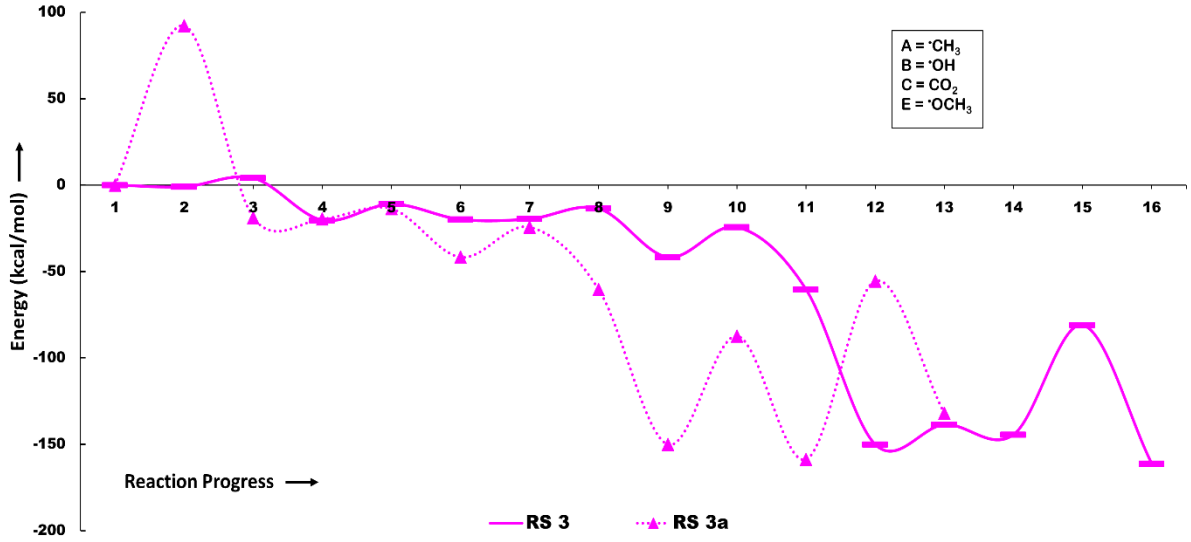

X-axis	1	2	3	4	5	6	7	8	9	10	11	12	13	14	15	16
RS 3	FA+4H·	FA3*+3 H·	TS3_1 +3H·	3_a+3 H·	TS3_2 +3H·	3_b+3 H·	3_b*+2 H·+E	TS3_3 +2H·+ E	3_c+2H ·+E	3_d+2 H·+E+ B	3_e+H· +E+B	3_f+E +B	TS3_4+ E+B	3_g+E +B	TS3_5 +E+B	3_h+E +B+C
RS 3a	FA+4H·	3_a1+4 H·+E	3_b+3 H·+E	3_b*+2 H·+E	TS3_3 +2H·+E	3_c+2 H·+E	3_d+2 H·+E+ B	3_e+H ·+E+B	3_f+E+ B	TS3_4 +E+B	3_g+E +B	TS3_5 +E+B	3_h+E+ B+C	--	--	--

Figure 5.20: Potential energy surfaces of reaction schemes 3 and 3a.

Under reaction scheme 1, cinnamic acid is first converted into ethylbenzene using decarboxylation of cinnamic acid followed by hydrogenation reactions; however, prior to the decarboxylation reaction of cinnamic acid, the hydrogen atom of OH undergoes a dihedral change using **TS1_3** (572.98*i* cm^{-1}) which requires a barrier height of 11.55 kcal/mol. From Figure 5.18, it is clearly visible that the structure **1_g** is unstable (see structures **1_f** and **1_g** in Figure 5.19) compared to the **1_f** conformer of cinnamic acid but this intermediate **1_g** is a mandatory structure to perform further decarboxylation reaction. During the decarboxylation reaction of **1_g** conformer of cinnamic acid, the hydrogen of COOH functional migrates to the carbon atom (α-carbon atom to COOH functional) with which COOH is attached. This process can be seen in the transition state structure **TS1_4** (1358.77*i* cm^{-1}) in Figure 5.19 which leads to the production of vinylbenzene and CO_2 molecules. Compared to the dihedral change process, i.e., **1_f** → [**TS1_3**]‡ → **1_g**, the decarboxylation reaction occurs with a large barrier height of 53.48 kcal/mol. Then, the produced structure vinylbenzene further undergoes for saturation of vinyl group to ethyl group using two single step hydrogenation reactions which

require activation barriers of 48.23 kcal/mol and 85.02 kcal/mol, respectively. It is observed that the production of ethylbenzene from cinnamic acid under RS 1 requires 85.02 kcal/mol of activation energy for the rate determining step **1_i → 1_j** which is an atomic hydrogen addition reaction to structure **1_i**.

The production of ethylbenzene from cinnamic acid is also considered under RS 3 using different reaction approach compared to RS 1. Under RS 3, the cinnamic acid first undergoes hydrogenation of C=C chain double bond followed by decarboxylation reaction to produce ethylbenzene, whereas, RS 1 employed decarboxylation of cinnamic acid followed by C=C chain double bond hydrogenation to produce ethylbenzene. Nevertheless, the saturation of C=C chain double bond of cinnamic acid in RS 3 using two single step hydrogenation reactions required activation barriers of 37.36 kcal/mol and 90.96 kcal/mol, respectively. Further, to avail the perfect environment for decarboxylation reaction of structure **3_f**, hydrogen atom of COOH functional of **3_f** undergoes dihedral change to produce structure **3_g** similar to the process occurred in RS 1. The reaction step **3_f → 3_g** occurred with a transition state structure **TS3_4** (577.53*i* cm^{-1}) in between the minimum energy path for which the barrier height is calculated as 11.51 kcal/mol. The dihedral change in RS 3 is very similar energetically compared to the dihedral change process in RS 1 (see Table 5.11). Also, the structure **3_g** is found to be unstable compared to the structure **3_f** similar to RS 1 (see electronic energies of **3_f** and **3_g** in Figure 5.20). Nevertheless, the decarboxylation reaction of structure **3_g** to produce ethylbenzene and CO_2 molecules using **TS3_5** (1950.88*i* cm^{-1}) required barrier height of 63.37 kcal/mol which is higher than the barrier height of decarboxylation in RS 1. In the production of ethylbenzene from cinnamic acid using RS 3, the rate controlling reaction step is **3_e → 3_f** which is single step hydrogenation reaction to structure **3_e**. Therefore, the activation energy for the rate controlling reaction step in the production of ethylbenzene from cinnamic acid under RS 3 is 90.96 kcal/mol which is higher compared to RS 1 for same reactants and products.

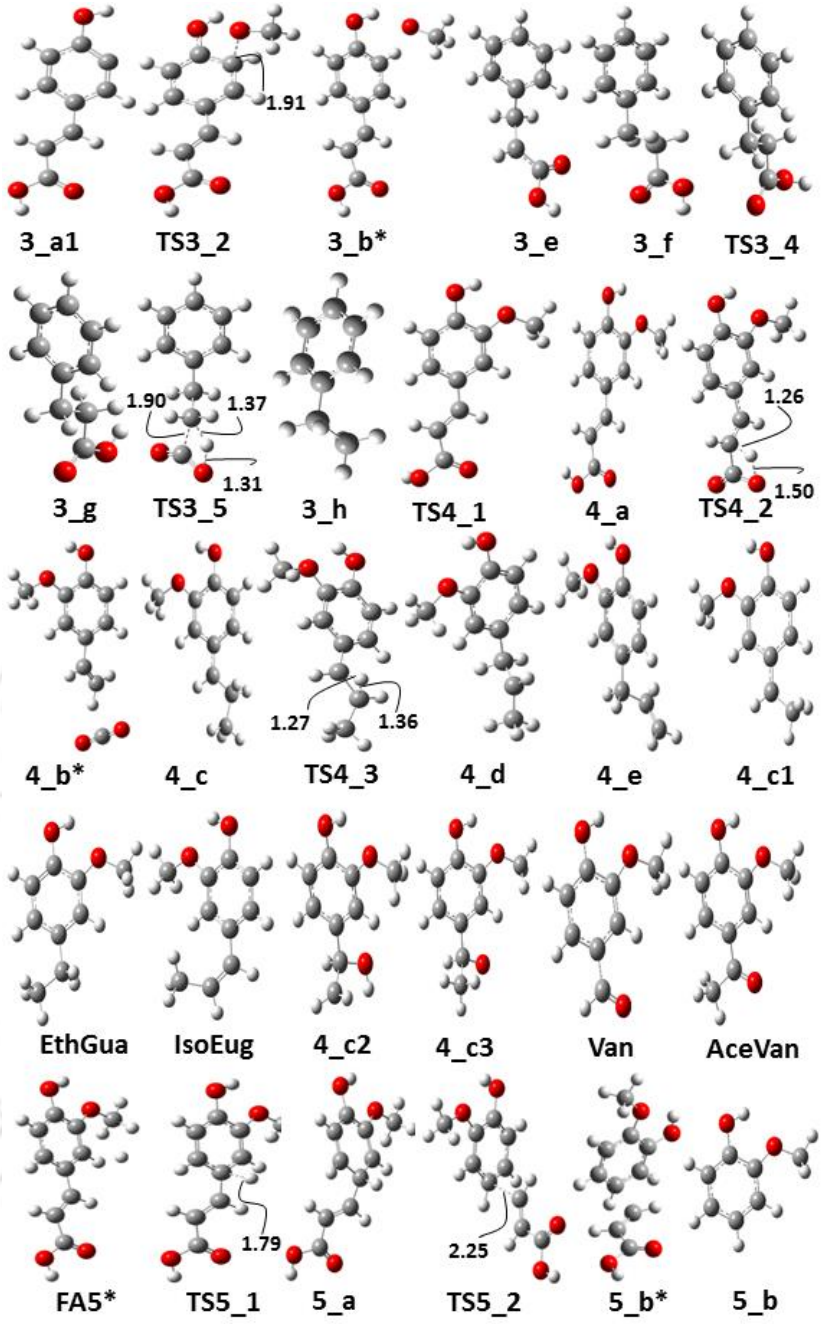

Figure 5.21: Optimized molecular structures of reaction schemes 3-5.

Finally, it can be concluded that the production of ethylbenzene from cinnamic acid using the reaction approach defined by RS 3 is not favourable from activation energy point of view. Therefore, cinnamic acid should first be undergone decarboxylation reaction as of RS 1 because the hydrogenation of C=C chain double bond prior to decarboxylation is not favourable as of RS 3. Although, the production of cinnamic acid from ferulic acid is observed favourable using reaction approach of RS 3, i.e., **FA → 3_a → 3_b → 3_c → 3_d**, compared to the

reaction approaches of RS 1 and RS 2 but further reduction of cinnamic acid into ethylbenzene is favourable using reaction approach of RS 1. Thus, the optimum reaction route for the production of ethylbenzene from ferulic acid should follow the reaction progress as **FA → 3_a → 3_b → 3_c → 3_d → 1_g → 1_h → 1_i → 1_j**.

5.3.5. Reaction Schemes 4 and 5

According to reaction scheme 4, ferulic acid is first subjected to direct decarboxylation reaction to produce *p*-vinylguaiacol as an intermediate product followed by the formation of several end products (see RS 4). The production of *p*-vinylguaiacol as an intermediate product is upvoted very often during various ferulic acid decomposition experiments carried out by researchers [82, 87, 88, 137–141]. Fiddler et al. [87] in their ferulic acid decomposition experiment have advocated the formations of various end products such as 4-methylguaiacol, 4-ethylguaiacol, 4-vinylguaiacol, guaiacol, vanillin, *cis*-isoeugenol, acetovanillone, and an unidentified component. Therefore, in this subsection, the formations of these products from ferulic acid along with their reaction mechanisms (see RS 4 and RS 5) and potential energy surfaces (Figure 5.22) are discussed. Optimized molecular structures involved in RS 4 and RS 5 are depicted in Figure 5.21 and potential energy surfaces are shown in Figure 5.22.

To initiate the decarboxylation reaction of ferulic acid, the ground state structure of ferulic acid first undergoes the formation of a relatively unstable structure (structure **4_a** in Figure 5.21). Instability of structure **4_a** is due to the spatial change of hydrogen atom of COOH functional which occurs *via* dihedral change process of ground state ferulic acid. It requires 11.41 kcal/mol of energy to surpass the barrier height for the formation of structure **4_a** which is 5.58 kcal/mol less stable compared to the ground state ferulic acid. Subsequently, the decarboxylation reaction of structure **4_a** occurs with an activation barrier of 52.53 kcal/mol and produces the product complex of *p*-vinylguaiacol and CO_2 molecules. The *p*-vinylguaiacol is very important intermediate product and, in addition, it channels to several

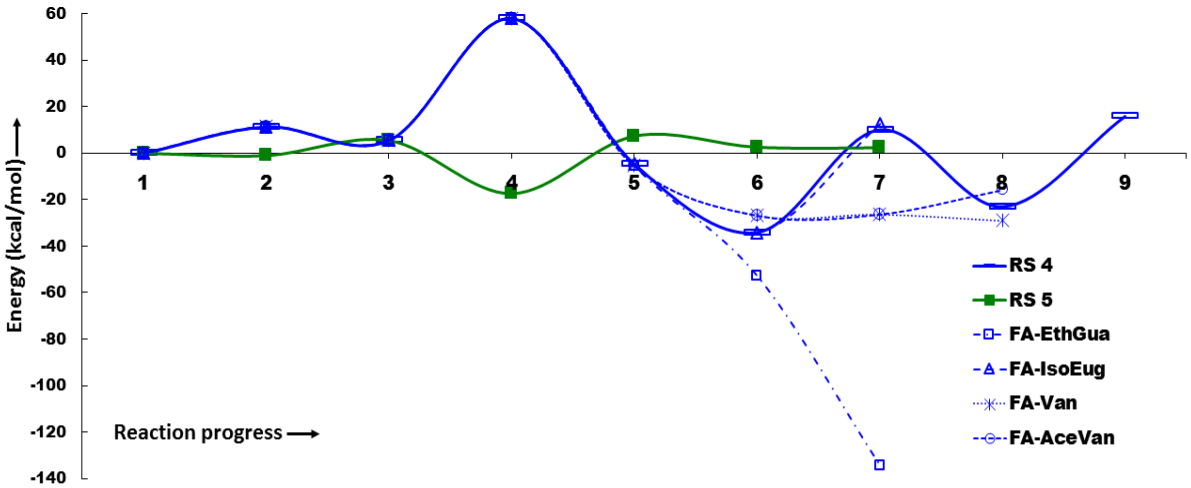

X-axis	1	2	3	4	5	6	7	8	9
RS 4	FA+A	TS4_1+A	4_a+A	TS4_2+A	4_b*+A	4_c+C	TS4_3+C	4_d+C	4_e+C+H·
FA-EthGua	FA+2H·	TS4_1+2H·	4_a+2H·	TS4_2+2H·	4_b+2H·+C	4_c1+H·+C	EthGua+C	--	--
FA-Van	FA+B	TS4_1+B	4_a+B	TS4_2+B	4_b+B+C	4_c2+C	4_c3+C	Van+A+B	--
FA-AveVan	FA+B	TS4_1+B	4_a+B	TS4_2+B	4_b+B+C	4_c2+C	4_c3+C	AceVan+C+H·	--
FA-IsoEug	FA+A	TS4_1+A	4_a+A	TS4_2+A	4_b*+A	4_c+C+H·	--	--	--
RS 5	FA+H·	FA5*	TS5_1	5_a	TS5_2	5_b*	5_b+I	--	--

Figure 5.22: Potential energy surfaces for reaction schemes 4 and 5 along with secondary reaction schemes of RS 4.

product possibilities (see RS 4). The saturation of C=C chain double bond may lead to the production of 4-ethylguaiacol which is an observed product in the study of Fiddler et al. [87]. The hydrogenation of C=C chain double bond occurs in two single step atomic hydrogen addition reactions with approximated activation barriers of 48.51 kcal/mol and 83.20 kcal/mol, respectively. On the other hand, in primary reaction scheme 4, *p*-vinylguaiacol leads to the production of eugenol component which is an important product in food industries and also, one of the important phenolic bio-oil model compound. For the production of eugenol, *p*-vinylguaiacol first associates a methyl group on the terminal carbon of C=C chain double bond with activation barrier of 30.02 kcal/mol. The association of methyl group develops a radical on α-carbon atom which is shifted to the β-carbon atom *via* transition state **TS4_3** on accounts of the barrier height of 44.26 kcal/mol. Further, a dehydrogenation reaction from terminal carbon of structure **4_d** is carried out which vanishes the radical on β-carbon and presents the carbon chain as an allyl group. The barrier height of reaction step **4_d** → **4_e** is 37.71 kcal/mol.

The produced structure is recognized as eugenol; however, the production of eugenol is not advocated by Fiddler et al. [87] in their experiment but they do show the formation of *cis*-isoeugenol from ferulic acid decomposition. The production of *cis*-isoeugenol can be achieved from the structure **4_c** using the dehydrogenation from β-carbon atom which occurs with a calculated activation barrier of 47.72 kcal/mol. In addition, the component *p*-vinylguaiacol, an intermediate from decomposition of ferulic acid, is often utilised in the production of vanillin in food industries [64, 81, 82, 138–143]. The production of vanillin occurs from the addition of OH functional group to the benzylic carbon atom followed by hydrogen migration from newly added OH to the nearest methylene group. The hydroxyl group addition to *p*-vinylguaiacol component is required to have an activation barrier of 30.02 kcal/mol in gas phase; however, this particular reaction step may be very favourable in aqueous phase. Nevertheless, the migration of hydrogen to methylene group is a very low barrier height (0.22 kcal/mol) reaction step and it can be achieved very easily. It produces the structure **4_c3** (see Figure 5.21 and RS 4) which is a common intermediate for the productions of vanillin and acetovanillone components. The production of vanillin from structure **4_c3** occurs *via* elimination of methyl group with a very low barrier height of 1.45 kcal/mol but the removal of hydrogen atom from structure **4_c3** (see RS 4 and Figure 5.22) requires comparatively higher energy (11.76 kcal/mol). Therefore, the production of vanillin may be dominating over the production of acetovanillone from *p*-vinylguaiacol component because of very low activation barriers. Since, vanillin component is very useful in food industries, therefore, its further breakdown is not necessary but, in the context of biomass and bio-oil, its further degradation becomes very necessary. The gas phase decomposition of vanillin is carried out in Chapter 5.1.

In the production of 4-ethylguaiacol from ferulic acid using *p*-vinylguaiacol as an intermediate product, the reaction step **4_c1** → **4_c1a** determines the overall reaction rate which requires activation energy of 83.20 kcal/mol. Clearly, this requires very high activation

energy and, therefore, its abundance in product mixture should be lower. However, in the case of eugenol production from FA, the activation energy of rate determining reaction step (**4_a** → **4_b**) is relatively lower 52.53 kcal/mol. In addition, the reaction step **4_a** → **4_b** also determines the reaction rate in the formation of *cis*-isoeugenol from FA, therefore, it requires the same activation energy as of in the formation of eugenol from FA. Similar phenomena are observed in the production of vanillin and acetovanillone from ferulic acid also because here too the decarboxylation reaction of structure **4_a** determines the overall rate. In summary, the productions of eugenol, *cis*-isoeugenol, vanillin, *p*-vinylguaiacol, vanillin, and acetovanillone require activation energy of 52.53 kcal/mol which is easily achievable at pyrolysis temperature conditions. Therefore, it validates the observations of Fiddler et al. [87] who observed all of these components in their product mixture obtained from decomposition of ferulic acid. However, the thermodynamic favourability of a particular product from ferulic acid under RS 4 can be explained using thermochemistry which is discussed later in this study. The formation of guaiacol, also observed as one of the product by Fiddler et al. [87], from ferulic acid is discussed in reaction scheme 5.

The production of guaiacol from ferulic acid is depicted in reaction scheme 5 which initiates from the insertion of hydrogen atom to the aromatic ring followed by the elimination of •CHCHCOOH group. However, direct cleavage of •CHCHCOOH group from ferulic acid followed by atomic hydrogen addition can be another option to accommodate the possibility of formation of guaiacol but earlier, in this study, direct cleavage of •CHCHCOOH from ferulic acid is found to have huge barrier height (see BDE of D5 in Table 5.10), therefore, this approach is not encouraged. The insertion of hydrogen atom to the $C_{aromatic}$-CHCHCOOH group is very low activation barrier demanding (6.43 kcal/mol) reaction step; however, the elimination of •CHCHCOOH functional group requires considerably large barrier height (24.69 kcal/mol) but this activation energy is still considerably very less than the direct cleavage of

•CHCHCOOH from ferulic acid (see BDE of D5 in Table 5.10). Therefore, the production of guaiacol from ferulic acid is calculated to have the activation energy of 24.69 kcal/mol for the rate controlling reaction step of **5_a** → **5_b**. Further, decomposition of guaiacol is discussed by various researchers either catalytically [44, 47, 76, 45, 102] or non-catalytically [50, 51] in gas phase. The gas phase decomposition of guaiacol is performed in next chapter.

5.3.6. Thermochemistry

The thermochemistry of each reaction scheme using reaction enthalpies and reaction free energies is reported at atmospheric pressure and at a wide temperature range of 598-898 K. The reaction schemes involving same reactant and end product but different side products hold different thermodynamic parameters, e.g., reaction schemes 1 and 3 produce ethylbenzene from ferulic acid but side products in both reaction schemes are different, therefore, both reaction schemes represent different reaction enthalpies and reaction free energies. On the other hand, the reaction schemes which report same reactants, end products, and side products, present same thermodynamic parameters such as reaction schemes 2, 2a, 3, and 3a. Both thermodynamic parameters, i.e., reaction enthalpy (ΔH) and reaction free energy (ΔG) of all reaction schemes at aforementioned temperature are shown in Table 5.12.

The reaction scheme 1 which produces ethylbenzene from ferulic acid (see RS 1) is reported to be extremely favourable reaction at each temperature because both thermodynamic parameters show huge negative ΔH and ΔG values (see Table 5.12) which report RS 1 as very spontaneous and exothermic reaction. The increment in temperature does not substantially increase its spontaneity; however, it increases its exothermicity by 5 kcal/mol on accounts of temperature shift from 598 K to 898 K. This reaction scheme can be favourable even at lower temperature compared to high temperature pyrolysis because of no substantial change in thermochemical parameters. However, the reaction schemes 2 and 2a which produce cinnamic

Table 5.12: Thermochemical parameters of each reaction scheme at atmospheric pressure and at temperature range of 598-898 K.

Pathways	Thermodynamic Parameters	Temperature (K)			
		598	698	798	898
1	ΔG	-185.96	-186.36	-186.52	-186.47
	ΔH	-182.81	-184.46	-186.11	-187.72
2, 2a	ΔG	-80.93	-83.66	-86.25	-88.72
	ΔH	-147.19	-153.46	-160.21	-167.33
3, 3a	ΔG	-153.14	-143.44	-133.22	-122.54
	ΔH	-209.40	-213.02	-216.72	-220.46
4	ΔG	0.83	-1.77	-4.39	-7.01
	ΔH	16.40	16.45	16.52	16.59
FA - EthGua	ΔG	-125.97	-123.72	-121.37	-118.94
	ΔH	-139.06	-139.81	-140.49	-141.12
FA-Van	ΔG	-50.85	-54.49	-58.08	-61.62
	ΔH	-28.93	-29.27	-29.63	-29.99
FA-AceVan	ΔG	-30.60	-33.21	-35.82	-38.43
	ΔH	-14.99	-14.99	-14.99	-14.98
FA-IsoEug	ΔG	-0.58	-2.83	-5.09	-7.37
	ΔH	12.91	12.94	13.00	13.06
5	ΔG	-8.47	-9.87	-11.22	-12.51
	ΔH	0.15	-0.27	-0.70	-1.12

acid from ferulic acid does show the effect of increasing temperature on its spontaneity and exothermicity. The spontaneity and exothermicity of RS 2 increase by 8 kcal/mol and 20 kcal/mol upon temperature increment from 598 K to 898 K. On the other hand, the reaction scheme 3 which also produces ethylbenzene from ferulic acid, similar to RS 1, show increment and decrement in reaction free energy and reaction enthalpy, respectively, of reaction upon temperature increment. Though, the reaction scheme 1 is much more spontaneous reaction at 598 K compared to that of RS 3 but the exothermicity of RS 3 is dominating at each temperature condition. Therefore, the production of ethylbenzene can be favourable using the approach of reaction scheme 1. On the other hand, the reaction scheme 4 which produces various end products, thermochemical parameters are shown separately for each temperature condition in

Table 5.12. The primary reaction scheme 4 which reduces to eugenol from ferulic acid is not feasible at 598 K but the temperature increment reduces its reaction free energies; however, the reaction enthalpy of RS 4 becomes even endothermic at 898 K compared to 598 K temperature condition. Similar phenomena about exothermicity are observed in the formation of *cis*-isoeugenol from ferulic acid (FA-IsoEug) but it is less endothermic compared to RS 4 at each temperature. Unlike to RS 4, FA-IsoEug reaction is spontaneous at even 598 K and its spontaneity at 898 K is slightly higher than that of RS 4. This validates the experimental analyses due to Fiddler et al. [87] because they observe the formation of *cis*-isoeugenol in the product mixture instead of eugenol. The production of ethylguaiacol from ferulic acid (FA-EthGua) is reported to have very favourable thermochemical properties (see Table 5.12) but this reaction is observed as high activation energy demanding pathway according to its potential energy surface. On the other hand, the production of vanillin from ferulic acid (FA-Van) is a promising route and a probable candidate because it is favourable at each temperature condition and, in addition, the temperature increment advocates better reaction condition. Furthermore, the activation energy of this reaction (52.53 kcal/mol) is achievable at high temperature pyrolysis conditions. The same is true for the production of acetovanillone from ferulic acid (FA-AceVan) and temperature increment does increase its spontaneity but its exothermicity remains almost same at each temperature. The production of guaiacol from ferulic acid, shown as RS 5, is also observed as one of the product in the experiment of Fiddler et al. [87]. At 598 K, the reaction is slightly endothermic; however, as the temperature increases it becomes exothermic by 1 kcal/mol. In addition, the temperature increment gradually reduces its reaction free energy, therefore, the production of guaiacol from ferulic acid will occur at higher temperature condition. The formations of eugenol and *cis*-isoeugenol do not attain exothermic conditions even at higher temperature, though, both reactions are spontaneous at 898 K, therefore, these two products should be less selective. However, the production of

vanillin showed promising characteristics at each temperature compared to the formation of acetovanillone, guaiacol, eugenol, and *cis*-isoeugenol, therefore, the presence of vanillin should be in greater extent in product mixture of ferulic acid decomposition.

5.4. DFT Analyses of Reaction Pathways on various Guaiacol Conversion Reactions in Gas Phase Environment

5.4.1. Reaction Schemes

The notations in Figure 5.23 are shown as, in general, **X_Y**, where **X** and **Y** denote the reaction pathway number and structure number in that particular reaction pathway, respectively. For instance, in **5_f**, **f** is the structure of reaction pathway 5. Similarly, the transition state structures are designated as **TSX_Y**, where **X** is reaction pathway number and **Y** is the transition state number in a given reaction pathway, e.g., **TS1_1** is the first transition state structure in reaction pathway 1.

Briefly, the first pathway which produces phenol goes through keto-enol tautomerization as the first step followed by methoxy radical removal and single step hydrogenation reaction, whereas, in the second pathway, guaiacol drives through hydroxyl group removal followed by single step hydrogenation to produce anisole. The third pathway suggests the direct removal of methoxy functional followed by hydrogenation which also produces phenol. In the gas phase decomposition of guaiacol, the sauration of phenyl ring to produce cyclo-products such as cyclohexane, cyclopentanone, cyclohexanone, etc. is highly unlikey but to accommodate the energetic view, the fourth reaction pathway adapts the reaction scheme given by Gao et al. [103] and produces the cyclopentanone. Fifth and Sixth reaction pathways produce cyclohexanone using different approaches. In reaction pathway 4, guaiacol first undergoes partial saturation of ring followed by dihedral change of hydrogen atom of hydroxyl functional. The formed intermediate undergoes through keto-enol tautomerization reaction followed by demethylation reaction and single step hydrogenation to the oxygen radical to produce 2-hydroxy-cyclohexen-1-one. This again drives through the keto-enol tautomerization followed by decarbonylation reaction to produce cyclopenatnone and CO

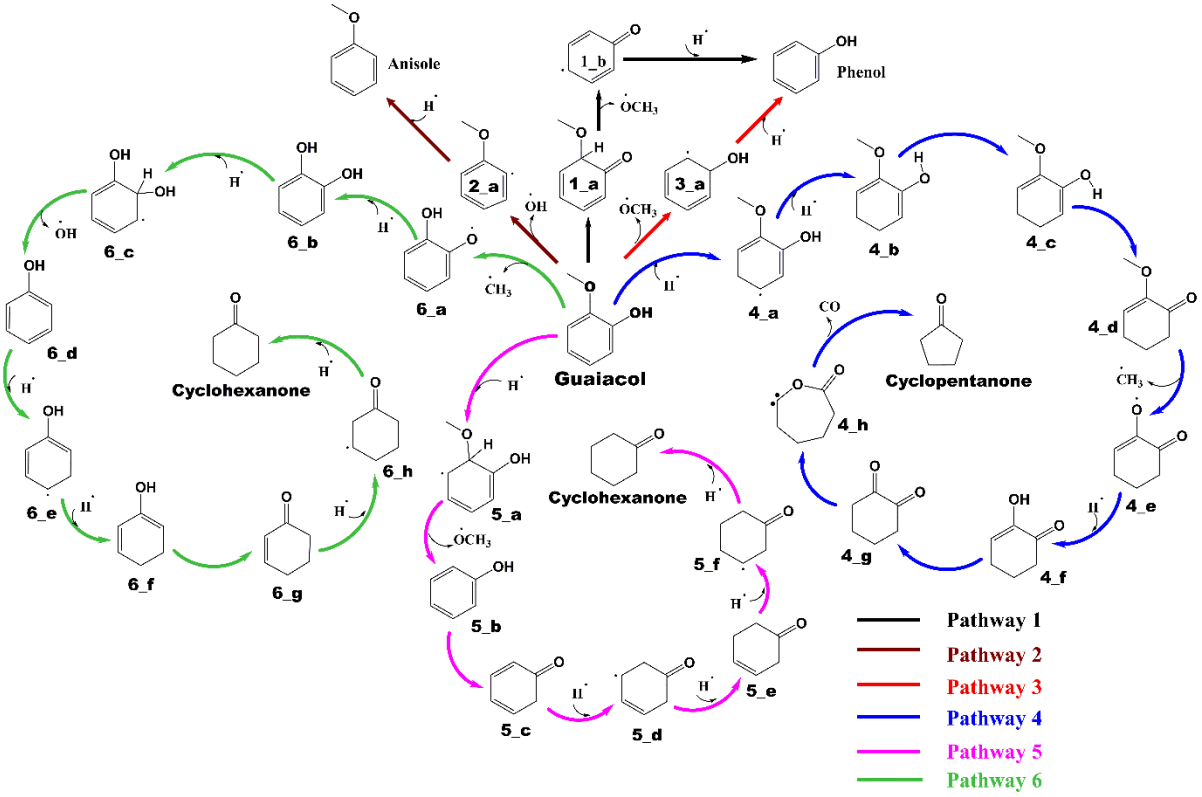

Figure 5.23: The reaction schemes of the conversion of guaiacol into various products.

molecules. The production of cyclohexanone from guaiacol has been considered using two competitive pathways 5 and 6. The main difference between pathways 5 and 6 is the type of oxy-functional removed. Pathway 5 undergoes demethoxylation followed by keto-enol tautomerization and four step hydrogenation reactions to saturate the ring, whereas, pathway 6 follows guaiacol demethylation reaction followed by dehydroxylation, keto-enol tautomerization and four step hydrogenation reactions to the ring saturation. Further, the production of cyclohexane is explained later in this study. Thes above discussed reaction pathways are performed computationally using Gaussian 09 software package under density functional theory perspective with employing B3LYP/6-311+g(d,p) theory in gas phase.

5.4.2. Bond Dissociation Energy (BDE)

The bond dissociation energies (BDEs) of guaiacol are shown in Table 5.13 which also contains the molecular structure of guaiacol with considered cleavages. The Dn (n=1,2,3,…,9) are the

sites of bond cleavages, e.g., D1 cleaves the methyl radical out of guaiacol and D2 cleaves the methoxy radical out of guaiacol and so on. Huang et al. [51] carried out the bond dissociation energy study for guaiacol component at B3LYP/6-31++g(d,p) level of theory using nine bond cleavages. Here we have reproduced BDEs due to Huang et al. [51] and calculated a new set at B3LYP/6-311+g(d,p) level of theory (see Table 5.13). It can be seen from this table that the present results show excellent agreement with those of Huang et al. [51] by using either theory. The most and least deviated BDEs from reproduced and literature are D6 and D2 respectively. The average deviation between the reproduced and literature value is calculated as 1.47 kcal/mol. Similarly, the average deviation from B3LYP/6-311+g(d,p)' BDE and literature values is 2.09 kcal/mol whereas the average deviation from BDE by B3LYP/6-311+g(d,p) and reproduced values is 0.62 kcal/mol. The least and highest BDEs are calculated as the O-CH_3 sigma bond and the hydrogen abstraction from D9 bond, respectively. The second least BDE is calculated as O-H sigma bond or D3. Therefore, it can be concluded that guaiacol would first undergo demethylation reaction and along with that dehydrogenation of hydroxyl functional could be the competitive pathway. This conclusion agrees with Huang et al. [51]. The BDEs in the ascending order of energies are given as D1 < D3 < D2 < D5 < D4 < D6 < D8 < D7 < D9.

Table 5.13: The bond dissociation energies (BDE) of various homolysis reactions of guaiacol.

Bond		**BDE (kcal/mol)**		
		Huang et al. [51]	**Present**	
		(6-31++g(d,p))	**6-31++g(d,p)**	**6-311+g(d,p)**
D1	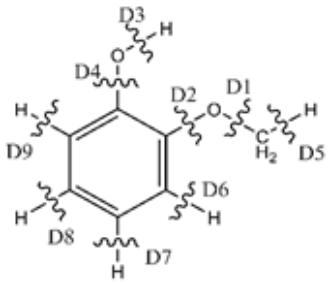	47.07	48.45	48.02
D2		92.09	93.10	92.46
D3		80.61	82.01	83.61
D4		107.09	108.56	107.99
D5		93.69	95.25	96.21
D6		108.6	110.27	111.41
D7		109.67	111.26	112.46
D8		109.67	111.24	112.43
D9		111.08	112.69	113.81

5.4.3. Reaction Pathways 1-3

It is shown in Figure 5.23 that the first three reaction pathways initiate from guaiacol and produce phenol, anisole, and phenol through keto-enol tautomerization, dehydroxylation, and demethoxylation as the first reaction steps, respectively. The potential energy surfaces of the first three pathways are shown in Figure 5.24 with involving molecular structures.

The first PES of guaiacol which produces phenol, shown as black coloured smooth line in Figure 5.24, first forms a higher energy state guaiacol (GUA^) to initiate the reaction which is calculated to be 8.57 kcal/mol less stable than the energy of ground state guaiacol. Further, the GUA^ goes through a keto-enol tauomerization reaction, i.e., the hydrogen migration from hydroxyl group to the aromatic carbon of $C_{aromatic}$-OCH_3 sigma bond. This step requires a barrier height of 75.04 kcal/mol and the imaginary frequency corresponding to **TS1_1** is calculated to be 2288.32*i* cm^{-1}. The '*i*' here demonstrates the imaginary frequency or negative frequency which affirms the transition state structure as the highest energy structure between a

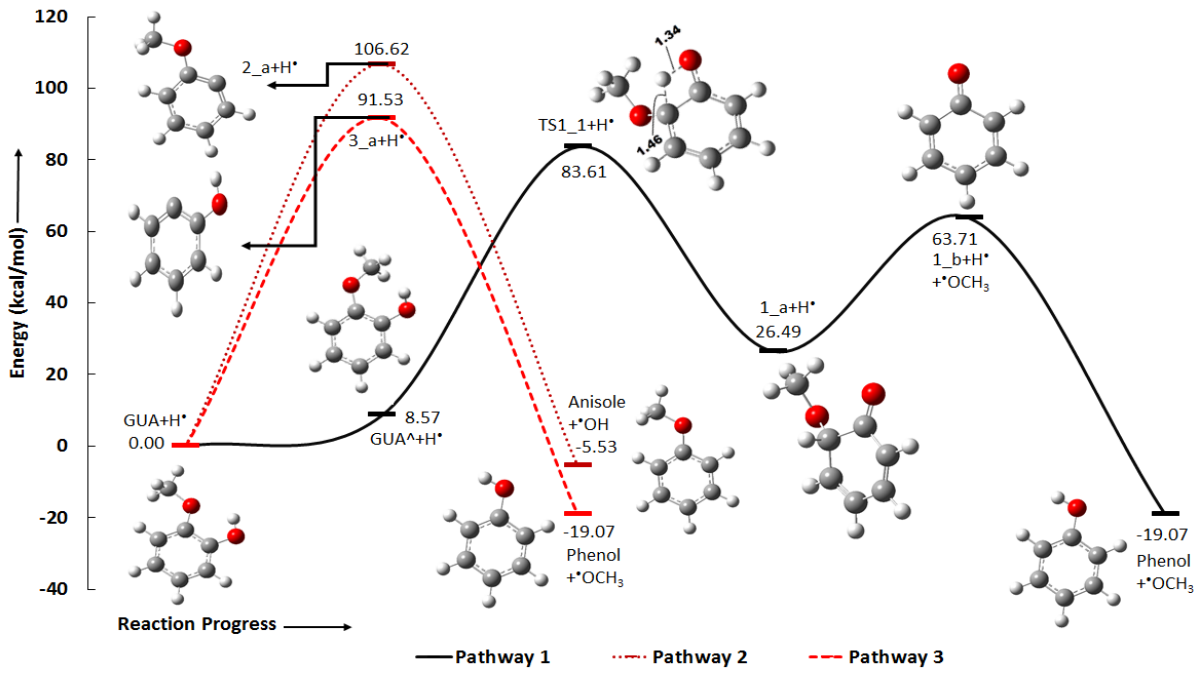

Figure 5.24: Potential energy surfaces of reaction schemes 1, 2, and 3 with corresponding optimized molecular structures at B3LYP/6-311+g(d,p) level of theory.

particular reactant and product. For instance, **TS1_1** is the highest energy state between the GUA^ and **1_a** structure which potentiates the spatial change of hydrogen atom. The inter-atomic distances of **TS1_1** are shown in angstroms unit (Å) and can be seen in Figure 5.24. Further, the second reaction step is the methoxy radical removal and as per BDE, this reaction requires 37.85 kcal/mol. The second reaction step is in excellent agreement with Liu et al. [50] who calculated this energy as 37.37 kcal/mol. The produced component (**1_b**) goes through a single step hydrogenation reaction to saturate the oxygen radical of **1_b** structure to produce phenol. This hydrogenation reaction requires an energy which is 84.08 kcal/mol from the BDE expression. Thus, it can be said that the rate determining step of reaction pathway 1 is the single step hydrogenation reaction and, therefore, an activation energy is 84.08 kcal/mol.

The second PES of the Figure 5.24 demonstrates the pathway 2 which converts guaiacol into anisole component. This figure also comprise the involving molecular structures. Boonyasuwat et al. [97] in their experiment stated the formation of anisole and catechol from guaiacol due to C-O hydrogenolysis over Ru catalysed surface, whereas, the transalkylation over support catalyzed Ru surfaces gave rise to catechol, methyl catechol, and dimethoxy benzene. Therefore, the second pathway is about the formation of anisole from guaiacol. The bond dissociation energies suggest very high energies as 107.99 kcal/mol and 113.64 kcal/mol for both elementary steps of pathway 2, respectively, therefore, this pathway cannot be favourable. Although, pathway 2 indicates a little exothermicity with 2-methoxy-phenyl intermediate. The hydroxyl functional abstraction from guaiacol has been carried out by Chiu et al. [47] over ruthenium catalyst and they have reported the barrier height as 27.47 kcal/mol. The approximated activation energies and true activation energies are given in Table 5.14 for all reaction steps of each reaction pathway.

The third reaction pathway which also produces phenol from guaiacol due to demethoxylation is depicted in Figure 5.24 with involving molecular structures. Third reaction

Table 5.14: The barrier heights in kcal/mol for each step of every reaction pathway.

RS	Bond Dissociation Energy (BDE)/Activation Energy (E_a)								
	Step 1	**Step 2**	**Step 3**	**Step 4**	**Step 5**	**Step 6**	**Step 7**	**Step 8**	**Step 9**
1	75.04	37.85	84.08	-	-	-	-	-	-
2	107.99	113.64	-	-	-	-	-	-	-
3	92.46	112.06	-	-	-	-	-	-	-
4	25.47	72.68	6.07	53.72	55.22	82.82	60.99	72.75	29.82
5	4.42	8.01	66.31	45.03	80.76	36.06	96.80	-	-
6	48.02	75.33	3.68	16.38	24.34	73.13	51.49	36.06	96.80

pathway carries out demethoxylation of guaiacol and produces 2-hydroxyphenyl as an intermediate and further, in order to produce phenol, a single atom hydrogenation is carried out over 2-hydroxyphenyl. The methoxy radical removal and a hydrogenation to 2hydroxy-phenyl cause BDEs of 92.46 kcal/mol and 112.06 kcal/mol, respectively. The first step's BDE is in good agreement with Liu et al. [50]'s value, 92.43 kcal/mol. Thus, the reaction pathway 3 can be compared with the reaction pathway 1 in the terms of activation energies. The reaction pathway 1 requires an activation energy of 84.08 kcal/mol, whereas, the reaction pathway 3 requires an activation energy of 112.06 kcal/mol. Both pathways report very high activation energies, nevertheless, two other approaches, i.e., reaction pathways 5 and 6 are also discussed to produce phenol from guaiacol.

5.4.4. Reaction Pathway 4

The reaction pathway 4 produces cyclopentanone from guaiacol with many important intermediates. Surprisingly, the cyclopentanone formation from guaiacol has been discussed by a very few authors experimentally and by only one computational work by Gao et al. [103]. Gao et al. [103] performed the guaiacol adsorption over platinum catalyst and reported that the partial hydrogenation of ring as the first step favours the reaction thermodynamically. Therefore, in this study, the partial hydrogenation of the phenyl ring is taken as the first step

for pathway 4. The produced intermediate after partial hydrogenation (structure **4_b** in Figure 5.23) is recognized as 6-methoxy-1,5-cyclohexa-dienol and this undergoes through keto-enol tautomerization (structure **4_d** in Figure 5.23) followed by demethylation reaction (structure **4_e** in Figure 5.23). The oxygen radical in structure **4_e** is hydrogenated (structure **4_f** in Figure 5.23) and again follows the keto-enol tautomerization to produce cyclohexane-1,2-dione component (structure **4_g** in Figure 5.23). Further, the structure **4_g** follows ring opening and decarbonylation reactions in order to produce the cyclopentanone. The PES of reaction scheme 4 is depicted in Figure 5.25 with involving molecular structures. The inter-atomic distances in the transition state structures are depicted in angstroms. As it is stated in the reaction scheme, the pathway 4 starts with partial hydrogenation of guaiacol by two step single atom hydrogenation reactions, the approximated barrier heights of both steps are 25.47 kcal/mol and 72.68 kcal/mol, respectively. The dihedral angle change of hydrogen atom of hydroxyl functional and keto-enol tautomerization reaction cause barrier heights of 6.07 kcal/mol and 53.72 kcal/mol, respectively. This follows up with demethylation of structure **4_d**, a single atom hydrogenation of **4_e** structure, and another keto-enol tautomerization of generated hydroxyl functional, causing barrier heights of 55.22 kcal/mol, 82.82 kcal/mol, and 60.99 kcal/mol, respectively. The produced molecular structure can be recognized as cyclohexane-1,2-dione (structure **4_g** in Figure 5.23). To produce the cyclopentanone molecule, structure **4_g** follows the ring opening and decarbonylation reaction with calculated barrier heights of 72.75 kcal/mol and 29.82 kcal/mol, respectively. It can be seen here that the ring opening reaction causes a huge amount of energy. The rate determining step can be recognized as **4_e** → **4_f** reaction step. Gao et al. [103] calculated the activation energy for guaiacol to cyclopenatnone as 35.59 kcal/mol over supported Pt catalyst surface, however, here the rate determining step for the reaction pathway 4 cause a barrier height of 82.82 kcal/mol. The imaginary frequencies corresponding to the transition state structures **TS4_1**, **TS4_2**, **TS4_3**,

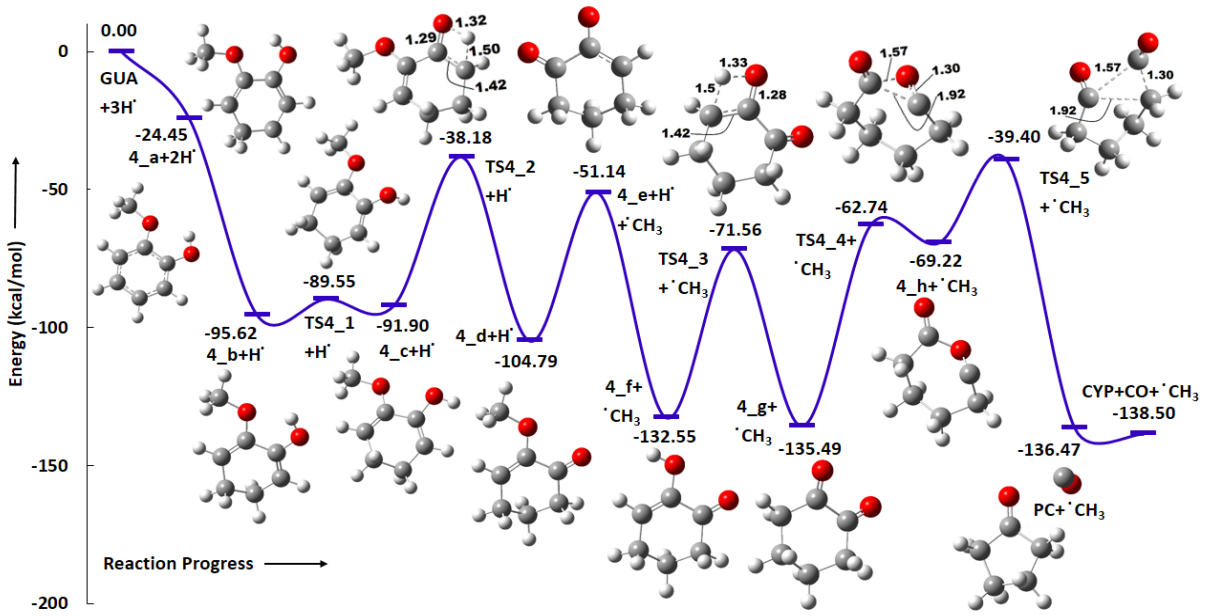

Figure 5.25: Potential energy surface of reaction scheme 4 with corresponding optimized molecular structures.

TS4_4, and **TS4_5** in Figure 5.25 are 417.6*i* cm^{-1}, 2195.5*i* cm^{-1}, 2257.3*i* cm^{-1}, 358.8*i* cm^{-1}, and 268.9*i* cm^{-1}, respectively.

5.4.5. Reaction Pathways 5 and 6

The reaction schemes 5 and 6 produce cyclohexanone from guaiacol using different pathways. It has been pointed out by many researchers that the formation of phenol can be directly achieved by guaiacol using demethoxylation and also with an intermediate as catechol using demethylation reaction followed by hydrodeoxygenation [76]. Bykova et al. [75, 144] in their experiment have indicated the formation of phenol using both ways over Ni-Cu and Ni-based sol-gel catalysts, however, the experiment of Moon et al. [145] over Ni_2P catalyst doesn't support the formation of catechol as an intermediate in the production of phenol. Therefore, to accommodate both possibilities, two pathways for the production of cyclohexanone have been discussed. Pathway 5 (Figure 5.26) first eliminates the methoxy functional to produce phenol as an intermediate, whereas, pathway 6 (Figure 5.27) undergoes demethylation reaction producing catechol which further converts into phenol component. Further, pathway 5

undergoes keto-enol tautomerization followed by a single atom hydrogenation while pathway 6 undergoes partial saturation of the ring.

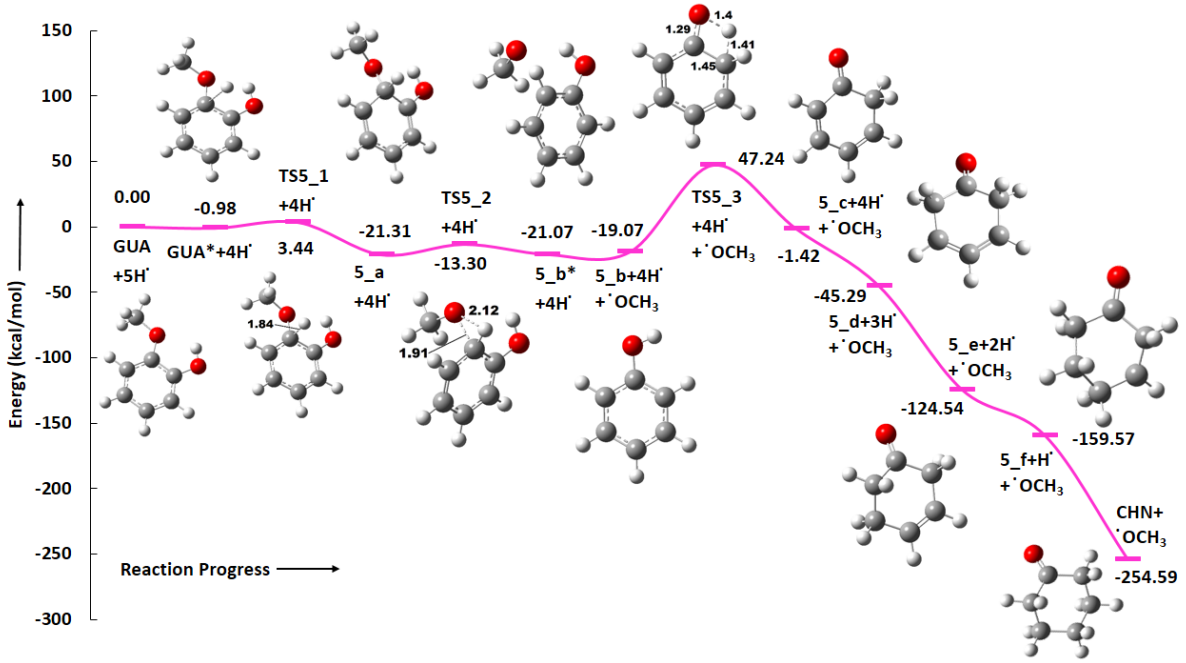

Figure 5.26: Potential energy surface of reaction scheme 5. The associated molecular structures are optimized at B3LYP/6-311+g(d,p) level of theory.

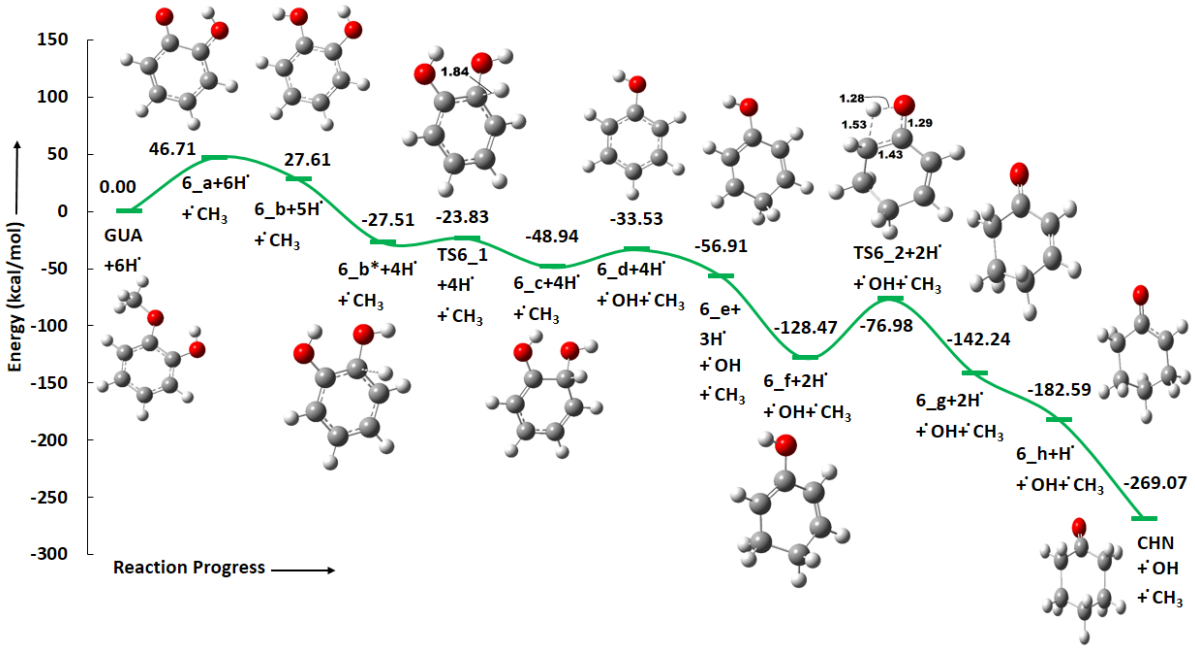

Figure 5.27: Potential energy surface of reaction scheme 6 associated with corresponding optimized molecular structures.

The five hydrogen atoms and guaiacol molecule make a minimum state structure (structure **GUA*** in Figure 5.26) in pathway 5 which undergoes to form the structure **5_a**. The transition state structure for this elementary step shows an energy of 3.44 kcal/mol relative to GUA+5H˙, however, the barrier height is calculated as 4.42 kcal/mol which is in the great accordance with the work of Huang et al. [51] and in the slight deviation with Liu et al. [50]. The second step where the methoxy functional is getting eliminated, produces phenol with a barrier height of 8.01 kcal/mol. On the other hand, the pathway 6 undergoes demethylation of guaiacol and forms hydrogen-catecholate as an intermediate. This is followed by a single atom hydrogenation to the oxygen radical of 'hydrogen-catecholate' which gives rise to the catechol component. The first and second elementary steps of guaiacol under pathway 6, require BDEs of 48.02 kcal/mol and 75.33 kcal/mol. The first step's BDE is in good agreement with the BDE given by Liu et al. [50], i.e., 47.78 kcal/mol at B3LYP/6-31++g(d,p) theory but they have not performed the second elementary step. It should again be noted that the BDEs are good approximations to the activation energies thus these two elementary steps would be requiring near about same activation energies as of BDEs [50, 51]. Further, pathway 6 adsorbs a hydrogen atom on aromatic carbon of $C_{aromatic}$-OH sigma bond to eliminate one hydroxyl functional (structure **6_b*** in the Figure 5.26) which occurs in two steps, first as to hydrogenate the $C_{aromatic}$-OH site and second as to remove hydroxyl functional, requiring barrier heights of 3.68 kcal/mol and 16.38 kcal/mol, respectively. The phenol structure appears in both pathways 5 and 6 as **5_b** and **6_d** structures (see Figure 5.23), respectively. This drives the pathway 5 to follow through the keto-enol tautomerization which requires a barrier height of 66.31 kcal/mol, whereas, phenol in pathway 6 goes through partial ring saturation using two single atom hydrogenation reactions requiring barrier heights of 24.34 kcal/mol and 73.13 kcal/mol, respectively. The structure **6_f** goes through keto-enol tautomerization with a barrier height of 51.49 kcal/mol. The produced structure **6_g** is similar to the structure **5_e** in pathway 5. Further,

these two structures are subsequently hydrogenated to produce the desired end product, cyclohexanone. The barrier heights are same for the last two single step hydrogenation reactions of both pathways; and are 36.06 kcal/mol and 96.8 kcal/mol, respectively.

There are three and two transition states in pathway 5 (Figure 5.26) and pathway 6 (Figure 5.27), respectively. The imaginary frequencies corresponding to **TS5_1**, **TS5_2**, and **TS5_3** of pathway 5 are 766.4*i* cm^{-1}, 424.6*i* cm^{-1}, and 2137.5*i* cm^{-1}, respectively while the imaginary frequencies corresponding to **TS6_1** and **TS6_2** of pathway 6 are calculated as 742.1*i* cm^{-1} and 2146.4*i* cm^{-1}, respectively.

5.4.6. Conversion of Phenol into Benzene

Non-catalytic decomposition of phenol into benzene occurs *via* cleavage of $C_{aromatic}$-OH bond with a hydrogen molecule. The interaction of phenol (**P**) and hydrogen ($\mathbf{H_2}$) at $C_{aromatic}$-OH bond site form an intermediate as **IM1**. The cleavage of C-O bond can be seen in the transition state structure, **TSP_B** (see Figure 5.28). Both hydrogen atoms cleave the $C_{aromatic}$-OH bond and associate with H-OH and phenyl-H producing water and benzene ring, respectively. The distance between 1C-15H is 1.48 Å but the equilibrium/optimized distance of C-H bond is about ~1.09 Å. This is because 1C and 15H atoms are in the process of bond formation. Similar case can be seen in the bond formation between 11O and 14H atoms. The imaginary frequency here for first order saddle point, **TSP_B**, has been reported as 2071.3*i* cm^{-1}. The vibrational analysis of imaginary frequency mode shows 14H-15H hydrogen atoms vibration to and from 11O-1C atoms. IRC analysis connects **IM1** and the products (benzene and water) through the minimum energy path with transition state structure as the highest energy state. However, from reaction progress point of view, **TSP_B** links benzene and water molecules as its two minima. The activation energy requirement for this reaction is 84.08 kcal/mol.

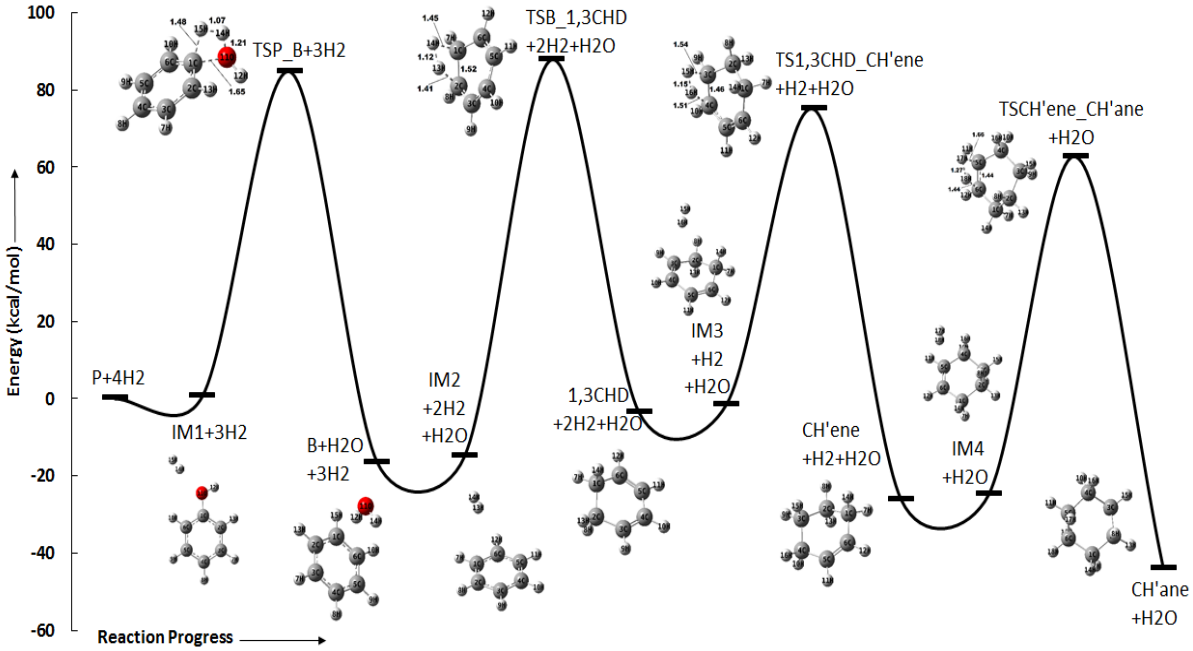

Figure 5.28: Potential energy surface for the conversion of phenol into benzene and hydrogenation of benzene into cyclohexane.

5.4.7. Hydrogenation of Benzene Ring

Saturation of benzene ring to cyclohexane requires three hydrogenation reactions subsequently: **a)** as the formation of 1, 3-cyclohexadiene from first benzene hydrogenation reaction, **b)** subsequent hydrogenation reaction of 1, 3-cyclohexadiene forms cyclohexene, and **c)** final hydrogenation reaction of cyclohexene forms cyclohexane molecule [44, 45]. Albeit, the hydrogenation to benzene ring consumes a considerable amount of hydrogen macroscopically that is why most researchers leave the reactions up to benzene or non oxy-functional aromatic rings [1]. Another reason is that for the gasoline blend, aromatic ring compounds enhance the octane number of gasoline fuel and so the performance of fuel and engine, therefore, it is not required to hydrogenate the benzene ring further into the cyclohexane [1]. However, for kinetics purpose and for the study of the cyclohexane formation from benzene molecule, we have carried out the benzene hydrogenation reaction to cyclohexane molecule. Here, the components 1, 3-cyclohexadiene, cyclohexene, and cyclohexane are represented as the

1,3CHD, **CH'ene**, and **CH'ane**, respectively. The notations to the transition states are also as the previous transition state notations, i.e., **TSB_1,3CHD** and so on.

5.4.7.1. Benzene to 1, 3-cyclohexadiene (B_1,3CHD)

As it is evident that benzene ring contains three double bonds and to convert all double bonds into single bonds, three subsequent hydrogenation reactions are required. The first hydrogenation reaction on the benzene structure yielding 1, 3-cyclohexadiene component has been reported in this section. As per Figure 5.28, benzene and hydrogen molecules (**B+H_2**) form an intermediate, **IM2**, which is a stationary state on the PES. However, **IM2** contains the benzene structure with two hydrogen atoms attacking to a saturation site of 1C=2C double bond. The main exposure of the hydrogen molecule as 13H and 14H is to saturate the double bonding. In order to do that, these two hydrogen atoms, as 14H and 13H, form sigma bonds with 1C and 2C atoms respectively and saturate the double bonding between 1C and 2C atoms. The **IM2** structure according to the reaction progress forms an activated complex as **TSB_1,3CHD** (2325.5*i* cm^{-1}). The product (see Figure 5.28), 1, 3CHD, contains only two double bondages and this structure is a local minimum and a stationary state on PES. The formation of 1, 3-cyclohexadiene has been studied by Saeys et al. [40, 41] in which they have carried out the reaction over catalyst, however, here, the non-catalytic behaviour is reported. From Figure 5.28, first hydrogenation reaction on benzene forms a barrierless intermediate as **IM2**; further, the activation energy requirement to surpass the barrier height for this reaction is 102.81 kcal/mol. The thermochemistry for this reaction indicates that this reaction is not exothermic. The endothermicity of this elementary reaction is verified with Saeys et al. [146, 147] as they performed two step H-atom reactions for the conversion of benzene into 1, 3-cyclohexadiene over Pt(111); both steps are reported endothermic by 11 kJ/mol and 38 kJ/mol respectively.

5.4.7.2. 1, 3-Cyclohexadiene to Cyclohexene (1,3CHD_CH'ene)

The hydrogenation reaction on the 1, 3-cyclohexadiene structure yielding cyclohexene component, has been reported in this section. 1, 3-Cyclohexadiene still contains two double bonds which are required to be saturated in order to get the cyclohexane structure but one double bond saturation of 1,3-cyclohexadiene first leads to cyclohexene. Further cyclohexene needs to be hydrogenated to form cyclohexane. As can be seen in Figure 5.28, hydrogen and 1, 3-cyclohexadiene first form a reactant complex as **IM3** in which 15H and 16H atoms are located to attack the pi bond site between 3C and 4C atom. The transition state structure, **TS1,3CHD_CH'ene** (1931.8*i* cm^{-1}), has been located on the PES possessing a relative energy of 74.98 kcal/mol to **P+4H2**. The second minimum other than **IM3**, is **CH'ene** or cyclohexene under this elementary step. The barrier height for this reaction is 76.42 kcal/mol and the thermochemistry predicts this reaction as spontaneous and exothermic.

5.4.7.3. Cyclohexene to Cyclohexane (CH'ene_CH'ane)

Hydrogenation reaction on cyclohexene yielding cyclohexane molecule has been reported in this section. This reaction is the last hydrogenation reaction to form the cyclohexane molecule from benzene. In order to do so, hydrogen molecule is placed at the double bond site between two carbon atoms which forms an intermediate as **IM4**. It can be seen in **TSCH'ene_CH'ane** structure (see Figure 5.28) that 5C=6C double bond is in ruptured condition due to the attack of 17H and 18H atoms. The single imaginary frequency associated to **TSCH'ene_CH'ane** has been reported as 2034.8*i* cm^{-1} and the vibrational mode in imaginary frequency result shows vibration of two hydrogen atoms to and from the 5C and 6C atoms. The barrier height for this reaction is calculated as 87.56 kcal/mol.

Among these three hydrogenation reactions, first benzene hydrogenation reaction is the only reaction which is not exothermic reaction otherwise remaining two hydrogenation

reactions are exothermic reaction. Kistiakowsky et al. [148] in their experiment of benzene hydrogenation concluded that benzene to 1, 3-cyclohexadiene reaction is an endothermic reaction at 355^{o}C by 5.57 kcal/mol. similarly, they reported 1, 3-cyclohexadiene to cyclohexene reaction as an exothermic reaction by 26.7 kcal/mol at the same temperature of 355^{o}C. The reaction of cyclohexene to cyclohexane is not reported by Kistiakowsky et al. [148] as a separate elementary reaction.

5.4.8. Thermochemistry

The thermochemical calculations of all six reaction schemes (Figure 5.23) are carried out at 1 atm pressure and 398-898 K at an interval of 100 K. The thermochemistry of all reactions are carried out in the form of reaction enthalpies (ΔH) and reaction free energies (ΔG) over the discussed temperatures and at constant 1 atm pressure (Table 5.15). The reaction pathways which are producing same products, the ΔG and ΔH for those reactions are same, for instance, pathways 1 and 3 are producing phenol, therefore, for pathways 1 and 3, ΔG and ΔH are same; but the same is not true for pathways 5 and 6 because pathway 5 requires only five hydrogen atoms, whereas, pathway 6 requires six hydrogen atoms to produce cyclohexanone. Also, the side products in both pathways are different.

The reaction free energies (ΔG) and reaction entahlpies (ΔH) of pathways 1 and 3 are same because of the same reactants and products. It can be seen that the reaction free energies and reaction enthalpies of reaction pathways 1 (and 3) and 2 are slightly decreasing with increasing temperature values, however, these reactions are already spontaneous and exothermic at 398 K but as the temperature is increasing, the reactions are becoming slightly more spontaneous and exothermic. However, the reaction pathway 4 differs with pathways 1 or 3 in the terms of spontaneity-temperature relationship but its exothermicity is in the accordance, i.e., it slightly increases with temperature increase. Therefore, it can be seen that the reaction pathway 4 is slightly loosing its spontaneity with increasing temperature but

Table 5.15: The thermochemistry parameters (ΔM) in kcal/mol for each reaction pathway.

Pathways	ΔM	Temperature (K)					
		398	**498**	**598**	**698**	**798**	**898**
1 & 3	**ΔG**	-26.14	-27.64	-29.05	-30.39	-31.68	-32.91
	ΔH	-20.00	-20.41	-20.82	-21.23	-21.63	-22.04
2	**ΔG**	-9.46	-10.32	-11.11	-11.85	-12.54	-13.19
	ΔH	-5.92	-6.22	-6.53	-6.86	-7.18	-7.51
4	**ΔG**	-139.28	-138.76	-138.04	-137.14	-136.10	-134.95
	ΔH	-140.88	-141.88	-142.90	-143.91	-144.90	-145.85
5	**ΔG**	-225.07	-215.46	-205.49	-195.26	-184.83	-174.26
	ΔH	-262.48	-264.32	-265.97	-267.42	-268.70	-269.82
6	**ΔG**	-241.49	-232.54	-223.23	-213.65	-203.84	-193.85
	ΔH	-276.24	-278.08	-279.81	-281.41	-282.89	-284.25

increasing its exothermicity with increasing temperature. However, the reaction free energy values at each temperature are already negative thus making it spontaneous reaction at each temperature. Similar trends can be seen for reaction pathways 5 and 6 as both pathways show increase in exothermicity with increasing temperature but both reactions become less spontaneous as temperature increases. The differences between ΔG values and ΔH values with rise in temperature from 398 K to 898 K for pathway 5 are 50.81 kcal/mol and -7.34 kcal/mol, respectively. Similarly, for pathway 6, these differences are 47.64 kcal/mol and -8.01 kcal/mol, respectively. Though, both reactions are spontaneous at each temperature values but loose their spontaneity with temperature increment. However, it can be safely said that pathway 6 is slightly favourable over pathway 5 from thermodynamic point of view.

5.5. Production of Benzene from 2-Hydroxybenzaldehyde by Various Reaction Paths using IRC Calculations within DFT framework

5.5.1. Reaction Schemes

All reactions schemes discussed in this work are shown in Figure 5.29. The reactions considered here are modelled based on the bond dissociation energies (BDEs); and each reaction is briefly described here. The notations in Figure 5.29 are shown as, in general, **X_Y**, where **X** and **Y** denote the reaction pathway number and structure number in that particular reaction pathway, respectively. For instance, in **5_b**, **b** is the structure of reaction pathway 5. Similarly, the transition state structures have been designated as **TSX_Y**, where **X** is reaction pathway number and **Y** is the transition state number in a given reaction pathway, e.g., **TS1_1** is the first transition state structure in reaction pathway 1.

The reaction scheme 1 is about the cleavage of formyl group followed by single step hydrogenation reaction to produce phenol. The phenol component further undergoes a single atom hydrogenation followed by hydroxyl removal to produce benzene. The reaction scheme 2 is about hydrogen migration reaction followed by cleavage of formyl group and an atomic hydrogen addition to produce phenol. The reaction scheme 3 is decarbonylation reaction of 2-hydroxybenzaldehyde to produce phenol component. The reaction scheme 4 describes a single atom hydrogenation at the aromatic carbon of $C_{aromatic}$-CHO sigma bond followed by the removal of formyl group to produce phenol. Similarly, the reaction scheme 5 describes a single atom hydrogenation at the aromatic carbon of $C_{aromatic}$-OH sigma bond followed by hydroxyl group removal (rather than formyl group removal of pathway 5) to produce benzaldehyde component. The reaction scheme 6 is the dehydrogenation reaction of formyl group followed by CO removal and a single step hydrogenation to produce phenol. The reaction scheme 7

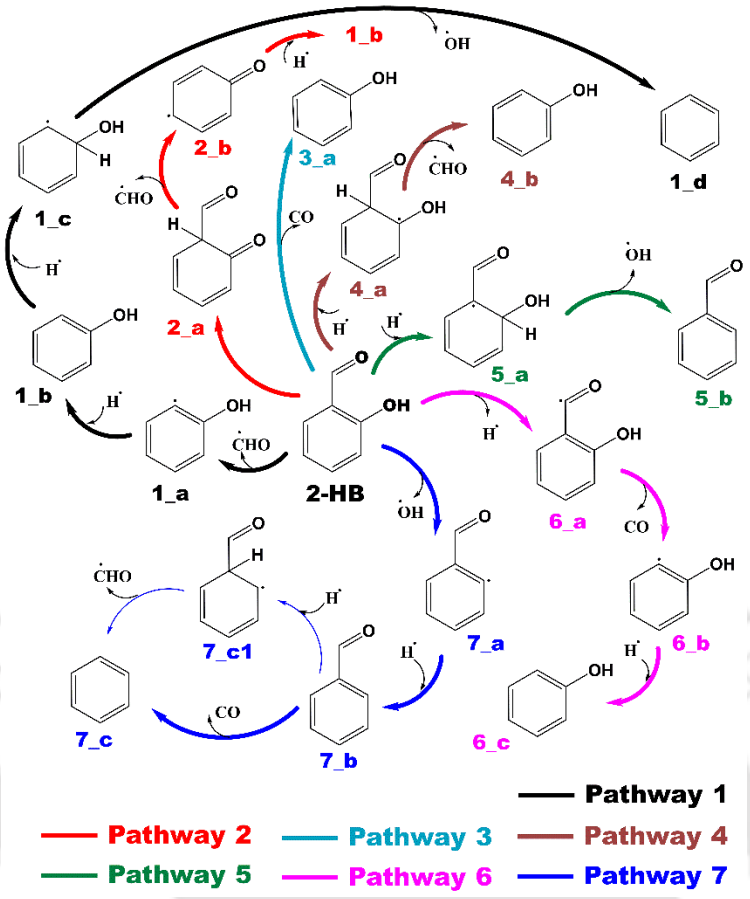

Figure 5.29: The proposed reaction schemes for the conversion of 2-hydroxybenzaldehyde.

directly cleaves the hydroxyl functional from 2-hydroxybenzaldehyde followed by hydrogenation reaction to produce benzaldehyde; however, the benzaldehyde further undergoes two sub-pathways. The first sub-pathway of scheme 7 is decarbonylation reaction of benzaldehyde to produce benzene while second sub-pathway forms a sigma bond with an additional hydrogen atom and aromatic carbon of $C_{aromatic}$-CHO bond followed by the removal of formyl group to produce benzene component.

5.5.2. Bond Dissociation Energies (BDEs)

The bond dissociation energies (BDEs) of 2-hydroxybenzaldehyde at different cleavage sites are calculated to initiate the reaction pathways as BDE plays key role to understand which bond is likely to be cleaved first. The applied theory for the calculation of BDE is B3LYP/6-311+g(d,p) level of theory.

Table 5.16: The bond dissociation energies (BDEs) of 2-hydroxybenzaldehyde.

Bond		BDE (kcal/mol)
D1	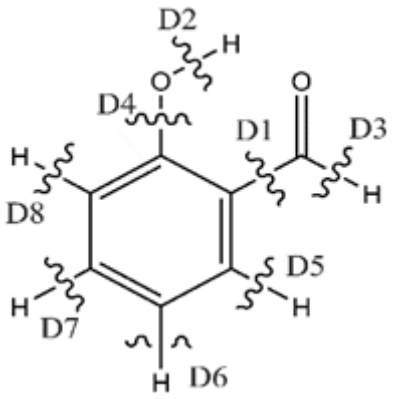	100.31
D2		97.82
D3		92.22
D4		114.24
D5		112.01
D6		113.28
D7		111.48
D8		114.39

As it can be seen from Table 5.16, the least required BDE is for D3 bond (dehydrogenation of formyl group) which means that dehydrogenation of formyl group can be favourable to initiate the reaction pathway. The reaction scheme 6 is devoted for the dehydrogenation of formyl group as the first reaction step. Similarly, the second most favourable cleavage is D2, i.e., dehydrogenation of hydroxyl functional. The formyl group cleavage as D1 is the third most favourable cleavage site and also competitive to D2 bond cleavage in energetics. The final BDEs of each bond cleavage are found to be in order of D3 < D2 < D1 < D7 < D5 < D6 < D4 < D8 according to their energetics.

5.5.3. Reaction Pathways 1-3

The potential energy surfaces of reaction pathways 1-3 are shown in Figure 5.30 which are optimized at B3LYP/6-311+g(d,p) level of theory; and the energetics are in kcal/mol. The corresponding molecular structures are optimized at B3LYP/6-311+g(d,p) level of theory and presented in Figure 5.33. The interatomic distances in the transition state structures shown in Figure 5.33 are in angstrom (Å) units. The BDEs and/or barrier heights involved in each reaction scheme are shown in Table 5.17.

In the reaction pathway 1, the formyl group cleavage is the first reaction step followed by a single step hydrogenation reaction to produce phenol. The phenol compound has been

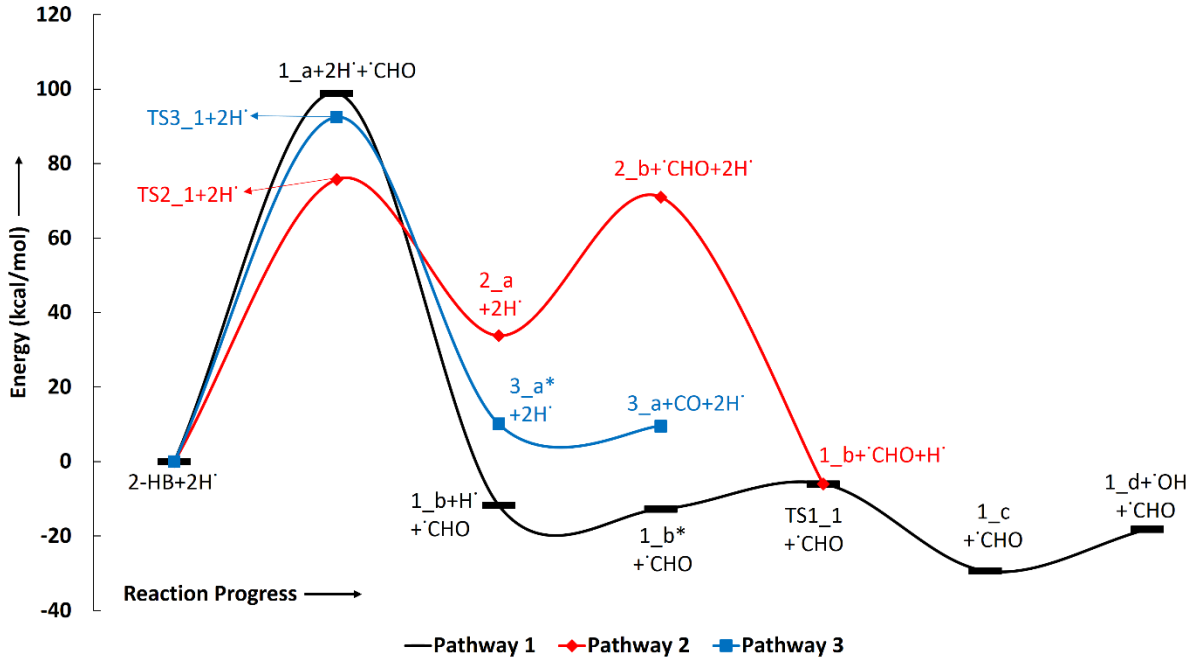

Figure 5.30: Potential energy surfaces of the reaction schemes 1-3.

hydrogenated using single hydrogen atom at the aromatic carbon of $C_{aromatic}$-OH followed by removal of the hydroxyl functional to produce benzene. Recalling that for some organic homolysis/heterolysis reactions, the transition state structures are very difficult to find, thus, bond dissociation energies can be great approximation to the barrier heights, therefore, BDEs are calculated for such reactions. The BDEs of cleavage of formyl group and hydrogenation reaction to **1_a** structure are 100.31 kcal/mol and 112.06 kcal/mol respectively. Similarly, the barrier height of third reaction step which is single step hydrogenation to the aromatic carbon of $C_{aromatic}$-OH sigma bond is 6.77 kcal/mol. Further, the BDE for removal of hydroxyl functional from **1_c** structure is 12.04 kcal/mol. The imaginary frequency corresponding to **TS1_1** is 954.81*i* cm^{-1}. The '*i*' corresponds to the imaginary or negative frequency.

The first reaction step under reaction pathway 2 is about hydrogen atom migration from hydroxyl functional to the aromatic carbon of $C_{aromatic}$-CHO sigma bond followed by the second reaction step which is the removal of formyl group from **2_a** structure. The barrier height of the first reaction step is calculated as 75.75 kcal/mol and BDE of the second reaction step is

Table 5.17: The BDEs and/or barrier heights of each reaction scheme.

Pathways	Activation Energies (Ea)			
	Step 1	**Step 2**	**Step 3**	**Step 4**
1	100.31	112.06	6.77	12.04
2	75.75	38.01	84.08	-
3	92.49	-	-	-
4	5.83	13.19	-	-
5	6.48	18.71	-	-
6	92.22	30.87	112.06	-
7	114.24	113.77	86.25	-
7a	same as pathway 7		5.50	11.31

38.01 kcal/mol. The imaginary frequency corresponding to **TS2_1** is 2022.32*i* cm^{-1}. The produced component **2_b** is further hydrogenated at the oxygen atom to produce phenol which requires BDE of 84.08 kcal/mol. Further, phenol can undergo the formation of benzene as per reaction scheme 1. On the other hand, third reaction scheme is the decarbonylation reaction of 2-hydroxybenzaldehyde to produce phenol. The energy required to surpass the barrier height is calculated to be 92.49 kcal/mol and the imaginary frequency corresponding to **TS3_1** is 1706.62*i* cm^{-1}. Huang et al. [51] carried out the same reaction using B3LYP/6-31++g(d,p) level of theory and reported activation energy of 94.96 kcal/mol.

The production of phenol from reaction pathways 1, 2, and 3 can be compared from the activation energy point of view and it can be seen that pathway 2 dominates over pathway 3; however, the activation energy requirement by reaction pathway 2 is also very high and needs to be further investigated to lessen the barrier height. In order to produce phenol, the reaction pathway 4 follows different approach which is discussed below.

5.5.4. Reaction Pathways 4 and 5

The potential energy surfaces of reaction schemes 4 and 5 are shown in Figure 5.31 which are optimized at B3LYP/6-311+g(d,p) level of theory; and the energetics are in kcal/mol. The corresponding molecular structures associated with their pathways are optimized at B3LYP/6-

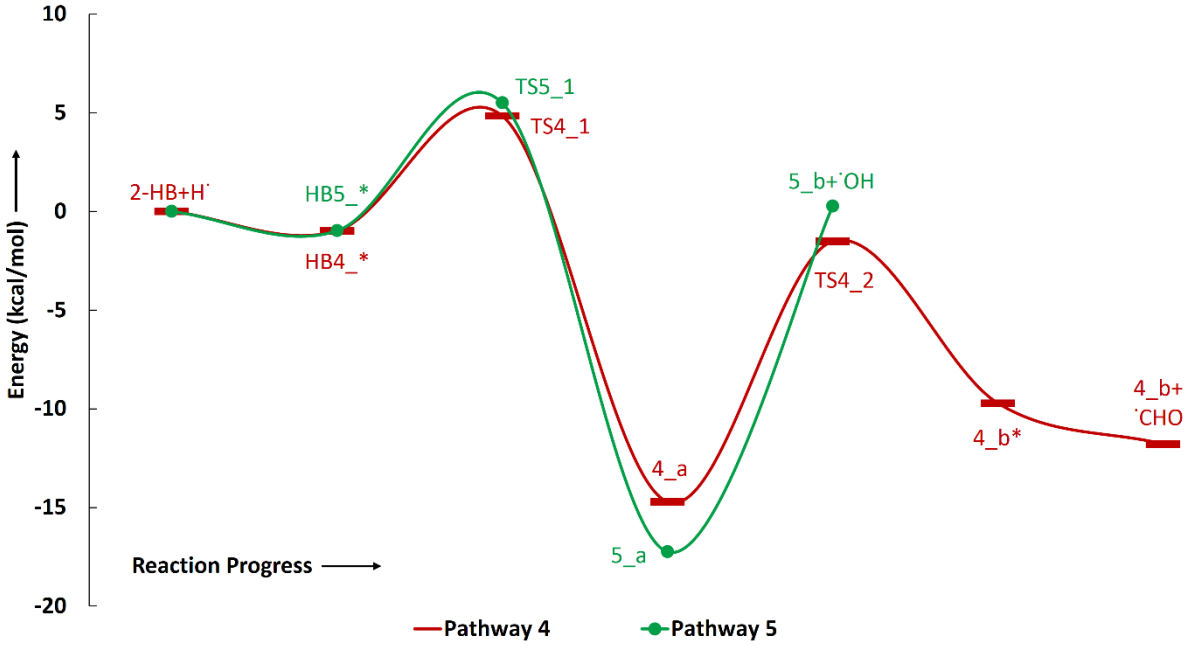

Figure 5.31: Potential energy surfaces of the reaction schemes 4-5.

311+g(d,p) level of theory and can be seen in Figures 5.33 and 5.34. The interatomic distances in the transition state structures of Figures 5.33 and 5.34 are in angstrom (Å) units.

The fourth reaction pathway is another approach to produce the phenol. The reaction starts with an additional hydrogen atom adsorption on the aromatic carbon of $C_{aromatic}$-CHO sigma bond followed by the formyl group removal reaction. The adsorption of an additional hydrogen atom on the aromatic carbon of $C_{aromatic}$-CHO bond requires the barrier height of 5.83 kcal/mol. Further, the barrier height of formyl group removal is 13.19 kcal/mol. Therefore, the rate determining step for this reaction pathway is formyl group process and its activation energy is 13.19 kcal/mol. The imaginary frequencies corresponding to **TS4_1** and **TS4_2** are calculated to be 851.57*i* cm^{-1} and 549.46*i* cm^{-1}, respectively.

The activation energies of reaction pathways 1, 2, and 3 have been calculated as 112.06 kcal/mol, 84.08 kcal/mol, and 92.49 kcal/mol, respectively. The difference between the activation energies of reaction pathways 4 and 1 is 98.87 kcal/mol and the difference between the activation energies of reaction pathways 4 and 3 is 79.3 kcal/mol. In addition, reaction

scheme 4 requires 70.89 kcal/mol less activation energy than reaction scheme 2 for the production of phenol from 2-HB. Therefore, it can be said that the reaction pathway 4 requires a considerably less amount of activation energy to produce phenol from 2-hydroxybenzaldehyde compared to pathways 1, 2, and 3. In other words, the hydrogenation reaction prior to the formyl group removal for production of phenol is favourable pathway compared to direct cleavage of formyl group of 2-hydroxybenzaldehyde followed by hydrogenation reaction (reaction pathway 1) or keto-enol tautomerization of 2-HB followed by removal and addition of formyl group and atomic hydrogen, respectively (reaction pathway 2) or decarbonylation reaction of 2-hydroxybenzaldehyde (reaction pathway 3).

Fifth reaction scheme is about the production of benzaldehyde from 2-hydroxybenzaldehyde through a single step hydrogenation at the aromatic carbon of $C_{aromatic}$-OH sigma bond followed by the removal of hydroxyl functional. The barrier height of hydrogenation reaction and the BDE of hydroxyl removal reaction are calculated as 6.48 kcal/mol and 18.71 kcal/mol, respectively. Thus, the rate determining step for the production of benzaldehyde under pathway 5 is the hydroxyl group removal reaction step, therefore, the activation energy is 18.71 kcal/mol. The imaginary frequency corresponding to **TS5_1** is 938.82*i* cm^{-1}. The adsorption of hydrogen atom in the pathway 5 is at the aromatic carbon of $C_{aromatic}$-OH sigma bond, whereas, in the pathway 4, the hydrogen atom has been adsorbed at the aromatic carbon of $C_{aromatic}$-CHO sigma bond. The energetics corresponding to both intermediates are very competitive (see Figure 5.31). The removal of hydroxyl functional as the cleavage of $C_{aromatic}$-OH sigma bond to produce benzaldehyde is carried out in the reaction pathway 7 to test the energy differences. The produced component from pathway 5, i.e., benzaldehyde component, can be further decomposed to the benzene using two mechanisms which are discussed below.

5.5.5. Reaction Pathways 6 and 7

The potential energy surfaces of reaction schemes 6 and 7 are shown in Figure 5.32 optimized at B3LYP/6-311+g(d,p) level of theory; and the energetics are in kcal/mol. The corresponding molecular structures can be seen in Figure 5.34 in which the interatomic distances in the transition state structures are in angstrom (Å) units.

In the reaction scheme 6, phenol is produced by different route unlike the approaches used in reaction pathways 1, 2, 3, and 4. The reaction pathway 6 is about the dehydrogenation reaction of formyl group of 2-hydroxybenzaldehyde component followed by the removal of carbon mono oxide and hydrogenation to produce phenol. As per the BDE (Table 5.16), the cleavage of hydrogen atom from formyl group is 92.21 kcal/mol. The produced component undergoes CO removal process with a barrier height of 30.87 kcal/mol. The imaginary frequency corresponding to **TS6_1** is calculated to be 127.99*i* cm^{-1}. The hydrogenation reaction of **6_b** component produces phenol with BDE of 112.06 kcal/mol. It can be seen that the single atom hydrogenation reaction determines the rate of reaction, therefore, the approximated activation energy for this reaction is 112.06 kcal/mol which is exactly similar to the activation energy of reaction pathway 1. Therefore, it can be said that this reaction pathway is also not favourable for the production of phenol component.

In the reaction pathway 7, benzene is produced from 2-hydroxybenzaldehyde by hydroxyl group cleavage as the first reaction step followed by a single step hydrogenation to produce benzaldehyde component. Further, the benzaldehyde component follows two pathways to produce benzene. Using the primary reaction pathway 7 (see Figure 5.29), the decarbonylation reaction of benzaldehyde produces benzene, whereas, using secondary reaction pathway 7a (see Figure 5.29), benzaldehyde undergoes a single step hydrogenation at the aromatic carbon of $C_{aromatic}$-CHO sigma bond followed by the removal of formyl group to produce benzene.

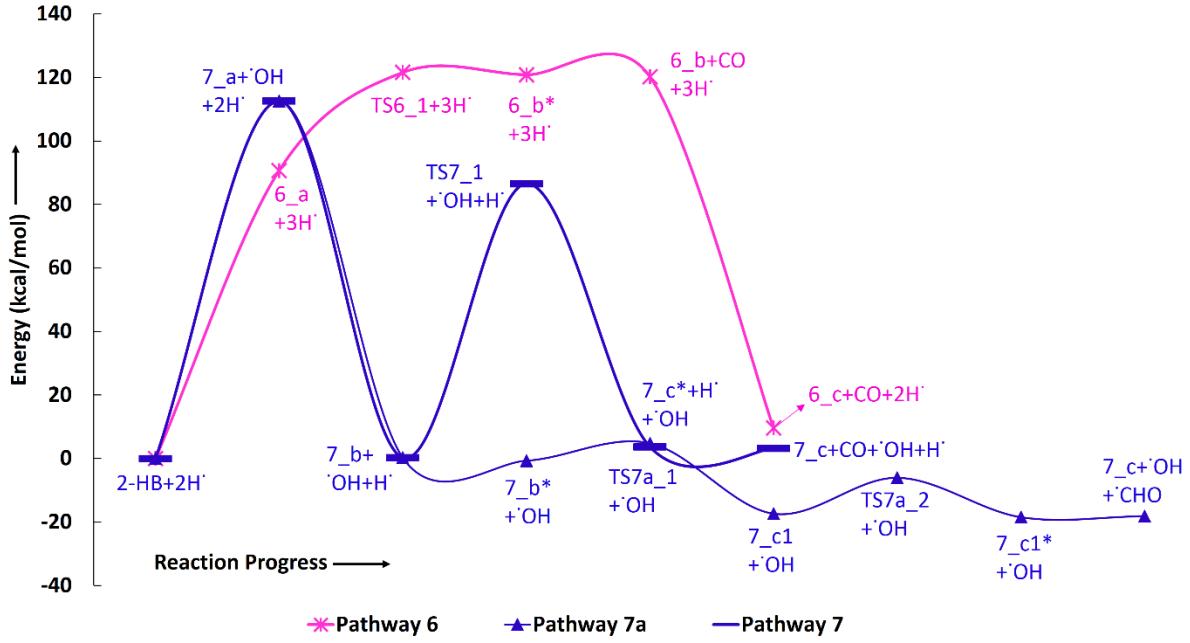

Figure 5.32: Potential energy surfaces of the reaction schemes 6-7.

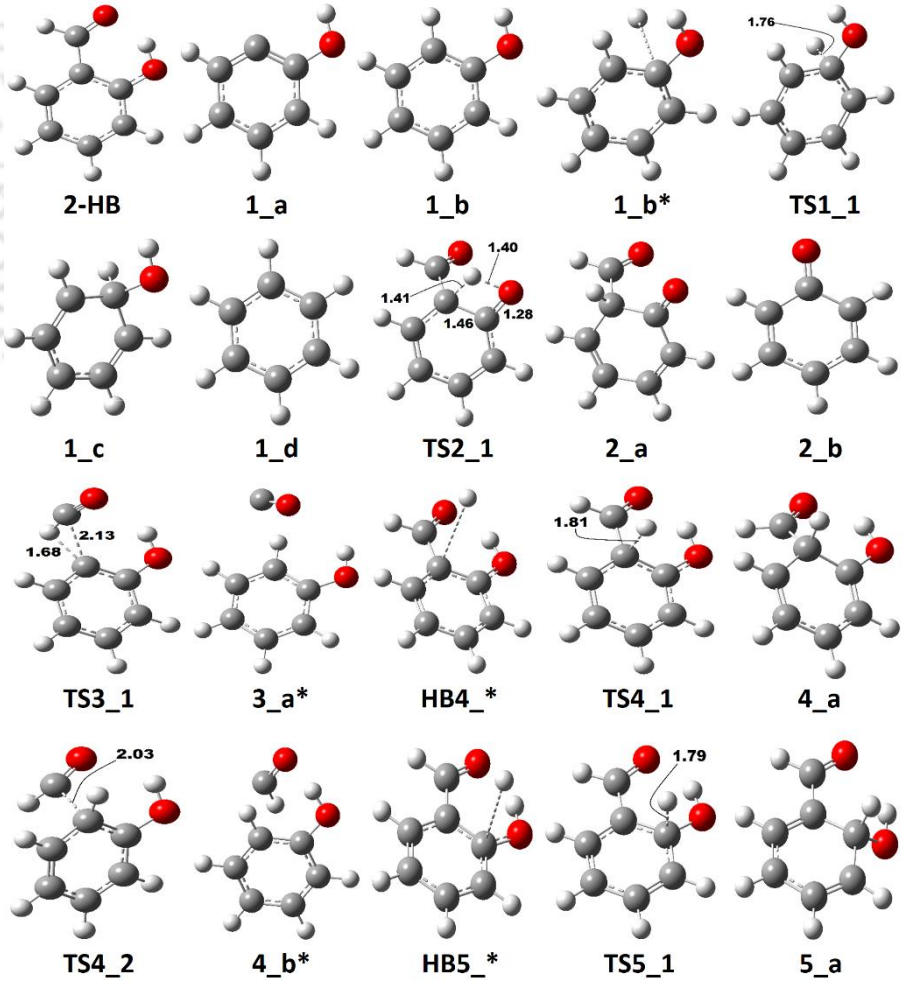

Figure 5.33: Molecular structures involved in the reaction schemes 1-5.

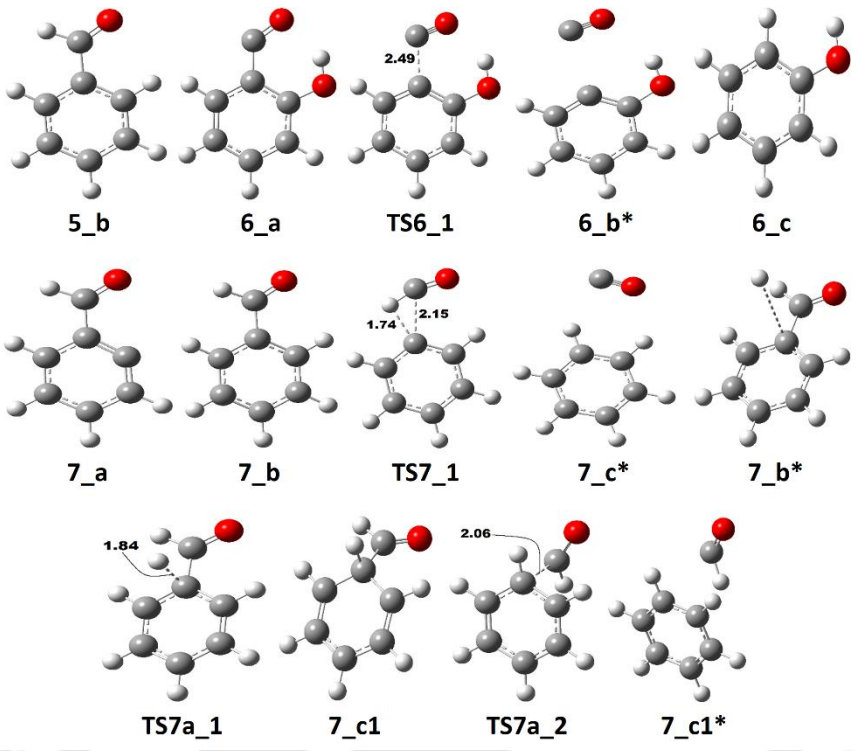

Figure 5.34: Molecular structures involved in the reaction schemes 5-7.

The hydroxyl functional removal from 2-hydroxybenzaldehyde followed by the hydrogenation reaction to produce benzaldehyde require BDEs of 114.24 kcal/mol and 113.77 kcal/mol, respectively. Recalling the reaction pathway 5, the production of benzaldehyde from 2-hydroxybenzaldehyde required an activation energy of 18.71 kcal/mol only, whereas, the reaction pathway 7 requires an activation energy of 114.24 kcal/mol. The difference between activation energies of 5 and 7 is 95.53 kcal/mol, therefore, the hydroxyl group cleavage followed by hydrogenation reaction is not possible without use of appropriate catalysts. Further, the conversion of benzaldehyde to benzene using decarbonylation requires a barrier height of 86.25 kcal/mol, whereas, the barrier heights of the hydrogenation reaction at the aromatic carbon of $C_{aromatic}$-CHO sigma bond and CHO removal are 5.50 kcal/mol and 11.31 kcal/mol, respectively. The imaginary frequency corresponding to **TS7_1** is 1678.08*i* cm^{-1}, whereas, the imaginary frequencies corresponding to **TS7a_1** and **TS7a_2** are 837.52*i* cm^{-1} and 528.25*i* cm^{-1}, respectively. It can be seen that the decarbonylation reaction of benzaldehyde under pathway 7 is not favourable compared to the secondary pathway 7a.

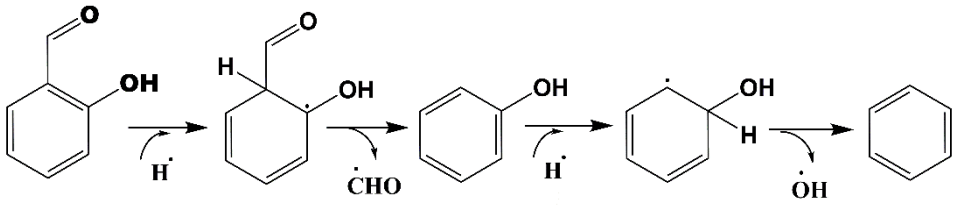

Figure 5.35: The optimum reaction pathway for the production of benzene from 2-hydroxybenzaldehyde.

Finally, in summary, it is found that the removal of oxy-functionals from 2-hydroxybenzaldehyde as the direct bond cleavages cannot be favourable compared to the single step hydrogenation followed by removal of oxy-functionals using two reaction steps. For instance, the direct cleavage of hydroxyl group from 2-hydroxybenzaldehyde, i.e., **2-HB → 7_a**, under reaction pathway 7 requires an activation energy of 114.24 kcal/mol, whereas, hydrogenation as the first reaction step followed by hydroxyl group removal under reaction pathway 5, i.e., **2-HB → 5_a → 5_b**, requires an activation energy of 18.71 kcal/mol only. Similarly, the direct cleavage of formyl group from 2-hydroxybenzaldehyde, i.e., **2-HB → 1_a**, under reaction pathway 1 requires activation energy of 112.06 kcal/mol, whereas, the hydrogenation as the first reaction step followed by formyl group removal under reaction pathway 4, i.e., **2-HB → 4_a → 4_b**, requires an activation energy of 13.19 kcal/mol only. Therefore, the optimum pathway of the production of benzene from 2-hydroxybenzaldehyde would progress as per the reaction pathway shown in Figure 5.35, i.e., the single step hydrogenation at the aromatic carbon of $C_{aromatic}$-CHO sigma bond followed by the removal of formyl group to produce phenol. Further, a single step hydrogenation at the aromatic carbon of $C_{aromatic}$-OH sigma bond followed by the removal of hydroxyl group to produce benzene. The notations of the optimum reaction progress can be given as **2-HB → 4_a → 4_b → 1_b → 1_c**. The rate determining step for the optimum reaction progress can be given as **4_a → 4_b** and the corresponding activation energy is found to be 13.19 kcal/mol.

5.5.6. Thermochemistry

The thermochemical investigation of optimum reaction pathway for the production of benzene from 2-hydroxybenzaldehyde (see Figure 5.35) is performed at a wide range of temperature, i.e., 473-873 K at an interval of 100 K. The pressure of the system has been kept constant at 1 atm. Thermodynamic parameters (ΔM) are evaluated in the terms of reaction free energies (ΔG) and reaction enthalpies (ΔH); both parameters can be seen in Table 5.18.

It can be seen from Table 5.18 that both thermochemical parameters are negative at 473 K, i.e., ΔG and ΔH at 473 K are -31.28 kcal/mol and -19.31 kcal/mol, respectively. This suggests that optimum reaction pathway is both spontaneous and exothermic, thus, the temperature of 473 K can provide a favourable environment for the reaction. However, decomposition reactions are often recorded at higher temperature, therefore, high temperature thermodynamics are also considered here. The temperature rise of 100 K from 473 K accounts significant increase in reaction free energy, however, reaction enthalpy does not get affected much. Further, at 873 K, reaction free energy and reaction enthalpy are evaluated as -40.47 kcal/mol and -22.15 kcal/mol, respectively. The temperature rise of 400 K increases the spontaneity and exothermicity of the reaction by 9.19 kcal/mol and 2.84 kcal/mol, respectively. It is observed that the high temperature process does not considerably affect the reaction enthalpy but affects the reaction free energy by a greater extent. Therefore, thermochemical investigation of optimum reaction pathway for the production of benzene from 2-hydroxybenzaldehyde in the range of 473-873 K concludes thermodynamic favourability.

Table 5.18: Thermochemical parameters (ΔM) of optimum reaction pathway.

Pathways	**ΔM**	**Temperature (K)**				
		473	**573**	**673**	**773**	**873**
Optimum	ΔG	-31.28	-33.75	-36.09	-38.33	-40.47
	ΔH	-19.31	-19.98	-20.68	-21.41	-22.15

Before concluding the discussions, it is worthy to address the concerns over use of H atom in the present numerical study. The H atoms used in this computational study are assumed to be derived from the aldehyde and hydroxyl groups present in the 2-hydroxybenzaldehyde. However, the H atoms are presumably taken from •CHO group in the process of producing CO with an activation energy of 38.50 kcal/mol. Analogous to a combined experimental and computational study of Liu et al. [71] on pyrolysis of vanillin which consist of an aldehyde group, here too it is expected that aldehyde group present in 2-hydroxybenzaldehyde would decompose to produce CO and H atom which can be used for the progress of reaction schemes presented in this study. Finally, the use of H atom shown in present reaction schemes does not indicate that H atom are used as starting point of the reaction but are assumed that they are produced by aforementioned possibility. Therefore, the sources of H atoms are assumed from the •CHO groups yielding CO as one of the product.

5.6. Quantum Chemical Study on Gas Phase Pyrolysis of *p*-Isopropenylphenol

5.6.1. Reaction Schemes

The general notations in the reaction schemes are organized in such a way that the characters **X** and **Y** in structure **X_Y** of any reaction scheme represent the reaction scheme number and structure number, respectively, in that particular reaction scheme. For example, **6_a** is the structure **a** of reaction scheme **6**.

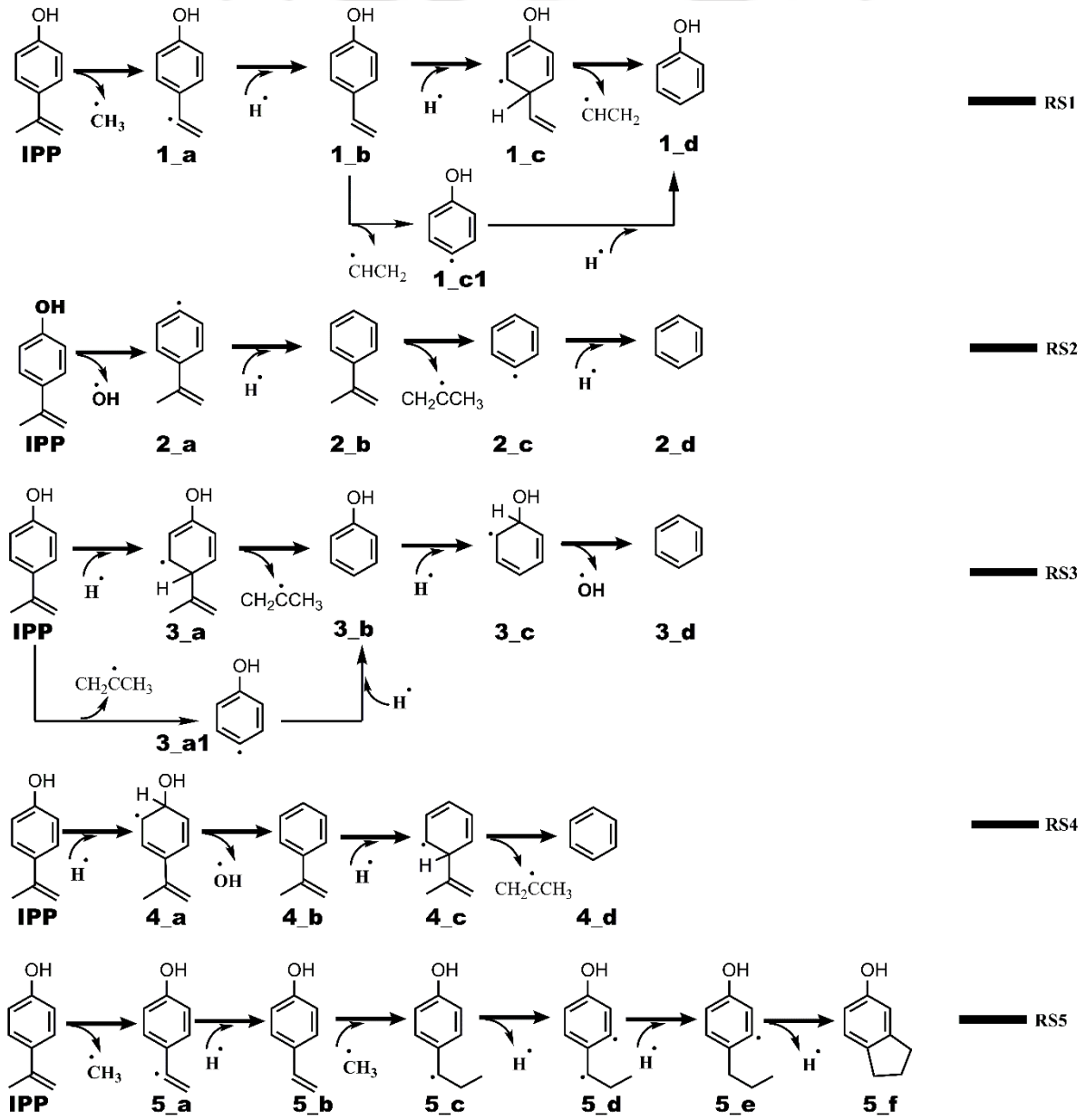

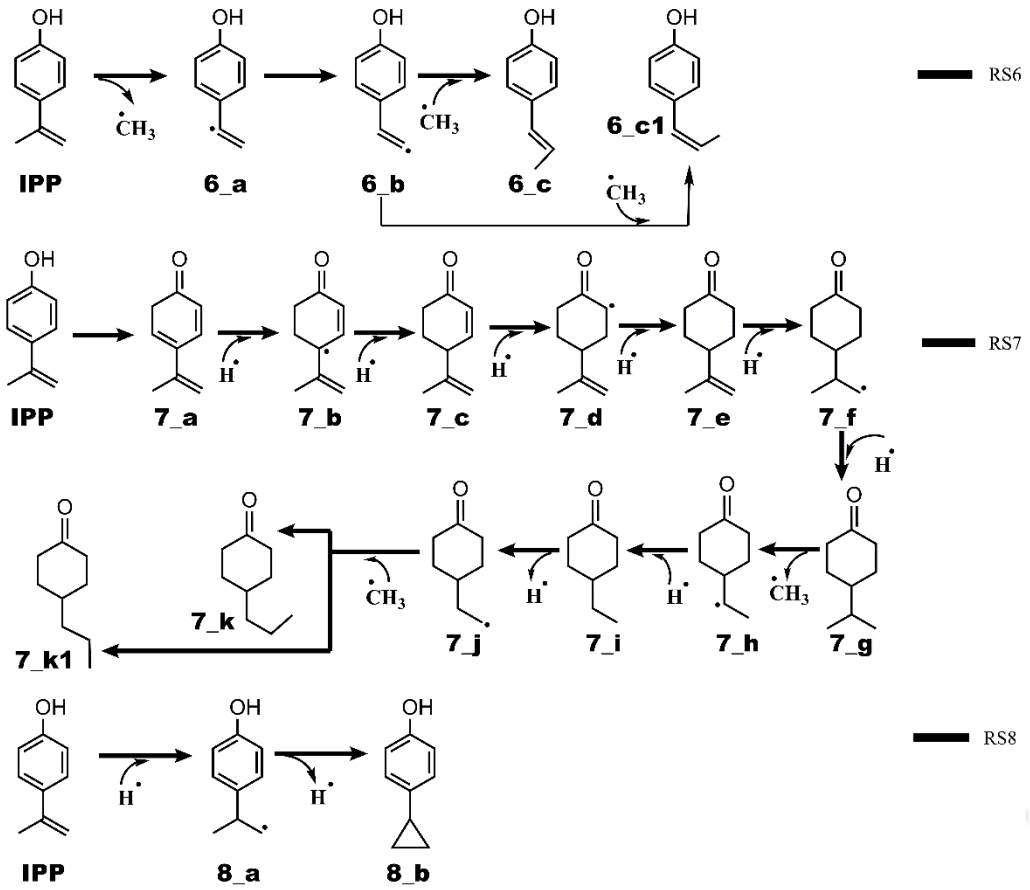

The production of phenol is considered in reaction scheme 1 (RS 1), which initiates from demethylation reaction of isopropenyl group of *p*-isopropenylphenol component followed by an atomic hydrogenation to saturate the generated radical due to demethylation. Further, an atomic hydrogenation reaction to the aromatic carbon of $C_{aromatic}$-vinyl is carried out to partially saturate the ring followed by elimination of vinyl group to produce phenol. The production of benzene from *p*-isopropenylphenol component is considered in reaction schemes 2-4 using different approaches. For instance, in reaction scheme 2 (RS 2), direct elimination of hydroxyl group is carried out to produce the structure **2_a** followed by an atomic hydrogen addition reaction to produce isopropenylbenzene (**2_b**). The component **2_b** (isopropenylbenzene) does not contain any oxygen atom and, in addition, it can be very important precursor in the production of cumene. Further, it can lead to the production of isopropylbenzene using saturation of the double bond but the production of hydrogen radicals to saturate the double

bond in the pyrolysis of *p*-IPP is highly unlikely, therefore, it should follow further reduction reactions. To understand further decomposition process, the elimination of isopropenyl group is carried out from structure **2_b** to produce phenyl which is hydrogenated to form benzene. The production of benzene by RS 3; however, is dealt with other approach. In RS 3, the component *p*-IPP undergoes partial hydrogenation at the carbon atom of $C_{aromatic}$-isopropenyl bond followed by cleavage of whole isopropenyl group to produce phenol. On the other hand, the *p*-IPP component in reaction scheme 4 undergoes partial hydrogenation at the carbon atom of $C_{aromatic}$-OH bond followed by the cleavage of hydroxyl group to produce isopropenylbenzene which further follows the similar approach to cleave the isopropenyl group of isopropenylbenzene to produce benzene. The reaction scheme 5 is about the production of indan-5-ol from *p*-IPP component using methyl and hydrogen arrangement reactions. Similar to RS 5, RS 6 also starts from methyl transfer reaction; however, the methyl radical of *p*-IPP is cleaved and further rearranged from benzyl carbon to terminal carbon atom of **6_b**; and produces two forms of 4-propenylphenol, i.e., *cis*- and *trans*-conformers (see RS 6). On the other hand, RS 7 produces *cis* and *trans* conformers of 4-propylcyclohexanone. Though, the occurrence of the reaction scheme 7 is highly dubious because of high hydrogen radicals requirement but to understand the mechanism of formation of 4-propylcyclohexanone, RS 7 is carried out. It initiates from the keto-enol tautomerization reaction followed by ring saturation reaction to produce 4-isopropenylcyclohexanone (structure **7_e**). This follows the saturation of propenyl to propyl group and produces 4-isopropylcyclohexanone. Further, 4-isopropylcyclohexanone undergoes methyl transfer reaction and forms two conformers of 4-propylcyclohexanone. The reaction scheme 8 involves atomic hydrogen addition and dissociation reactions, respectively, to convert the isopropenyl group into cyclopropyl group. All reactions are carried out in gas phase using B3LYP/6-311+g(d,p) level of theory under the framework of density functional theory (DFT).

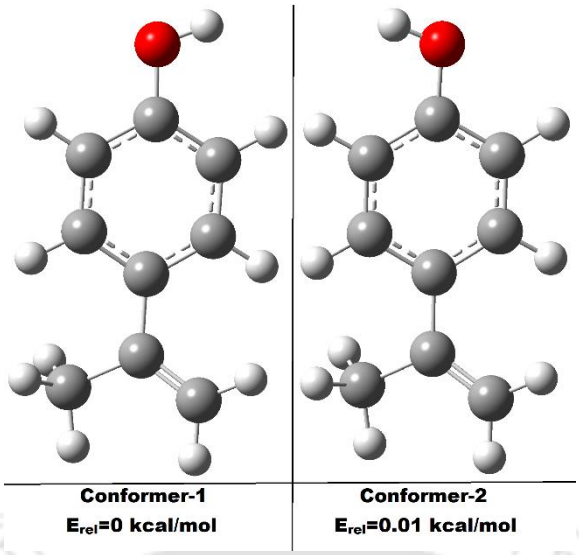

Figure 5.36: The competitive energetic conformers of *p*-IPP component. E_{rel} is relative energy to the electronic energy (added with zero point vibrational energy) of conformer 1.

The molecule *p*-IPP can have various conformers with comparable energetics; however, two conformers of *p*-IPP component resembling very close energetics are shown in Figure 5.36 as conformer **1** and conformer **2**. The applied level of theory, i.e., B3LYP/6-311+g(d,p) suggests that conformer **1** possesses the ground state as it shows lower energy, therefore, higher stability than conformer **2**. The electronic energy added with zero point vibrational energy of conformer **2** is 0.013 kcal/mol higher than conformer **1**. Though, the difference between both conformers is not very significant but it can have considerable impact in the prediction of PES, therefore, all further calculations are performed using conformer **1**.

5.6.2. Bond Dissociation Energy

The concept of bond dissociation energy is very important in the organic homolysis reactions because it provides two important information: i) approximate activation energy of organic homolysis reaction for which transition state structures are hard to locate, and ii) it unravels the dissociation mechanism of molecule which becomes very useful in order to know the favourable reaction pathway. Therefore, the bond dissociation energy (BDE) of *p*-IPP is carried

Table 5.19: The bond dissociation energies at B3LYP/6-311+g(d,p) level of theory.

Bond	Structure	BDE (kcal/mol)
D1	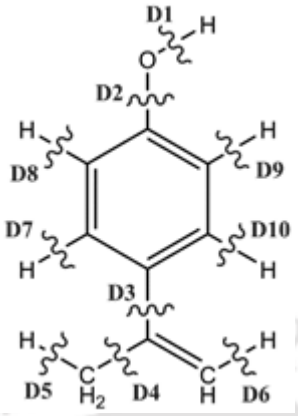	81.02
D2		105.39
D3		102.49
D4		82.47
D5		86.04
D6		110.25
D7		110.36
D8		113.62
D9		111.81
D10		110.41

out in this study to know the favourable dissociation mechanism using B3LYP/6-311+g(d,p) level of theory. The BDEs for each bond dissociation are shown in Table 5.19 including the ground state structure of *p*-IPP with considered bond dissociation sites. It can be seen from Table 5.19 that the dissociation of hydrogen atom from hydroxyl group, i.e., O-H bond, is the least energy demanding bond cleavage site. Further, the cleavage of methyl group from isopropenyl group of *p*-IPP component is second least energy demanding compared to D1. The hydrogen dissociation from hydroxyl group causes the oxygen atom to be in double bonding with next aromatic carbon. On the other hand, the aromatic carbon where isopropenyl group is attached appeared to be generated with radical because of electron distribution due to hydrogen dissociation. It can be seen that these two bond cleavages are very competitive in energetics, therefore, the dissociation reaction of *p*-IPP using these two cleavages is highly recommending. Similar to the D1 dissociation, i.e., hydrogen atom dissociation from OH group, the elimination of H from methyl group is the third most favourable bond cleavage amongst all bond cleavages. Apart from these three bond dissociations, all other bond cleavages are very high energy demanding, for instance, the hydrogen eliminations from ring structure are in the range of 110-113 kcal/mol. Further, the direct cleavages of functionals, i.e., cleavages of OH and isopropenyl groups are also high energy demanding. Nevertheless, the bond dissociation energies in the

ascending order of their BDEs are found to be D1 < D4 < D5 < D3 < D2 < D6 < D7 < D10 < D9 < D8. Therefore, the conversion of *p*-IPP component would be favourable with the bond cleavage of O-H as the first reaction step. Also, it will be comparably favourable with the cleavage of methyl group because O-H and methyl group cleavages are very close in energetics.

5.6.3. Pathways involving direct functional cleavage followed by atomic hydrogenation

The reaction schemes involving direct cleavages of functional groups are placed in RS 1 and RS 2. The potential energy surfaces of RS 1 and RS 2 are depicted in Figure 5.37 and the corresponding optimized molecular structures are shown in Figure 5.39. The bond dissociation energies and/or barrier heights corresponding to each reaction step of all reaction schemes are presented in Table 5.20.

The cleavage of methyl group is the least energy demanding bond dissociation in BDE calculations. Therefore, RS 1 involves the cleavage of methyl group followed by an atomic hydrogen addition reaction. However, the transition state structures for both reactions are very difficult to locate, therefore, the calculation of approximate activation energies is carried out by employing BDE calculations which report approximated activation energies for both reactions as 82.47 kcal/mol and 99.59 kcal/mol, respectively. The atomic hydrogen addition reaction to the structure **1_a** is highly kinetic demanding barrier height; however, looking from energetic point of view, the demethylation reaction is also highly energy demanding. In other words, achieving the activation barrier of 82.47 kcal/mol will be quite high and the reaction would not be an easy task without very high temperature pyrolysis. Nevertheless, the conversion of 4-vinylphenol into phenol is carried out using different route to investigate the energy requirement. In this route, the hydrogen addition reaction is carried out first followed by the cleavage of vinyl group for which the barrier height and BDE are 6.19 kcal/mol and

22.37 kcal/mol, respectively. However, the direct removal of vinyl group followed by atomic hydrogen addition are also carried out to compare the energy differences; and, the BDEs for both reaction steps are 109.0 kcal/mol and 112.81 kcal/mol, respectively. Therefore, it can be seen that the direct cleavages are not seemingly favourable. However, another reaction scheme,

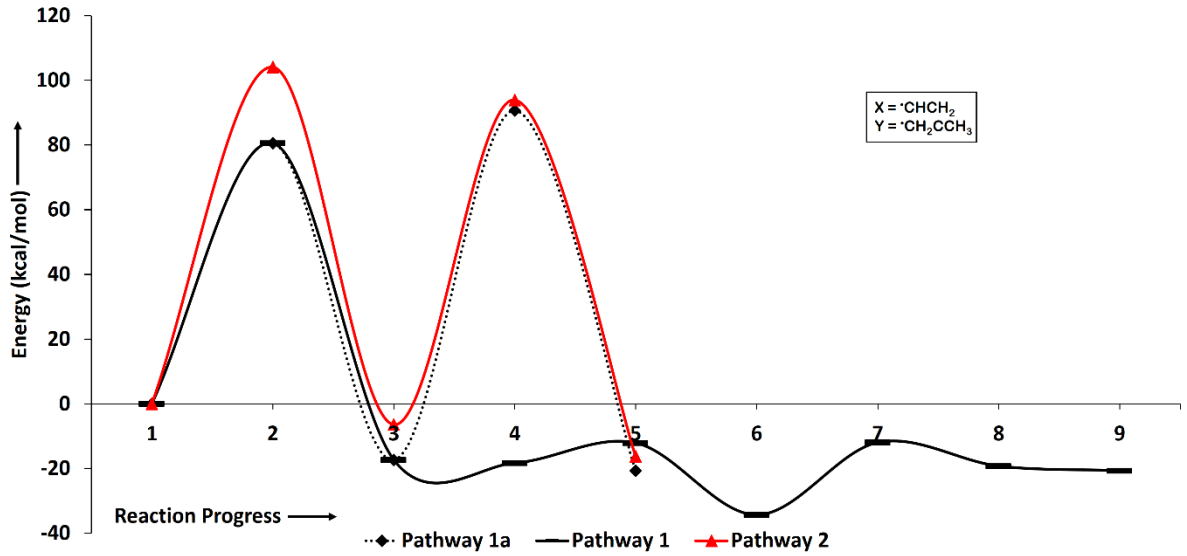

X-axis	1	2	3	4	5	6	7	8	9
Pathway 1	IPP+2H·	1_a+2H·+·CH_3	1_b+H·+·CH_3	1_b*+·CH_3	TS1_1+·CH_3	1_c+·CH_3	TS1_2+·CH_3	1_d*+·CH_3	1_d+X+·CH_3
Pathway 1a	Same as above			1_b1+X+·CH_3+H	1_d+H·+·CH_3	--	--	--	--
Pathway 2	IPP+2H	2_a+2H·+·OH	2_b+H·+·OH	2_c+H·+Y+·OH	2_d+Y+·OH	--	--	--	--

Figure 5.37: Potential energy surfaces of reaction pathways 1, 1a, and 2.

Table 5.20: The activation barriers of each reaction step of all reaction schemes.

RSs	Bond Dissociation Energies/Barrier Heights of reaction steps										
	1	**2**	**3**	**4**	**5**	**6**	**7**	**8**	**9**	**10**	**11**
1	82.47	99.59	6.19	22.37	--	--	--	--	--	--	--
1a	same as RS 1		109.00	112.81	--	--	--	--	--	--	--
2	105.39	111.98	101.29	111.58	--	--	--	--	--	--	--
3	5.39	19.87	6.77	12.02	--	--	--	--	--	--	--
3a	102.49	112.81	same as RS 3		--	--	--	--	--	--	--
4	5.84	16.14	5.76	19.83	--	--	--	--	--	--	--
5	82.47	99.59	29.21	117.00	90.94	9.32	--	--	--	--	--
6	82.47	53.63	96.17	--	--	--	--	--	--	--	--
6a	same as RS 6		93.52	--	--	--	--	--	--	--	--
7	67.03	56.13	67.28	40.83	88.75	31.29	98.17	72.53	95.23	99.24	80.07
7a	same as RS 7										80.96
8	4.29	52.49	--	--	--	--	--	--	--	--	--

i.e., RS 2, is devoted once again for the calculations of activation barriers based on direct cleavages to be assured for the prior given statement. The reaction scheme 2 involves direct cleavage of OH group of *p*-IPP component which requires BDE energetic of 105.39 kcal/mol. Further, the atomic hydrogenation reaction to structure **2_a** to saturate the generated radical due to the cleavage of OH group requires 111.98 kcal/mol energy. Similarly, the cleavage of isopropenyl group from isopropenylbenzene and single step hydrogenation reaction to phenyl ring required bond dissociation energies of 101.29 kcal/mol and 111.58 kcal/mol, respectively. Therefore, it becomes clear that the direct cleavages followed by single step hydrogenation reactions are not favourable for this component because of very high activation barrier.

The reaction scheme 1 consists of two transition state structures which are denoted as **TS1_1** and **TS1_2** in Figure 5.39. The imaginary frequencies for both transition states are reported as 906.63*i* cm^{-1} and 414.16*i* cm^{-1}, respectively.

5.6.4. Pathways involving partial ring hydrogenations followed by functional cleavage

As it has been seen that the direct cleavages of functional groups are not energetically worthy, therefore, another approach is used now. This is similar to the last two reaction steps used in RS 1, i.e., **1_b** → **1_c** → **1_d**. However, in this approach, the atomic hydrogen is added prior to the cleavage of functional groups and this is employed in reaction schemes 3 and 4. The primary reaction scheme 3 undergoes the single step hydrogenation reaction to the aromatic carbon of $C_{aromatic}$-isopropenyl of *p*-IPP component with barrier height of 5.39 kcal/mol. Further, this follows through the cleavage of isopropenyl group with a calculated barrier height of 19.87 kcal/mol. It is seen that the formation of phenol in RS 1 using the prior approach (cleavage of functional followed by atomic hydrogen addition) required approximated activation energies of 82.47 kcal/mol, 99.59 kcal/mol, 109.0 kcal/mol, and 112.81 kcal/mol for

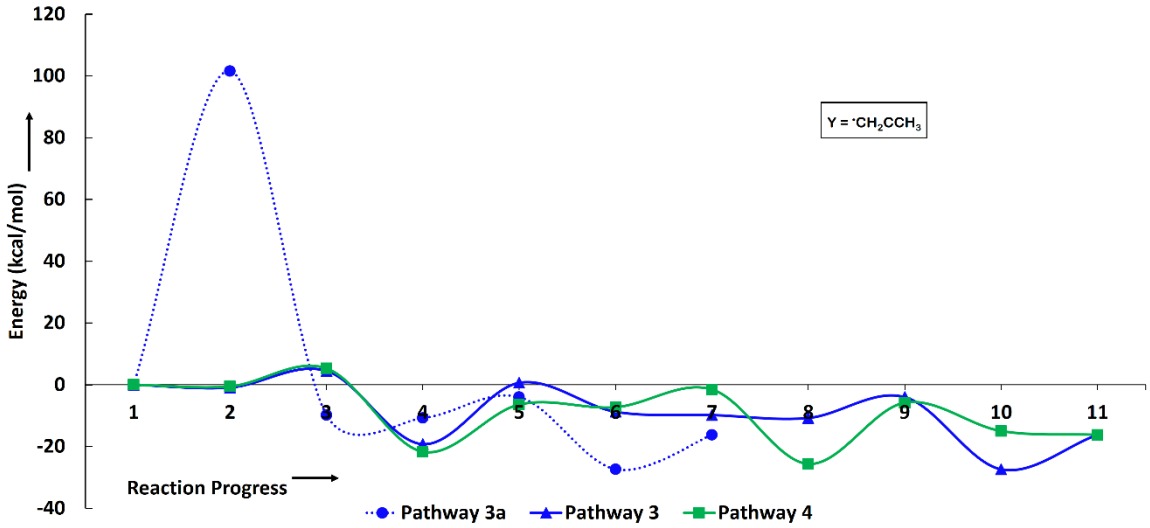

X-axis	1	2	3	4	5	6	7	8	9	10	11
Pathway 3	IPP+2H·	IPP3*+H·	TS3_1+H·	3_a+H·	TS3_2+H·	3_b*+H·	3_b+H·+Y	3_b**+Y	TS3_3+Y	3_c+Y	3_d+Y+·OH
Pathway 3a	IPP+2H·	3_a1+2H·+Y	3_b+H·+Y	3_b**+Y	TS3_3+Y	3_c+Y	3_d+Y+·OH	--	--	--	--
Pathway 4	IPP+2H·	IPP4*+H·	TS4_1+H·	4_a+H·	4_b+H·+·OH	4_b*+·OH	TS4_2+·OH	4_c+·OH	TS4_3+·OH	4_d*+·OH	4_d+·OH+Y

Figure 5.38: Potential energy surfaces of reaction pathways 3, 3a, and 4.

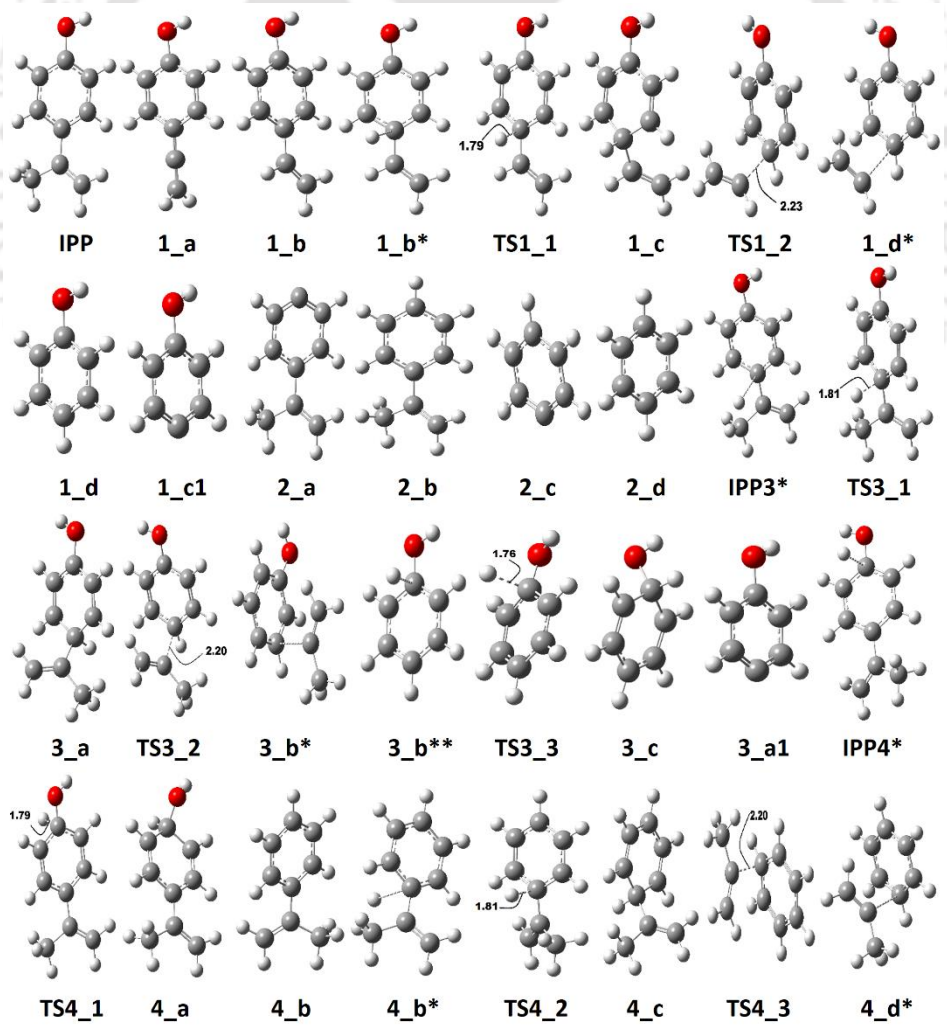

Figure 5.39: Optimized molecular structures corresponding to reaction schemes 1-4.

reaction steps **IPP → 1_a → 1_b → 1_c1 → 1_d**, respectively. Therefore, it can be analyzed that the least energy required reaction step in potential energy surface of RS 1 for the formation of phenol is methyl group elimination, i.e., 82.47 kcal/mol. Though, the direct cleavage of isopropenyl group of *p*-IPP component is not carried out in RS 1 but it can be analogous to the energetics of direct cleavage of isopropenyl of isopropenylbenzene in RS 2 which required 101.29 kcal/mol. To correctly predict the formation of phenol from *p*-IPP using direct cleavage approach, a secondary reaction scheme (RS 3a) has been added with primary reaction scheme 3. RS 3a carries out the elimination of isopropenyl group of *p*-IPP with a calculated BDE of 102.49 kcal/mol followed by a single step hydrogenation to the 4-hydroxyphenyl to produce phenol with a BDE of 112.81 kcal/mol. Therefore, it can be seen that the direct cleavages are not favourable rather, the coupling of hydrogen atom to the phenyl ring where functional is located followed by the homolysis of $C_{aromatic}$-functional will be highly favourable. The conversion of phenol into benzene under RS 3 is carried out using this approach and the highest barrier height is reported to be of 12.02 kcal/mol. Similarly, the conversion of *p*-IPP into benzene under RS 4 is also carried out using this approach with intermediate product of isopropenylbenzene. The highest individual barrier height for RS 4 is 19.83 kcal/mol for the reaction step **4_c → 4_d** which is the elimination of isopropenyl group from isopropenylbenzene to produce benzene.

The rate determining step for the conversion of *p*-IPP component into benzene using RS 3 is recognized as **3_a → 3_b** because of dominating activation energy. On the other hand, the reaction step **4_c → 4_d** appears as the rate determining step under RS 4 which controls the overall reaction. It is also observed that the activation energies of both rate determining steps of RS 3 and RS 4 are quite similar and have deviation of 0.04 kcal/mol. Therefore, both reactions can be thought as competitive reaction schemes for production of benzene from *p*-IPP component. Nevertheless, the least activation energy is reported for RS 4 compared to RS

3. On the other hand, similar to reaction scheme 1, reaction schemes 3 and 4 also comprise of transition state structures denoted as **TS3_1**, **TS3_2**, **TS3_3**, **TS4_1**, **TS4_2**, and **TS4_3** in Figure 5.39 for which the imaginary frequencies are 866.94*i* cm^{-1}, 426.58*i* cm^{-1}, 954.81*i* cm^{-1}, 927.50*i* cm^{-1}, 895.05*i* cm^{-1}, and 421.15*i* cm^{-1}, respectively.

5.6.5. Pathways involving methyl group rearrangement

The reaction pathways involving methyl group rearrangement are marked as reaction schemes 5 and 6 which undergoes the formations of indan-5-ol and 4-propenylphenols, respectively. The potential energy surfaces and corresponding optimized molecular structures for both reaction schemes are depicted in Figures 5.40 and 5.42, respectively.

The indanols are often produced industrially using *p*-isopropenylphenol component as the reactant [30]; however, the theoretical prediction of this pathway is not available in literature. Therefore, the production of indan-5-ol component from *p*-IPP is elucidated theoretically. Though, the theoretical literature about *p*-IPP component is unavailable but theoretical literature about indan-5-ol component is available. Giuliano et al. [149] have carried

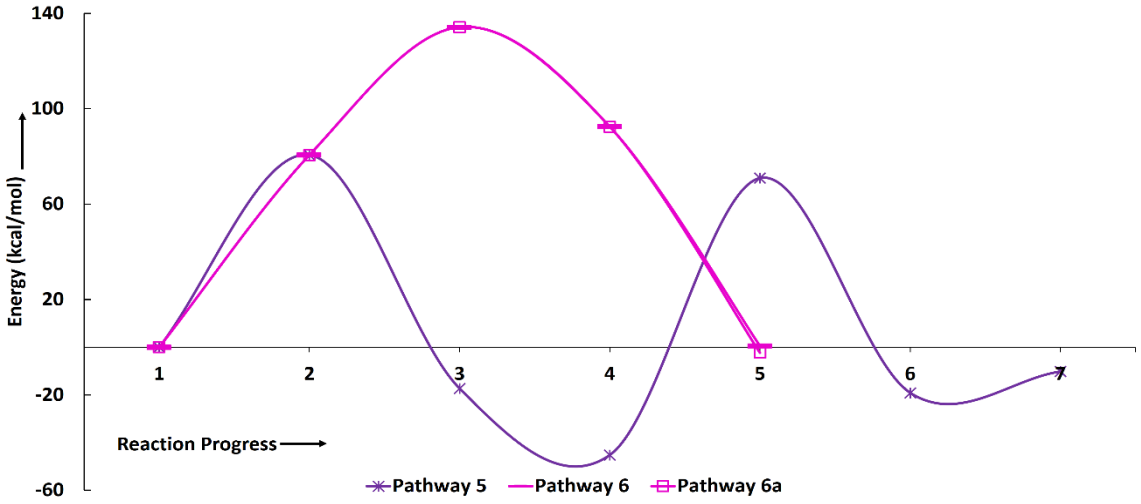

X-axis	1	2	3	4	5	6	7
Pathway 5	IPP+2H·	5_a+·CH_3+2H·	5_b+H·+·CH_3	5_c+H·	5_d+2H·	5_e+H·	5_f+2H·
Pathway 6	IPP	6_a+·CH_3	TS6_1+·CH_3	6_b+·CH_3	6_c	--	--
Pathway 6a	IPP	6_a+·CH_3	TS6_1+·CH_3	6_b+·CH_3	6_c1		

Figure 5.40: Potential energy surfaces of reaction pathways 5, 6, and 6a.

out conformational analyses of indan-5-ol component, therefore, the validation of indan-5-ol component has been carried out and presented after the discussion of its potential energy surface later in this subsection. The proposed reaction mechanism for the production of indan-5-ol involves the formation of 4-vinylphenol using demethylation of *p*-IPP component followed by an atomic hydrogen addition reaction. The energetics for these two reaction steps are already covered in the reaction scheme 1, therefore, it is not discussed here to avoid repetitions. However, to recap, the formation of 4-vinylphenol from both reaction steps required bond dissociation energies of 82.47 kcal/mol and 99.59 kcal/mol, respectively. This follows the methyl group addition reaction to the terminal carbon of 4-vinylphenol which generates a radical on the benzylic carbon atom (see structure **5_c** in RS 5). This reaction step is recorded as considerably very less kinetic demanding reaction compared to the demethylation reaction of *p*-IPP component (see Table 5.20). Further, a dehydrogenation reaction of *meta* positioned (from hydroxyl group) aromatic hydrogen is carried out with required BDE of 117.0 kcal/mol to saturate the generated radical at benzylic carbon which requires an approximated individual activation energy of 90.94 kcal/mol. This hydrogen addition reaction to the benzylic carbon saturates the chain and produces the intermediate **5_e**. However, the structure **5_e** still comprises of an unsaturated aromatic carbon atom because of the earlier hydrogen dissociation reaction. Now, another hydrogen atom dissociation is carried out from terminal carbon atom of propyl group so that it could get attached to the unsaturated aromatic carbon to produce indan-5-ol component. The association reaction of unsaturated terminal carbon of propyl group and unsaturated aromatic carbon atom requires very less bond dissociation energy, i.e., 9.32 kcal/mol, probably because of higher tendency to fill the atomic orbital by forming covalent bond.

The molecular structure of indan-5-ol component (**5_f**) optimized at B3LYP/6-311+g(d,p) level of theory is depicted with labelled carbon atoms to see the trends between

bond distances of present study and that of the work of Giuliano et al. [149]. They carried out their simulations using MP2/6-311++g(d,p) level of theory. The present conformer of indan-5-ol agrees with theoretical study performed by Giuliano et al. [149] that the present conformer is the most stable conformer compared to another indan-5-ol conformer in which the hydrogen of hydroxyl group is 180^{o} opposite side (analogous to the conformers of *p*-IPP component in Figure 5.36). The bond distances in indan-5-ol component (see indan-5-ol structure in Figure 5.42) are reported as: O-H = 0.9626 Å (0.9625 Å), C6-O = 1.3730 Å (1.3738 Å), C1-C2 = 1.5494 Å (1.5442 Å), C2-C3 = 1.5493 Å (1.5442 Å), C3-C4 = 1.5135 Å (1.5122 Å), C4-C5 = 1.3921 Å (1.3975 Å), C5-C6 = 1.3974 Å (1.4018 Å), C6-C7 = 1.3970 Å (1.4024 Å), C7-C8 = 1.3935 Å (1.3993 Å), C8-C9 = 1.3928 Å (1.3988 Å) where the corresponding values in the parentheses are due to Giuliano et al. [149]. Therefore, it can be seen that the present molecular structure of indan-5-ol is in excellent agreement with that of Giuliano et al. [149].

The reaction scheme 6 is about the formations of *trans*- and *cis*-4-propenylphenols using *p*-IPP component as reactant. The first reaction step is common with reaction schemes 1 and 5, i.e., demethylation of *p*-IPP component which requires 82.47 kcal/mol of bond dissociation energy, therefore, it is not discussed here again. After the demethylation reaction, a radical is generated at the benzylic carbon atom of structure **6_a** which is migrated to the terminal carbon after a proton transfer reaction which requires 53.63 kcal/mol of individual activation barrier. Further, the produced structure after proton transfer reaction, i.e., **6_b**, undergoes a methylation reaction. Structure **6_b** holds two possible formations of 4-propenylphenols, i.e., *cis* or *trans* structures. But prior to energetic analyses, it will be hard to predict that which conformer would be most stable; therefore, along with reaction scheme 6 which produces *trans* conformer of 4-propenylphenol, a secondary reaction scheme 6a is also added which produces *cis* conformer of 4-propenylphenol. According to BDE analyses, the formations of *trans* and *cis* conformers of 4-propenylphenol under RS 6 and RS 6a require

energetics of 96.17 kcal/mol and 93.52 kcal/mol, respectively. The formation of *trans* conformer of 4-propenylphenol demands a slightly high activation barrier compared to the formation of *cis* conformer. In addition, according to the PES of reaction scheme 6 (see Figure 5.40), the *cis* conformer of 4-propenylphenol seems to be more stable than *trans* conformer. Though, the formation of *cis* conformer is highly likely according to activation barrier but the thermochemical analyses of both reaction schemes can be different and will be discussed in 'Thermochemistry' section which can elucidate that which pathway would withstand at high temperature pyrolysis? On the other hand, the reaction scheme 6 contains only one transition state structure denoted as **TS6_1** and its imaginary frequency is 2074.97*i* cm^{-1}.

5.6.6. Pathway involving ring saturation

The ring saturation of *p*-IPP component, however, is unlikely to occur in the pyrolysis process because of high demand of hydrogen radicals but, for the theoretical insight purpose, the ring saturation reactions of *p*-IPP component is considered in RS 7. Similar to the reaction scheme 6, this reaction also produces two conformers of the product. The potential energy surface and corresponding molecular structures are depicted in Figures 5.41 and 5.42, respectively.

Prior to the ring saturation reaction of *p*-IPP component, a keto-enol tautomerization reaction is carried out to convert the hydroxyl group of *p*-IPP into ketone group. This reaction occurs with a calculated barrier height of 67.03 kcal/mol. Recalling the BDE study, the dissociation of hydrogen atom from hydroxyl group of *p*-IPP component required least energy amongst all bond cleavages; although, the dissociation of hydrogen atom and keto-enol tautomerization reaction are totally different. The keto-enol tautomerization of *p*-IPP component in the first reaction step of RS 7 is a hydrogen migration reaction from hydroxyl group leaving it to convert into ketone group. Further, it can be seen that the ring is partially hydrogenated, therefore, four subsequent single step hydrogenation reactions to the ring are carried out in order to convert it into cyclo-ring structure. The hydrogen atom addition reactions

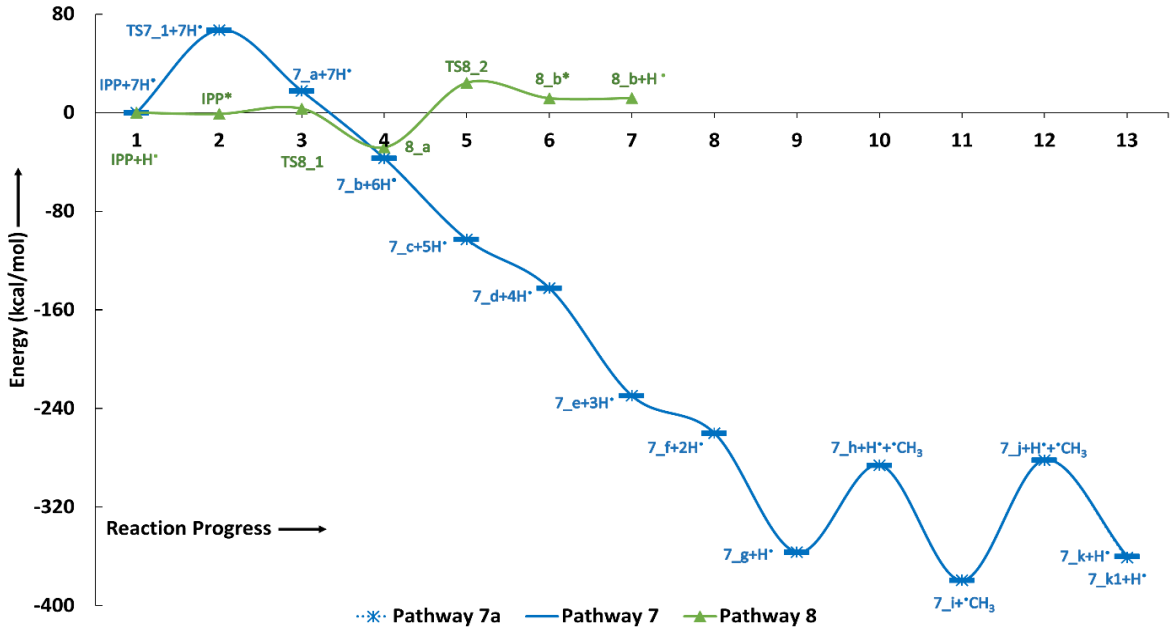

Figure 5.41: Potential energy surfaces of reaction pathways 7, 7a, and 8.

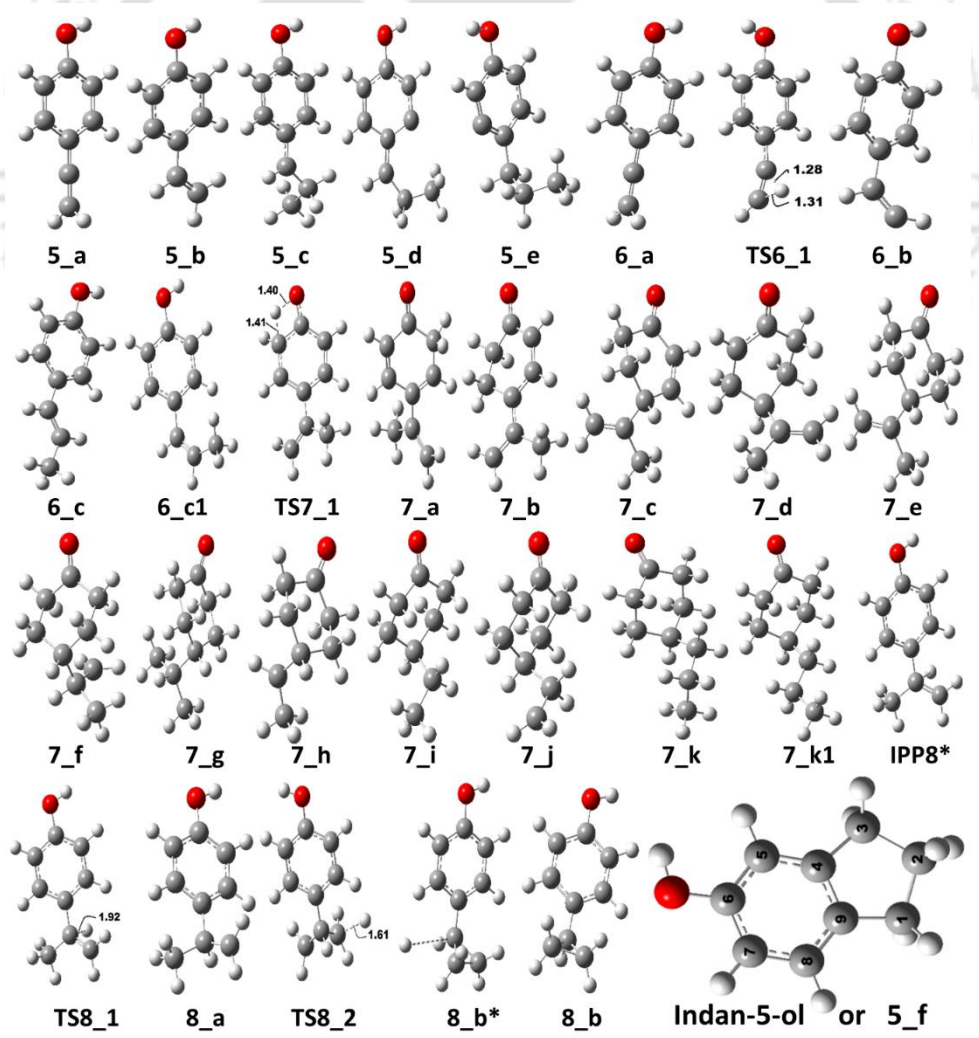

Figure 5.42: Optimized molecular structures of corresponding reaction schemes 5-8.

are started from the *meta* positioned (to keto group) aromatic carbon atom (**7_a** → **7_b**) followed by *para* positioned (to keto group) aromatic carbon atom (**7_b** → **7_c**) which require energies of 56.13 kcal/mol and 67.28 kcal/mol of BDE. This follows up further two single step hydrogenation reaction steps as **7_c** → **7_d** → **7_e** with calculated bond dissociation energies of 40.83 kcal/mol and 88.75 kal/mol, respectively. The produced structure after keto-enol tautomerization and ring saturation reactions is identified as 4-isopropenylcyclohexanone. Further, the double bond of isopropenyl group is saturated which converts it into isopropyl group with BDEs of 31.29 kcal/mol and 98.17 kca/mol. The structure **7_g** itself can be considered as a product and it has various applications industrially, for instance, as a precursor [150, 151] but further rearrangement of methyl group is carried out to convert the isopropyl to open chain propyl. In order to do this, the demethylation of **7_g** is carried out followed by an atomic hydrogen addition reaction to the benzylic carbon of **7_h** structure, where a new radical is generated upon demethylation, is performed to produce the structure **7_i**, i.e., 4-ethylcyclohexanone (see Table 5.20 for barrier heights). Further, a dissociation of hydrogen atom occurs from the terminal carbon of 4-ethylcyclohexanone to expose the possibility for the coupling of methyl group to produce 4-propylcyclohexanone. Similar to the reaction scheme 6, the reaction scheme 7 also possesses the possibilities of formations of two product conformers, i.e., *cis* and *trans*. However, unlike RS 6, the *trans* conformer of product in RS 7 is more stable compared to that of *cis* conformer. However, the production of *cis* conformer of product demands slightly less activation barrier height compared to *trans*-4-propylcyclohexanone (see Table 5.20). The imaginary frequency corresponding to **TS7_1** is 2146.39*i* cm^{-1}.

5.6.7. Pathway involving rearrangement of isopropenyl into cyclopropyl

The reaction scheme 8 is about the rearrangement of isopropenyl group of *p*-IPP component into an important intermediate called 4-cyclopropylphenol. It is used in the synthesis of

pharmaceutical and agriculture industries [152]. The production of 4-cyclopropylphenol, in this study, does not consume any hydrogen; however, it involves in the reaction with *p*-IPP component and is being extracted upon the formation of product. The potential energy surface and corresponding optimized molecular structures, respectively, are depicted in Figure 5.41 and Figure 5.42.

The production of 4-cyclopropylphenol from *p*-IPP component involves the formation of an intermediate (shown as **8_a** in Figure 5.42) which attaches a hydrogen atom to the benzylic carbon. The hydrogen atom addition reaction to the *p*-IPP component occurs with a very less and kinetically favourable barrier height of 4.29 kcal/mol. The structure **IPP8*** (Figure 5.42) reports an equilibrium structure of a hydrogen atom attacking to the benzyl carbon atom of *p*-IPP. The addition of a hydrogen atom on benzylic carbon generated a radical on the terminal carbon atom (see RS 8) which activates that carbon fragment to be bonded with the methyl group. Along with this reaction, the elimination of a hydrogen atom from the binding methyl group occurs which co-valences the association of both carbon atoms. The barrier height for this reaction is considerably higher, i.e., 52.49 kcal/mol, than the first reaction step which is hydrogen atom addition reaction. Now, the structure **8_b*** is an equilibrium of 4-cyclopropylphenol and a hydrogen atom which is separated from the product complex and the energy of extraction is shown in the PES (Figure 5.41). There are two first order saddle points located on the potential energy surface of reaction scheme 8 as **TS8_1** and **TS8_2** for which the imaginary frequencies are 779.19*i* cm^{-1} and 1138.75*i* cm^{-1}, respectively.

5.6.8. Thermochemistry

The thermochemical investigation of decomposition of *p*-isopropenylphenol (*p*-IPP) is carried out to understand the effect of thermodynamic properties of reactions, e.g., reaction free energy and reaction enthalpy. Both thermodynamic parameters (ΔG and ΔH) are listed in Table 5.21

for a wide range of temperature from 398 K to 898 K at an interval of 100 K. The pressure is fixed at 1 atmospheric condition for all processes. Those reaction schemes whose reactants and products are same, the ΔG and ΔH for those reactions are also same, e.g., reaction schemes 1, 1a, 2, 3, 3a, and 4. Both reaction schemes 1 and 1a lead to the production of phenol. On the other hand, reaction schemes 2, 3, 3a, and 4 lead to the production of benzene; however, using different reaction pathways.

The reaction schemes 1 and 1a which produce phenol from *p*-IPP component are kinetically favourable because of negative reaction free energies and reaction enthalpies at each temperature condition. Though, the increasing temperature does not affect the reaction free

Table 5.21: The thermodynamic properties (ΔM) of all reaction schemes at 1 atm pressure and at 398-898 K.

Pathways	**ΔM**	**Temperature (K)**					
		398	**498**	**598**	**698**	**798**	**898**
1,1a	ΔG	-49.01	-49.91	-50.45	-50.65	-50.52	-50.10
	ΔH	-44.62	-46.33	-48.28	-50.43	-52.74	-55.17
2,3,3a,4	ΔG	-44.18	-44.82	-45.05	-44.91	-44.45	-43.69
	ΔH	-40.81	-42.70	-44.78	-47.02	-49.37	-51.82
5	ΔG	-24.77	-22.19	-19.33	-16.21	-12.86	-9.29
	ΔH	-34.44	-35.79	-37.25	-38.82	-40.47	-42.21
6	ΔG	-20.50	-19.17	-17.60	-15.80	-13.79	-11.56
	ΔH	-25.26	-26.40	-27.70	-29.15	-30.71	-32.38
6a	ΔG	-16.00	-14.20	-12.15	-9.87	-7.38	-4.67
	ΔH	-22.64	-23.79	-25.11	-26.57	-28.15	-29.82
7	ΔG	-321.17	-302.54	-283.26	-263.47	-243.25	-222.69
	ΔH	-393.80	-397.08	-400.22	-403.21	-406.08	-408.82
7a	ΔG	-322.29	-303.73	-284.51	-264.77	-244.62	-224.11
	ΔH	-394.68	-397.97	-401.11	-404.10	-406.96	-409.70
8	ΔG	-4.40	-2.41	-0.16	2.32	5.01	7.91
	ΔH	-11.79	-12.99	-14.31	-15.77	-17.33	-19.00

energies significantly because it is improved only by 1.01 kcal/mol from 398 K to 898 K but the reaction becomes very exothermic upon temperature increment. Similar reaction exothermicity can be seen for reaction pathways 2, 3, 3a, and 4 which lead to the production of benzene because the reaction enthalpies of these reaction pathways also get significantly better with temperature increment. But the reaction free energies of these reactions (2, 3, 3a, and 4) show different behaviour. These reactions show positive behaviour of temperature increment because they become more spontaneous with increasing temperature from 398 K to 598 K but beyond 598 K, all of these reaction pathways start to become slightly less favourable. Therefore, the temperature condition of 598 K for reaction pathways 2, 3, 3a, and 4 seems optimum because the reaction free energy is at its lowest with reaction being exothermic nature. The spontaneity of reaction scheme 5 which produces indan-5-ol from *p*-IPP component worsens with increasing temperature; however, this reaction is still spontaneous at 898 K but with degraded value compared to 398 K. The reaction enthalpy of this reaction decreases with increasing temperature which means the reaction becomes more exothermic with increasing temperature. The net hydrogen requirement is zero in the formation of indan-5-ol from *p*-IPP and also the reaction is favourable at each temperature condition, therefore, the production of indan-5-ol is highly possible. Although, this component may cause the formation of cyclic high molecular weight carbon fractions which may lead to the coke formation. The reaction schemes 6, 6a, 7, and 7a also behave similar to the reaction scheme 5, i.e., their reaction free energies and reaction enthalpies worsen and improve with increasing temperature, respectively. Although, all these reaction schemes are still kinetically advantageous at 898 K. It can be seen that the *trans* conformer of 4-propenylphenol is more favourable compared to *cis* conformer at each temperature condition, therefore, the possibility of formation of *trans*-4-propenylphenol from *p*-IPP component is more compared to the *cis* conformer. Similarly, the possibility of formation of *trans*-4-propylcyclohexanone dominates over the *cis* conformer because of the

more favourability of thermodynamic parameters at each temperature condition. On the other hand, the formation of 4-cyclopropylphenol from *p*-IPP component, i.e., RS 8, follows similar but with slight disagreement. Though, the reaction scheme 8 is more exothermic with increasing temperature but this reaction becomes unspontaneous after 598 K. The reaction free energy value at 598 K is very insignificant. In addition, both thermodynamic parameters from 398 K – 598 K are not upright compared to other reaction schemes.

5.7. DFT Study on the Production of Toluene from Decomposition Reactions of 2-Hydroxy-6-methylbenzaldehyde

5.7.1. Reaction Schemes

The notation of molecular structures in the reaction schemes presented in Figure 5.43 are given as **X_Y**; where **Y** is the molecular structure in reaction pathway **X**. Similar notations are considered in each potential energy surface and molecular structure shown in Figures 5.44-5.47. In addition, the transition state structure involved in any elementary reaction step is designated as **TSX_Y**; where **Y** is the transition state structure number in reaction pathway **X**. For example, **5_b** in Figure 5.43 denotes structure **b** in the reaction pathway 5 and similarly, **TS8_1** is first transition state structure of reaction pathway 8.

Theoretically, the gas phase decomposition of 2-hydroxy-6-methylbenzaldehyde (HMB) component may occur by several routes, therefore, its decomposition has been considered using nine primary and one secondary reaction pathways as shown in Figure 5.43. The reaction pathway (RP) 1 describes that HMB component is subjected to the direct elimination of formyl group producing the radical structure **1_a**; which further undergoes a single step hydrogenation reaction to produce *m*-cresol. Further, hydrogenation at the carbon atom of $C_{aromatic}$-OH bond followed by elimination of hydroxyl group produces toluene as end product. The second reaction pathway is about the hydrogen migration reaction from hydroxyl group to the aromatic carbon atom of $C_{aromatic}$-CHO bond. This trails the elimination of formyl functional group followed by hydrogenation of the oxygen atom to produce *m*-cresol. Further decomposition of *m*-cresol follows the similar reaction route as of RP 1 for production of toluene. On the other hand, RP 3 (third reaction pathway) is about the decarbonylation reaction of HMB to directly produce *m*-cresol along with side product CO. The reaction pathway 4 starts with hydrogenation of the aromatic carbon of $C_{aromatic}$-CHO bond of HMB followed by

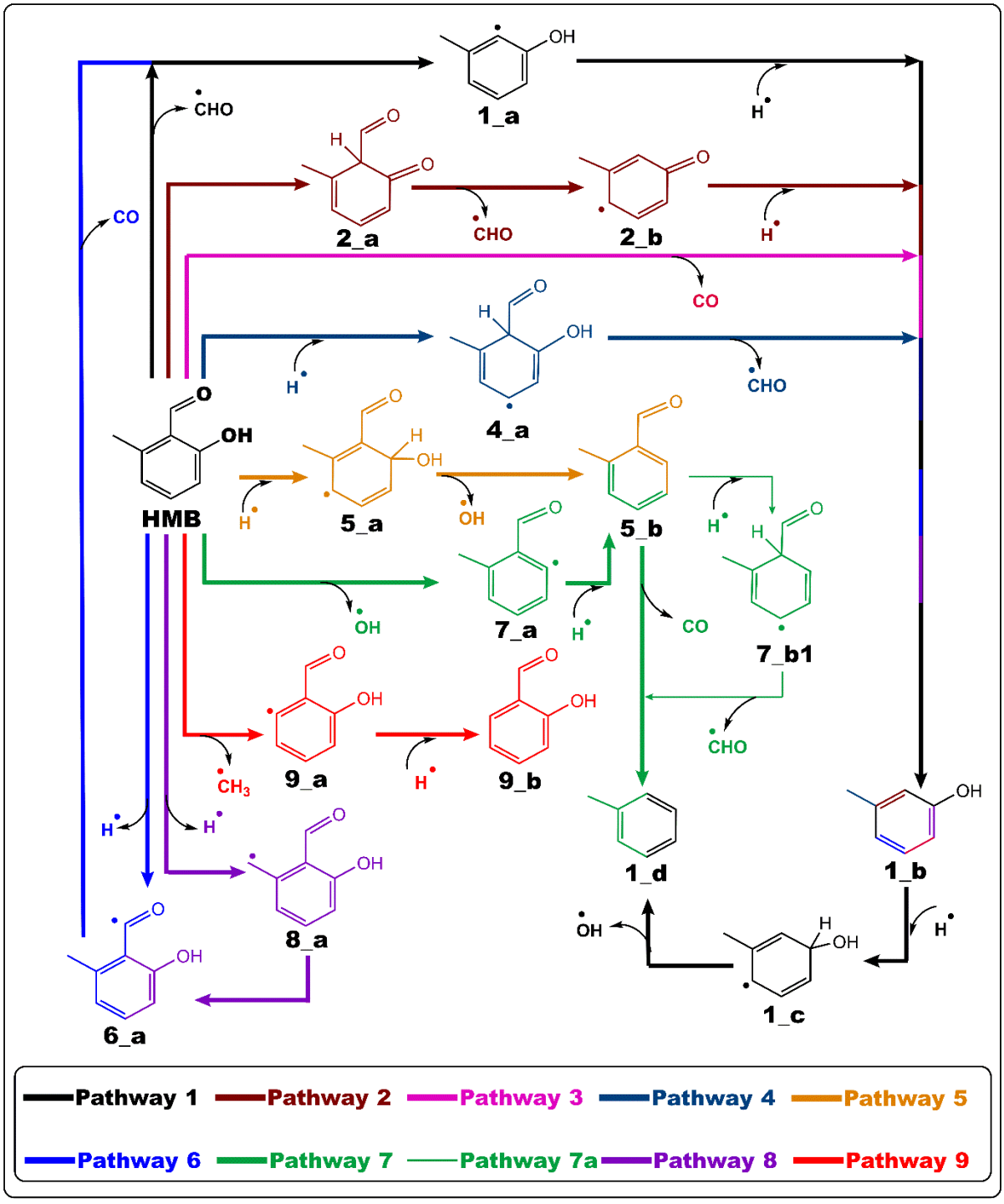

Figure 5.43: Various reaction pathways (RP) for the conversion of 2-hydroxy-6-methylbenzaldehyde.

elimination of formyl group for the production of *m*-cresol. Similarly, the reaction pathway 5 starts with hydrogenation of the aromatic carbon of $C_{aromatic}$-OH bond of HMB followed by removal of OH group to produce 2-formyltoluene. The reaction pathway 6 presents the

dehydrogenation of formyl functional group of HMB followed by elimination of CO group to produce the structure **1_a** which further proceeds according to RP 1. The reaction pathway 7 starts by direct elimination of OH group of HMB followed by a single step hydrogenation of the aromatic carbon to produce 2-methylbenzaldehyde. Further, the primary reaction pathway 7 (RP 7) undergoes decarbonylation reaction to produce toluene while the secondary reaction pathway 7, i.e., pathway 7a, first undergoes the hydrogenation of the aromatic carbon of $C_{aromatic}$-CHO bond of 2-methylbenzaldehyde component followed by elimination of formyl group to produce toluene. The reaction pathway 8 starts with dehydrogenation of methyl group of HMB followed by hydrogen migration reaction from formyl group to the methylene group producing the structure **6_a** which further proceeds the reaction route of RP 6. Finally, the reaction pathway 9 is about the direct elimination of methyl group of HMB component followed by hydrogenation of the aromatic carbon producing 2-hydroxybenzaldehyde.

Prior to discuss potential energy surfaces, it is beneficial to discuss the ground state geometry of HMB component because there may be several local minima of HMB on potential energy surface (PES). Table 5.22 depicts two competitive optimized molecular structures of HMB with their relative energetics (kcal/mol). The main difference between both structures is the dihedral position of formyl group. In configuration 1 (*Config. 1*), the oxygen atom of formyl

Table 5.22: Comparison of relative energy (kcal/mol) of conformations of 2-hydroxy-6-methylbenzaldehyde.

Configurations	Config. 1	Config. 2
Molecular Structures	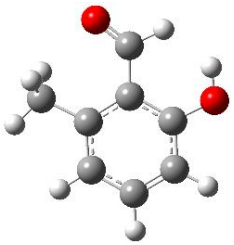	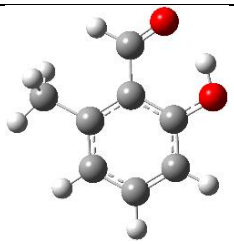
Relative E	9.96	0

group faces towards methyl group, whereas, in configuration 2 (*Config. 2*), the oxygen atom of formyl group interacts with hydrogen atom of hydroxyl group of HMB component. It can be seen that due to this change in dihedral angle, *Config. 2* is more stable geometry compared to the *Config. 1* and the relative energy of *Config. 1* to *Config. 2* is 9.96 kcal/mol, i.e., the latter structure is 9.96 kcal/mol more stable compared to *Config. 1*. Therefore, all subsequent calculations are performed based on *Config. 2*.

5.7.2. Bond Dissociation Energy (BDE)

Bond dissociation energy of a particular chemical bond of a molecule represents the strength of that chemical bond or in other words it provides a preliminary information about the energy requirement for a particular potential bond site that could be broken. In HMB component, there exists 9 possible sites where the bond scission can be possible and are depicted as Dn (n = 1, 2, 3, …, 9) along with their bond dissociation energies in kcal/mol as shown in Table 5.23. BDEs are carried out at B3LYP/6-311+g(d,p) level of theory. It can be seen from Table 5.23 that the most favourable bond site for scission is D9 which is dehydrogenation of methyl group of HMB requiring 87.60 kcal/mol of energy. According to favourability, D9 bond scission is followed by D3 and D5 cleavages which are dehydrogenation of formyl group and demethylation of HMB, respectively. However, the differences in energetics of D3 and D5 relative to least energy demanding bond scission, i.e., D9, are significant. On the other hand, D1 and D2 bond cleavages representing the scissions of formyl group and hydrogen atom from hydroxyl group of HMB, respectively, are competitive in energetics and do not deviate considerably. Nevertheless, the bond scissions of HMB in ascending order of energy requirement is D9 < D3 < D5 < D1 < D2 < D7 < D6 < D4 < D8. Further, it is observed during BDE analyses that dehydrogenations of phenyl hydrogen atoms are not at all favourable indicating that the decomposition of HMB into lower fractions would lead through the cleavages of either functional groups or hydrogen atoms of functional groups only. The most

Table 5.23: Bond dissociation energy (kcal/mol) analysis of 2-hydroxy-6-methylbenzaldehyde.

Bond		BDE
D1	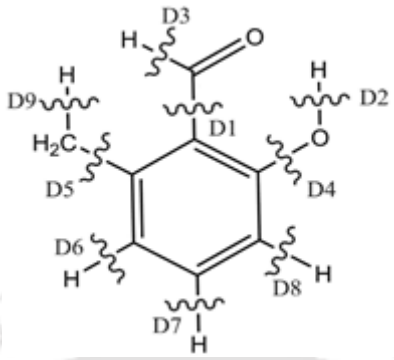	98.18
D2		98.29
D3		90.56
D4		114.23
D5		94.50
D6		112.68
D7		111.21
D8		114.60
D9		87.60

probable path for the decomposition of HMB is through dehydrogenation of methyl group, therefore, in the investigations of potential energy surfaces, a separate reaction profile is added to incorporate this possibility. In addition, other dominant bond scissions, i.e., D3, D5 and D1 are also a part of PES investigation of HMB.

5.7.3. Formation of *m*-cresol

The production of *m*-cresol from HMB is performed using six reaction approaches, i.e., pathways 1, 2, 3, 4, 6, and 8 as shown in Figure 5.43. The potential energy surfaces of these six reaction pathways are shown in Figure 5.44 and the corresponding optimized molecular structures are displayed in Figure 5.45. The activation energy (kcal/mol) of each elementary reaction step of all reaction pathways is given in Table 5.24.

According to the reaction pathway 1 (RP 1), the direct elimination of formyl group of HMB produces structure **1_a**. This direct elimination reaction occurs with a calculated bond dissociation energy of 98.18 kcal/mol. BDE can be a very good approximation for the activation energy of any organic homolysis reaction, thus the elementary reaction step HMB → **1_a** requires 98.18 kcal/mol of activation energy. This certainly is a very high energy requirement to cleave the $C_{aromatic}$-CHO bond and cannot be achieved by the low temperature

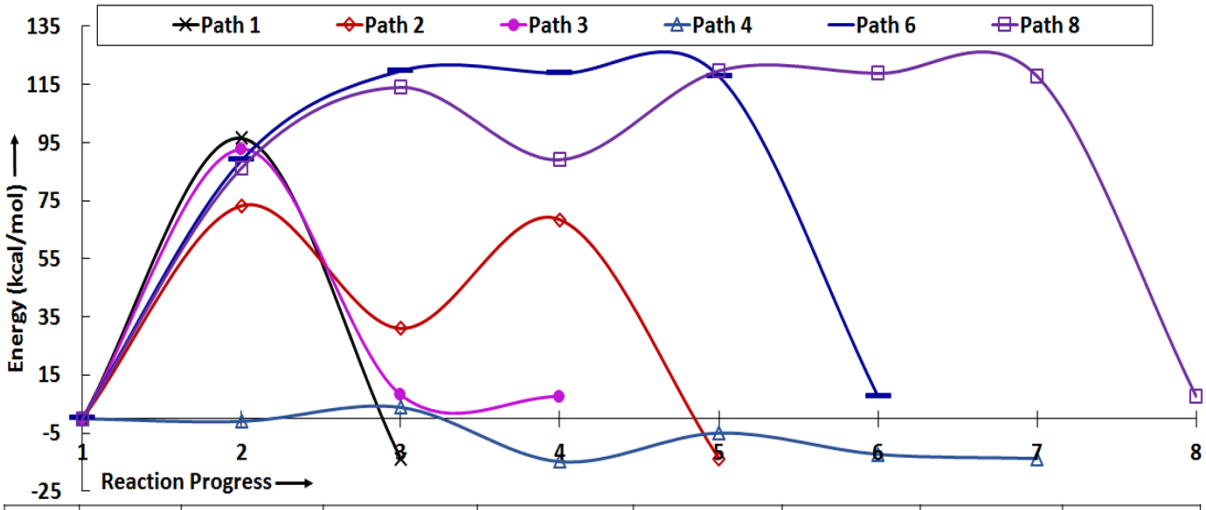

x-axis	1	2	3	4	5	6	7	8
Path 1	HMB+2H	1_a+2H+CHO	1_b+H+CHO	---	---	---	---	---
Path 2		TS2_1+2H	2_a+2H	2_b+CHO+2H	1_b+CHO+H	---	---	---
Path 3		TS3_1+2H	3_a*+2H	1_b+2H	---	---	---	---
Path 4		HMB4_*+H	TS4_1+H	4_a+H	TS4_2+H	4_b*+H	1_b+CHO+H	---
Path 6		6_a+3H	TS6_1+3H	6_b*+3H	1_a+3H+CO	1_b+2H+CO	---	---
Path 8		8_a+3H	TS8_1+3H	6_a+3H	TS6_1+3H	6_b*+3H	1_a+3H+CO	1_b+CO+2H

Figure 5.44: Potential energy surfaces of reaction pathways 1-4, 6 and 8.

pyrolysis reactions. However, after the reduction of formyl group, the lone aromatic carbon atom of structure **1_a** contracts its spatial position and forms double bonds with both neighbouring carbon atoms. In addition, the reduction of formyl group also alters the spin multiplicity of **1_a** structure because of alteration in number of electrons. In other words, the initial HMB is found in singlet spin state, whereas, after dissociation of formyl group, produced structure **1_a** is of doublet spin state. Further, to produce *m*-cresol by protonating the lone aromatic carbon atom of **1_a**, a single step hydrogenation reaction is carried out which demands a barrier height of 111.74 kcal/mol. It can be seen that the hydrogenation reaction is even energetically demanding than the formyl group reduction from HMB, therefore, the hydrogenation reaction of structure **1_a** would control the reaction rate for the formation of *m*-cresol from HMB on demand of 111.74 kcal/mol of activation energy. Therefore, the direct elimination of formyl oxy-functional group of HMB is not a favourable reaction approach to proceed and thus consequently other approaches are presented below.

Table 5.24: Activation barrier (kcal/mol) of each elementary reaction step of all reaction pathways.

Pathways	Activation Energy (E_a)			
	Step 1	**Step 2**	**Step 3**	**Step 4**
Formation of *m*-cresol from HMB				
1	98.18	111.74		
2	73.28	38.41	83.52	
3	92.77			
4	4.83	9.85		
6	90.56	30.84	111.74	
8	87.60	27.73	30.84	111.74
Formation of 2-formyltoluene from HMB				
5	6.26	18.85		
7	114.23	113.40		
Formation of 2-HB from HMB				
9	94.50	112.01		
Formation of toluene				
1	6.72	12.26		
7	84.71			
7a	4.41	9.62		

The reaction pathway 2 (RP 2) is about the hydrogen migration reaction from hydroxyl group of HMB to the aromatic carbon of $C_{aromatic}$-CHO bond as first step requires relatively lower barrier height compared to the first step of RP 1. This keto-enol tautomerization reaction occurs with a transition state structure **TS2_1** (2008.73*i* cm^{-1}) which gives a barrier height of 73.28 kcal/mol. Further, the elimination of CHO from structure **2_a** produces structure **2_b** which possesses a radical on one of the aromatic carbon. The elementary reaction step **2_a** → **2_b** requires comparatively low barrier height, i.e., 38.41 kcal/mol. Further, in order to generate *m*-cresol from structure **2_b**, a single step hydrogenation reaction is carried out which requires 83.52 kcal/mol of activation energy. It can be seen that the hydrogenation reaction of structure **2_b** determines the overall reaction rate and thus the activation energy of this reaction pathway is 83.52 kcal/mol. Clearly, this reaction approach demands significantly lower activation energy compared to RP 1 but is still quite a high activation energy demand.

On the other hand, the reaction pathway 3 (RP 3) undergoes the direct decarbonylation reaction of HMB and produces *m*-cresol without any intermediate structure. The direct decarbonylation reaction of HMB occurs with a transition state structure depicted in Figure 5.45 as **TS3_1** whose imaginary frequency is 1754.03*i* cm^{-1}. The production of *m*-cresol by reaction pathway 3 requires 92.77 kcal/mol of activation energy to surpass the barrier height. It is quite a high activation energy and even higher than the activation energy demand of reaction pathway 2 but lower than reaction pathway 1. Because of such high activation energy, the production of *m*-cresol from HMB by reaction pathway 3 is not feasible. In summary, due to such high activation energy demands, reaction pathways 1, 2 and 3 would be very slow and perhaps can only be achieved at very high temperature condition or in the presence of a suitable catalyst.

The reaction pathway 4 (RP 4) is also about the production of *m*-cresol from HMB but by a different approach compared to reaction pathways 1, 2, and 3. It initiates with the hydrogenation of the aromatic carbon atom of $C_{aromatic}$-CHO bond prior to cleave the formyl group of HMB. However, prior to hydrogenation of the phenyl ring, HMB and hydrogen atom form a reactant complex as **HMB4_*** (see Figure 5.45). The insertion of H atom into aromatic ring occurs with an activated complex **TS4_1** (778.68*i* cm^{-1}) which requires a very low barrier height of 4.83 kcal/mol for its formation. This transition state structure **TS4_1** links its two minima on the potential energy surface as **HMB4_*** as reactant and structure **4_a** as intermediate product; however, qualitatively, the formation of **TS4_1** occurs from the interaction and initiation point of reactants, i.e., HMB and a hydrogen atom. Thus, produced structure **4_a** depicts the inserted hydrogen atom in the aromatic ring which consequences the generation of a radical (see **4_a** in Figure 5.43). Further, the elimination of formyl group from structure **4_a** is carried out and this reaction occurs with a transition state structure located as **TS4_2** (511.99*i* cm^{-1}). The calculated barrier height due to the second elementary reaction step,

i.e., **4_a** → **4_b** is 9.85 kcal/mol. This barrier height is almost double compared to the first barrier height of reaction pathway 4 (RP 4); therefore, the second elementary reaction step, i.e., **4_a** → **4_b** will control the overall reaction rate at an expanse of the activation energy of 9.85 kcal/mol. It can be seen that the reaction pathway 4 requires almost 8-11 times lower activation energy compared to reaction pathways 1, 2, and 3 for the production of *m*-cresol from HMB.

Other reaction pathways which involve the production of *m*-cresol are reaction pathways 6 and 8. The reaction pathway 6 (RP 6) particulars the dehydrogenation of the formyl group of HMB as a first step. The approximated activation barrier calculated from BDE calculation for this reaction step suggests the energy requirement of 90.56 kcal/mol to achieve this bond homolysis. The removal of hydrogen atom from the formyl group generates a radical on carbon atom of C=O bond (see structure **6_a** in Figure 5.43). Further, the structure **6_a** is followed through the elimination of CO fragment at an expanse of 30.84 kcal/mol of energy. However, the elimination of CO from structure **6_a** gives rise to the structure **1_a** which is the product of direct elimination of CHO group from HMB by reaction pathway 1 (RP 1). Further, a single step hydrogenation reaction to structure **1_a** to produce *m*-cresol involves the same energetics as of discussed in reaction pathway 1, i.e., the barrier height of 111.74 kcal/mol. Thus, it should be noted that the atomic hydrogen addition reaction to structure **1_a** determines the rate of reaction pathway 6 (RP 6) and the conversion of HMB is not advocated by this reaction route. On the other hand, the reaction pathway 8 (RP 8) starts with the dehydrogenation of methyl group of HMB requiring slightly less energetics compared to the dehydrogenation of formyl group of HMB. The produced structure after dehydrogenation of methyl group of HMB can be seen in Figures 5.43 and 5.45 as structure **8_a**. Further, the radical generated on CH_2 group is saturated by migrating the hydrogen atom of the formyl group of structure **8_a**; however, the migration of hydrogen atom from formyl group to CH_2 group produces structure **6_a** (see Figure 5.43). This hydrogen migration reaction involves a transition state structure

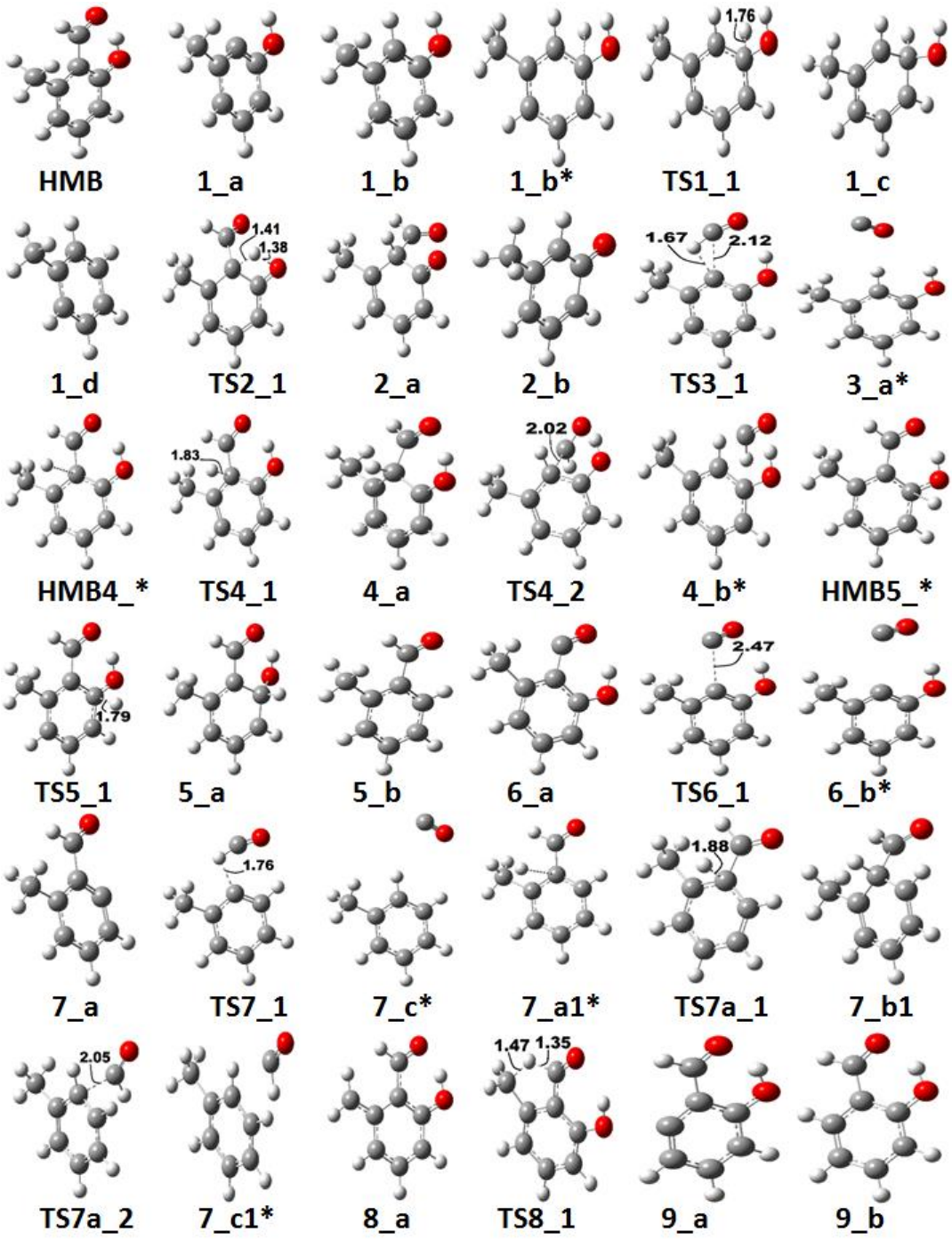

Figure 5.45: Optimized molecular structures involved in the conversion of 2-hydroxy-6-methylbenzaldehyde.

TS8_1 for which the imaginary frequency is calculated as 1798.13*i* cm^{-1}. The elementary reaction step **8_a** → **6_a** requires 27.73 kcal/mol of energy to surpass the barrier height to produce structure **6_a**. Further energetics of reaction steps, i.e., **6_a** → **1_a** and **1_a** → **1_b** follows same energetics requiring 30.84 kcal/mol and 111.74 kcal/mol, respectively, as already

described in reaction pathways 6 (RP 6) and 1 (RP 1). Finally, both reaction pathways 6 and 8 witness the same rate determining reaction step and a very high activation energy. Further, this high activation energy is same as of the reaction pathway 1 (RP 1), therefore, these two reaction pathways are also not feasible.

In summary, as discussed in 'Bond dissociation energy' subsection that the dehydrogenations of methyl and formyl groups of HMB are two least energy demanding bond scissions, the potential energy surface finds an alternative to these bond scissions and reaction pathway 4 (RP 4) found to be optimum pathway for producing *m*-cresol from HMB. The activation energy requirement by RP 4 is much lower (9.85 kcal/mol) compared to reaction pathways RP 1 (111.74 kcal/mol), RP 2 (83.52 kcal/mol), RP 3 (92.77 kcal/mol), RP 6 (111.74 kcal/mol), and RP 8 (111.74 kcal/mol) which are not likely to be attainable at moderate temperatures and without appropriate catalysts.

5.7.4. Formation of 2-formyltoluene

The reaction pathways 1-4, 6 and 8 discussed the possibility of formation of *m*-cresol as an intermediate from HMB to produce toluene as end product; however, attaining the production of toluene from HMB can also be achieved by the formation of 2-formyltoluene as an intermediate product. The production of 2-formyltoluene (FT) from HMB is discussed by RP 5 and RP 7. The potential energy surfaces of both reaction pathways are shown in Figure 5.46 and the corresponding optimized molecular structures are depicted in Figure 5.45. The activation energy of each reaction step is presented in Table 5.24.

The reaction pathway 5 (RP 5) initiates with the attachment of hydrogen atom to the aromatic carbon of $C_{aromatic}$-OH sigma bond and produces structure **5_a**. This elementary reaction step occurs with a transition state structure **TS5_1** which consequences the activation energy demand of 6.26 kcal/mol in potential energy surface; however, the minima linked to

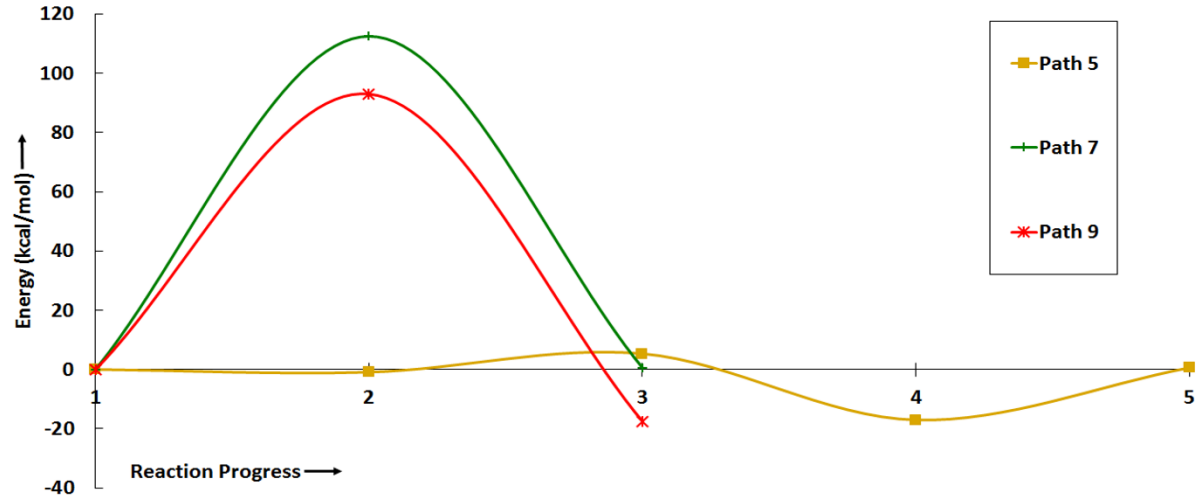

x-axis	1	2	3	4	5
Path 5	HMB+H	HMB5_*	TS5_1	5_a	5_b+OH
Path 7		7_a+H+OH	5_b+OH	---	---
Path 9		9_a+H+CH_3	9_b+CH_3	---	---

Figure 5.46: Potential energy surfaces of reaction pathways 5, 7, and 9.

TS5_1 structure are **HMB5_*** and **5_a** (see Figure 5.46). The structure **HMB5_*** is an equilibrium structure of two entities, i.e., HMB and a hydrogen atom. Further, the elimination of OH group from structure **5_a**, in this study, is reported without finding the location of transition state structure. Nevertheless, according to BDE analysis, the removal of OH group is required to have an activation energy of 18.85 kcal/mol. The activation energy (18.85 kcal/mol) due to the rate determining step of reaction pathway 5, i.e., OH elimination reaction step, is not very high and can be easily achieved at moderate temperature condition but the analysis of the direct elimination of OH group from HMB, i.e., reaction pathway 7 is highly recommended to investigate the energy differences. The reaction pathway 7 employs the direct elimination of formyl group from HMB followed by the addition of hydrogen atom to the lone aromatic carbon atom. The BDE analyses of both reaction steps, i.e., HMB → **7_a** and **7_a** → **5_b**, suggest the activation energies as 114.23 kcal/mol and 113.40 kcal/mol, respectively. Clearly, this reaction approach cannot be endorsed for the production of 2-formyltoluene because of almost 6 times higher activation energy requirement compared to that of the reaction pathway 5, therefore, the formation of FT from HMB would progress through the insertion of

hydrogen atom into phenyl ring followed by the elimination of OH group as denoted by RP 5. Finally, by comparison, it should be noted that the production of 2-formyltoluene (by RP 5) requires almost double barrier height compared to the production of *m*-cresol (by RP 4) from HMB, therefore, the conversion of HMB into lower fractions would produce *m*-cresol as intermediate if the production of 2-formyltoluene is aimed.

5.7.5. Formation of 2-hydroxybenzaldehyde

The formation of 2-hydroxybenzaldehyde (2-HB) is another possibility by the decomposition of HMB compound. Its production occurs by the cleavage of methyl group from HMB followed by a single step hydrogenation reaction. The potential energy surface and optimized molecular structures for the production of 2-HB are shown in Figures 5.46 and 5.45, respectively. The cleavage of methyl group is not advocated from HMB because of carbon element reduction but it is seen during BDE analysis that methyl group cleavage of HMB is one of the lowest energy demanding bond scissions, therefore, in the decomposition of HMB, the cleavage of methyl group would occur. The scission of methyl group of HMB requires a high activation energy of

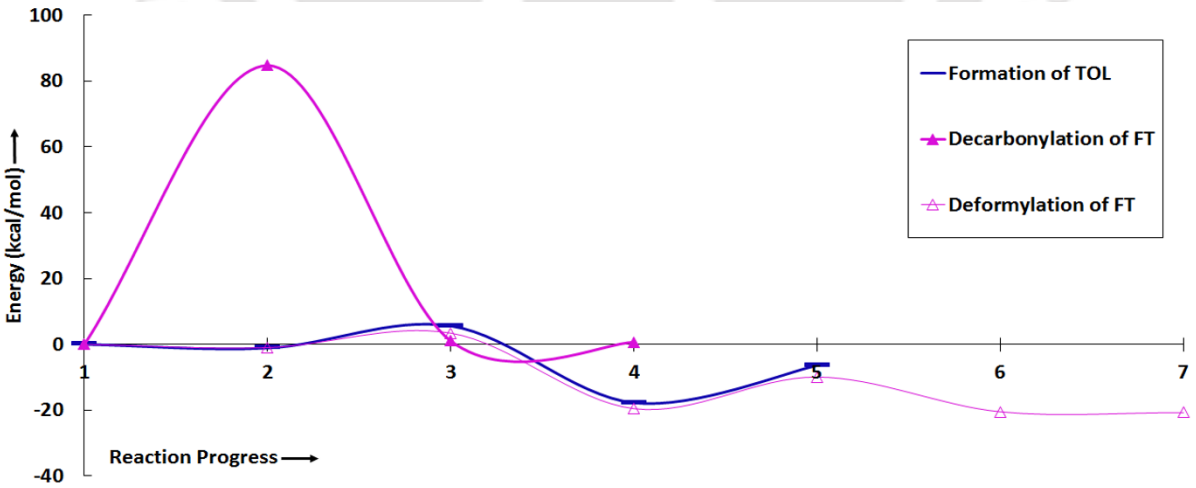

x-axis	1	2	3	4	5	6	7
——	1_b+H	1_b*	TS1_1	1_c	1_d+OH		
—▲—	5_b+H	TS7_1+H	7_c*+H	1_d+H+CO			
—△—		7_a1*	TS7a_1	7_b1	TS7a_2	7_c1*	1_d+CHO

Figure 5.47: Potential energy surfaces for the formation of toluene.

94.50 kcal/mol; whereas, the addition of H atom to lone aromatic carbon atom to produce 2-HB is even higher activation energy demanding, i.e., 112.01 kcal/mol. Thus, the activation energy for the production of 2-HB from HMB is 112.01 kcal/mol. The other possible favourable reaction pathway for the formation of 2-HB is stepwise dehydrogenation of methyl group of HMB. In this process, the very first reaction step would be the dehydrogenation of methyl group which, according to BDE analysis (see D9 in Table 2), requires 87.60 kcal/mol of activation barrier. Therefore, in either cases, the production of 2-HB from HMB is not favourable; however, high temperature decomposition may give rise to the production of 2-HB. On the other hand, the further conversion of 2-HB can be found in previous chapter that reports the activation energy for the production of benzene from 2-HB as 13.19 kcal/mol using most favourable reaction pathway. Furthermore, the hydrodeoxygenation of 2-HB component over Pd(111) catalyst surface is also detailed in the forthcoming chapter.

5.7.6. Formation of toluene

The formation of toluene is achieved from two intermediates, namely, *m*-cresol and 2-formyltoluene. The potential energy surfaces and molecular structures involved in the formation of toluene from both compounds are shown in Figures 5.47 and 5.45, respectively.

Two possible reaction pathways for the decomposition of FT into toluene considered in this study are: i) decarbonylation reaction (**5_b → 1_d**), and ii) deformylation reaction (**5_b → 7_b1 → 1_d**) of FT. The decarbonylation reaction of FT component is high kinetic demanding pathway because of high activation energy of 84.71 kcal/mol. However, the second reaction approach, i.e., deformylation reaction requires a low activation energy comparatively. The deformylation reaction of structure **5_b** initiates by the addition of H atom to the carbon of $C_{aromatic}$-CHO bond. The hydrogenation at the aromatic carbon of $C_{aromatic}$-CHO bond requires only 6.72 kcal/mol of barrier height; however, the subsequent reaction of elimination

of CHO functional from structure **7_b1** requires almost double barrier height compared to the single step hydrogenation reaction. Nevertheless, the activation energy of deformylation pathway is 12.26 kcal/mol which is very low compared to that of the direct decarbonylation reaction of FT.

On the other hand, the production of toluene component from *m*-cresol can be carried out by two elementary reaction steps, i.e., **1_b → 1_c** and **1_c → 1_d**. The elementary reaction step **1_b → 1_c** is about the addition of H atom to the carbon atom of $C_{aromatic}$-OH bond, whereas, the reaction step **1_c → 1_d** is the elimination of OH functional group requiring energy barriers of 4.41 kcal/mol and 9.62 kcal/mol, respectively. Therefore, the production of toluene from *m*-cresol would occur with an activation energy of 9.62 kcal/mol; and OH elimination reaction is overall rate controlling step.

Thus, finally the optimum reaction pathway for the production of toluene from HMB follows the reaction progress as HMB → **4_a → 1_b → 1_c → 1_d**. In other words, in the optimum reaction progress, HMB first undergoes the addition of hydrogen atom at its aromatic carbon of $C_{aromatic}$-CHO bond followed by elimination of CHO functional group. This produces *m*-cresol as an intermediate which further undergoes an addition of H atom at the aromatic carbon of $C_{aromatic}$-OH functional group followed by OH elimination reaction step. In this process, the elimination of OH functional group from structure **1_c**, i.e., the elementary reaction step **1_c → 1_d** controls the overall reaction rate for which the activation energy is 12.26 kcal/mol. This is a low activation energy compared to the pyrolysis process condition and, therefore, it can easily be achieved.

5.7.7. Thermochemistry

The thermochemical analyses of optimum reaction pathway and reaction pathway 9 are carried out at a wide range of temperature, i.e., 473-873 K at an interval temperature of 100 K. The

pressure of the system has been kept constant at 1 atm. Two thermodynamic parameters, i.e., reaction free energy (ΔG) and reaction enthalpy (ΔH) are investigated in thermochemical analysis; and all values are presented in Table 5.25. It can be seen from this table that the optimum reaction pathway is favourable even at a lower temperature of 473 K because negative values of both thermodynamic parameters. The reaction free energy and reaction enthalpy at 473 K are calculated as -32.41 kcal/mol and -18.72 kcal/mol, respectively. However, as the temperature increases from 473 K to 573 K, both parameters are seen gradually becoming more favourable because of increase in spontaneity and exothermicity. However, in general, the pyrolysis process of lignin fraction is carried out in the range of 673-873 K, therefore, analysing both thermodynamic parameters at 873 K is required, thus ΔG and ΔH are reported as -43.06 kcal/mol and -21.54 kcal/mol, respectively. It can be seen that the difference of 400 K of temperature, i.e., temperature increasing from 473 K to 873 K, both parameters significantly decrease indicating increased favourability. On the other hand, the reaction pathway 9 which produces 2-hydroxybenzaldehyde from HMB is also favourable even at lower temperature of 473 K and the temperature increment further increases the spontaneity and exothermicity of reaction. However, it is observed that compared to the thermodynamic parameters of optimum reaction pathway, the thermodynamic parameters of pathway 9 are not decent which consequences the higher conversion of HMB into toluene.

Table 5.25: Thermodynamic parameters (M = G or H) of optimum pathway for toluene production and reaction pathway 9.

Pathways	**ΔM**	**Temperature (K)**				
		473	**573**	**673**	**773**	**873**
Optimum	ΔG	-32.41	-35.24	-37.95	-40.55	-43.06
	ΔH	-18.72	-19.38	-20.09	-20.81	-21.54
9	ΔG	-22.95	-24.01	-25.02	-25.97	-26.89
	ΔH	-17.84	-18.10	-18.41	-18.75	-19.10

5.8. Molecular Simulations of Palladium Catalysed Hydrodeoxygenation of 2-Hydroxybenzaldehyde using Density Functional Theory

5.8.1. Reaction Schemes

The catalytic hydrodeoxygenation of 2-hydroxybenzaldehyde, i.e., $C_6H_4(OH)(CHO)$, in the presence of Pd(111) catalyst by four different reaction schemes (RS) is depicted in the Figure 5.48. The chemical formulae of components are given below each structure and the reaction number is depicted using Arabic numerals. The process starts by the adsorption of 2-HB from gas phase to the catalyst surface followed by four possible pathways. These four possible pathways in Figure 5.48 represent, respectively, from left to right, dehydrogenation of formyl group of 2-HB (RS 1), cleavage of formyl group (RS 2), cleavage of hydroxyl group (RS 3), and dehydrogenation of hydroxyl group of 2-HB (RS 4). Further, the structure $C_6H_4(OH)(CO)^*$ of RS 1 undergoes the elimination of CO to form $C_6H_4(OH)^*$ which further follows the hydrogenation reaction to form phenol component. On the other hand, the formed structure $C_6H_4(OH)^*$ due to formyl group cleavage of 2-HB is made to remain unaffected, however, the dehydrogenation of adsorbed formyl group is carried out for production of phenol compound. The desorption of phenol from the catalyst surface to the gas phase is indicated by numeral 6 in Figure 5.48 and, further adsorption of phenol is carried out using most stable configuration to proceed to reaction path 8 shown in the figure. The hydroxyl group cleavage of phenol component produces $C_6H_5^*$ structure which further associates with a hydrogen atom to form benzene (see reaction numbers 8 and 9, respectively). The benzene component is then desorbed into the gas phase through desorption process 10 shown in the figure. On the other hand, the reaction numbers 14 and 23 produced $C_6H_4(CHO)^*$ and $C_6H_4(O)(CHO)^*$, respectively. The structure $C_6H_4(CHO)^*$ associates with a hydrogen atom and forms benzaldehyde component,

whereas, structure $C_6H_4(O)(CHO)^*$ undergoes the oxygen atom elimination reaction and merges to the structure $C_6H_4(CHO)^*$. The benzaldehyde component can be desorbed to gas phase at this stage but additional conversion is still required, therefore, benzaldehyde component follows two pathways for its conversion, i.e., i) dehydrogenation of formyl group followed by the removal of CO to form the structure $C_6H_5^*$, and ii) the cleavage of whole

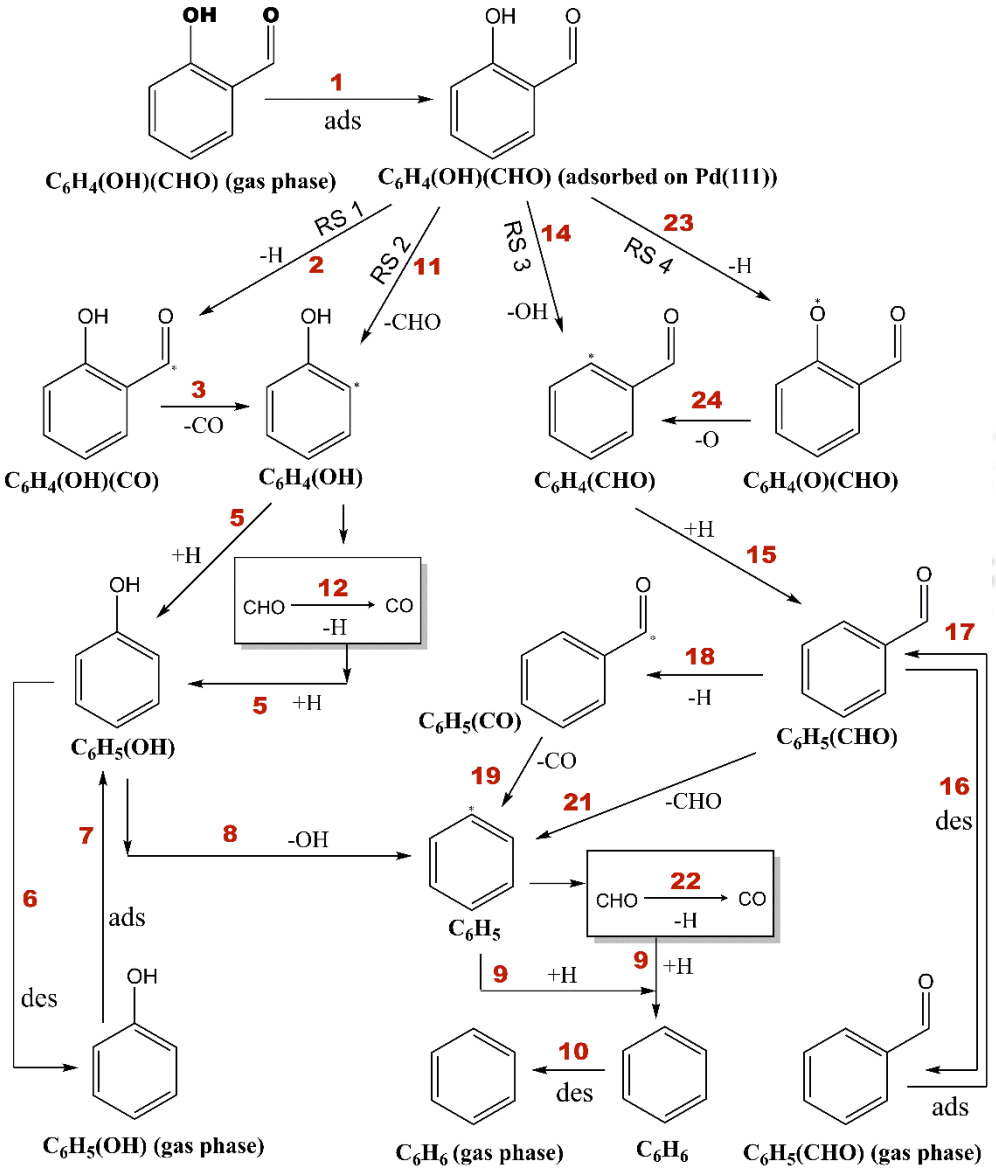

Figure 5.48: The reaction schemes of conversion of 2-hydroxybenzaldehyde on Pd(111) catalyst surface. The notations 'ads' and 'des' are representing adsorption and desorption of species from gas phase and catalyst surface, respectively. Red Arabic numerals represent elementary reaction step number.

formyl group to form the structure $C_6H_5^*$ directly followed by the dehydrogenation of adsorbed formyl group. The formation of benzene is same in both phenol and benzaldehyde conversion processes.

The reaction mechanisms shown in Figure 5.48 are numerically performed over Pd(111) catalyst. The catalyst cluster model is designed using 12 palladium atoms in a plane (see Figure 4.2). Stability analyses of the catalyst model (see Table 4.1) reveal the ground state in septet spin multiplicity. The applied level of theory for all quantum chemical calculations is B3PW91 under density functional theory framework. The basis set for C, H, and O atoms is chosen as 6-311+g(d,p), whereas, LANL2DZ basis set is designated for Pd atoms.

Before discussing the potential energy surfaces of reaction schemes depicted in Figure 5.48, it is necessary to understand the adsorption behaviours and modes of 2-HB over the proposed Pd(111) catalyst cluster model. Several adsorption configurations obtained by the optimization simulations keeping Pd atoms fixed as shown in Figure 5.49; and configuration '3' is found as most stable configuration. The relative adsorption energies of all configurations are presented in Table 5.26. Further, the spin state analysis is carried out for the configuration '3' and the ground state structure lies in septet state (see Table 5.27). It is observed in the literature [44, 45] that molecules with phenyl ring usually adsorbs in four configurations, namely, *atop*, *hcp*, *fcc*, and *bridge* on a given type of Metal(111) surface. In the case of adsorption of 2-HB over Pd(111), it is reported that the structure '3' of 2-HB is most stable and it lies parallely on the Pd(111) surface with bridge 30^o configuration. It may adsorb with other orientations of *bridge* site as well, i.e., bridge 0^o, but the ground state of 2-HB occurs in bridge 30^o orientation. The movement of the substrate to the border of the cluster is common in such studies. The metal atoms that are in the border of the cluster have a high acidic character and usually interact strongly with the substrate [130, 153]. The substrate moves to the direction of the metal atoms with lower coordination number but all carbon atoms of the benzenoid ring

Table 5.26: Relative adsorption energies (kcal/mol) of various configurations of 2-HB.

Structure	1	2	3	4	5	6
Relative E_{ads}	13.2	12.5	0.0	14.2	11.1	10.2

Table 5.27: Spin multiplicities and relative energies (kcal/mol) of configuration '3' of 2-HB.

SM	1	3	5	7	9	11
Relative E	17.2	6.0	1.5	0	15.1	32.3

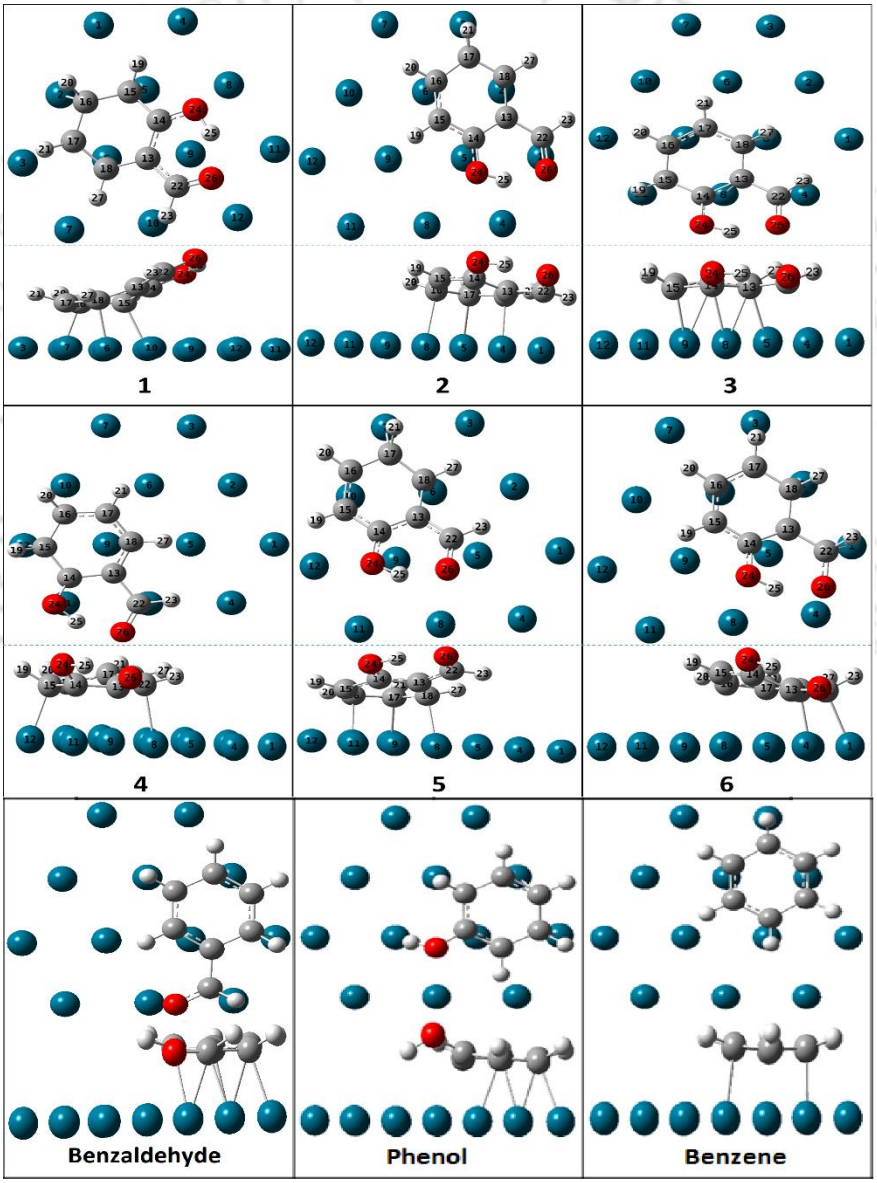

Figure 5.49: Adsorption configurations of 2-hydroxybenzaldehyde and other aromatic species on 12 atom-Pd(111) catalyst surface.

are still interacting with the metal cluster [130, 153]**.** The average Pd-C bond distance in the ground state structure of 2-HB over Pd(111) surface is ~2.15 Å. The longer bond distances between the surface metal atoms and the substrate usually suggest weaker adsorption and thus weaker interaction between the surface and substrate. Further, the bond distances of $C_{aromatic}$-OH and $C_{aromatic}$-CHO of adsorbed 2-HB are 1.32 Å and 1.48 Å, respectively, whereas, the corresponding distances in gas phase optimized 2-hydroxybenzaldehyde are reported as 1.33 Å and 1.45 Å, respectively. In addition, all hydrogen atoms linked to the ring bend away from the surface upon adsorption. It can be seen from the configuration '3' of 2-HB (Figure 5.49) that C(15) and C(18) labelled carbon atoms are σ-bonded to the corresponding Pd metal atoms. On the other hand, the carbon atoms labelled as C(14)-C(13) and C(16)-C(17) share the metal atoms with π-bonding modes. The adsorption energy of configuration '3' is -31.84 kcal/mol in septet spin multiplicity; and, the relative adsorption energies of other spin states are depicted in Table 5.27. The adsorption energies of other important intermediates such as phenol, benzaldehyde, and benzene are reported in Table 5.28. Further, the xyz coordinates, electronic energy, and zero point vibrational energy (ZPVE) of all adsorbed species such as 2-HB, phenol, benzene, and benzaldehyde are provided in Appendix Table 2.

The adsorption configuration and energy of phenol can be seen in Figure 5.49 and Table 5.28, respectively. The ground state of phenol over Pd(111) lies in quintet spin state. The adsorption of phenol over present Pd(111) catalyst model occurs in bridge 30^{o} orientation with calculated adsorption energy of -31.21 kcal/mol; and it is in very good agreement with the adsorption energy value of phenol over bulk Pd(111) reported by Orita and Itoh [154]. The average Pd-C bond length is found as ~2.17 Å which suggests very strong interaction between catalyst surface and adsorbate. On the other hand, $C_{aromatic}$-O bond distance in adsorbed phenol over present Pd(111) surface is found as 1.38 Å which is also in very good agreement with $C_{aromatic}$-O bond length of 1.37 Å bond length reported by Li et al. [155]. Furthermore, the bond

Table 5.28: Comparison of adsorption energies of various adsorbed components on Pd(111) surface.

Structures	E_{ads} (kcal/mol)	Literature (kcal/mol)
2-HB	-31.84	---
Phenol	-31.21	-32.05 (bri30^o) [154]
Benzaldehyde	-37.30	---
Benzene	-33.0	-35.81 (bri30^o) [154]

length between nearest Pd atom and oxygen atom is found as 2.78 Å with all hydrogen atoms of phenyl ring inclined away from the catalyst surface; however, the hydrogen atom attached to hydroxyl group is attracted towards the catalyst surface. Similarly, the adsorption of benzene (see Figure 5.49) over Pd(111) catalyst surface is stable in bridge 30^o configuration with the adsorption energy of -35.81 kcal/mol. The adsorption of benzene over bulk Pd(111) catalyst surface is performed by Orita and Itoh [154] and they also found that benzene molecule binds most stably in bridge 30^o orientation with adsorption energy of -33.0 kcal/mol. The differences in the energetics may be originating from the cluster size and symmetry; however, the difference between present E_{ads} and literature results does not deviate much (see Table 5.28). In the literature [154] and in the present work, it is found that the bridge 30^o orientations of 2-HB, phenol, benzene, and benzaldehyde are most stable orientations, therefore, all subsequent conversions are discussed based on these initial structures.

The notations of molecular structures in Figures 5.50-5.54 are specified as **X_Y**; where **X** and **Y** are reaction scheme number and molecular structure number in that particular reaction scheme, respectively. For instance, structure **1_4** is molecular structure number 4 of reaction scheme 1. Similarly, transition state structures are denoted as **TSA_B**; where **A** and **B** are reaction scheme number and transition state structure number in that particular reaction scheme, respectively. For example, **TS4_2** is second transition state structure of reaction scheme 4.

5.8.2. Formation of Phenol on Pd(111)

The formation of phenol from 2-HB by dehydrogenation of formyl group of 2-HB (RS 1) and removal of formyl group cleavage itself from 2-HB (RS 2) is discussed in this subsection. The potential energy surfaces for the conversion of 2-HB into phenol using reaction schemes 1 and 2 are depicted in Figure 5.50; and the corresponding optimized molecular structures involved in these two pathways are shown in Figure 5.51. Figure 5.50 demonstrates the reaction progress of each reaction scheme with corresponding electronic energies of involved molecular structures. The **TSX_Y** notations in Figure 5.50 are first order saddle points on potential energy surface which link their respective minima structures through minimum energy path. For instance, the first order saddle point **TS1_1** link 2-HB and **1_1** as its reactant and product through minimum energy path. The interatomic distances in transition state structures in Figure 5.51 are presented in angstrom (Å). The adsorption/desorption energies, barrier heights, imaginary frequencies corresponding to transitions state structure of reaction, and reaction energies are presented in Table 5.29. In addition, the forward reaction rate constants (s^{-1}) at 1 atm and a wide range of temperature 498-698 K are also shown in Table 5.29. The pre-exponential factors of Arrhenius equations and equilibrium constants at mentioned temperature range are listed in Table 5.30.

The adsorption of 2-HB on the Pd(111) metal surface is barrierless exothermic reaction step with adsorption energy of -31.84 kcal/mol. Further, the hydrogen atom of CHO part of 2-HB gets activated and its elimination from the formyl group of $C_6H_4(OH)(CHO)$ to form $C_6H_4(OH)(CO)^*$ requires a calculated barrier height of 18.21 kcal/mol (see Figure 5.50). The B3PW91 functional optimized co-adsorbed species $C_6H_4(OH)(CO)^*$ and adsorbed H atom on Pd(111) surface are depicted by the structure **1_1** in Figure 5.51. The carbon atom of formyl group after the elimination of hydrogen atom binds with the Pd metal atom while the adsorbed

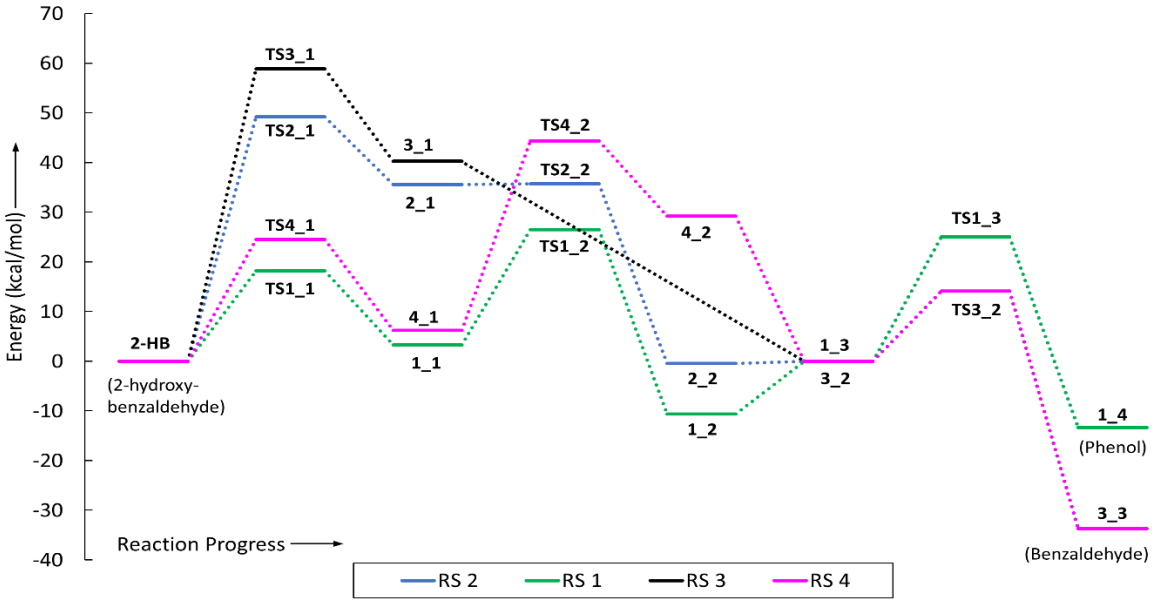

Figure 5.50: Potential energy surface for the conversion of 2-hydroxybenzaldehyde over Pd(111) surface using reaction schemes 1-4. The components 2-hydroxybenzaldehyde, phenol, and benzaldehyde are adsorbed species over Pd(111) surface.

hydrogen atom interacts with two metal atoms in the bridge configuration. The C-C bond distance of $C_{aromatic}$-CO of adsorbed structure $C_6H_4(OH)(CO)^*$ remains almost same as of the C-C bond distance in adsorbed $C_{aromatic}$-CHO of $C_6H_4(OH)(CHO)$, i.e., 1.32 Å, but the bond length $C_{aromatic}$-OH increases to 1.34 Å upon dehydrogenation of formyl group forming adsorbed $C_6H_4(OH)(CO)^*$. Similar to the structure **1_1**, the transition state structure for this reaction is denoted as **TS1_1** in Figure 5.51 which shows the bonding patterns between H and Pd(111) surface; and $C_6H_4(OH)(CO)^*$ and Pd(111) surface. The imaginary frequency of **TS1_1** is 1047.52*i* cm^{-1}. Although, this elementary reaction step requires less energy barrier but it is slightly unfavourable thermodynamically (see ΔE in Table 5.29). The structure $C_6H_4(OH)(CO)^*$ (structure **1_1**) undergoes the cleavage of CO from the ring and it occurs with a barrier height of 23.24 kcal/mol. The cleaved CO adsorbs in the bridge configuration with the attachment of carbon atom to two surface metal atoms with Pd-C bond distances of 1.92 Å and 2.13 Å, respectively. On the other hand, the carbon atom of 2-hydroxyphenyl bonds with

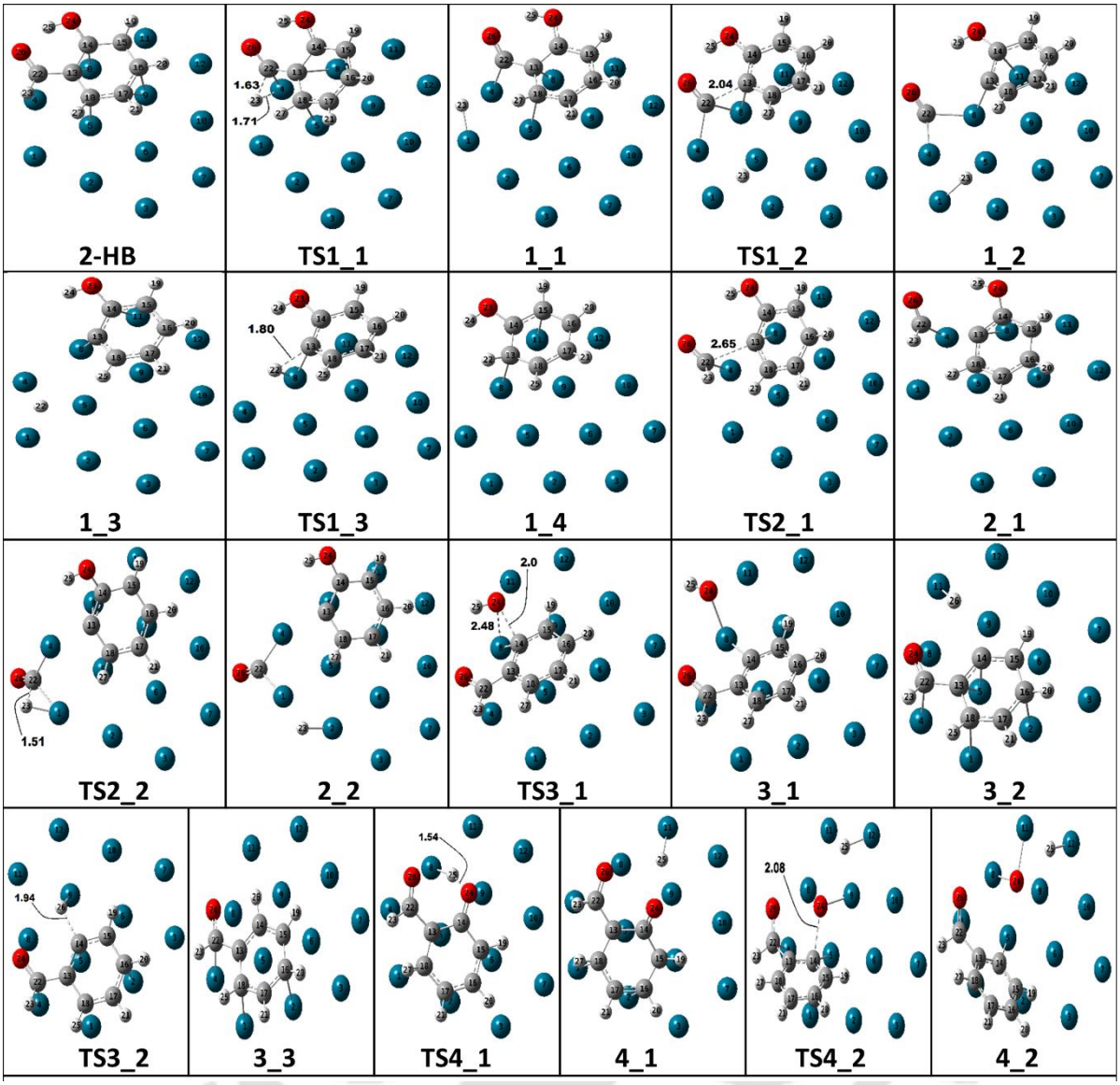

Figure 5.51: Structures involved in productions of phenol and benzaldehyde from 2-HB on Pd(111) catalyst surface.

nearest surface metal atom with 2.09 Å distance between them. The transition state structure, **TS1_2** (412.53*i* cm^{-1}), for this reaction is shown in Figure 5.51 where the equilibrium $C_{aromatic}$-CO bond distance states as 2.04 Å. The dissociation of CO from $C_6H_4(OH)(CO)^*$ is thermodynamically possible because of a significant amount of energy release upon CO dissociation (ΔE = -9.97 kcal/mol); however, the activation barrier is ~5 kcal/mol higher compared to the activation barrier of dehydrogenation of formyl group of 2-HB. Further, desorption of CO molecule is carried out to vacate the surface active sites for further reactions

and desorption energy for the same is 25.18 kcal/mol. Subsequently, after CO removal, an adsorbed hydrogen atom and $C_6H_4(OH)^*$ proceed to the formation of phenol. The adsorbed phenol after hydrogen association reaction to 2-hydroxyphenyl is in bridge 30^o configuration with all hydrogen atoms attached to the ring are tilted away from the surface. The activated complex for this minimum energy path is located as **TS1_3** (1138.32*i* cm^{-1}) in which the equilibrium bond distance between adsorbed H atom and non-hydrogen $C_{aromatic}$ of 2-hydroxyphenyl is 1.80 Å (see Figure 5.51) and the angle between H_{adatom}-Pd-$C_{aromatic}$ is found as 58.03^o. The barrier height and the reaction energy for the formation of phenol from the hydrogenation of 2-hydroxyphenyl are calculated as 25.05 kcal/mol and -13.32 kcal/mol, respectively. The formation of phenol from association of adsorbed H atom to 2-hydroxyphenyl is slightly more activation barrier demanding than the CO cleavage reaction from $C_6H_4(OH)(CO)^*$; however, it is more favourable elementary reaction step compared to CO cleavage process. Due to higher activation barrier, the association reaction of adsorbed H atom to 2-hydroxyphenyl controls overall reaction and therefore, can be recognized as rate determining reaction step for the production of phenol from 2-hydroxybenzaldehyde over Pd(111) surface. However, the kinetic analyses for this reaction step will explore the favourability condition of this reaction which is discussed in the 'Kinetic Modelling' subsection.

The reaction scheme 2 initiates with the direct cleavage of formyl group from $C_6H_4(OH)(CHO)$ with a calculated energy barrier of 49.23 kcal/mol. It can be seen in structure **2_1** (Figure 5.51) that formyl functional adsorbs on surface metal atom bonded with carbon atom. The bond length between Pd and carbon of CHO is 1.91 Å, whereas, the bond distance between Pd and non-hydrogen carbon atom of ring structure is reported as 1.99 Å. Similarly, the bond length of $C_{aromatic}$-CHO in **TS2_1** (413.11*i* cm^{-1}) is 2.65 Å which extends further to 2.73 Å as the transition state structure undergoes for product formation. This elementary

reaction step cannot be favourable reaction because of such high activation barrier which cannot be achieved at low temperature conditions. The equilibrium constant at high temperature presented in the kinetic modelling section will clarify the abundance of product in product mixture. Moreover, the elimination of CHO group from $C_6H_4(OH)(CHO)$ is not energy releasing reaction step as the reaction energy for this is significantly positive, i.e., 35.59 kcal/mol. The elimination of hydrogen atom from adsorbed CHO part requires a considerably less barrier height, i.e., 0.16 kcal/mol and it can be seen in structure **2_2** (see Figure 5.51) that H atom gets dissociated from CHO and adsorbed to the next surface metal atom. Then, the carbon atom of CO after dissociation of H from CHO interacts with two surface atoms forming bridge configuration. Afterwards, the CO is desorbed into gas phase in order to vacate the active surface sites of Pd(111). The desorption of CO from structure **2_2** is more energy demanding compared to the desorption of CO from structure **1_2**; however, this difference in energetics stems from the spatial changes of structures because structure **2_2** binds tightly with the catalyst surface that is why it requires more energy to desorb into gas phase. Further, the formation of phenol from hydrogenation reaction of 2-hydroxyphenyl is same as of reaction scheme 1, i.e., with barrier height of 25.05 kcal/mol. Clearly, this reaction approach for the formation of phenol is highly kinetic demanding approach because it requires 24.18 kcal/mol more activation energy than the reaction scheme 1 which is the elimination of hydrogen from formyl group of 2-HB followed by the CO cleavage reaction from $C_6H_4(OH)(CO)^*$ and hydrogenation reaction to $C_6H_4(OH)^*$ to produce the phenol component.

It is clear that the phenol production from 2-HB using reaction scheme 1, i.e., dehydrogenation of formyl group followed by CO elimination and association of H atom to 2-hydroxyphenyl is favourable compared to the reaction scheme 2. The rate determining step for the conversion of 2-HB to phenol under reaction scheme 1 is recognised as the reaction step 5 which is the association of hydrogen atom to 2-hydroxyphenyl; and, the activation energy for

Table 5.29: The adsorption/desorption energies (E_{ads}/E_{des}), activation energies (E_a), reaction energies (ΔE), imaginary frequencies of transition states (υ), and reaction rate constants (k_f) of each elementary reaction step. The desorption energies are the ones which are positive in E_{ads}/E_{des} column.

R. No.		Reaction Steps	E_{ads}/E_{des}	E_a	ΔE	υ	k_f (s^{-1}) at 1 atm				
			(kcal/mol)			(cm^{-1})	498 K	548 K	598 K	648 K	698 K
1	RS 1	$C_6H_4(OH)(CHO)$ (g) + * → $C_6H_4(OH)(CHO)$*	-31.84	---	---	---	---	---	---	---	---
2		$C_6H_4(OH)(CHO)$* + * → $C_6H_4(OH)(CO)$* + H*	---	18.21	3.27	1047.52*i*	1.12E+05	6.64E+05	2.95E+06	1.05E+07	3.14E+07
3		$C_6H_4(OH)(CO)$* + * → $C_6H_4(OH)$* + CO*	---	23.24	-9.97	412.53*i*	1.33E+03	1.26E+04	8.20E+04	4.02E+05	1.57E+06
4		$C_6H_4(OH)$* + CO* → $C_6H_4(OH)$* + * + CO (g)	25.18	---	---	---	---	---	---	---	---
5		$C_6H_4(OH)$* + H* → $C_6H_5(OH)$* + *	---	25.05	-13.32	1138.32*i*	1.32E+02	1.44E+03	1.05E+04	5.68E+04	2.41E+05
6		$C_6H_5(OH)$* → $C_6H_5(OH)$ (g) + *	31.11	---	---	---	---	---	---	---	---
7	Phenol	$C_6H_5(OH)$ (g) + * → $C_6H_5(OH)$*	-31.21	---	---	---	---	---	---	---	---
8		$C_6H_5(OH)$* + * → C_6H_5* + OH*	---	50.92	35.48	350.99*i*	7.87E-10	9.67E-08	5.34E-06	1.60E-04	2.94E-03
9		C_6H_5* + H* → C_6H_6* + *	---	16.72	-26.38	1370.38*i*	1.43E+05	7.08E+05	2.69E+06	8.36E+06	2.21E+07
10		C_6H_6* → C_6H_6 (g) + *	26.62	---	---	---	---	---	---	---	---
11	RS 2	$C_6H_4(OH)(CHO)$* + * → $C_6H_4(OH)$* + CHO*	---	49.23	35.59	413.11*i*	5.24E-08	5.94E-06	3.09E-04	8.79E-03	1.56E-01
12		$C_6H_4(OH)$* + CHO* + * → $C_6H_4(OH)$* + CO* + H*	---	0.16	-36.05	604.74*i*	2.05E+13	2.36E+13	2.68E+13	3.01E+13	3.35E+13
13		$C_6H_4(OH)$*+CO*+H* → $C_6H_4(OH)$*+H*+*+CO(g)	30.64	---	---	---	---	---	---	---	---
14	RS 3	$C_6H_4(OH)(CHO)$* + * →$C_6H_4(CHO)$* + OH*	---	58.90	40.28	322.02*i*	1.60E-12	4.23E-10	4.42E-08	2.26E-06	6.62E-05
15		$C_6H_4(CHO)$* + H* → $C_6H_5(CHO)$* + *	---	14.13	-33.73	619.08*i*	3.40E+06	1.32E+07	4.09E+07	1.06E+08	2.42E+08
16		$C_6H_5(CHO)$* → $C_6H_5(CHO)$ (g) + *	37.30	---	---	---	---	---	---	---	---
17	Benzaldehyde	$C_6H_5(CHO)$ (g) + * → $C_6H_5(CHO)$*	-37.30	---	---	---	---	---	---	---	---
18		$C_6H_5(CHO)$* + * → $C_6H_5(CO)$* + H*	---	17.01	2.79	768.35*i*	1.14E+05	5.97E+05	2.39E+06	7.76E+06	2.14E+07
19		$C_6H_5(CO)$* + H* + * → C_6H_5* + H* + CO*	---	16.29	-3.89	487.29*i*	8.08E+05	4.04E+06	1.56E+07	4.91E+07	1.32E+08
20		C_6H_5* + H* + CO* → C_6H_5* + H* + * + CO (g)	32.79	---	---	---	---	---	---	---	---
21		$C_6H_5(CHO)$* + * → C_6H_5* + CHO*	---	47.93	36.12	347.09*i*	1.81E-08	1.71E-06	7.61E-05	1.89E-03	2.99E-02
22		C_6H_5* + CHO* + * → C_6H_5* + CO* + H*	---	0.42	-37.27	559.27*i*	3.49E+12	3.80E+12	4.08E+12	4.36E+12	4.62E+12
23	RS 4	$C_6H_4(OH)(CHO)$* + * → $C_6H_4(O)(CHO)$* + H*	---	24.53	6.23	538.82*i*	4.94E+02	5.39E+03	3.97E+04	2.17E+05	9.35E+05
24		$C_6H_4(O)(CHO)$* + * → $C_6H_4(CHO)$* + O*	---	44.39	29.20	354.11*i*	1.45E-06	1.02E-04	3.54E-03	7.21E-02	9.61E-01

the same is reported to be 25.05 kcal/mol. In the previous Chapter 5.5, the activation energy of direct decarbonylation reaction of 2-HB to produce phenol in the absence of catalyst was reported as 92.49 kcal/mol. In addition, the rate determining step for the production of phenol from 2-HB using the current reaction scheme 1 was found as the association reaction of hydrogen atom to 2-hydroxyphenyl; however, that reaction was performed in the absence of catalyst with activation energy of 112.06 kcal/mol.

The rate controlling reaction step for RS 2, though it is not favourable, is reaction step 11 for which the activation energy is 49.23 kcal/mol. Due to such a high activation energy, this rate determining reaction step is highly foreseeable as very slow reaction.

5.8.3. Formation of Benzaldehyde on Pd(111)

The formation of benzaldehyde from 2-HB over Pd(111) surface is shown as RS 3 and RS 4. RS 3 is about direct dehydroxylation reaction (reaction step 14) followed by hydrogenation of 2-formylphenyl to form benzaldehyde (reaction step 15). RS 4 describes the dehydrogenation of hydroxyl group (reaction step 23) followed by cleavage of oxygen atom (reaction step 24) and hydrogenation of 2-formylphenyl to form benzaldehyde (reaction step 15), respectively. The potential energy surfaces for reaction schemes 3 and 4 are depicted in Figure 5.50; and, the corresponding molecular structures are shown in Figure 5.51. The imaginary frequencies of transition state structures involved in reaction schemes 3 and 4 and the barrier heights of each elementary reaction step are shown in Table 5.29.

The hydrodeoxygenation (HDO) process of alcohol group containing bio-oil compounds occur *via* direct C-O cleavage reaction due to hydrogen gas in the presence of catalytic system; and, the resultant cleaved alcohol group associates with hydrogen atom using polar covalent bonding to produce water compound [1, 55, 56]. However, the H dissociation

of OH group of 2-HB followed by the cleavage of oxygen atom of $C_6H_4(O)(CHO)^*$ is also carried out in order to compare the barrier heights with direct OH removal process. The direct dehydroxylation reaction of 2-HB over Pd(111) surface is very high energy demanding pathway with 58.90 kcal/mol of energy barrier. It is because of the difficult ring stabilization after $C(sp^2)$−O bond cleavage. Furthermore, it is highly unfavourable reaction because of the calculated reaction energy of 40.28 kcal/mol. Therefore, under conventional conditions, it may not follow the forward path or in other words, the probability of product formation is very low. The intermediate structure **3_1** (see Figure 5.51) depicts the co-adsorption of OH and 2-formylphenyl on the Pd(111) surface. The first order saddle point (**TS3_1**) can be seen in Figure 5.51 for the direct dehydroxylation reaction for which the imaginary frequency (υ) is 322.02i cm^{-1}. The hydroxyl group with oxygen atom interacting with the catalyst surface and 2-formylphenyl over catalyst surface are at equilibrium (see **TS3_1** in Figure 5.51) condition. The distance between $C_{aromatic}$ and OH is increased beyond the normal C-O bond distance thus attained a high energy state in minimum energy path which locates two minima as **2-HB** and structure **3_1** (see Figure 5.50). Further, the hydroxyl functional is desorbed from the surface and a hydrogen atom is adsorbed to bond with adsorbed 2-formylphenyl over the catalyst surface. The association of adsorbed hydrogen atom with 2-formylphenyl to produce benzaldehyde requires considerably less barrier height, i.e., 14.13 kcal/mol and it is significantly high energy releasing reaction as the reaction energy is -33.73 kcal/mol. Thus formed benzaldehyde itself is an important compound and can be used extensively as an intermediate product in industries, therefore, the desorption of benzaldehyde is carried out and it is a high energy consuming process because it requires 37.30 kcal/mol of energy to shift from catalyst surface in to the gas phase. In other words, the benzaldehyde component binds very tightly to the Pd(111) surface compared to 2-HB. It can be seen that this approach for the production of benzaldehyde from 2-HB over Pd(111) surface is highly kinetic demanding,

therefore, another approach (i.e., RS 4) needs to be unravelled. Nevertheless, another approach for the production of benzaldehyde is the dehydrogenation of hydroxyl group, in RS 4, for which the barrier height is 24.53 kcal/mol (see Figure 5.50); and, it is slightly endothermic reaction. The oxygen atom of the OH group tilts away from the surface after dissociation of hydrogen atom due to repelling force. The bond distance between nearest Pd surface metal atom and oxygen is reported as 3.43 Å and Pd-H bond length is 1.64 Å. The transition state structure **TS4_1** (538.82*i* cm^{-1}) shows the stretch movement of H atom from oxygen to the surface metal atom. Further, $C_{aromatic}$-O cleavage reaction of $C_6H_4(O)(CHO)^*$ requires approximately double barrier height compared to the dehydrogenation of hydroxyl group of 2-HB with considerably high endothermicity compared to the first step of RS 4. Subsequent step of the formation of benzaldehyde from 2-formylphenyl is same as of RS 3 with an energy barrier of 14.13 kcal/mol.

It is observed that the formation of benzaldehyde using both RS 3 and RS 4 is not thermodynamically feasible; however, RS 4 requires 14.51 kcal/mol less activation energy than RS 3. It can also be seen that each elementary reaction step of both reaction schemes except hydrogenation reaction to 2-formylphenyl to form benzaldehyde is not favourable. The formation of benzaldehyde from 2-HB using reaction scheme 4 (dehydrogenation of hydroxyl group of 2-HB followed by oxygen atom elimination and association of H atom to 2-formylphenyl) is more advantageous than RS 3 (direct dehydroxylation of 2-HB followed by addition of H atom to 2-formylphenyl). The rate controlling step of RS 4 is recognised as the oxygen atom cleavage from $C_6H_4(O)(CHO)^*$ for which the activation barrier is 44.39 kcal/mol. Apart from not being favourable, the rate controlling step for RS 3 is found as hydroxyl group cleavage reaction step (reaction step 14) and the activation energy for the same is 58.90 kcal/mol. The activation energies of both reaction schemes 3 and 4 are very high and cannot be achieved at low temperature conditions, therefore, the dissociation of 2-HB to lower

fractions using reaction schemes 3 and 4 does not seem favourable. As per Chapter 5.5, the production of benzaldehyde from 2-HB using current reaction scheme 3 required activation energy of 114.24 kcal/mol in the absence of catalyst.

5.8.4. Conversion of Phenol

As discussed earlier, the reaction schemes 1 and 2 produce phenol which is an important intermediate and can be utilised in several ways but further conversion of phenol to produce aromatic hydrocarbon is also considered to analyse the major end product of 2-HB over Pd(111) surface. The desorption of phenol required an energy of 31.11 kcal/mol; however, further adsorption study of phenol (see **Phe** structure in Figure 5.51) reveals that it could be adsorbed in even stable configuration. In this case, adsorption of phenol occurs with adsorption energy of -31.21 kcal/mol through bridge 30^{o} configuration with the Pd(111) surface. The PES of the production of benzene from phenol over Pd(111) surface is depicted in Figure 5.52; and the corresponding molecular structures are shown in Figure 5.53. The interatomic distances in transition state structures of Figure 5.53 are depicted in angstrom units and the imaginary frequencies corresponding to the transition states structures are reported in Table 5.29.

There are various approaches to produce benzene from phenol, for instance, i) direct dehydroxylation followed by hydrogenation reaction to phenyl ring; ii) partial hydrogenation to the carbon atom of $C_{aromatic}$-OH followed by dehydroxylation reaction; iii) migration of H of OH functional to the carbon atom of $C_{aromatic}$-O followed by the cleavage of oxygen atom; and iv) dissociation of H of OH functional to produce phenoxy followed by cleavage and association of oxygen and hydrogen atoms, respectively, from phenoxy and to phenyl. The conversion of phenol is considered using direct dehydroxylation route to cleave hydroxyl group which can be hydrogenated to produce water compound. The present procedure is constructive pathway for production of benzene from phenol, in the context of bio-oil HDO process, comp-

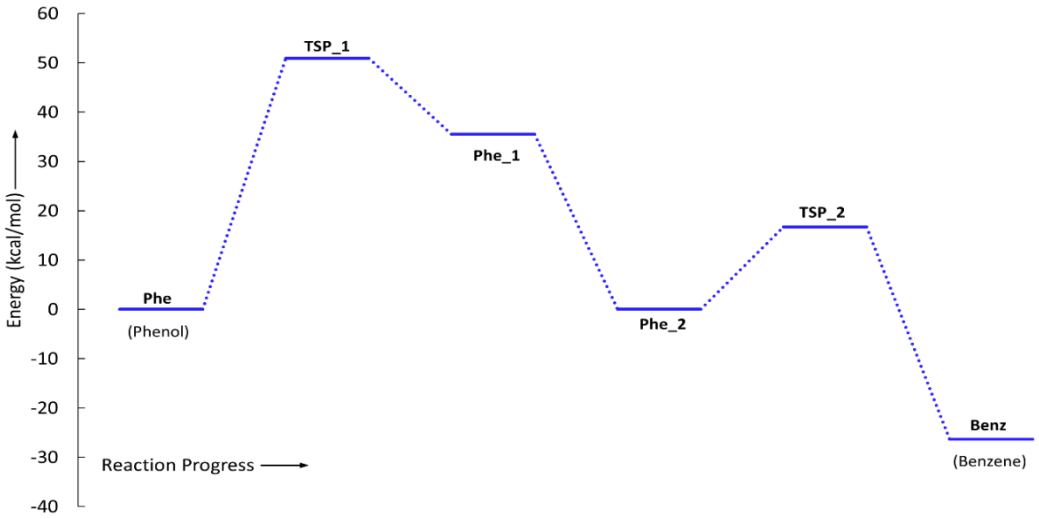

Figure 5.52: Potential energy surface for the formation of benzene from phenol over Pd(111) catalyst surface. The phenol (reactant) and benzene (product) structures in PES are adsorbed structure on Pd(111) catalyst surface.

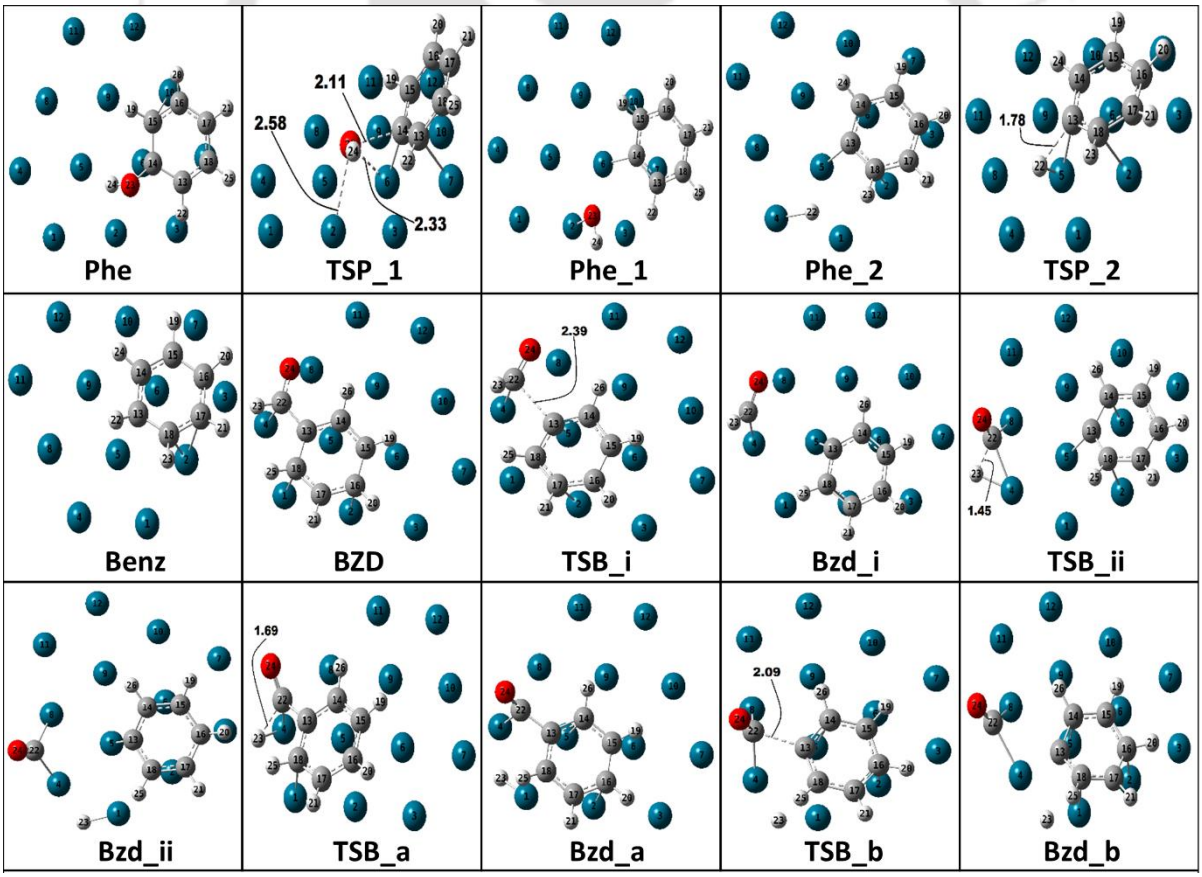

Figure 5.53: Structures involved in the production of benzene from phenol and benzaldehyde on Pd(111) catalyst surface.

-ared to the second approach of benzene production from phenol on Ru(0001) system [44]. Therefore, the cleavage of $C_{aromatic}$-OH bond of phenol is carried out and it requires an energy barrier of 50.92 kcal/mol on Pd(111) surface. The bond length of $C_{aromatic}$-OH in the adsorbed structure **Phe** is 1.38 Å which further stretches to 2.11 Å (see structure **TSP_1** in Figure 5.53) when it reaches the first order saddle point **TSP_1** (350.99*i* cm^{-1}). Finally, the OH functional is cleaved and adsorbed on the surface with a metal atom and now, the distance between $C_{aromatic}$ and OH is 3.29 Å, whereas, Pd-O in structure **Phe_1** is 1.96 Å. The same reaction step is carried out by Lu et al. [44, 45] over Pt(111) and Ru(0001) bulk surfaces and they have found the barrier heights as 53.96 kcal/mol and 26.52 kcal/mol, respectively. Similarly, Rubeš et al. [156] calculated this barrier height as 24.68 kcal/mol over Ru/C surface. Low activation barriers on Ru and Ru supported catalysts, e.g., Ru/TiO_2, are due to the oxophilic nature of metal catalyst which has strong interaction with oxygen and, therefore, a reduction in activation barrier can be perceived for C-O cleavages over oxophilic metals [157]. The activation barrier value of direct cleavage of OH from phenol over Pd(111) surface is very high which cannot be possible at normal or slightly high temperature. The temperature increment may lead to the acceleration of reaction by increasing its reaction rates. Nevertheless, the hydrogenation of the phenyl ring requires an energy barrier of only 16.72 kcal/mol (see Figure 5.52). The barrier heights for hydrogenation of phenyl ring on Pt(111) and Ru(0001) bulk surfaces are reported as 15.68 kcal/mol and 12.68 kcal/mol, respectively [44, 45]. It can be concluded that the present values over Pd(111) surface are in line with other competitive catalytic systems.

5.8.5. Conversion of Benzaldehyde

The reaction schemes 3 and 4 produce an important intermediate benzaldehyde which is further converted to benzene using two pathways: i) dehydrogenation of formyl group (reaction step 18) followed by CO removal (reaction step 19) and a hydrogenation reaction on to phenyl ring

to produce benzene (reaction step 9), ii) direct removal of formyl group (reaction step 21) followed by the dehydrogenation of adsorbed formyl group (reaction step 22) and a hydrogenation reaction to phenyl ring to produce benzene (reaction step 9). The potential energy surfaces for the conversion of benzaldehyde using both pathways are depicted in Figure 5.54 and corresponding optimized structures involved in the conversion of benzaldehyde are depicted in Figure 5.53. Further, the activation energies and imaginary frequencies are reported in Table 5.29.

The configuration of benzaldehyde adsorbed over Pd(111) surface (see structure **BZD** in Figure 5.53), i.e., bridge 30^{o}, after the hydrogenation reaction to 2-formylphenyl is found as the most stable configuration, therefore, this configuration has been considered for further calculations. The adsorption energy of most stable configuration of benzaldehyde over Pd(111)

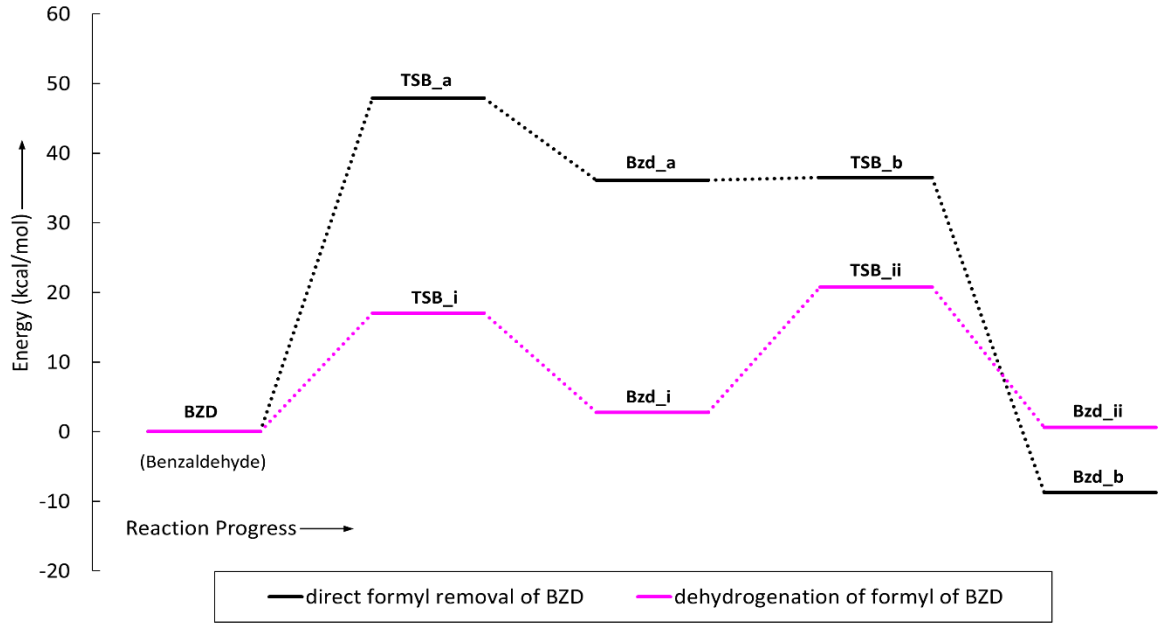

Figure 5.54: Potential energy surfaces for the formation of benzene from benzaldehyde using two reaction mechanisms. The formation of benzene from **Bzd_b** and **Bzd_ii** structures proceeds similar to the formation of benzene in PES of phenol conversion. The benzaldehyde (reactant) structure is adsorbed onto the catalyst surface.

surface is -37.30 kcal/mol. The average Pd-C bond distances in bridge 30^{o} configuration of benzaldehyde over Pd(111) are 2.22 Å and the bond distance between C-O is 1.29 Å. Further, the nearest Pd atom is 2.19 Å away from the oxygen atom and all the hydrogen atoms attached to phenyl are bent away from the surface.

The dehydrogenation of formyl group from benzaldehyde is analogous to the dehydrogenation reaction of formyl group of 2-HB. The activation barrier required for this case (reaction step 18 in Figure 5.48) is calculated as 17.01 kcal/mol, whereas, the activation barrier of reaction step 2 (see Figure 5.48) is 18.21 kcal/mol. Furthermore, the reaction step 18, i.e., the dehydrogenation reaction of formyl group of benzaldehyde also shows a little endothermicity compared to reaction step 2. Bond length between the carbon atom of CHO functional and nearest surface Pd atom decreases to 2.01 Å in structure **Bzd_a** of Figure 5.53 from 2.32 Å (see structure **BZD** of Figure 5.53) due to dissociation of hydrogen atom. The H atom upon dissociation adsorbs to the surface interacting with two surface metal atoms. However, further removal of CO is carried out and it requires a slightly less barrier height, i.e., 16.29 kcal/mol, with a little exothermicity. The adsorption of CO can be seen in structure **Bzd_b** which bridges with two surface metal atoms while the adsorbed H atom does not deviate much spatially from its previous position. On the other hand, phenyl ring after CO elimination reaction adsorbs parallely on to the surface. To carry out further reaction, i.e., association of H atom to the phenyl ring, the desorption of CO from surface is carried out in order to reproduce the active sites. The CO desorption from structure **Bzd_b** in Figure 5.51 requires an energy of 32.79 kcal/mol. Subsequent association of hydrogen atom to the phenyl ring to produce benzene proceeds the same way as of reaction step 9 in phenol conversion, i.e., with barrier height of 16.72 kcal/mol. On the other hand, the direct removal of formyl group from benzaldehyde is highly kinetically demanding elementary reaction step for which the activation barrier is 47.93 kcal/mol. Furthermore, direct cleavage of formyl group from benzaldehyde is

highly endothermic too (ΔE = 36.12 kcal/mol). The elimination of hydrogen atom from adsorbed CHO requires a significantly less barrier height as 0.42 kcal/mol (see Figure 5.54); however, unlike to formyl cleavage of benzaldehyde, it reports a high amount of exothermicity (see Table 5.29). Desorption of CO from structure **Bzd_ii** in Figure 5.53 follows and requires the same energetic as of the desorption energy of CO from structure **Bzd_b** in Figure 5.53 because of almost same coordinates.

It is clear from the results that the direct removal of formyl group from benzaldehyde (reaction step 21) may not be favourable because of high activation energy (47.93 kcal/mol); however, the dehydrogenation of formyl group of benzaldehyde (reaction step 18) followed by cleavage of oxygen atom (reaction step 19) and association of H atom to the phenyl ring (reaction step 9) may be considerably favourable because of significantly low activation energy 17.01 kcal/mol. The dissociation reaction of hydrogen from formyl functional of benzaldehyde determines the rate of reaction and it is slightly slower than the CO removal reaction from $C_6H_5(CO)^*$. Since, direct cleavage of CHO functional is highly kinetic demanding, therefore, the favourable pathway of benzene production from benzaldehyde will initiate from dehydrogenation of formyl group of benzaldehyde.

5.8.6. Kinetic Modelling

The reaction kinetics of any reaction is an important part which describes the rate of reaction using reaction rate constants, order, etc. Therefore, in this study, the reaction kinetics of 2-HB conversion using all elementary reaction steps of each reported reaction scheme are carried out for a wide range of temperature, i.e., 498-698 K at an interval temperature of 50 K and constant atmospheric pressure. The reaction rate constant values are listed in Table 5.29 and the pre-exponential factors and equilibrium constants are listed in Table 5.30 for all reported temperature values.

It is established earlier that the rate controlling step for the production of phenol from 2-HB, under RS 1, is the reaction step of association of H atom to the 2-hydroxyphenyl and the corresponding rate constant at 498 K is in the order of 10^2 s^{-1}. However, it improves further as the temperature gradually increases, e.g., at 598 K, it reaches to the order of 10^4 s^{-1}. Further elevation at 698 K, the reaction rate constant is reported as 2.41×10^5 s^{-1} which is a very good environment for the reaction. On the other hand, the Arrhenius constant for this reaction remains in the range of 10^{13} in between temperature range of 498-698 K. In addition, the evaluation of equilibrium rate constants suggest that the product formation will be higher as the reported K_{eq} value at 498 K is 4.06×10^5; however, further increment in temperature reduces the product fraction and increases the reactant fraction in product mixture because the K_{eq} values decrease with the increasing temperature. The rate constants of reaction steps, i.e., dehydrogenation reaction of formyl group of 2-HB (reaction step 2) and the CO removal (reaction step 3) of structure $C_6H_4(OH(CO)^*$ are also very large (see Table 5.29). The direct elimination of CHO from 2-HB is not favourable because of high activation energy and low reaction rate constants. The temperature increment strongly influences the reaction rate constants which increases from 10^{-8} s^{-1} to 10^{-1} s^{-1} by increasing the temperature in the range of 498-698 K. The non-favourability of reaction is reaffirmed with the calculations of equilibrium rate constants because even at 698 K, K_{eq} values remain in the order of 10^{-14}. Similarly, the process of direct OH cleavage from 2-HB is also not favourable because of high activation energy (58.9 kcal/mol) and very low rate constant values (order of 10^{-12} s^{-1} at 498 K to order of 10^{-5} s^{-1} at 698 K). However, the process of cleavage of hydrogen from hydroxyl group of 2-HB followed by elimination of oxygen atom from $C_6H_4(O)(CHO)^*$ is slightly favourable compared to direct elimination of OH from 2-HB component. Because the activation energy is lower, the rate constants of rate controlling step are very significant compared to direct OH removal process.

Table 5.30: The pre-exponential factors (A) and equilibrium constants (K_{eq}) of each elementary reaction step.

R. No.		Reaction Steps	Pre-exponential factor (A) at 1 atm					K_{eq} at 1 atm				
			498 K	548 K	598 K	648 K	698 K	498 K	548 K	598 K	648 K	698 K
1	RS 1	$C_6H_4(OH)(CHO)$ (g) + * → $C_6H_4(OH)(CHO)$*	---	---	---	---	---	---	---	---	---	---
2		$C_6H_4(OH)(CHO)$* + * → $C_6H_4(OH)(CO)$* + H*	1.10E+13	6.51E+13	1.34E+13	1.03E+15	1.58E+13	5.99E-02	8.61E-02	1.17E-01	1.53E-01	1.93E-01
3		$C_6H_4(OH)(CO)$* + * → $C_6H_4(OH)$* + CO*	2.11E+13	2.00E+14	2.57E+13	6.41E+15	2.99E+13	3.81E+04	1.56E+04	7.44E+03	3.96E+03	2.30E+03
4		$C_6H_4(OH)$* + CO* → $C_6H_4(OH)$* + * + CO (g)	---	---	---	---	---	---	---	---	---	---
5		$C_6H_4(OH)$* + H* → $C_6H_5(OH)$* + *	1.30E+13	1.42E+14	1.51E+13	5.59E+15	1.68E+13	4.06E+05	1.14E+05	3.93E+04	1.59E+04	7.27E+03
6		$C_6H_5(OH)$* → $C_6H_5(OH)$ (g) + *	---	---	---	---	---	---	---	---	---	---
7	Phenol	$C_6H_5(OH)$ (g) + * → $C_6H_5(OH)$*	---	---	---	---	---	---	---	---	---	---
8		$C_6H_5(OH)$* + * → C_6H_5* + OH*	1.75E+13	2.15E+15	2.18E+13	3.55E+18	2.59E+13	2.75E-16	6.95E-15	1.02E-13	9.79E-13	6.78E-12
9		C_6H_5* + H* → C_6H_6* + *	3.12E+12	1.55E+13	3.49E+12	1.83E+14	3.81E+12	6.31E+10	5.14E+09	6.34E+08	1.07E+08	2.33E+07
10		C_6H_6* → C_6H_6 (g) + *	---		---		---	---		---		---
11	RS 2	$C_6H_4(OH)(CHO)$* + * → $C_6H_4(OH)$* + CHO*	2.12E+14	2.41E+16	3.05E+14	3.57E+19	4.06E+14	1.76E-20	2.02E-18	1.06E-16	3.03E-15	5.40E-14
12		$C_6H_4(OH)$*+CHO* + * → $C_6H_4(OH)$* + CO* + H*	2.40E+13	2.76E+13	3.06E+13	3.53E+13	3.75E+13	3.85E+16	1.49E+15	1.01E+14	1.03E+13	1.48E+12
13		$C_6H_4(OH)$*+CO*+H* →$C_6H_4(OH)$*+H*+*+CO(g)	---	---	---	---	---	---	---	---	---	---
14	RS 3	$C_6H_4(OH)(CHO)$* + * →$C_6H_4(CHO)$* + OH*	1.13E+14	3.00E+16	1.49E+14	1.60E+20	1.84E+14	3.63E-17	1.54E-15	3.48E-14	4.85E-13	4.62E-12
15		$C_6H_4(CHO)$* + H* → $C_6H_5(CHO)$* + *	5.41E+12	2.10E+13	5.97E+12	1.69E+14	6.43E+12	2.59E+14	1.07E+13	7.44E+11	7.76E+10	1.11E+10
16		$C_6H_5(CHO)$* → $C_6H_5(CHO)$ (g) + *	---	---	---	---	---	---	---	---	---	---
17	Benzaldehyde	$C_6H_5(CHO)$ (g) + * → $C_6H_5(CHO)$*	---	---	---	---	---	---	---	---	---	---
18		$C_6H_5(CHO)$* + * → $C_6H_5(CO)$* + H*	3.32E+12	1.74E+13	3.93E+12	2.26E+14	4.53E+12	3.67E-02	5.05E-02	6.65E-02	8.43E-02	1.04E-01
19		$C_6H_5(CO)$* + H* + * → C_6H_5* + H* + CO*	1.14E+13	5.72E+13	1.40E+13	6.95E+14	1.67E+13	7.56E+02	5.71E+02	4.56E+02	3.79E+02	3.26E+02
20		C_6H_5* + H* + CO* → C_6H_5* + H* + * + CO (g)	---	---	---	---	---	---	---	---	---	---
21		$C_6H_5(CHO)$* + * → C_6H_5* + CHO*	1.97E+13	1.87E+15	2.52E+13	2.07E+18	3.06E+13	9.39E-16	2.71E-14	4.44E-13	4.71E-12	3.55E-11
22		C_6H_5* + CHO* + * → C_6H_5* + CO* + H*	5.35E+12	5.82E+12	5.83E+12	6.69E+12	6.27E+12	3.08E+16	9.89E+14	5.66E+13	5.05E+12	6.37E+11
23	RS 4	$C_6H_4(OH)(CHO)$* + * → $C_6H_4(O)(CHO)$* + H*	2.88E+13	3.14E+14	3.67E+13	1.27E+16	4.48E+13	2.92E-03	5.48E-03	9.31E-03	1.46E-02	2.17E-02
24		$C_6H_4(O)(CHO)$* + * → $C_6H_4(CHO)$* + O*	4.38E+13	3.07E+15	5.92E+13	2.18E+18	7.61E+13	2.00E-12	3.39E-11	3.62E-10	2.70E-09	1.52E-08

The reaction rate constant of the rate determining step of RS 4 is 0.96 s^{-1} at 698 K, whereas, the rate constant of reaction step 14 at 698 K is 6.62×10^{-5} s^{-1}. The equilibrium rate constant values of both rate determining steps, i.e., reaction steps 14 and 24 remain close to zero even at 698 K which shows a very less or no product formation. On the other hand, the reaction rate constants corresponding to the OH cleavage of phenol at each temperature remain close to zero. Further, the equilibrium rate constants clearly suggest major fraction of reactant in the product mixture because K_{eq} values remain in the range of 10^{-12} even at 698 K. Therefore, the conversion of phenol into benzene does not seem feasible over Pd(111) catalyst surface.

It is clear from the kinetic analyses that the conversion of 2-HB over Pd(111) would prefer the production of phenol as an intermediate instead of benzaldehyde because of the low activation barrier and high reaction rate constants. Therefore, the major product of 2-HB conversion over Pd(111) surface would be phenol. In addition, the production of phenol from 2-HB should follow the reaction route as of RS 1, i.e., dehydrogenation of formyl functional of 2-HB followed by elimination of CO to produce 2-hydroxyphenyl; further, the H atom association with adsorbed 2-hydroxyphenyl in order to produce phenol component. Further, the production of benzene from phenol using direct dehydroxylation is not kinetically favourable over Pd(111) surface because of very high activation energy and low rate constants, therefore, other approaches need to be tested.

5.9. Elucidation of Gas Phase Hydrodeoxygenation Mechanism of Guaiacol over Pd(111) Catalyst Surface: The DFT Framework

5.9.1. Reaction Schemes

The reaction mechanisms considered for studying hydrodeoxygenation (HDO) of guaiacol over Pd(111) catalyst is shown in Figure 5.55. The numerals in red colour indicate the elementary reaction step number and asterisk (*) marks denote adsorbed species, e.g., $C_6H_4(OH)(OCH)^*$.

To be specific about reaction schemes presented in Figure 5.55, the first reaction step (RS) is about the adsorption of guaiacol from gas phase on to Pd(111) catalyst surface, which is a barrierless step, therefore, no transition state structure occurred in this step. Further, adsorbed guaiacol species undergoes three bond scission possibilities represented by reaction steps **2**, **I**, and **A** shown in Figure 5.55. The reaction step **2** is about the cleavage of methyl group directly from adsorbed guaiacol component over Pd(111). The reaction steps **I** and **A** are abstractions of hydrogen atom from methoxy and hydroxyl groups of guaiacol, respectively. The reaction step **3** indicates the formation of catechol from the structure $C_6H_4(OH)(O)^*$ produced in reaction step **2** by undergoing an atomic hydrogenation at the oxygen atom. This structure also undergoes oxygen atom elimination (RS **12**) to produce $C_6H_4(OH)^*$. Thereafter, catechol is desorbed into gas phase according to reaction step **4**, dehydrogenated to form $C_6H_4(OH)(O)^*$ for further reduction (RS **5**), and dehydrated to directly produce $C_6H_4(O)^*$ species (RS **6**). The production of phenol from $C_6H_4(O)^*$ structure produced from RS **6** requires two sequential hydrogen atom addition reactions as RS **7** and RS **8** (see Figure 5.55). RS **7** is an atomic hydrogenation of the aromatic carbon of $C_6H_4(O)^*$ to produce $C_6H_5(O)^*$ while RS **8**

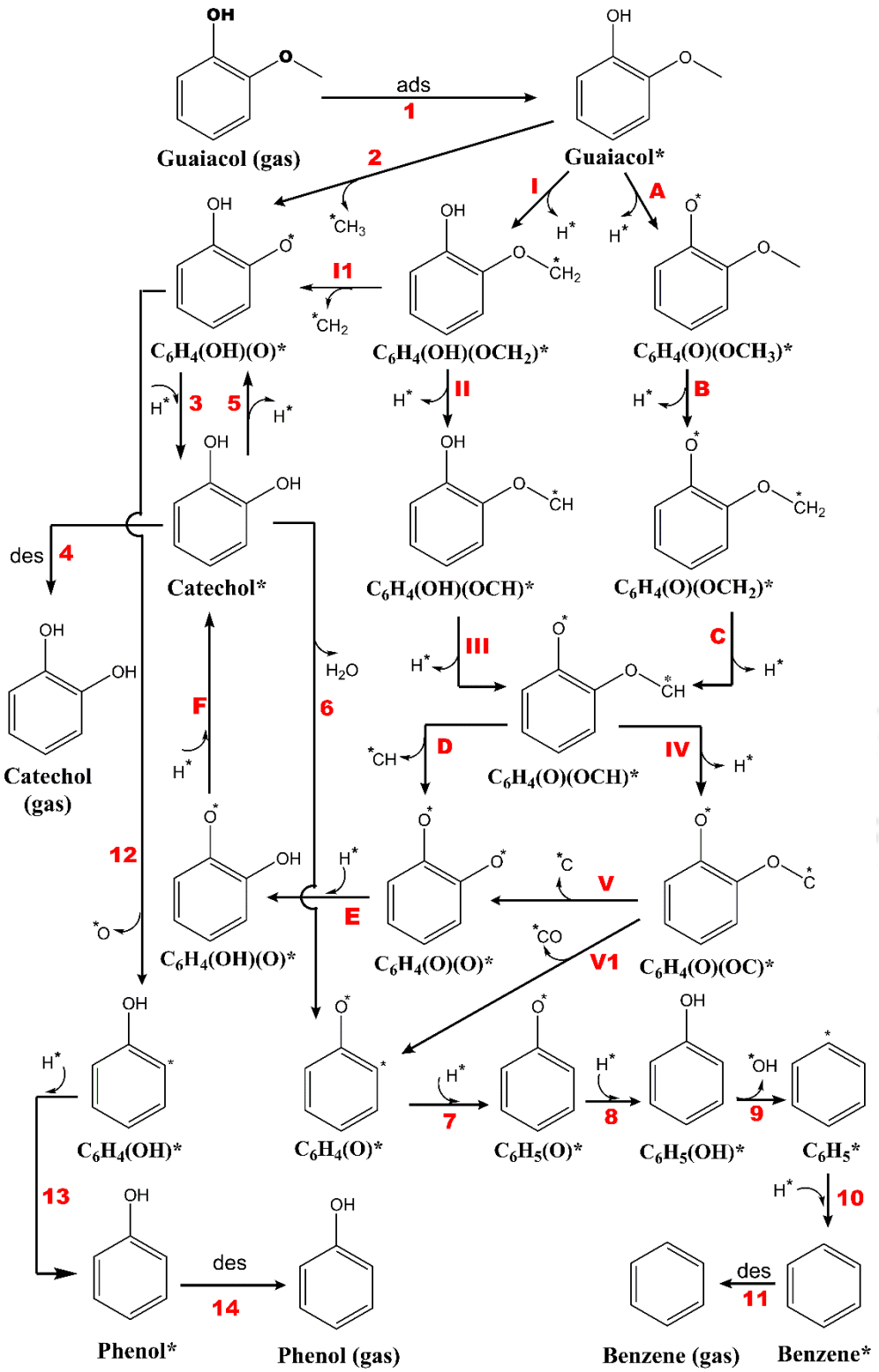

Figure 5.55: Reaction scheme of HDO of guaiacol over Pd(111) catalyst. Red numerals denote reaction step number and their kinetic information can be accessed in Table 5.33 and Table 5.34 using reaction step number.

is about the atomic hydrogen reaction to the oxygen of $C_6H_5(O)^*$ to produce phenol. Further, it is subjected to direct dehydroxylation (RS **9**) to produce $C_6H_5^*$ which is followed by hydrogenation of $C_6H_5^*$ (RS **10**) to produce benzene. Then benzene is desorbed into gas phase according to reaction step **11**. The structure produced from RS **5** undergoes $C_{aromatic}$-O cleavage to produce $C_6H_4(OH)^*$ (RS **12**) which further associates with hydrogen atom (RS **13**) to form phenol. Desorption process of phenol from catalyst surface to gas phase is depicted by barrierless reaction step **14**. The structures produced from reaction steps **I** and **A** further undergo hydrogen abstraction processes using reaction steps **II** and **B** to produce $C_6H_4(OH)(OCH)^*$ and $C_6H_4(O)(OCH_2)^*$ species, respectively. The reaction step **I** is also followed by direct removal of CH_2 (RS **I1**) which then merges to the structure $C_6H_4(OH)(O)^*$. Further, the production of $C_6H_4(O)(OCH)^*$ occurs by the dehydrogenation reactions of OH (RS **III**) and OCH_2 (RS **C**) groups of $C_6H_4(OH)(OCH)^*$ and $C_6H_4(O)(OCH_2)^*$, respectively. Thereafter, further reduction of $C_6H_4(O)(OCH)^*$ undergoes two possibilities, i.e., either by hydrogen elimination (RS **IV**) or direct CH removal (RS **D**) from OCH group. The adsorbed structure $C_6H_4(O)(O)^*$, produced from RS **D**, undergoes two sequential hydrogenation reactions as denoted by reaction steps **E** and **F** to produce catechol. The structure $C_6H_4(O)(OC)^*$ produced from RS **IV** also follows two pathways which occur either by carbon atom removal (RS **V**) to merge into structure $C_6H_4(O)(O)^*$ or by direct CO elimination (RS **V1**) to merge into structure $C_6H_4(O)^*$.

The reaction mechanisms shown in Figure 5.55 are numerically performed over Pd(111) catalyst. The catalyst cluster model is designed using 12 palladium atoms in a plane (see Figure 4.2). Stability analyses of the catalyst model (see Table 4.1) reveal the ground state in septet spin multiplicity. The applied level of theory for all quantum chemical calculations is

B3PW91 under density functional theory framework. The basis set for C, H, and O atoms is chosen as 6-311+g(d,p), whereas, LANL2DZ basis set is designated for Pd atoms.

5.9.2. Adsorption Energy

Theoretical results on HDO of guaiacol over Pd(111) catalyst surface are not available in the literature; however, the adsorption energy of guaiacol must be in line with the adsorption energies of other aromatic species such as phenol, benzaldehyde, and benzene described in the Chapter 5.8. Guaiacol component, comprised of an aromatic ring, is found most stable in *bridge 30°* configuration (see *config. 1* in Figure 5.56) over Pd(111) surface with adsorption energy of -33.09 kcal/mol. Another energetically competitive configuration of guaiacol is also found while simulating the adsorption of guaiacol over Pd(111) catalyst shown as *config. 2* in Figure 5.56; however, *config. 2* is 3.59 kcal/mol unstable compared to *config. 1*. The ground state structure of *config. 1* of guaiacol lies in quintet spin state which is observed during spin state multiplicity analyses (Table 5.31). Therefore all further studies such as reaction profiles and reaction kinetics are carried out based on *config. 1* of guaiacol in quintet spin state. The average Pd-$C_{aromatic}$ bond lengths of *config. 1* are observed as ~2.44 Å which clearly suggests chemisorption process. In *config. 1*, the bond distances between nearest Pd metal atom and O

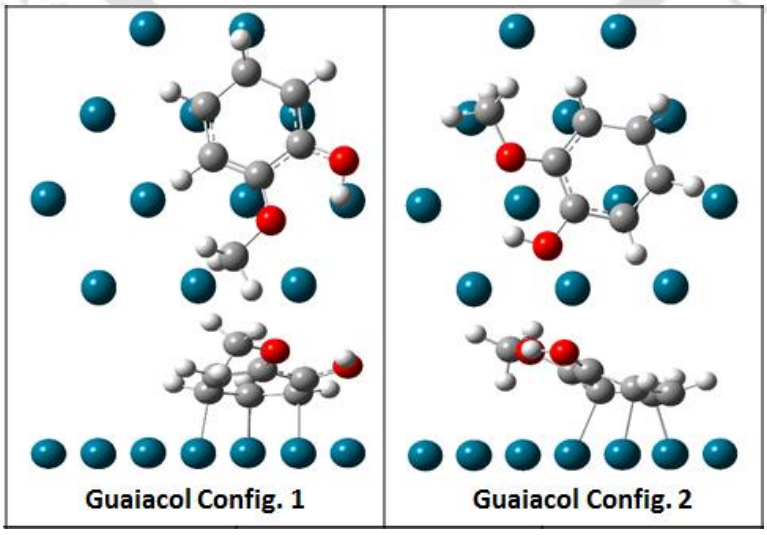

Figure 5.56: Adsorption configurations of guaiacol over Pd(111) catalyst surface.

Table 5.31: Spin multiplicities and relative energies of configuration '1' of guaiacol.

SM	1	3	5	7	9
E_{Rel} (kcal/mol)	13.84	1.67	0.00	7.63	31.14

Table 5.32: Adsorption energies of phenolic species over Pd(111) catalyst surface.

Species	**E_{ads} (kcal/mol)**	
	Present	**Literature**
Guaiacol	-33.09	---
Phenol	-31.21	-32 [154]
Benzene	-35.81	-33 [154]
Catechol	-33.70	---

atoms of OH and OCH_3 are found as 3.32 Å and 3.49 Å, respectively, which can be seen in the side view of *config. 1* as tilts in both oxy-functional groups upon adsorption over Pd(111) catalyst surface. In general, long bond distances between catalyst atoms and adsorbate indicate weaker adsorption and consequently weaker interaction between the catalyst and adsorbate; however, the benzenoid ring interacts strongly with the surface because of low average Pd-$C_{aromatic}$ bond lengths. Further, the bond lengths between $C_{aromatic}$-OH and $C_{aromatic}$-OCH_3 of gas phase guaiacol compound are 1.36 Å and 1.37 Å, respectively, which contracts to 1.34 Å and 1.35 Å, respectively, upon adsorption of guaiacol (*config. 1*) from gas phase on to the Pd(111) catalyst surface. It is seen in *config. 1* of Figure 5.56 that guaiacol adsorbs stably towards the edge of Pd(111) catalyst surface. This type of movement of the adsobate to the cluster edge is common because border metal atoms of the cluster demonstrate higher acidic character and, therefore, they generally bind strongly with the substrate [130, 153].

As per the expectation, it can be seen from Table 5.32 that the adsorption energy of guaiacol (-33.09 kcal/mol) over present Pd(111) catalyst model is in line with the adsorption energies of phenol, benzene, and catechol [46, 45, 154]. Further information regarding adsorption energies and configurations of phenol and benzene can be found in Chapter 5.8.

The activation barriers, reaction energies, reaction free energies and reaction enthalpies of all reaction steps are supplied in Figures 5.57 and 5.58, and the corresponding molecular structures of reactants, intermediates, transition states and products are shown in Figures 5.59-5.61. The notations in Figures 5.59-5.61 are given as **X_Y**; where **Y** is either **R** (reactant) or **P** (product) of any particular elementary reaction step number **X**. For example, **13_R** and **V_P** are reactant and product of reaction steps **13** and **V**, respectively. Similarly, transition state structure (imaginary frequency shown in Table 5.33) involved in each elementary reaction step is notified using **TSn**; where **n** denotes reaction step number. For instance, **TS2** and **TSIV** are transition state structures involved in reaction steps **2** and **IV**, respectively.

5.9.3. Formation of Catechol

As shown in Figure 5.55, guaiacol component first adsorbs over Pd(111) catalyst surface (reaction step **1**) from the bulk gas phase with a barrierless exothermic energy release of 33.09 kcal/mol. Further, the adsorbed guaiacol species undergoes three bond scissions, namely, methyl group cleavage and hydrogen atom cleavages from OH and OCH_3 groups. The direct elimination of the methyl group from the adsorbed guaiacol occurs with an activation barrier of 45.53 kcal/mol (Figure 5.57) which is a high activation barrier. In addition, this particular reaction step is not thermodynamically feasible as well because of high amounts of positive reaction energy, ΔE, reaction free energy, ΔG, and reaction enthalpy, ΔH (Figure 5.58). Therefore, this pathway cannot be recommended for HDO of guaiacol. Similar results were reported by Lu et al. [45] in their HDO study of guaiacol over Pt(111) bulk catalyst as they found the activation barrier for methyl group cleavage as 46.12 kcal/mol using Pt(111) catalyst. On the other hand, the direct elimination of OH group from guaiacol over Pd(111) surface requires a very high activation barrier of 61.10 kcal/mol (much higher than direct methyl group cleavage) to surpass the barrier height and to produce 2-methoxyphenyl. Lu et al. [45] also

concluded that the direct elimination of OH from guaiacol over Pt(111) catalyst is a very high kinetic demanding reaction step; however, Chiu et al. [47], on the other hand, found this reaction as considerably low barrier height demanding reaction over Ru(0001) catalyst surface. The higher barrier heights for direct $C_{aromatic}$-OH scission over Pd(111) and Pt(111) catalyst surfaces are due to the non-oxophillic nature of the catalyst surfaces and the stabilization of phenyl ring over the surface. However, oxophillic surfaces require considerably less barrier height for similar bond scissions because of strong interaction with oxygen, e.g., Ru or TiO_2 supported Ru catalytic systems [157]. Therefore, less activation barrier can be observed for C-O cleavages over oxophilic metals. The existing hydrodeoxygenation works of guaiacol over Pt(111) [46, 45] suggests that direct eliminations of functional groups such as CH_3, OH, and OCH_3 are highly kinetic demanding and since Pd catalyst shows similar characteristics, these functional eliminations are not endorsed in this study. On the other hand, an atomic hydrogen addition reaction to the oxygen atom of hydrogen-catecholate species on Pd(111) catalyst surface to produce catechol (Figure 5.59 for molecular structures) requires only 14.28 kcal/mol of barrier height, however, its production through methyl group cleavage from adsorbed guaiacol compound is not recommended. Nonetheless, the desorption of catechol from Pd(111) catalyst surface to the gas phase (reaction step **4**) requires 33.70 kcal/mol of energy.

Since, the direct eliminations of methyl and hydroxyl functional groups of guaiacol over Pd(111) catalyst surface require high amount of energetics, eliminations of hydrogen atoms from hydroxyl and methoxy functional groups of guaiacol are considered as reaction steps **A** and **I**, respectively. The abstraction of hydrogen atom from hydroxyl group of guaiacol occurs with a barrier height of 11.51 kcal/mol, whereas, the abstraction of hydrogen atom from methoxy group requires comparatively higher barrier height as 20.28 kcal/mol. The molecular structures of minima and transition state structures of reaction steps **A** and **I** are shown in

Figures 5.60 and 5.61, respectively. It should be noted that hydrogen reduction reactions from both oxy-functional groups required considerably less amount of energies compared to the direct scissions of functional groups, therefore, these reaction steps may lead to possible favourable pathways for the formation of product.

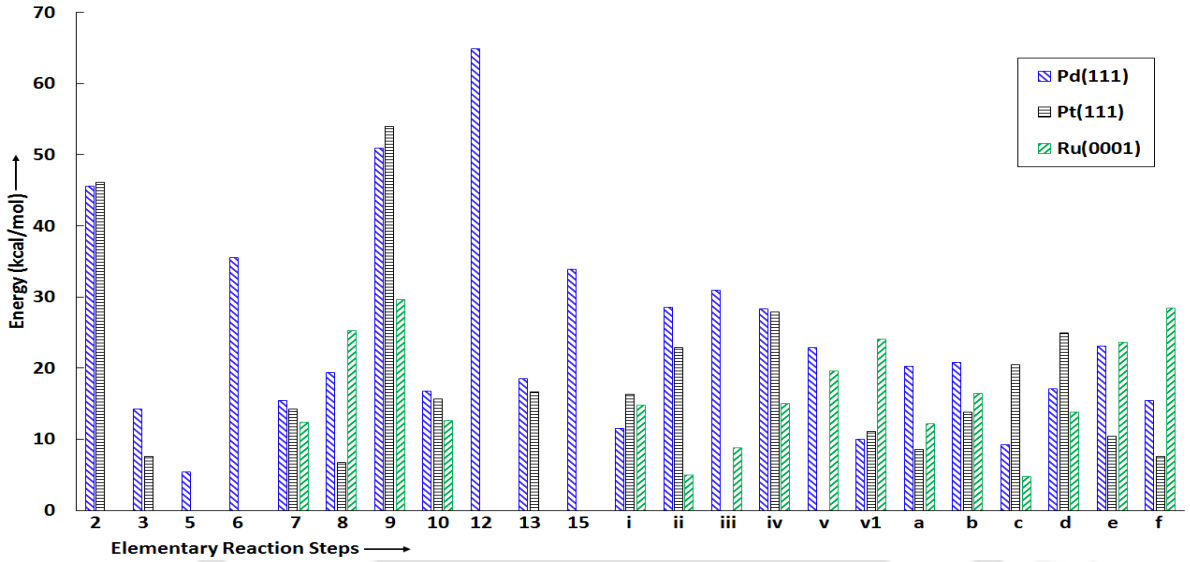

Figure 5.57: Activation barrier (kcal/mol) of each elementary reaction step using Pd(111) catalyst surface and corresponding values over Pt(111) [45] and Ru(0001) [47] bulk catalysts.

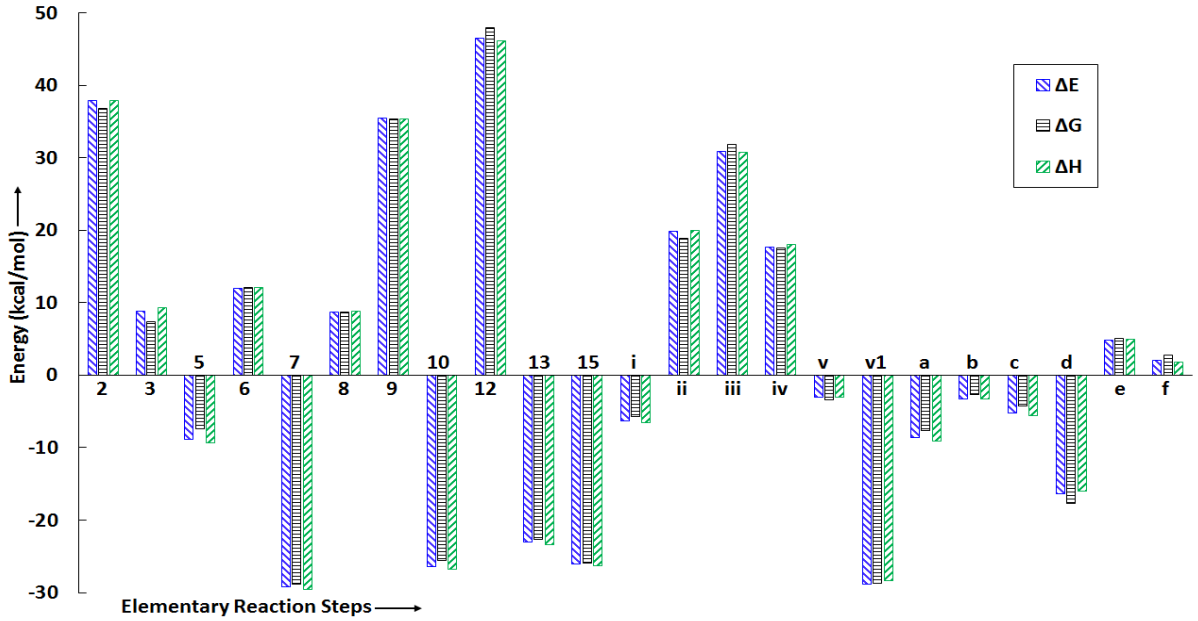

Figure 5.58: Reaction energy, reaction free energy, and reaction enthalpy of each reaction step involved in HDO of guaiacol over Pd(111) catalyst.

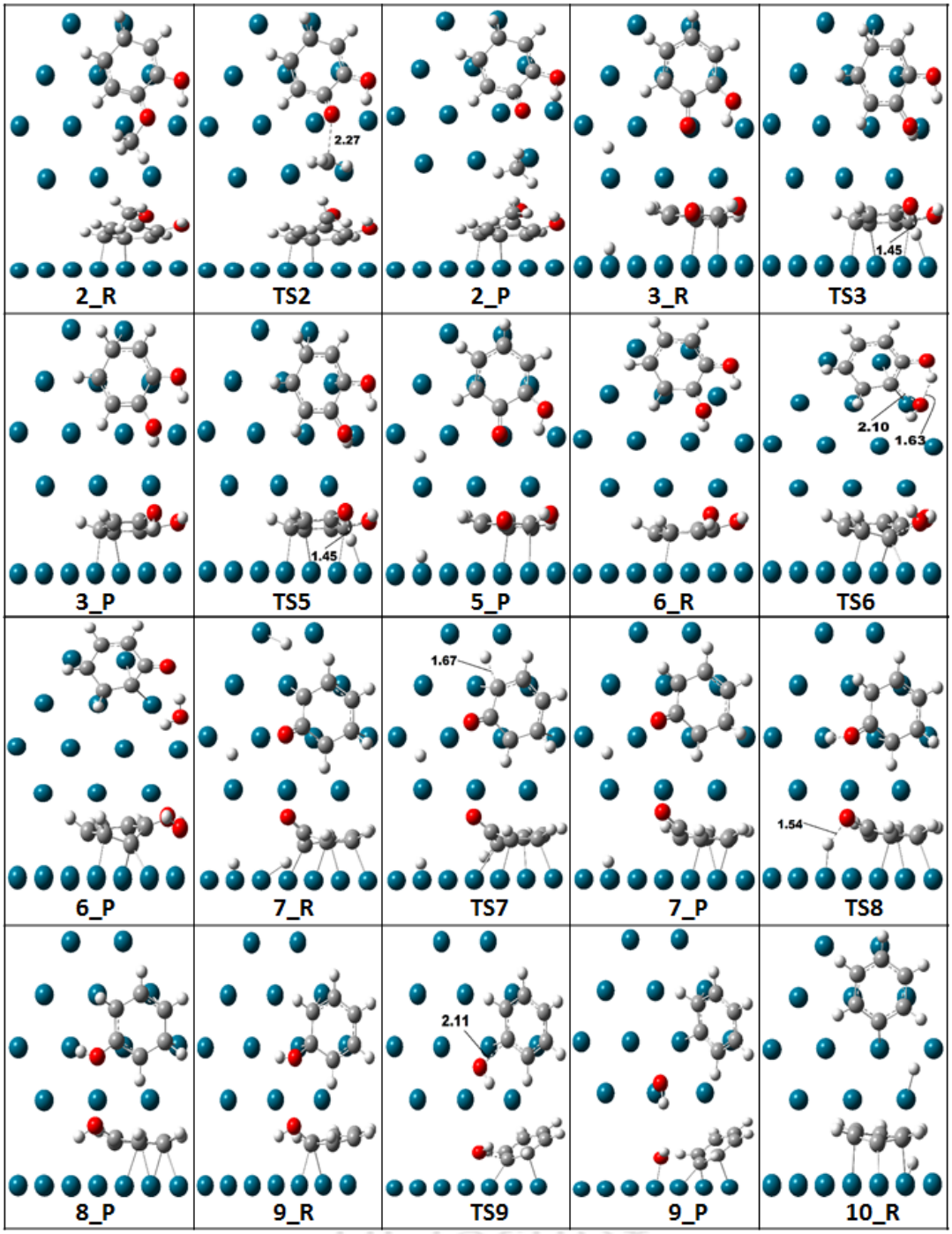

Figure 5.59: Optimized molecular structures involved in reaction steps **2-3** and **5-10**.

The dehydrogenation of methoxy group of guaiacol (RS **I**) over Pd(111) surface requires comparatively high activation barrier than Pt(111) [45] and Ru(0001) [47] surfaces; however, dehydrogenation of hydroxyl group of guaiacol is more advantageous over Pd(111) than Ru(0001) [47] surface but less advantageous compared to Pt(111) [45] catalyst surface.

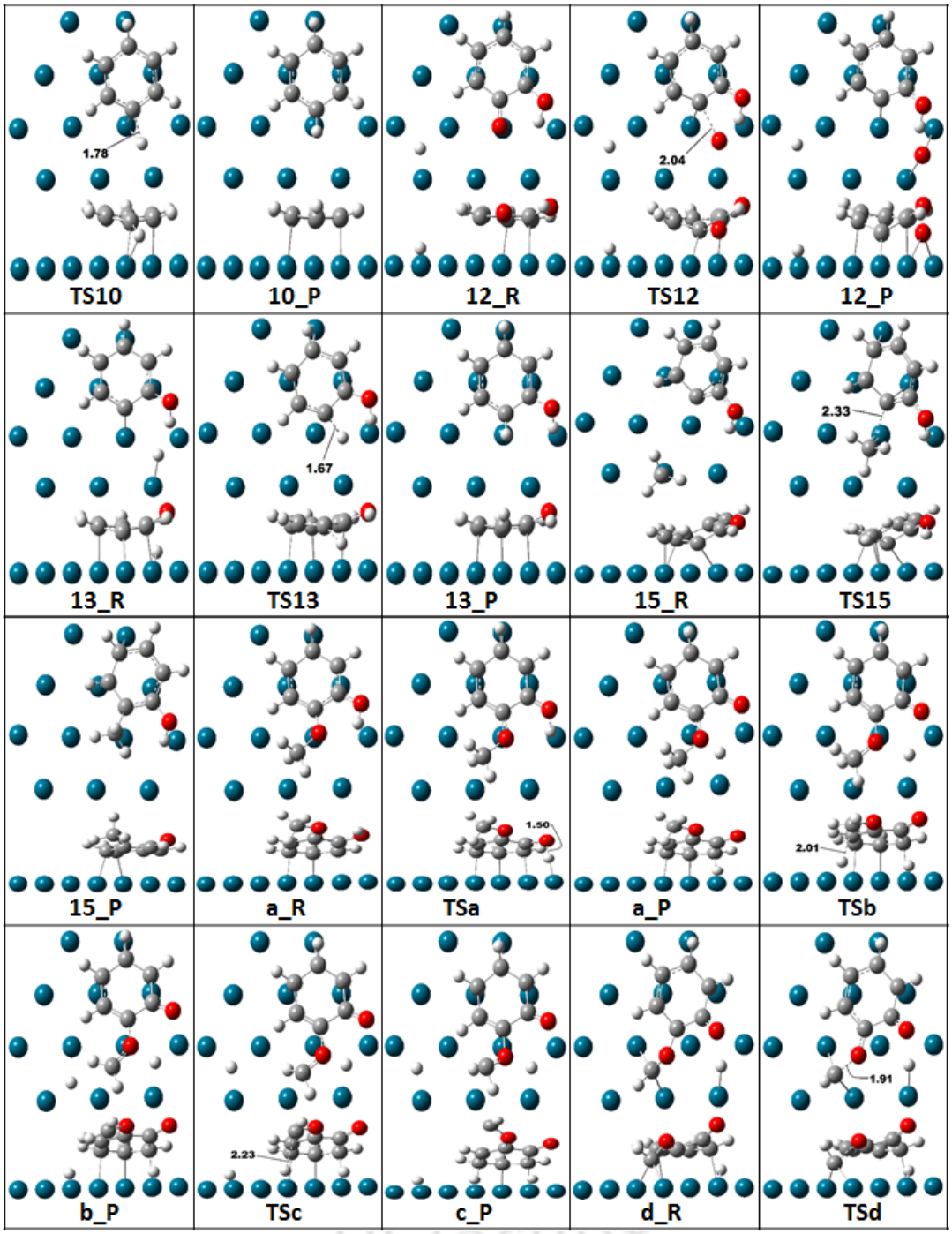

Figure 5.60: Optimized molecular structures involved in reaction steps **10**, **12**, **13**, and **A-E**.

Furthermore, it is shown in Figure 5.58 that both hydrogen atom scission reactions are thermodynamically favourable because of negative energetics of ΔG and ΔH, whereas, a huge amount of unfavourability is reported for the direct scission of methyl group of guaiacol (ΔG= 36.30 kcal/mol and ΔH = 37.62 kcal/mol) at 473 K in the same figure. However, comparing

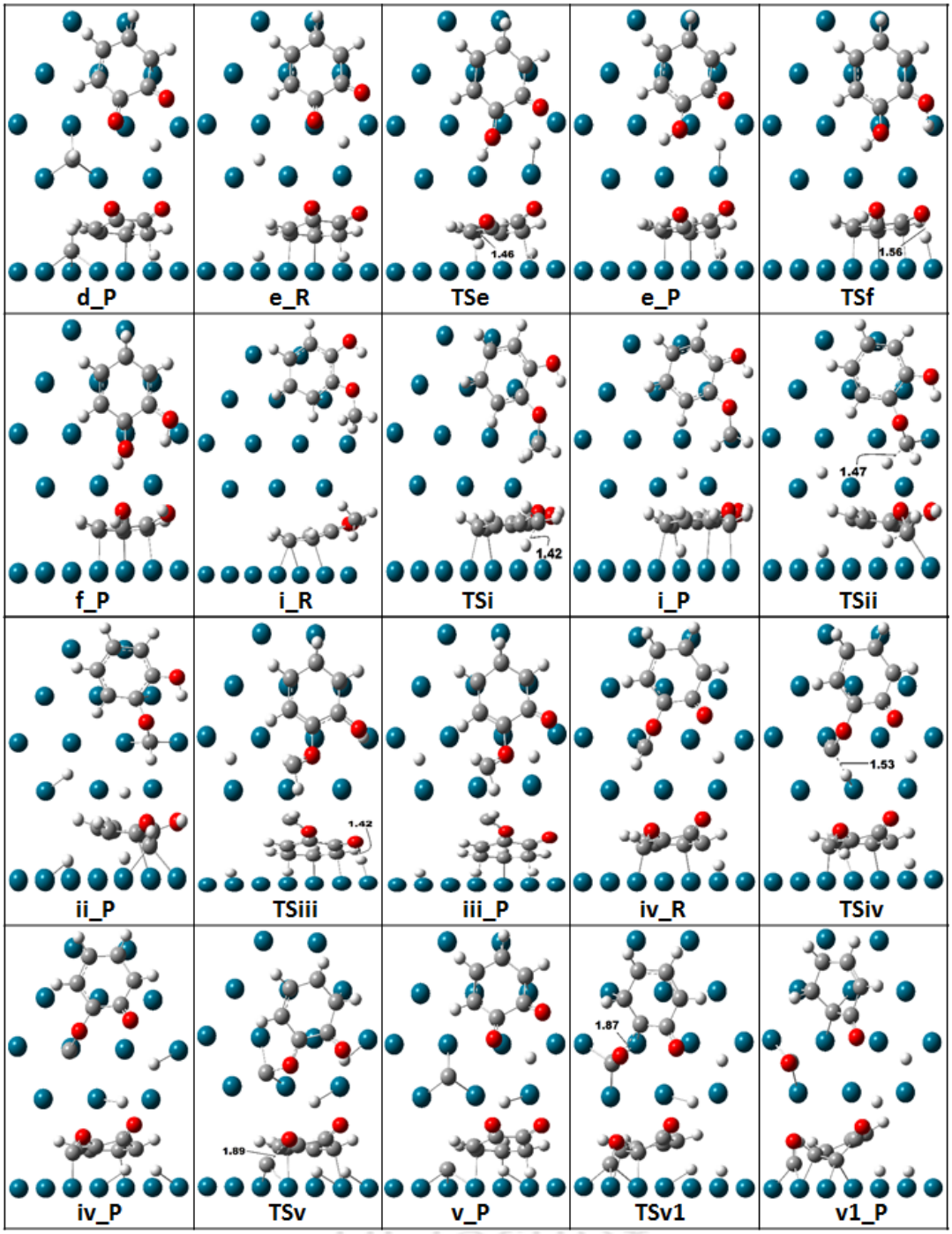

Figure 5.61: Optimized molecular structures involved in reaction steps **E-F**, **I-V**, **I1**, and **V1**.

both hydrogen abstraction reactions, the abstraction of H from hydroxyl group (RS **A**) is slightly higher spontaneous with similar exothermicity at 473 K (see Figure 5.58). The produced structure from reaction step **I**, i.e., $C_6H_4(OH)(OCH_2)^*$ further undergo reductions of H and CH_2 from OCH_2 group according to reaction steps **II** and **I1** and the corresponding barrier

heights are 20.77 kcal/mol and 23.06 kcal/mol. The corresponding reaction free energy and reaction enthalpy (Figure 5.58) suggest favourability in the reduction of CH_2 compared to the reduction of hydrogen atom. The reaction step **II** is considerably unfavourable as the ΔG and ΔH are as high as 22.77 kcal/mol and 22.0 kcal/mol, respectively. The scission of CH_2 group from $C_6H_4(OH)(OCH_2)^*$ led to the production of hydrogen-catecholate species which further follows the production of catechol using an atomic hydrogen addition reaction as described earlier. On the other hand, the produced structure from reaction step **II** undergoes another hydrogen atom elimination but from hydroxyl group (E_a = 9.20 kcal/mol) and produces $C_6H_4(O)(OCH)^*$. Similarly, the reaction step **A** undergo two subsequent hydrogen atom elimination reactions from OCH_3 group with activation barriers of 28.52 kcal/mol and 30.96 kcal/mol, respectively and merge to the structure $C_6H_4(O)(OCH)^*$. It is clear that, though, the reaction step **A** required low barrier height compared to reaction step **I** but latter reactions, i.e., **B** and **C** are not favourable at all (see Figures 5.57 and 5.58). In addition, the elimination of H atom from OCH_2 of $C_6H_4(OH)(OCH_2)^*$ using RS **II** is not kinetically possible as well. Therefore, the formation of catechol is more likely to occur using reaction steps **I** and **I1**.

Further conversion of $C_6H_4(O)(OCH)^*$ is carried out to see other possibilities of product formation. Subsequent dissociation of $C_6H_4(O)(OCH)^*$ may occur either by removal of H or CH directly and it is observed during the energetic analysis that the elimination of CH requires 11.24 kcal/mol less activation barrier compared to the hydrogen atom reduction. However, removal of carbon from OC of $C_6H_4(O)(OC)^*$ (reaction step **V**) requires slightly less energy compared to H removal from CH functional. Nevertheless, it is also probable that CO can be eliminated directly from $C_6H_4(O)(OC)^*$ instead of C to produce $C_6H_4(O)^*$; and it is found that elimination of CO is highly advantageous compared to the elimination of carbon atom. Compared to the reduction of CH from $C_6H_4(O)(OCH)^*$, it can be seen that eliminations of H

and C from $C_6H_4(O)(OCH)^*$ and $C_6H_4(O)(OC)^*$, respectively, are not recommendable based on their energy requirements and thermodynamic feasibilities (see Figures 5.57 and 5.58). Therefore, it is highly probable that further reaction progress of $C_6H_4(O)(OCH)^*$ species undergoes elimination of CH instead of subsequent eliminations of H and C atoms. Further, $C_6H_4(O)(O)^*$ species leads to the production of catechol using two subsequent hydrogenation reactions, i.e., **E** and **F** with barrier heights of 23.07 kcal/mol and 15.48 kcal/mol, respectively. It should be observed that both reaction steps **3** and **F** undergo the production of catechol using hydrogenation of hydrogen-catecholate species but report different barrier heights. It is because of the different hydrogenation locations of oxygen atoms of hydrogen-catecholate structure (see Figures 5.55, 5.59 and 5.61).

5.9.4. Formation of Phenol

As presented in Figure 5.55, the production of phenol is aimed theoretically by three different mechanisms. Briefly, the first mechanism is about the dehydrogenation of hydroxyl group of catechol followed by scission of C-O bond and hydrogenation of the aromatic carbon atom (reaction steps **5**, **12**, and **13**). Then the second mechanism describes the hydrogen atom migration from one hydroxyl group of catechol to second hydroxyl group to directly eliminate water compound (reaction step **6** in Figure 5.55) which produces $C_6H_4(O)^*$ species. Finally, the third mechanism initiates directly from $C_6H_4(O)^*$ species which is produced after CO elimination from $C_6H_4(O)(OC)^*$ (RS **V1**). However, another possibility may be the direct scission of one hydroxyl group of catechol followed by hydrogenation of the aromatic carbon atom but this approach is not considered in this study because it is already reported in the previous subsection (Formation of Catechol) that the direct functional group cleavage is a very high energy demanding mechanism. This phenomenon is consistent with literature results by Lu et al. [45] who reported HDO of guaiacol over Pt(111) catalyst by cleaving the $C_{aromatic}$-OH

bond of catechol requiring 58.11 kcal/mol of activation energy. Thus, the conversion of catechol to phenol is carried out using dehydrogenation of hydroxyl group followed by elimination and addition of oxygen and hydrogen atoms, respectively. The dehydrogenation of hydroxyl group is very less energy demanding reaction and is achieved only by 5.45 kcal/mol of barrier height; however, the oxygen atom removal from hydrogen-catecholate is a very high energy demanding step (E_a = 64.93 kcal/mol) and thus, it may not be possible on Pd(111) catalyst surface. In addition to the low barrier height requirement, the dehydrogenation reaction of catechol is also kinetically favourable as both thermodynamic parameters, i.e., reaction free energy and reaction enthalpy are negative in energetics. Further, the subsequent hydrogenation reaction to aromatic carbon of $C_6H_4(OH)^*$ species requires considerably less amount of energetic (E_a = 18.45 kcal/mol) compared to oxygen atom removal from $C_6H_4(OH)(O)^*$ structure and is kinetically favourable as well. On the other hand, the migration of hydrogen of hydroxyl group of catechol from first hydroxyl group to second to produce water compound requires 35.53 kcal/mol of energy to surpass the reaction barrier. In addition to high barrier height requirement, this reaction is unfavourable thermodynamically (Figure 5.58), therefore, only reaction route remains is the direct elimination of CO from $C_6H_4(O)(OC)^*$ species to produce $C_6H_4(O)^*$ structure. The direct elimination of CO from $C_6H_4(O)(OC)^*$ is already discussed in the subsection of 'Formation of Catechol', hence, it is not discussed here again to avoid repetitions. Furthermore, the production of phenol from $C_6H_4(O)^*$ can be possible by two single step hydrogenation reactions; first hydrogenation to aromatic carbon to produce $C_6H_5(O)^*$ followed by the second hydrogenation to oxygen atom of phenolate species. The hydrogenation reaction to aromatic carbon of $C_6H_4(O)^*$ requires 15.42 kcal/mol of activation barrier and it is both spontaneous and exothermic; however, the hydrogenation to phenolate requires slightly higher barrier height, i.e., 19.38 kcal/mol and also, this reaction report unfavourability at 473 K; but the favourable environment can easily be achieved at temperature

conditions greater than 473 K as described elsewhere in a subsequent subsection on "Kinetic Modelling".

5.9.5. Conversion of Phenol

The conversion of phenol into benzene is well established [44, 47, 45] and can be achieved using various approaches as discussed in Chapter 5.8 The conversion of phenol into benzene in this study is considered using direct $C_{aromatic}$-OH cleavage which is constructive pathway for the production of benzene from phenol in the context of bio-oil HDO process. Refer to Figure 5.57 for activation barriers, Figure 5.58 for thermodynamic parameters and Figures 5.59 and 5.60 for optimized molecular structures associated with this pathway.

The formation of benzene from phenol is already discussed in Chapter 5.8; however, it is discussed here too to recap briefly. The cleavage of $C_{aromatic}$-OH bond of phenol requires an energy barrier of 50.92 kcal/mol on Pd(111) surface with high amount of unspontaneity and endothermicity. The direct $C_{aromatic}$-OH bond scission of phenol is also performed by Lu et al. [44, 45] over Pt(111) and Ru(0001) bulk surfaces and they also reported high barrier heights as 53.96 kcal/mol and 26.52 kcal/mol, respectively. Similarly, Rubeš et al. [156] calculated this activation barrier as 24.68 kcal/mol over Ru/C surface. The reason for differences in activation energies could be the oxophillic nature of the Ru catalyst surface and the phenyl ring stabilization over the surface (see Figure 5.59). Further, the association of hydrogen atom to the phenyl ring requires an activation barrier of only 16.72 kcal/mol (see Figure 5.57). This is in the line with similar observations due to Pt(111) and Ru(0001) bulk surfaces as these surfaces reported this activation barrier as 15.68 kcal/mol and 12.66 kcal/mol, respectively [44, 45]. It is seen that the activation barrier value (E_a = 50.92 kcal/mol) of direct scission of OH from phenol to produce benzene over Pd(111) surface is very high; and hence suggesting the absence of benzene component in the product mixture.

Finally, in summary, present Pd12-(111) catalytic model showed a very good agreement with bulk Pd(111) catalyst in terms of the adsorption energies of phenol and benzene [44, 46, 45, 92, 154, 155]. As is known that Pd catalyst exhibit similar characteristic as of Pt catalysts, the present catalytic model resulted similar observations regarding the dominating reaction progress as of Pt(111) bulk catalyst [45] but significant differences between energetics are found for each reaction step by these two catalysts. Similar to Pt(111) [45] catalyst surface, Pd(111) catalyst favours HDO of guaiacol using elimination of hydrogen from OCH_3 group of adsorbed guaiacol (RS **I**) followed by the removal of CH_2 from $C_6H_4(OH)(OCH_2)^*$ species (RS **I1**). Further, hydrogen-catecholate species undergoes hydrogenation reaction to produce catechol. During the formation of catechol over Pd(111) catalyst surface, the elimination of CH_2 from $C_6H_4(OH)(OCH_2)^*$ species controls the overall reaction rate, whereas, the dehydrogenation of methoxy group of guaiacol controls the rate of reaction partially. The production of catechol from guaiacol over Pt(111) catalyst [45] requires activation energy of 17.07 kcal/mol. Though, the Pt(111) [45] catalyst surface offers less activation energy compared to Pd(111) catalyst, the present observation are in good agreement compared to those reported by Lu et al. [45].

5.9.6. Kinetic Modelling

Kinetic analyses of all reaction steps (RS) involved in HDO of guaiacol over Pd(111) catalyst surface is carried out at atmospheric pressure and at a wide range of temperature from 473 K to 673 K with an interval temperature of 50 K. The reaction rate constants and Arrhenius constants of all reaction steps for mentioned temperature range are shown in Table 5.33. On the other hand, the reverse reaction rate constants and equilibrium reaction rate constants of all reaction steps are presented in the Table 5.34.

Table 5.33: Thermodynamic parameters of each elementary reaction step involved in HDO of guaiacol over Pd(111) catalyst surface.

RS.	Reaction	υ (cm^{-1})	k_f (s^{-1})					A (s^{-1})				
			473 K	523 K	573 K	623 K	673 K	473 K	523 K	573 K	623 K	673 K
1	$C_6H_4(OH)(OCH_3)$ (gas) + * → $C_6H_4(OH)(OCH_3)$*	---	---	---	---	---	---	---	---	---	---	---
2	$C_6H_4(OH)(OCH_3)$* + * → $C_6H_4(OH)(O)$* + *CH_3	373.24*i*	5.00E-08	6.20E-06	3.36E-04	9.72E-03	1.72E-01	5.49E+13	6.64E+13	7.86E+13	9.17E+13	1.06E+14
3	$C_6H_4(OH)(O)$* + H* → $C_6H_4(OH)(OH)$* + *	712.47*i*	6.99E+06	3.45E+07	1.31E+08	4.02E+08	1.06E+09	2.76E+13	3.19E+13	3.64E+13	4.10E+13	4.58E+13
4	$C_6H_4(OH)(OH)$* → $C_6H_4(OH)(OH)$ (gas) + *	---	---	---	---	---	---	---	---	---	---	---
5	$C_6H_4(OH)(OH)$* + * → $C_6H_4(OH)(O)$* + H*	712.47*i*	5.68E+09	1.08E+10	1.87E+10	3.00E+10	4.52E+10	1.88E+12	2.06E+12	2.26E+12	2.46E+12	2.67E+12
6	$C_6H_4(OH)(OH)$* + * → $C_6H_4(O)$* + H_2O*	280.61*i*	2.37E-04	9.63E-03	2.06E-01	2.72E+00	2.45E+01	6.19E+12	6.78E+12	7.36E+12	7.92E+12	8.45E+12
7	$C_6H_4(O)$* + H* → $C_6H_5(O)$* + *	904.73*i*	3.80E+05	1.93E+06	7.40E+06	2.29E+07	6.01E+07	5.07E+12	5.37E+12	5.64E+12	5.89E+12	6.12E+12
8	$C_6H_5(O)$* + H* → $C_6H_5(OH)$* + *	523.29*i*	7.00E+03	5.37E+04	2.89E+05	1.19E+06	3.98E+06	6.30E+12	6.73E+12	7.12E+12	7.48E+12	7.81E+12
9	$C_6H_5(OH)$* + * → C_6H_5* + OH*	350.99*i*	4.87E-11	9.78E-09	7.84E-07	3.12E-05	7.23E-04	1.64E+13	1.86E+13	2.07E+13	2.28E+13	2.49E+13
10	C_6H_5* + H* → C_6H_6* + *	1370.38*i*	5.66E+04	3.30E+05	1.42E+06	4.85E+06	1.38E+07	3.02E+12	3.22E+12	3.40E+12	3.57E+12	3.74E+12
11	C_6H_6* → C_6H_6 (gas) + *	---	---	---	---	---	---	---	---	---	---	---
12	$C_6H_4(OH)(O)$* + * → $C_6H_4(OH)$* + O*	390.15*i*	1.38E-18	1.14E-15	2.96E-13	3.18E-11	1.72E-09	1.39E+12	1.56E+12	1.74E+12	1.92E+12	2.10E+12
13	$C_6H_4(OH)$* + H* → $C_6H_5(OH)$* + *	1171.41*i*	1.65E+04	1.15E+05	5.73E+05	2.22E+06	7.02E+06	5.53E+12	5.91E+12	6.26E+12	6.60E+12	6.91E+12
14	$C_6H_5(OH)$* → $C_6H_5(OH)$ (gas) + *	---	---	---	---	---	---	---	---	---	---	---
I	$C_6H_4(OH)(OCH_3)$* + * → $C_6H_4(OH)(OCH_2)$* + H*	589.13*i*	8.43E+06	2.85E+07	7.89E+07	1.87E+08	3.93E+08	1.98E+16	8.51E+15	4.29E+15	2.43E+15	1.51E+15
I1	$C_6H_4(OH)(OCH_2)$*+H*+*→ $C_6H_4(OH)(O)$*+H*+*CH_2	520.12*i*	3.38E+06	1.54E+07	5.41E+07	1.56E+08	3.86E+08	1.54E+17	6.70E+16	3.40E+16	1.93E+16	1.20E+16
II	$C_6H_4(OH)(OCH_2)$* + H* + * → $C_6H_4(OH)(OCH)$* + 2H**	315.73*i*	1.18E-01	2.61E+00	3.41E+01	2.97E+02	1.88E+03	4.65E+08	1.25E+09	2.84E+09	5.72E+09	1.04E+10
III	$C_6H_4(OH)(OCH)$*+2H**+*→$C_6H_4(O)(OCH)$*+3H***	143.67*i*	5.79E+07	1.51E+08	3.36E+08	6.60E+08	1.18E+09	1.04E+12	1.06E+12	1.09E+12	1.12E+12	1.15E+12
IV	$C_6H_4(O)(OCH)$* + H* + * → $C_6H_4(O)(OC)$* + 2H**	727.62*i*	2.47E+00	5.42E+01	7.10E+02	6.25E+03	4.04E+04	3.12E+13	3.83E+13	4.64E+13	5.53E+13	6.52E+13
V	$C_6H_4(O)(OC)$* + 2H** + * → $C_6H_4(O)(O)$* + 2H** + C*	532.29*i*	1.08E+02	1.17E+03	8.31E+03	4.33E+04	1.77E+05	4.11E+12	4.32E+12	4.50E+12	4.67E+12	4.82E+12
V1	$C_6H_4(O)(OC)$* + 2H** + * → $C_6H_4(O)$* + 2H** + CO*	476.83*i*	7.89E+07	2.38E+08	5.94E+08	1.29E+09	2.49E+09	3.19E+12	3.49E+12	3.78E+12	4.05E+12	4.31E+12
A	$C_6H_4(OH)(OCH_3)$* + * → $C_6H_4(O)(OCH_3)$* + H*	869.49*i*	5.05E+06	1.70E+07	4.65E+07	1.09E+08	2.26E+08	1.05E+12	1.10E+12	1.14E+12	1.19E+12	1.23E+12
B	$C_6H_4(O)(OCH_3)$* + H* + * → $C_6H_4(O)(OCH_2)$* + 2H**	995.28*i*	1.28E-01	2.57E+00	3.12E+01	2.56E+02	1.55E+03	1.93E+12	2.14E+12	2.37E+12	2.60E+12	2.85E+12
C	$C_6H_4(O)(OCH_2)$*+2H**+*→$C_6H_4(O)(OCH)$*+3H***	715.34*i*	1.50E-03	3.73E-02	5.31E-01	4.97E+00	3.36E+01	3.04E+11	3.23E+11	3.42E+11	3.61E+11	3.81E+11
D	$C_6H_4(O)(OCH)$* + H* + * → $C_6H_4(O)(O)$* + H* + *CH	553.95*i*	2.11E+05	1.32E+06	6.04E+06	2.17E+07	6.46E+07	1.70E+13	1.87E+13	2.03E+13	2.18E+13	2.33E+13
E	$C_6H_4(O)(O)$* + 2H** → $C_6H_4(OH)(O)$* + H* + *	1156.32*i*	3.76E+01	4.18E+02	3.07E+03	1.65E+04	6.89E+04	1.71E+12	1.82E+12	1.93E+12	2.04E+12	2.13E+12
F	$C_6H_4(OH)(O)$* + H* → $C_6H_4(OH)(OH)$* + *	557.00*i*	1.28E+05	6.45E+05	2.46E+06	7.60E+06	1.99E+07	1.81E+12	1.89E+12	1.97E+12	2.05E+12	2.11E+12

Table 5.34: Reverse reaction rate constants and equilibrium constants of each elementary reaction step in HDO of guaiacol over Pd(111) catalyst.

RS	Reaction	k_r (s^{-1})					K_{eq}				
		473 K	523 K	573 K	623 K	673 K	473 K	523 K	573 K	623 K	673 K
1	$C_6H_4(OH)(OCH_3)$ (gas) + * → $C_6H_4(OH)(OCH_3)$*	---	---	---	---	---	---	---	---	---	---
2	$C_6H_4(OH)(OCH_3)$* + * → $C_6H_4(OH)(O)$* + *CH_3	2.96E+09	8.03E+09	1.88E+10	3.91E+10	7.42E+10	1.69E-17	7.72E-16	1.79E-14	2.49E-13	2.32E-12
3	$C_6H_4(OH)(O)$* + H* → $C_6H_4(OH)(OH)$* + *	5.68E+09	1.08E+10	1.87E+10	3.00E+10	4.52E+10	1.23E-03	3.18E-03	6.96E-03	1.34E-02	2.34E-02
4	$C_6H_4(OH)(OH)$* → $C_6H_4(OH)(OH)$ (gas) + *	---	---	---	---	---	---	---	---	---	---
5	$C_6H_4(OH)(OH)$* + * → $C_6H_4(OH)(O)$* + H*	6.99E+06	3.45E+07	1.31E+08	4.02E+08	1.06E+09	8.12E+02	3.14E+02	1.44E+02	7.45E+01	4.28E+01
6	$C_6H_4(OH)(OH)$* + * → $C_6H_4(O)$* + H_2O*	1.09E+02	1.33E+03	1.07E+04	6.27E+04	2.85E+05	2.18E-06	7.21E-06	1.92E-05	4.33E-05	8.59E-05
7	$C_6H_4(O)$* + H* → $C_6H_5(O)$* + *	3.16E-08	3.41E-06	1.64E-04	4.29E-03	6.95E-02	1.20E+13	5.66E+11	4.50E+10	5.34E+09	8.64E+08
8	$C_6H_5(O)$* + H* → $C_6H_5(OH)$* + *	7.10E+07	2.23E+08	5.78E+08	1.29E+09	2.57E+09	9.87E-05	2.41E-04	5.01E-04	9.22E-04	1.55E-03
9	$C_6H_5(OH)$* + * → C_6H_5* + OH*	1.15E+06	6.54E+06	2.78E+07	9.46E+07	2.71E+08	4.22E-17	1.49E-15	2.82E-14	3.30E-13	2.67E-12
10	C_6H_5* + H* → C_6H_6* + *	2.11E-07	1.94E-05	8.23E-04	1.93E-02	2.84E-01	2.69E+11	1.70E+10	1.73E+09	2.52E+08	4.87E+07
11	C_6H_6* → C_6H_6 (gas) + *	---	---	---	---	---	---	---	---	---	---
12	$C_6H_4(OH)(O)$* + * → $C_6H_4(OH)$* + O*	6.46E+04	4.85E+05	2.58E+06	1.06E+07	3.56E+07	2.14E-23	2.35E-21	1.15E-19	2.99E-18	4.82E-17
13	$C_6H_4(OH)$* + H* → $C_6H_5(OH)$* + *	9.99E-07	7.78E-05	2.86E-03	5.96E-02	7.96E-01	1.65E+10	1.48E+09	2.00E+08	3.72E+07	8.83E+06
14	$C_6H_5(OH)$* → $C_6H_5(OH)$ (gas) + *	---	---	---	---	---	---	---	---	---	---
I	$C_6H_4(OH)(OCH_3)$* + * → $C_6H_4(OH)(OCH_2)$* + H*	6.81E+04	4.46E+05	2.11E+06	7.79E+06	2.37E+07	1.24E+02	6.39E+01	3.73E+01	2.40E+01	1.65E+01
I1	$C_6H_4(OH)(OCH_2)$* + H* + * → $C_6H_4(OH)(O)$* + H* + *CH_2	7.47E+03	5.06E+04	2.46E+05	9.30E+05	2.88E+06	4.52E+02	3.04E+02	2.20E+02	1.68E+02	1.34E+02
II	$C_6H_4(OH)(OCH_2)$* + H* + * → $C_6H_4(OH)(OCH)$* + 2H**	3.93E+09	9.26E+09	1.89E+10	3.45E+10	5.76E+10	3.00E-11	2.82E-10	1.80E-09	8.61E-09	3.27E-08
III	$C_6H_4(OH)(OCH)$* + 2H** + * → $C_6H_4(O)(OCH)$* + 3H***	1.32E+06	6.05E+06	2.14E+07	6.18E+07	1.53E+08	4.40E+01	2.50E+01	1.57E+01	1.07E+01	7.69E+00
IV	$C_6H_4(O)(OCH)$* + H* + * → $C_6H_4(O)(OC)$* + 2H**	1.99E+08	6.78E+08	1.88E+09	4.48E+09	9.47E+09	1.24E-08	8.01E-08	3.77E-07	1.39E-06	4.26E-06
V	$C_6H_4(O)(OC)$* + 2H** + * → $C_6H_4(O)(O)$* + 2H** + C*	2.04E+00	3.00E+01	2.77E+02	1.79E+03	8.79E+03	5.29E+01	3.89E+01	3.00E+01	2.42E+01	2.01E+01
V1	$C_6H_4(O)(OC)$* + 2H** + * → $C_6H_4(O)$* + 2H** + CO*	3.05E-06	1.61E-04	4.26E-03	6.67E-02	6.94E-01	2.58E+13	1.48E+12	1.40E+11	1.93E+10	3.59E+09
A	$C_6H_4(OH)(OCH_3)$* + * → $C_6H_4(O)(OCH_3)$* + H*	1.97E+04	1.27E+05	5.96E+05	2.18E+06	6.60E+06	2.57E+02	1.33E+02	7.80E+01	4.99E+01	3.42E+01
B	$C_6H_4(O)(OCH_3)$* + H* + * → $C_6H_4(O)(OCH_2)$* + 2H**	3.27E+07	8.15E+07	1.73E+08	3.27E+08	5.63E+08	3.90E-09	3.16E-08	1.80E-07	7.83E-07	2.76E-06
C	$C_6H_4(O)(OCH_2)$* + 2H** + * → $C_6H_4(O)(OCH)$* + 3H***	1.44E+12	1.54E+12	1.64E+12	1.73E+12	1.81E+12	1.05E-15	2.42E-14	3.24E-13	2.88E-12	1.85E-11
D	$C_6H_4(O)(OCH)$* + H* + * → $C_6H_4(O)(O)$* + H* + *CH	4.53E-04	1.42E-02	2.44E-01	2.67E+00	2.05E+01	4.67E+08	9.32E+07	2.47E+07	8.13E+06	3.16E+06
E	$C_6H_4(O)(O)$* + 2H** → $C_6H_4(OH)(O)$* + H* + *	8.96E+03	6.08E+04	2.98E+05	1.14E+06	3.60E+06	4.19E-03	6.87E-03	1.03E-02	1.44E-02	1.92E-02
F	$C_6H_4(OH)(O)$* + H* → $C_6H_4(OH)(OH)$* + *	4.80E+06	2.04E+07	6.75E+07	1.85E+08	4.40E+08	2.65E-02	3.17E-02	3.65E-02	4.10E-02	4.51E-02

As has been discussed in a previous subsection that scission of methyl functional group from guaiacol is not advantageous from activation energy point of view, the kinetic analysis of this reaction reaffirms previous observations because the reaction rate constants of reaction step **2**, i.e., scission of methyl group from guaiacol, are very less at each temperature condition (Table 5.33). However, the increment of temperature accelerates the reaction but even at 673 K, the reaction does not become feasible. Further, it is very clear that direct demethylation of guaiacol is not going to be feasible even at 673 K because K_{eq} value is in the order of 10^{-12} (Table 5.34) which suggests that reversibility of the reaction prevails dominatingly, therefore, it further affirms the previous observations about the direct scission of the methyl group. It has also been concluded in a previous subsection that HDO of guaiacol does not progress through reaction steps **A**, **B**, and **C**; though, reaction step **A** requires considerably lower barrier height compared to RS **I**. It can be seen that the rate constants of RS **A** and RS **I** are of comparatively same order at each temperature condition suggesting the possibility of either hydrogen reduction process (i.e., either RS **A** or RS **I**). But, the following reaction step(s) in both reaction progresses, i.e., **B** preceded by RS **A** and, **II** and **I1** preceded by RS **I**, suggest to follow the reaction progress of **I1** compared to **B** and **II**. Because the rate constants (see Table 5.33) of RS **I1** provide extremely favourable environment for the reaction progress compared to that of RS **B** and RS **II**. It can be seen in Table 5.33 that at each temperature condition, the reaction rate constants due to RS **I1** dominate over RS **B** and RS **II**. The rate determining step of formation of catechol from HDO of guaiacol over Pd(111) catalyst, i.e., reaction step **I1** is considerably advantageous even at temperature of 473 K because the reaction rate constant is of 10^6 order. Further, as temperature increases to 673 K, its rate constant increases to the order of 10^8 s^{-1}. On the other hand, the rate constant of RS **II** at 473 K is in the order of 10^{-1} s^{-1} and as the temperature increases, the rate constants of RS **II** improve and become larger than of order of 10^0 but they

never overcome the corresponding rate constants due to RS **I1**. However, it is also an observable fact that the differences in both reactions' rate constants (RS **II** and RS **I1**) at each temperature are in the range of 10^5-10^7 s^{-1} which is a huge difference. Therefore, the previous observations in energy barrier analysis about the favourable reaction approach of formation of catechol from HDO of guaiacol over Pd(111) surface are further affirmed by kinetic analysis. In addition, the kinetic analysis also affirmed that the abundance of catechol in the product mixture will be higher because further reduction reactions are very slow and not likely to occur even at high temperatures considered in this study.

5.10. Pt- and Pd-doped Graphene Sheets as Catalysts for Upgrading Bio-oil Model Compounds: Chemisorption Study by DFT

In the recent past, a significant amount of research has been dedicated to synthesize the viable catalyst for bio-oil upgrading but till date, no optimum catalytic system has been synthesized which can be inexpensive, easily available, highly active and product selective. It has been recently reviewed that noble metal catalysts are better option for upgrading bio-oil compared to conventional hydrotreating catalysts, i.e., sulfided NiMo or CoMo [16]. Further, the catalyst supports, for instance, Al_2O_3, SiO_2, TiO_2, MgO, C, etc. could play a vivacious role in being product selective along with the metal catalysts [16]. Unlike acidic and basic catalyst supports, the carbon supports show better stability in both acidic and basic environments and, thus, they have received a considerable amount of attention as catalyst support in bio-oil upgrading [16, 158]. Furthermore, numerous types of carbon supports are tested, e.g., activated carbon, carbon black and carbon nanostructures; however, amongst all, carbon nanostructures such as graphene sheets, carbon nanotubes and carbon nanofibers are momentously sought after recently as catalyst support because of their impressively high surface area, tensile strength, thermal stability, recyclability, etc. [159, 160]. A comprehensive review is recently presented by Lam and Luong [161] on superiority of carbon as catalyst support in the conversion of biomass to fuel and valuable products.

Carbon nanostructures, especially, graphene sheets have become widely popular because of their outstanding mechanical and chemical properties, e.g., pristine graphene at room temperature has a very high electron mobility of ~10000 $cm^2V^{-1}s^{-1}$, theoretical specific surface area of 2630 m^2g^{-1}, 2.3% white light absorbance with negligible reflectance, thermal conductivity of 3000-5000 $Wm^{-1}K^{-1}$, and a Young's modulus of 1 TPa [162–166]. Graphene is

a two-dimensional sheet with strong sp^2-hybridised carbon atoms in hexagonal monolayer [163]. Further, due to sp^2 bindings among carbon atoms, it is chemically inert and shows weak interaction with the reaction center which consequences the possibility of graphene as catalyst support to hetero metal atoms [158, 167]. Therefore, this combination of noble metal catalyst on graphene support would considerably influence the selectivity and yield of desired products in bio-oil upgrading process. For graphene as catalyst, chemical inertness paves its way; however, recent studies indicate that doping of heteroatom especially transition metal (TM) atom at the defect site of graphene could substantially increase its electronic structure and chemical reactivity [158, 168, 169]. Thus, a transition metal doped graphene sheets have a great potential in catalysis.

Despite such great advantages, only a very little research work in bio-oil upgrading area utilizing graphene sheet as catalyst support or metal doped graphene sheet as catalyst exist in the literature. For instance, Wu et al. [170] performed hydrogenation of levulinic acid to produce ϒ-valerolactone (GVL) over graphene supported ruthenium nanoparticles. They observed high catalytic activity and reported 96 % of GVL yield at low temperature of only 30^{o}C. In addition, they also concluded that electron rich Ru nanoparticles are due to π-electron structure of graphene which enhances the activity of hydrogenation of C=O bonds in levulinic acid. Similarly, Shi et al. [171] carried out conversion reactions of aromatic bio-oil compounds over Ru nanoparticles encapsulated within nitrogen doped graphene (Ru-G) sheets. In addition, they also compared their results with other supports such as activated carbon, SiO_2, Al_2O_3, Fe_3O_4, and MgO; showed that hydrogenation of all aromatic compounds with very high percentages of selectivity and conversion over Ru-G sheets compared to all other supports. Wang et al. [172] analysed the difference between the performance of reduced graphene oxide (rGO) and benzenesulphonic acid functionalized reduced graphene oxide (rGO-S) supported Ru nanoparticles for hydrogenation of levulinic acid to produce GVL. They observed higher

yield of GVL over Ru/rGO-S compared to Ru/rGO because of bifunctionality of catalytic system. On the other hand, theoretical works applying graphene supported catalytic HDO of bio-oil are only a few. The application of graphene as catalyst support for Ru nanoparticles is carried out by Rubeš et al. [156] for HDO of phenol numerically. The $C_{aromatic}$-OH bond scission over bare Ru nanoparticles were reported unstable; however, graphene supported Ru nanoparticles stabilized the C-O bond scission which, in turn, reduced the energy requirement. Only other theoretical work is due to the Fellah [173] who carried out decarbonylation reaction of furfural to produce furan over Pt-doped graphene sheet. They reported overall activation energy as 19.6 kcal/mol with the conclusion of furan formation elementary reaction step as the rate controlling reaction step.

In this work, the adsorption characteristics of a few phenolic bio-oil model compounds such as phenol, anisole, guaiacol, salicylaldehyde (2-HB), and vanillin (see Figure 5.62 for molecular structures) over Pd- and Pt-doped graphene sheets are considered under the density functional theory (DFT) framework. In this process, various adsorption configurations of model compounds are considered and reported their kinetics over Pd- and Pt-doped graphene sheets over a wide range of temperature, i.e., 400-800 K at an interval temperature of 100 K.

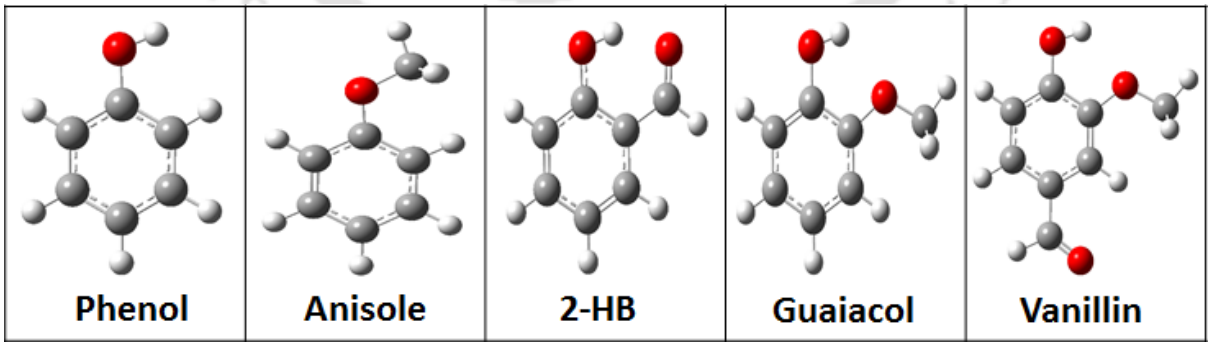

Figure 5.62: Considered phenolic species, i.e., phenol, anisole, salicylaldehyde (2-HB), guaiacol, and vanillin.

Pristine graphene sheet is developed employing 14 benzene rings which included 42 carbon atoms. The dangling carbon atoms at the edges are terminated using 16 hydrogen atoms (Figure 5.63a). Further, a single vacancy is created in the graphene sheet by removing a carbon atom (Figure 5.63b) so that to allow the deposition of Pd or Pt metal atom. The existence of defect site in graphene sheet could allow the deposition of transition metal atoms and recently, various literature observations have avowed this phenomena [168, 169, 174]. The deposition of heteroatom over graphene vacancy is a very vital amendment because it modifies the electronic and magnetic properties of graphene that may be helpful in synthesizing a novel and advanced catalyst [167, 168, 174]. Nevertheless, upon deposition of Pd or Pt atom over the monovacant site of graphene, metal atom binds with neighbouring carbon atoms of graphene with release of high energy (see Figures 5.63c and 5.63d for Pd and Pt doping, respectively).

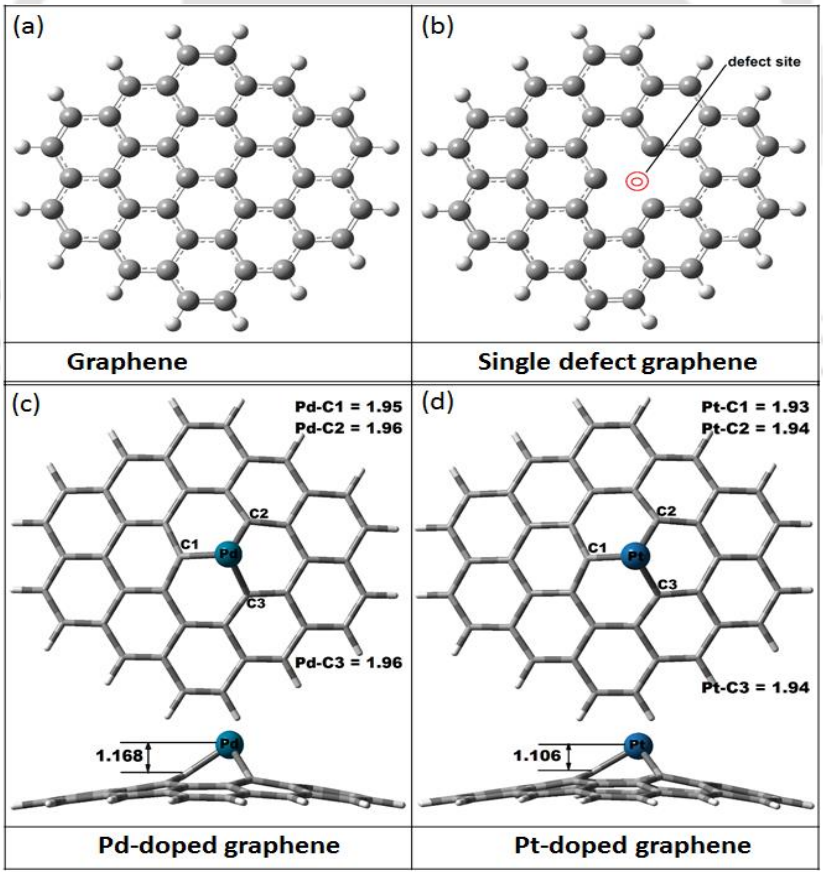

Figure 5.63: Structures of graphene, monovacant graphene, Pd-doped, and Pt-doped graphene sheets.

Table 5.35: The stability analyses of metal doped graphene surfaces.

SM	E_{Rel} (kcal/mol)	
	Pd-doped	Pt-doped
1	0.00	0.00
3	20.96	24.40
5	67.98	68.60
7	130.22	126.40
9	197.03	194.21

The spin state analyses of metal doped graphene is performed through single point energy calculations at various spin multiplicities (SM = 2S + 1, where S is total spin of the system) and the relative energies at various spin multiplicities are presented in Table 5.35. Further, the metal atom doped graphene is applied for the adsorption of phenolic species, i.e., phenol, anisole, guaiacol, 2-HB, and vanillin with fixed spatial movement of graphene surface. The adsorption energies of metal atoms over monovacant graphene and phenolic components over metal doped graphene are evaluated using following equations:

$$E_{ads}\ (Pd\ or\ Pt) = E_{Pd\ or\ Pt\ doped\ graphene} - (E_{Pd\ or\ Pt} + E_{monovacant\ graphene}) \quad (5.1)$$

$$E_{ads}\ (Phenolic\ Components) = E_{adsorbate+metal\ doped\ graphene} - (E_{adsorbate} + E_{metal\ doped\ graphene}) \quad (5.2)$$

Further, the chemical hardness (η), chemical potential (μ) and electronegativity (χ) of metal doped graphene sheets are evaluated using following equations, respectively:

$$\eta \cong (I - A)/2 \quad (5.3)$$

$$\mu \cong -(I + A)/2 \quad (5.4)$$

$$\chi \cong -\mu \quad (5.5)$$

where, $I \approx -\varepsilon_{HOMO}$ and $A \approx -\varepsilon_{LUMO}$ of metal doped graphene sheets.

Geometry optimization of each structure is performed using B3PW91 [125, 126] functional under the framework of density functional theory (DFT) [118, 119]. The Los Alamos LANL2DZ [127] effective core potential basis set is utilised for Pt and Pd atoms, whereas, triple-zeta Pople's basis set, 6-311+g(d,p) [175], is employed for all H, C and O atoms. A normal mode vibrational frequency calculation is performed on each structure to testify the location of structure on PES. Furthermore, the thermodynamic parameters are calculated at atmospheric pressure and a wide range of temperature of 400-800 K at 100 K interval temperature.

5.10.1. Deposition of metal atoms over monovacant graphene

A graphene sheet with monovacancy can be obtained by elimination of a carbon atom from graphene sheet (see Figure 5.63a) which leaves three sp^2 carbons dangling (see Figure 5.63b). However, upon deposition of Pd or Pt atom over defect site of graphene, the dangling carbon atoms of defective graphene bind with metal. The Pd atom doped graphene can be seen in Figure 5.63c where the carbon atoms labelled as 1, 2, and 3 are bonded with Pd atom. The bond lengths of Pd to C1, C2, and C3 are evaluated as 1.95 Å, 1.96 Å, and 1.96 Å, respectively. Due to large radius of Pd atom compared to carbon atoms, Pd atom stems out of the graphene sheet upon deposition and its vertical distance from graphene plane is found as 1.168 Å. On the other hand, the bond lengths of Pt to C1, C2, and C3 are calculated as 1.93 Å, 1.94 Å, and 1.94 Å, respectively. Similar to Pd doped graphene, Pt atom also stems out of the graphene plane by 1.106 Å of vertical distance. The binding energies of Pd and Pt atoms with defective graphene sheets are calculated as -114.77 kcal/mol and -175.60 kcal/mol, respectively. The binding energy of Pd with defective graphene is in very good agreement with the work of Ferrante et al. [174] and López et al. [176] who evaluated these energies as -116.7 kcal/mol and -118.3 kcal/mol, respectively. On the other hand, the binding energy of Pt with defective graphene is also in good agreement with Tang et al. [177] who calculated it as -167 kcal/mol. These

extremely high binding energies (high negative values) due to deposition of both metal atoms to the defective graphene show strong chemisorption process. Further, to locate their ground state spin multiplicities, a stability analysis is carried out on each metal doped surface. The stability analyses of both metal doped graphene sheets illustrates their ground state in singlet spin state (see Table 5.35). Furthermore, the chemical hardnesses, chemical potentials and electronegativities of Pd-doped graphene (PdGr) and Pt-doped graphene (PtGr) sheets are evaluated using equations (5.3)-(5.5) as 23.87 kcal/mol and 23.29 kcal/mol; -79.75 kcal/mol and -81.19 kcal/mol; and 79.75 kcal/mol and 81.19 kcal/mol, respectively. The Cartesian coordinates of graphene, Pd-doped, and Pt-doped graphene sheets are given in Appendix Table 3 along with their electronic energies and zero-point vibrational energies (ZPVE).

5.10.2. Adsorption of phenol

The adsorption of phenol over both metal doped surfaces occurs through two configurations, i.e., one with the interaction of oxygen atom of hydroxyl group to metal atom (configuration 1 of Figure 5.64) and the other with the interaction of aromatic ring carbon atoms to metal atom (configuration 2 of Figure 5.64). The stability analyses of both configurations over PdGr and PtGr are performed for locating the favourable spin multiplicity of ground state; and, the ground states of all configurations over each surface lie in singlet spin state (see Appendix Table 4). The adsorption energies of both configurations over each metal doped graphene sheet are presented in Table 5.36.

It is observed that PdGr binds more tightly with phenol compared to PtGr because of higher energy release of both adsorption configurations; and, also because of lower binding distances between metal and interacting atoms of adsorbate. For instance, the binding distance of oxygen atom of OH group of phenol from Pd atom of PdGr is evaluated as 2.40 Å (see configuration 1 of Figure 5.64), whereas, the corresponding distance over PtGr is reported as

2.42 Å. Similarly, the average bond lengths of interacting aromatic carbon atoms of phenol to PdGr and PtGr are 2.77 Å and 2.96 Å, respectively. Therefore, a strong adsorption of phenol can be seen over PdGr compared to PtGr surface. It is worth to note here that both metal doped surfaces do not offer the interaction of whole benzenoid ring because of an oxy-functional attached to it. Furthermore, thermochemistry analyses reveal strong release of energies for both adsorption configurations of phenol over each catalyst surface. In addition, the available free energies of both adsorption configurations are quite high. However, it is observed that both catalytic surfaces offer similar thermochemistry because of similar adsorption free energies (see Table 5.36) and adsorption enthalpies (see Table 5.37).

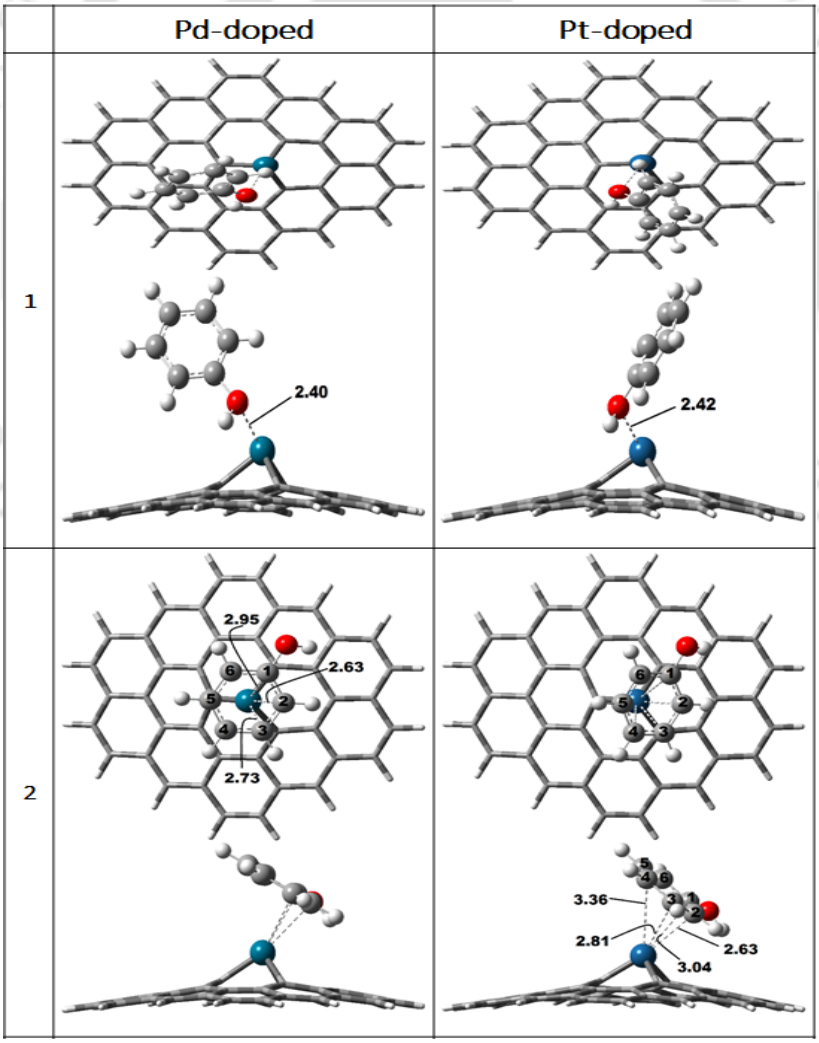

Figure 5.64: Adsorption configurations of phenol.

Table 5.36: Adsorption energies of each model compound over both metal doped graphene sheets with and without D3 corrections.

Species	Adsorption configuration	E_{ads} (kcal/mol)			
		Pd-doped		Pt-doped	
		B3PW91	B3PW91-D3	B3PW91	B3PW91-D3
Phenol	**1**	-9.65	-23.58	-8.14	-22.88
	2	-10.50	-25.28	-8.75	-26.69
2-HB	**1**	-7.47	-27.28	-5.91	-27.57
	2	-2.47	-21.42	-7.73	-26.37
	3	-6.99	-23.08	-9.45	-31.09
Anisole	**1**	-10.38	-25.88	-7.68	-26.28
	2	-7.34	-19.52	-5.48	-20.97
Guaiacol	**1**	-10.91	-28.06	-8.81	-27.23
	2	-6.56	-21.38	-5.09	-22.23
	3	-9.28	-26.80	-7.44	-25.22
Vanillin	**1**	-7.10	-27.76	-6.48	-25.34
	2	-5.14	-19.86	-3.62	-21.09
	3	-12.17	-24.40	-11.26	-26.51
	4	-7.19	-26.33	-4.80	-26.24

Based on free energies of adsorption, evaluations of equilibrium rate constants are carried out and proposed relations of ln $\mathbf{K_{eq}}$ vs. **1/T** (see Table 5.38) for each adsorption case at a temperature range of 400-800 K. The pressure of the system is kept constant at 1 atm for each thermochemical analysis. Due to very close values of equilibrium constants, the ln $\mathbf{K_{eq}}$ vs. **1/T** plots are difficult to read, therefore, all K_{eq} values are presented in Table 5.38 with corresponding ln $\mathbf{K_{eq}}$ vs. **1/T** relations for discussed temperature range. Still, ln $\mathbf{K_{eq}}$ vs. **1/T** plots are presented in Appendix Figure 1. A very high equilibrium rate constant can be observed for each adsorption configuration of phenol over both catalytic surfaces. At 400 K, K_{eq} value of configuration 1 of phenol over PdGr is in the order of 10^{131}, whereas, for configuration 2, it is in the order of 10^{132}. On the other hand, both configurations of phenol over PtGr represent K_{eq} values in the range of 10^{131}.

Table 5.37: The free energy of adsorption (G_{ads}) and adsorption enthalpy (H_{Ads}) of each model compound over both catalyst surfaces.

Metal doped	Adsorbed Species	Adsorption Configuration	G_{Ads} (kcal/mol)					H_{Ads} (kcal/mol)				
			400 K	500 K	600 K	700 K	800 K	400 K	500 K	600 K	700 K	800 K
Pd-doped graphene	Phenol	1	-240.62	-223.42	-202.69	-178.59	-151.32	-302.19	-318.39	-337.41	-358.66	-381.67
		2	-241.23	-223.98	-203.20	-179.06	-151.75	-303.03	-319.20	-338.20	-359.43	-382.43
	2-HB	1	-238.80	-221.63	-200.94	-176.88	-149.65	-300.24	-316.42	-335.43	-356.67	-379.68
		2	-234.05	-216.90	-196.22	-172.18	-144.98	-295.48	-311.62	-330.59	-351.79	-374.76
		3	-238.41	-221.31	-200.67	-176.67	-149.51	-299.65	-315.80	-334.79	-356.01	-379.00
	Anisole	1	-240.19	-222.75	-201.77	-177.43	-149.92	-302.79	-318.95	-337.95	-359.17	-382.17
		2	-238.73	-221.66	-201.06	-177.10	-149.97	-299.82	-315.98	-334.97	-356.20	-379.20
	Guaiacol	1	-241.23	-223.89	-203.03	-178.80	-151.40	-303.38	-319.54	-338.53	-359.76	-382.76
		2	-238.42	-221.41	-200.87	-176.97	-149.90	-299.29	-315.44	-334.42	-355.63	-378.61
		3	-241.54	-224.65	-204.23	-180.45	-153.50	-301.88	-318.05	-337.06	-358.30	-381.30
	Vanillin	1	-238.31	-221.16	-200.49	-176.44	-149.24	-299.70	-315.87	-334.87	-356.10	-379.10
		2	-236.78	-219.71	-199.10	-175.14	-148.01	-297.91	-314.05	-333.03	-354.24	-377.23
		3	-243.38	-226.26	-205.60	-181.58	-154.40	-304.70	-320.86	-339.85	-361.08	-384.07
		4	-238.85	-221.82	-201.26	-177.33	-150.24	-299.80	-315.95	-334.93	-356.15	-379.14
Pt-doped graphene	Phenol	1	-240.07	-222.97	-202.35	-178.38	-151.25	-301.29	-317.39	-336.34	-357.53	-380.50
		2	-239.59	-222.24	-201.37	-177.15	-149.77	-301.82	-317.91	-336.85	-358.03	-380.99
	2-HB	1	-238.48	-221.50	-201.00	-177.15	-150.13	-299.23	-315.33	-334.27	-355.46	-378.42
		2	-237.71	-219.95	-198.68	-174.06	-146.29	-301.62	-317.67	-336.56	-357.69	-380.61
		3	-239.24	-221.46	-200.17	-175.53	-147.74	-303.21	-319.27	-338.17	-359.32	-382.25
	Anisole	1	-239.99	-223.01	-202.52	-178.68	-151.68	-300.76	-316.82	-335.74	-356.90	-379.85
		2	-237.79	-220.81	-200.32	-176.47	-149.46	-298.57	-314.63	-333.55	-354.72	-377.67
	Guaiacol	1	-240.62	-223.53	-202.93	-178.97	-151.84	-301.84	-317.92	-336.85	-358.03	-380.98
		2	-237.13	-220.02	-199.41	-175.44	-148.32	-298.40	-314.46	-333.37	-354.52	-377.47
		3	-240.03	-223.08	-202.61	-178.79	-151.81	-300.67	-316.75	-335.68	-356.86	-379.82
	Vanillin	1	-239.72	-222.91	-202.60	-178.93	-152.09	-299.77	-315.85	-334.78	-355.96	-378.91
		2	-236.55	-219.64	-199.23	-175.47	-148.55	-297.01	-313.06	-331.97	-353.12	-376.06
		3	-242.08	-224.73	-203.86	-179.64	-152.26	-304.35	-320.42	-339.35	-360.53	-383.48
		4	-237.43	-220.50	-200.06	-176.26	-149.30	-298.02	-314.08	-332.99	-354.16	-377.11

Table 5.38: The equilibrium constants (K_{eq}) and relations of ln $\mathbf{K_{eq}}$ vs. **1/T** of all adsorbed configurations.

Metal doped	Adsorbed Species	Adsorption Configuration	K_{eq}					ln K_{eq} vs. 1/T
			400 K	500 K	600 K	700 K	800 K	
Pd doped graphene	Phenol	1	8.77E+131	1.02E+98	1.25E+74	9.11E+55	3.08E+41	ln K_{eq} = -51.339(1/T) + 338.91
		2	1.90E+132	1.81E+98	1.93E+74	1.28E+56	4.03E+41	ln K_{eq} = -51.463(1/T) + 339.76
	2-HB	1	8.80E+130	1.69E+97	2.86E+73	2.65E+55	1.07E+41	ln K_{eq} = -51.033(1/T) + 336.42
		2	2.20E+128	1.41E+95	5.39E+71	8.96E+53	5.63E+39	ln K_{eq} = -50.284(1/T) + 329.96
		3	5.41E+130	1.21E+97	2.28E+73	2.29E+55	9.81E+40	ln K_{eq} = -50.935(1/T) + 335.87
	Anisole	1	5.13E+131	5.18E+97	5.75E+73	3.94E+55	1.27E+41	ln K_{eq} = -51.424(1/T) + 338.43
		2	8.13E+130	1.74E+97	3.18E+73	3.12E+55	1.31E+41	ln K_{eq} = -50.963(1/T) + 336.30
	Guaiacol	1	1.89E+132	1.65E+98	1.66E+74	1.06E+56	3.24E+41	ln K_{eq} = -51.515(1/T) + 339.79
		2	5.48E+130	1.34E+97	2.70E+73	2.83E+55	1.26E+41	ln K_{eq} = -50.877(1/T) + 335.85
		3	2.80E+132	3.55E+98	4.58E+74	3.49E+56	1.22E+42	ln K_{eq} = -51.286(1/T) + 340.04
	Vanillin	1	4.76E+130	1.05E+97	1.95E+73	1.94E+55	8.25E+40	ln K_{eq} = -50.946(1/T) + 335.75
		2	6.93E+129	2.40E+96	6.10E+72	7.55E+54	3.80E+40	ln K_{eq} = -50.663(1/T) + 333.65
		3	2.89E+133	1.80E+99	1.45E+75	7.90E+56	2.15E+42	ln K_{eq} = -51.720(1/T) + 342.64
		4	9.42E+130	2.03E+97	3.74E+73	3.68E+55	1.56E+41	ln K_{eq} = -50.957(1/T) + 336.44
Pt doped graphene	Phenol	1	4.38E+131	6.50E+97	9.42E+73	7.85E+55	2.94E+41	ln K_{eq} = -51.178(1/T) + 338.11
		2	2.38E+131	3.10E+97	4.13E+73	3.24E+55	1.16E+41	ln K_{eq} = -51.257(1/T) + 337.55
	2-HB	1	5.88E+130	1.47E+97	3.01E+73	3.22E+55	1.45E+41	ln K_{eq} = -50.858(1/T) + 335.90
		2	2.24E+130	3.08E+96	4.28E+72	3.48E+54	1.29E+40	ln K_{eq} = -51.216(1/T) + 335.15
		3	1.54E+131	1.42E+97	1.50E+73	1.01E+55	3.21E+40	ln K_{eq} = -51.466(1/T) + 337.23
	Anisole	1	3.97E+131	6.78E+97	1.09E+74	9.74E+55	3.86E+41	ln K_{eq} = -51.087(1/T) + 337.95
		2	2.47E+130	7.32E+96	1.69E+73	1.98E+55	9.53E+40	ln K_{eq} = -50.748(1/T) + 334.96
	Guaiacol	1	8.85E+131	1.15E+98	1.52E+74	1.20E+56	4.28E+41	ln K_{eq} = -51.259(1/T) + 338.86
		2	1.07E+130	3.31E+96	7.89E+72	9.42E+54	4.63E+40	ln K_{eq} = -50.720(1/T) + 334.10
		3	4.15E+131	7.23E+97	1.17E+74	1.05E+56	4.19E+41	ln K_{eq} = -51.078(1/T) + 337.99
	Vanillin	1	2.81E+131	6.14E+97	1.16E+74	1.16E+56	5.02E+41	ln K_{eq} = -50.938(1/T) + 337.51
		2	5.13E+129	2.26E+96	6.81E+72	9.61E+54	5.36E+40	ln K_{eq} = -50.503(1/T) + 333.23
		3	5.59E+132	3.85E+98	3.36E+74	1.95E+56	5.57E+41	ln K_{eq} = -51.647(1/T) + 340.94
		4	1.57E+130	5.35E+96	1.36E+73	1.70E+55	8.62E+40	ln K_{eq} = -50.662(1/T) + 334.45

This, in turn, justifies the previous prediction of poor adsorption energy of phenol over PtGr surface compared to PdGr surface. A high positive amount of K_{eq} value, in general, represents higher product formation or in other words, the equilibrium shifts towards product. Therefore, it can be observed that both catalytic surfaces offer a favourable environment for adsorption of gas phase phenol component. However, the temperature increment does not favour the adsorption spontaneity because adsorption free energies of both configurations of phenol over each catalytic surface reduce with increase of temperature (see Table 5.37). On the other hand, adsorption enthalpies of both configurations of phenol over PdGr and PtGr surfaces increase with increasing temperature. Therefore, it can be concluded that the adsorption of gas phase phenol over either catalyst surfaces are highly recommendable even at lower possible temperature compared to high temperature process.

5.10.3. Adsorption of Anisole

Two most stable adsorption configurations of anisole are: 1) with the interactions of aromatic carbon atoms to the metal doped graphene, and 2) with the interaction of oxygen atom of methoxy group of anisole to the metal doped graphene. The stability analyses of both configurations over each catalyst surface are carried out to find the favourable spin multiplicity of ground state; and, for all adsorption cases, the ground state structures lie in singlet spin state (see Appendix Table 4). The PdGr surface acts efficiently compared to PtGr because of tight binding of each configuration with PdGr surface. The binding distances of oxygen atom of methoxy group to Pd and Pt atoms (see configuration 2 in Figure 5.65) are calculated as 2.46 Å and 2.50 Å, respectively. On the other hand, the average distances of interacting phenyl carbon atoms of anisole (see configuration 1 of Figure 5.65) with Pd and Pt metal atoms of metal doped graphene sheets are reported as ~2.86 Å and ~2.89 Å, respectively. It is clear from binding distances of anisole to the catalyst surfaces that PdGr surface offers tight binding and thus better adsorption compared to PtGr surface. However, the adsorbed geometries of anisole

in configuration 2 over PdGr and PtGr surfaces sense disturbance in their dihedral angle compared to gas phase anisole species because their methyl groups bend by 16.85^{o} and 20.87^{o}, respectively from the phenyl plane.

Thermochemical parameters such as free energies of adsorption and adsorption enthalpies of adsorbed anisole configurations over each surface are presented in Table 5.37. Similar to the case of phenol adsorptions, the thermochemical parameters of anisole are also very high. For instance, the free energy and enthalpies of configurations 1 and 2 over PdGr are -240.19 kcal/mol and -238.41 kcal/mol, respectively; and, on the other hand, the same over PtGr are reported as -239.99 kcal/mol and -237.79 kcal/mol (see Table 5.37), respectively. Similarly, the equilibrium constant values of configurations 1 and 2 over PdGr and PtGr surfaces are in the similar order of 10^{131} and 10^{130} (see Table 5.38), respectively.

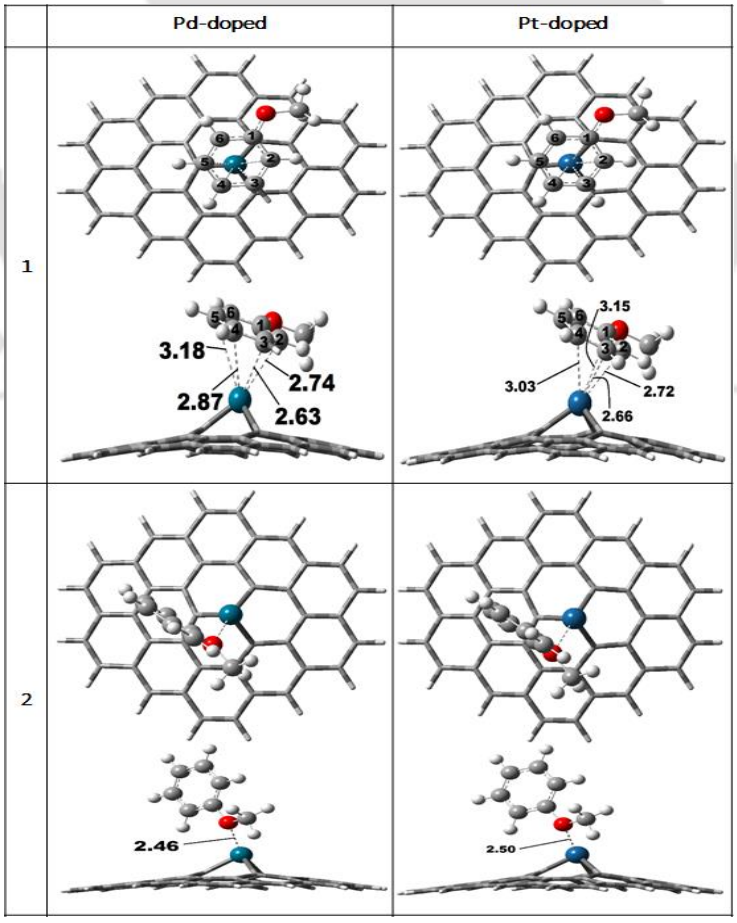

Figure 5.65: Adsorption configurations of anisole.

The linear plots of ln $\mathbf{K_{eq}}$ vs. **1/T** are shown in Appendix Figure 1. According to the adsorption energies (Table 5.36) and thermochemical parameters (Tables 5.37 and 5.38), it appears that PdGr surface is more convivial for the adsorbate compared to PtGr surface. However, between both anisole adsorption configurations over each catalytic surface, configuration 1 is more stable compared to configuration 2 because of increased number of atoms' interactions with catalyst surfaces thus strong adsorption energy.

5.10.4. Adsorption of Guaiacol

As shown in Figure 5.66, guaiacol adsorbs over metal doped graphene sheets by three possible configurations, i.e., i) by phenyl ring (configuration 1), ii) by oxygen atom of methoxy group (configuration 2), and iii) by oxygen atom of hydroxyl group (configuration 3). The adsorption energies of these three configurations are presented in Table 5.36. Similar to the previous cases of stability analyses, all configurations of guaiacol over each surface are most stable in singlet state (see Appendix Table 4). It is seen in Table 5.36 that the adsorptions of guaiacol *via* phenyl ring over both metal doped surfaces are highly stable compared to the interactions of oxygen atoms, i.e., configurations 2 and 3; however, the interaction of hydroxyl group to the metal doped graphene sheets (configuration 2) is comparatively more advantageous than configuration 2 because of better adsorption energy. In configuration 1, the average distances of interacting phenyl carbon atoms to the PdGr and PtGr are reported as 2.82 Å and 2.89 Å, respectively. Both catalytic surfaces do not offer complete phenyl interaction (see configuration 1 of Figure 5.66) to their metals but they allow partial interaction, for instance, phenyl carbon atoms labelled as 3, 4, and 5 are the only carbon atoms which interact exceedingly to the PdGr surface, whereas, over PtGr, only two phenyl carbon atoms show higher interaction with the metal. On the other hand, same binding lengths are found between oxygen atoms and Pd in configurations 2 and 3 of PdGr but PtGr surface offers different binding distances for both configurations (see Figure 5.66).

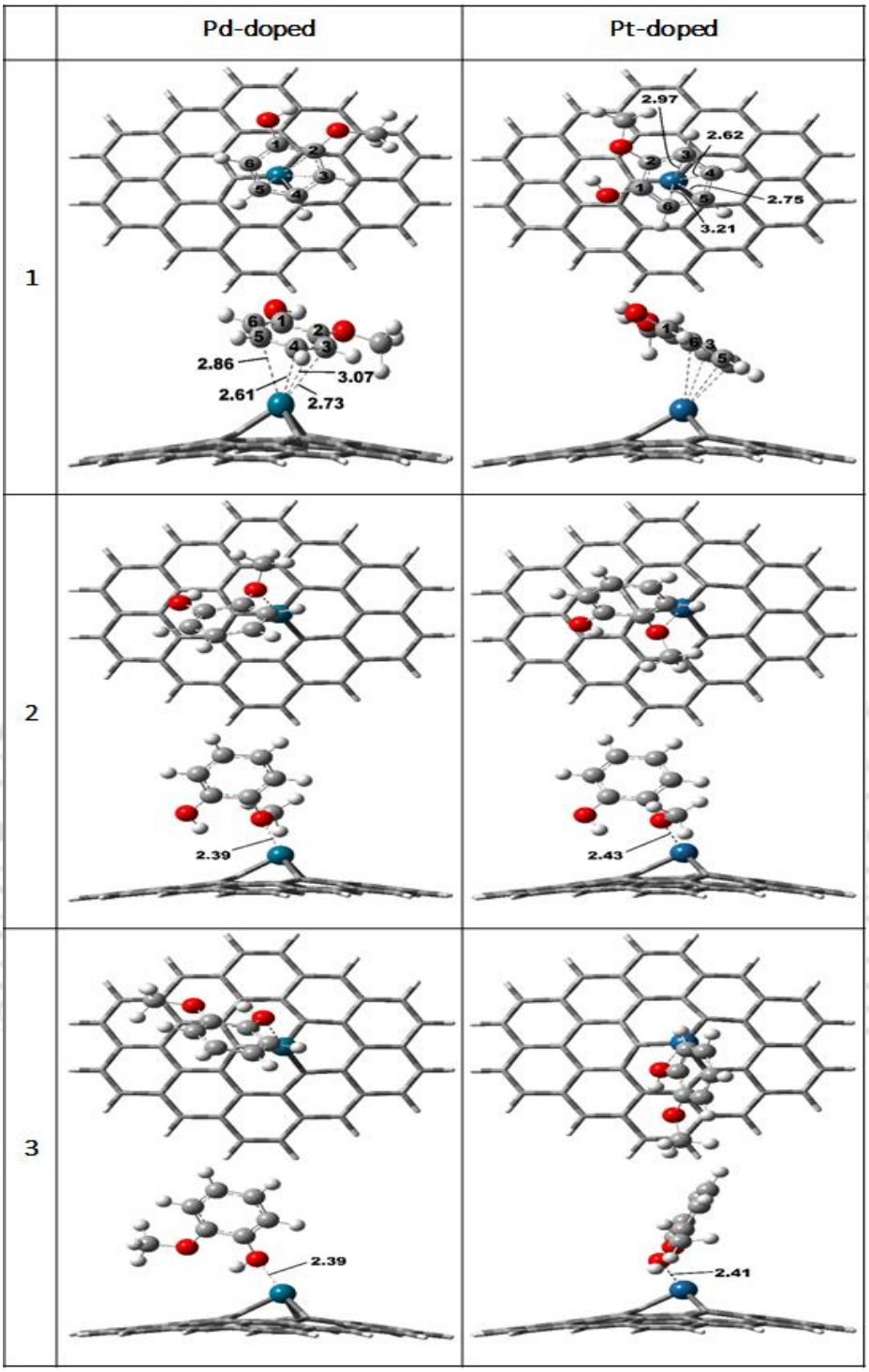

Figure 5.66: Adsorption configurations of guaiacol.

Similar to previous phenolic adsorptions, the adsorption of guaiacol is also highly endergonic; however, gradual increase in temperature reduces the available free energy of both catalytic systems. On the other hand, the energy release due to adsorption of guaiacol over both surfaces increases upon temperature increment. At 800 K, the free energy reduces at its

minimum but the enthalpy maximizes to its highest; however, even at this temperature both catalytic systems are reported to be highly endergonic. Furthermore, based on the free energy of system, the equilibrium constant values suggest a higher shifting tendency of equilibrium towards product which means both surfaces extremely favour the adsorptions.

5.10.5. Adsorption of Salicylaldehyde (2-HB)

The adsorption of 2-HB over PdGr and PtGr surfaces occurs by three configurations: i) by hydroxyl group, ii) by formyl group, and iii) by phenyl ring. All adsorption configurations are shown in Figure 5.67 and their adsorption energies are presented in Table 5.36. Further, the stability analyses (see Appendix Table 4) of all configurations over each catalyst surface report the ground state in singlet spin state. The adsorption of 2-HB *via* configuration 1, i.e., by hydroxyl group outperforms other configurations in terms of adsorption energy over PdGr surface, whereas, configuration 3, i.e., adsorption of 2-HB *via* phenyl ring outperforms other adsorption configurations over PtGr surface. It is observed that adsorption of formyl group *via* interaction of C=O of 2-HB over PdGr surface presents very poor adsorption; however, PtGr surface differs from this phenomenon. In configuration 2 of 2-HB over PdGr surface, the binding distances of C and O of formyl group to the Pd metal are reported as 2.49 Å and 2.84 Å, respectively but over PtGr surface, these distances are quite lower, i.e., 2.21 Å and 2.31 Å, respectively. Unlike PdGr surface, less binding distances of C=O to the Pt metal presents very good binding capability and thus comparatively better adsorption energy. Nevertheless, in configuration 1, the binding length of oxygen atom to Pd metal is lower compared to that of Pt metal which is the reason behind far better adsorption over former catalytic surface. But, in configuration 3, i.e., adsorption of 2-HB *via* phenyl ring, PtGr surface provides better adsorption energy compared to PdGr and the average binding distances of interacting phenyl carbon atoms to the former and latter surfaces are evaluated as ~2.89 Å and ~2.54 Å, respectively. Similar patterns as of adsorption energies are observed during the thermochemical

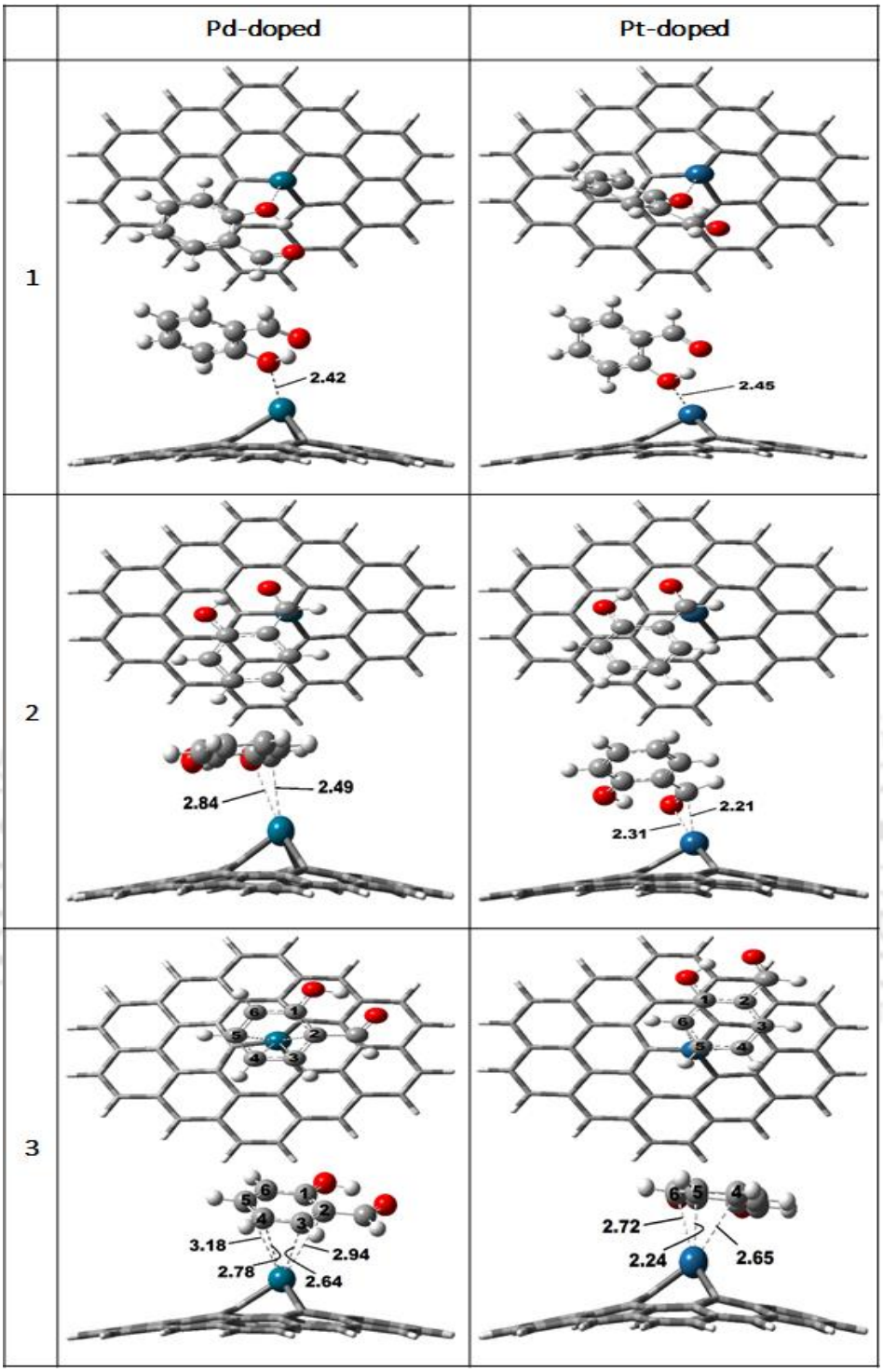

Figure 5.67: Adsorption configurations of salicylaldehyde (2-HB).

analyses (see Table 5.37) as well, i.e., configurations 1 and 3 over PdGr and PtGr surfaces, respectively present better thermodynamic values compared to other configurations because their free energies and enthalpies of adsorption at each temperature condition are higher (highly negative) than that of other configurations. In addition, the equilibrium constant values of

configurations 1 and 3 over PdGr and PtGr surfaces, respectively suggest higher equilibrium shift towards formation of adsorption complexes.

5.10.6. Adsorption of Vanillin

The adsorption of vanillin over PdGr and PtGr surfaces occurs by four possible configurations: i) by hydroxyl group, ii) by methoxy group, iii) by formyl group, and iv) by phenyl ring. All adsorption configurations of vanillin are shown in Figure 5.68. The stability analyses of all four configurations over both catalytic surfaces report their ground state in singlet spin multiplicity (see Appendix Table 4).

It is reported that the interactions of oxygen atoms of hydroxyl and methoxy groups with PdGr occur strongly compared to PtGr surface because of high adsorption energy (high negative). The binding distances of Pd-OH and Pt-OH (configuration 1) are found as 2.43 Å and 2.46 Å, respectively, whereas, the binding distances of Pd-OCH_3 and Pt-OCH_3 are reported as 2.43 Å and 2.48 Å, respectively. On the other hand, the adsorption of vanillin *via* formyl group (configuration 3) occurs differently than what was observed in the case of formyl group interaction of 2-HB because the former interacts through only oxygen atom of formyl group of vanillin, whereas, the latter interacted through C=O bond of 2-HB. The binding lengths of oxygen atoms in configuration 3 to the PdGr and PtGr surfaces are reported as 2.29 Å and 2.28 Å, respectively. It can be seen that both surfaces offer similar binding length and also, similar adsorption energies. But the adsorption of vanillin *via* phenyl ring is highly advantageous over PdGr surface because of better adsorption energy and strong binding to the surface compared to PtGr surface. The average bond lengths of interacting phenyl carbon atoms to PdGr and PtGr surfaces are reported as 2.87 Å and 3.05 Å, respectively. Due to similar binding lengths of aromatic carbons to PdGr surface, vanillin in configuration 4 adsorbs over PdGr in almost *atop* orientation, whereas, PtGr surface offers partial phenyl interaction to its surface. According to

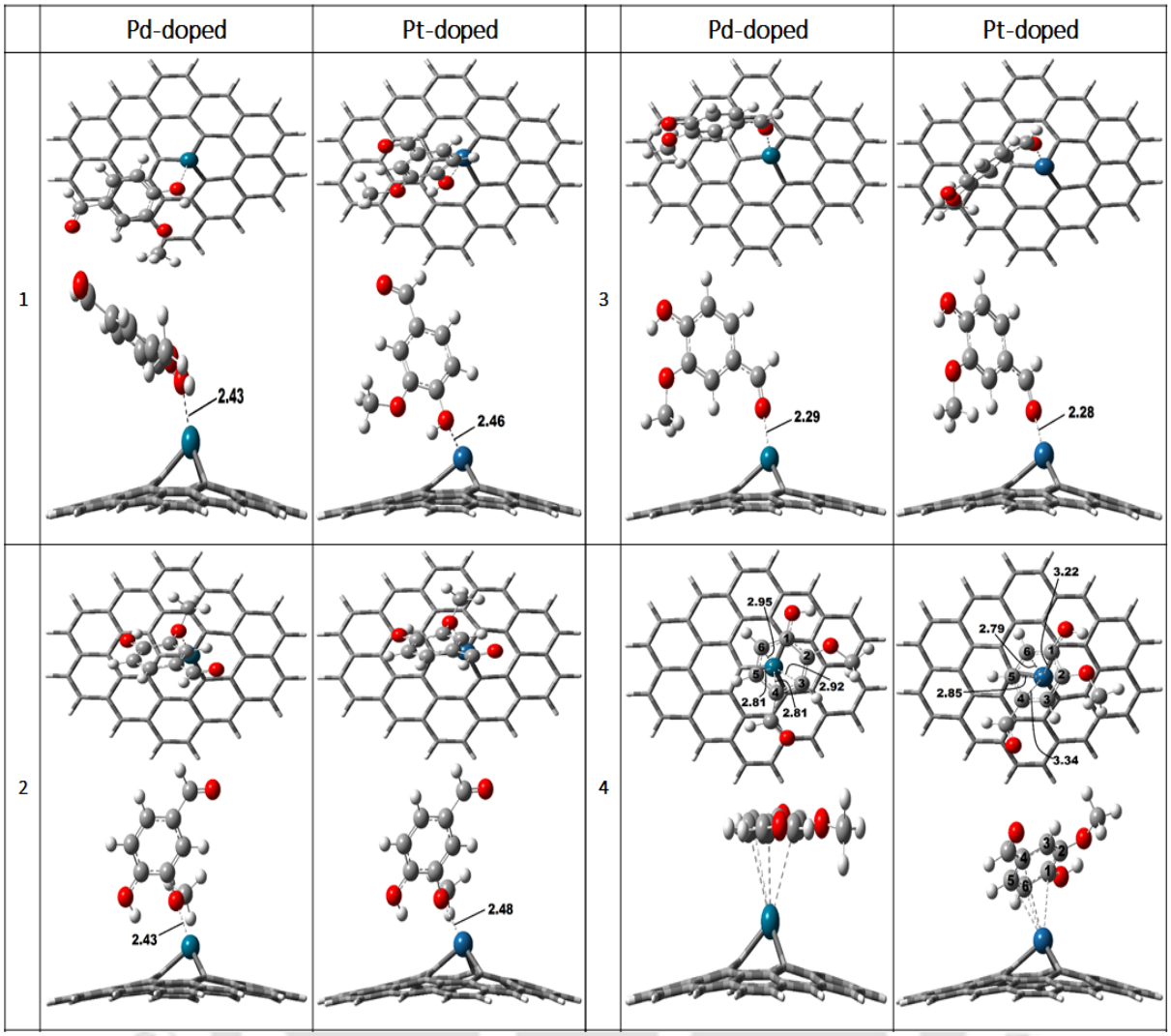

Figure 5.68: Adsorbed configurations of vanillin.

the thermochemical parameters (Tables 5.37 and 5.38) and adsorption energetics (Table 5.36), the configuration 3 appears as most stable vanillin configuration which interacts through oxygen atom of formyl group to the metal doped graphene surfaces. On the other hand, configuration 2 which interacts to the metals *via* oxygen atom of methoxy group is least stable configuration compared to other vanillin configurations. However, regarding configurations 1 and 4, both surfaces report contrary results because PdGr surface predicts configuration 1 as second least stable configuration, whereas, PtGr surface avows the same for configuration 4. The equilibrium constants of all configurations (see Table 5.38 and Appendix Figure 2) over both catalytic surfaces are in the range of 10^{129}-10^{133} at 400 K which indicate higher

favourability towards shifting of equilibrium towards the formation of adsorption complexes. However, these values reduce very quickly upon the increment of temperature and reach to the range of 10^{40}-10^{42} at 800 K, therefore, lower possible temperature, considering the fact that boiling point of vanillin is ~558 K, will be highly favourable environment for adsorption processes.

Finally, in summary, it has been seen that in most of the cases, Pd-doped graphene performed better than Pt-doped graphene surface whether in terms of adsorption energies, thermodynamic parameters or strong binding capabilities; however, in a few cases, PtGr outperformed PdGr surface such as configurations 2 and 3 of 2-HB and configuration 3 of vanillin. Further, it has been observed that adsorption energies of all configurations are quite poor irrespective of better binding capabilities; it is due to the single doping of metal into graphene. The reliability of the present work can be accessed by the observations of binding energies of Pd and Pt metal atoms to the defected graphene sheets. The binding energies of both metals with defected graphene are in very good agreements with literature values [174, 176, 177]. Apart from low adsorption energies of phenolic species over PdGr and PtGr surfaces, the binding lengths between adsorbates and catalyst surfaces suggest strong chemisorption process. Further, it is also affirmed by the analysis of thermochemical parameters such as free energy of adsorptions, adsorption enthalpies, and equilibrium constants at various temperature because each of these parameters are quite high. Similar to the adsorption energy trend, thermochemical parameters also suggest better performance of palladium doped graphene sheet for most cases. Palladium doped graphene catalyst showed exceptional characteristics compared to platinum doped graphene, therefore, it may have very high potential in bio-oil upgrading catalysis because of the easy availability and inexpensiveness of palladium metals compared to Pt.

5.11. Thermochemistry analyses for transformation of C6 glucose compound into C9, C12 and C15 alkanes using density functional theory

The hydrolysis conversion process of cellulose and/or glucose is widely accepted mechanism for the productions of liquid alkanes and platform chemicals [1, 11]. The formation of long chain hydrocarbons is accomplished through C-C coupling reactions, i.e., increasing the number of carbon atoms beyond the original number by coupling with carbonaceous compounds. The production of biofuels from biomass has been discussed by several researchers [4, 12, 14, 178–182, 54, 183]. Huber et al. [57] reported an aqueous phase experiment in which they proposed reaction mechanisms for the formations of three long chain alkanes *viz.* C9, C12, and C15 alkanes using glucose *via* C-C coupling, aldol condensation, hydrogenation/dehydration, and hydrodeoxygenation reactions. In this work, we have numerically modelled the reaction schemes proposed by Huber et al. [57] to report the thermochemistry of the reaction schemes. The re-plotted figure of reaction mechanisms given by Huber et al. [57] is depicted in Figure 5.69. In this figure, the model compound C6 glucose is transformed into three long hydrocarbon chains *viz.* C9, C12, and C15 alkanes *via* different reactions. The reactions are briefly described here, for instance, under C6 glucose to C_{12} alkane transformation reaction, the dehydration of glucose produces 5-HMF (demonstrated as **B** in Figure 5.69) compound followed by two molecular hydrogenation reactions which produce **C**. The aldol-self condensation of **C** produces **D** component followed by hydrogenation reaction producing **E** and further hydrodeoxygenation reaction of **E** produces C12 alkane [57]. Similarly, C6 glucose to C9 alkane transformation reaction involves dehydration of glucose which produces 5-HMF followed by the production of **C1** using aldol-crossed condensation

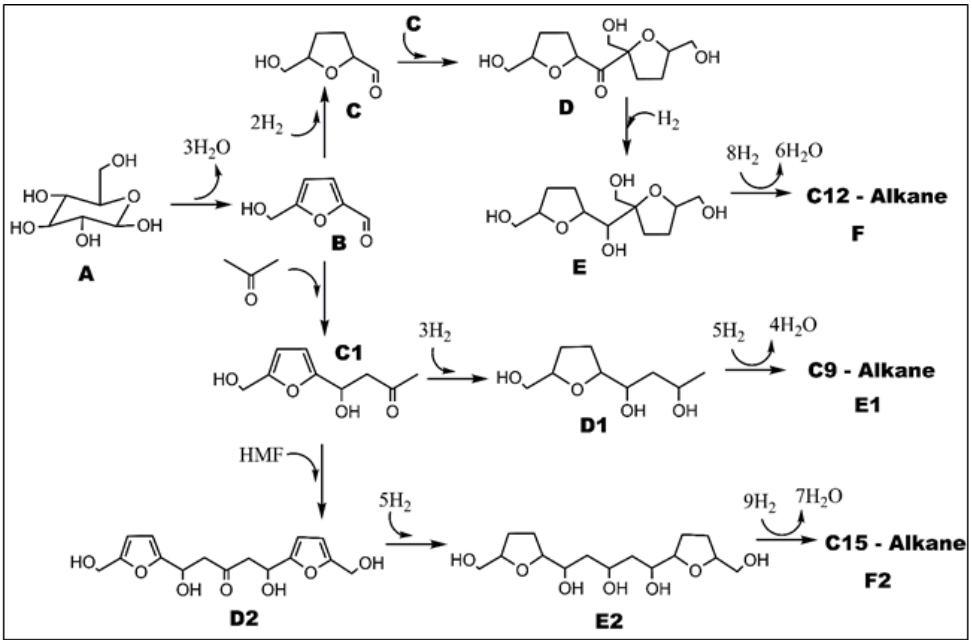

A	Glucose
B	5-hydroxy-methyl-furfural
C	5-(hydroxymethyl)tetrahydrofuran-2-carbaldehyde
D	((2R,5S)-2,5-bis(hydroxymethyl)tetrahydrofuran-2-yl)(5-(hydroxymethyl)tetrahydrofuran-2-yl)methanone
E	((2R,5S)-2-(hydroxy(5-(hydroxymethyl)tetrahydrofuran-2-yl)methyl)tetrahydrofuran-2,5-diyl)dimethanol
C1	4-hydroxy-4-(5-(hydroxymethyl)furan-2-yl)butan-2-one
D1	1-(5-(hydroxymethyl)tetrahydrofuran-2-yl)butane-1,3-diol
D2	1,5-dihydroxy-1,5-bis(5-(hydroxymethyl)furan-2-yl)pentan-3-one
E2	1-((5R)-5-(hydroxymethyl)tetrahydrofuran-2-yl)-5-(5-(hydroxymethyl)tetrahydrofuran-2-yl)pentane-1,3,5-triol

Figure 5.69: The reaction schemes of C6 glucose molecule conversion into long chain alkanes proposed by Huber et al. [57] (replotted with permission).

reaction with acetone. Three molecular hydrogenation reactions to **C1** give rise to **D1** component which further hydrodeoxygenated to produce C9 alkane [57]. In the C6 glucose to C15 alkane production, the aldol-crossed condensation of **C1** with 5-HMF produces **D2** component followed by five molecular hydrogenation reactions to produce **E2**. Further hydrodeoxygenation of **E2** produces C15 alkanes [57].

The work of Huber et al. [57] is reported in the aqueous environment, therefore, the aqueous phase environment has been created using SMD (Solvation Model based on Density) model [184] and water has been taken as the solvent. Along with this, we have also carried out gas phase computations to comprehend the variations. The optimization and vibrational frequency calculations are carried out at B3LYP/6-31+g(d,p) theory while single point energy (SPE) calculations are performed at M05-2X/6-311+g(3df,2p)//B3LYP/6-31+g(d,p) level of theory. To accommodate the wide range of values, thermodynamic parameters such as Gibbs free energies, entropies, enthalpies, etc. have been investigated for a wide range of temperature, i.e., 300-900 K at an interval of 100 K. The pressure has been kept constant as 1 atm.

5.11.1. Single Point Energetics (SPEs)

The single point energy differences of glucose transformation reaction into various long chain hydrocarbons (C9, C12, and C15 alkanes) are shown in Figure 5.70 and the corresponding optimized molecular structures can be seen in Figure 5.71.

The dehydration of glucose (**A**) molecule into 5-hydroxy-methyl-furfural (**B**+3H_2O) is common in all reaction pathways and the energy difference (ΔE) of the same in gas phase has been calculated as 25.33 kcal/mol; however, ΔE of same reaction in aqueous phase is 14.60 kcal/mol only. As expected, the aqueous phase reactions can be advantageous compared to gas phase reactions and the difference between gas phase SPE and aqueous phase SPE is 10.73 kcal/mol. This reaction has been found exothermic and spontaneous at 298 K and 1 atm pressure in both gas and aqueous phases; however, aqueous phase dominates over gas phase by 12.67 kcal/mol in spontaneity and 13.06 kcal/mol in exothermicity. Assary et al. [182] also calculated this reaction as exothermic and spontaneous using G4MP2 level of theory. The reaction pathway of glucose to C9 alkane is discussed in next subsection.

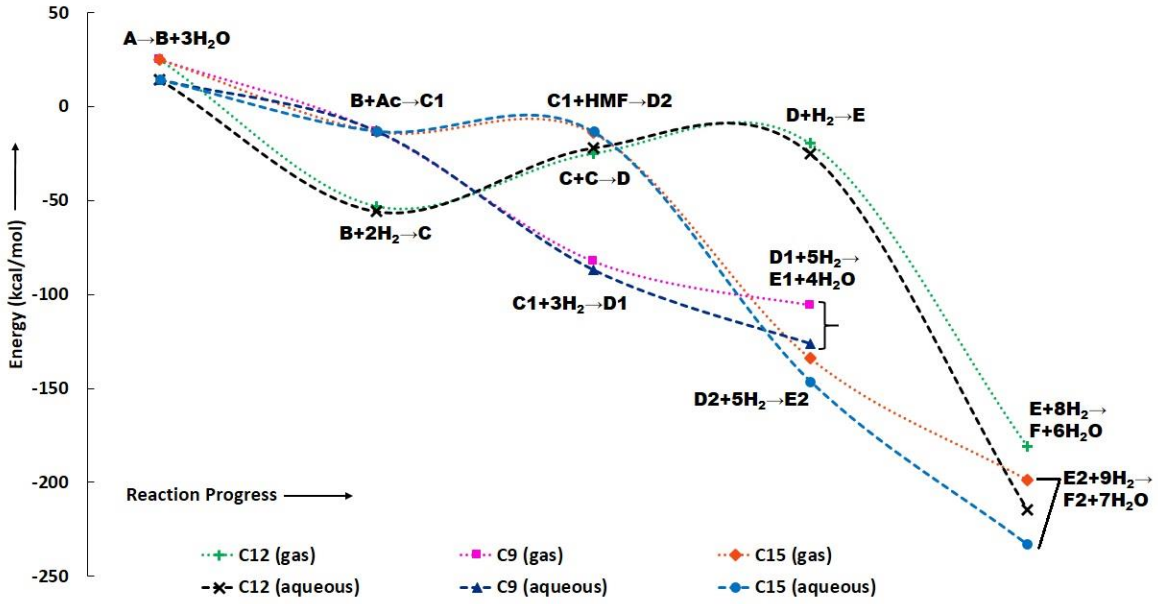

Figure 5.70: The energy difference (ΔE) diagrams of the conversion of C6 sugar into various long chain alkanes in gas and aqueous phase environments.

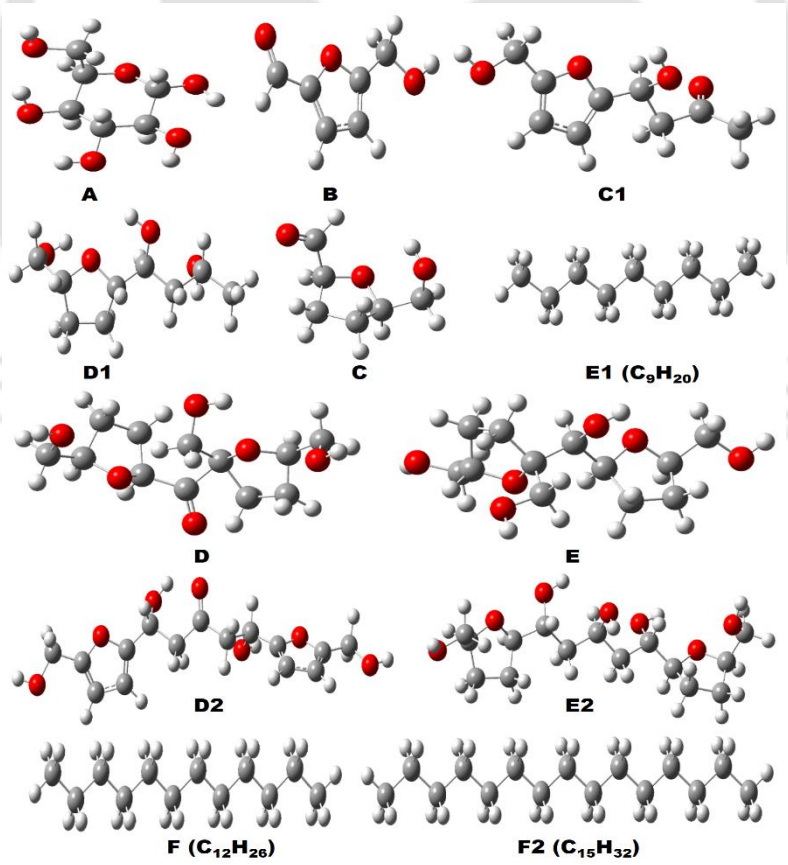

Figure 5.71: Optimized molecular structures involved in conversion of C6 sugar into various long chain alkanes.

5.11.1.1. C6 glucose to C9 alkane

The ΔE of aldol crossed-condensation reaction which produces **C1** from '**B** and acetone' (**B**+**Ac**→**C1**) is calculated as -13.10 kcal/mol and -12.85 kcal/mol in gas and aqueous phases, respectively. It can be seen that the aqueous environment does not affect much because there is only 0.25 kcal/mol energy difference between both phases. The produced component **C1** follows through three molecular hydrogenation reactions to produce **D1** by saturating the ring and converting the ketone into alcohol. The energy differences of this reaction are -82.44 kcal/mol and -86.95 kcal/mol, respectively for gas and water phases. Further hydrodeoxygenation of **D1** gives rise to the C_9H_{18} alkane and the ΔE for the same in gas and water phases are -105.90 kcal/mol and -126.37 kcal/mol, respectively. The thermochemistry calculation at T=298 K and P=1 atm shows that all reactions are exothermic and spontaneous in both phases except aldol crossed-condensation of **B** with acetone which produces **C1** (see Tables 5.39 and 5.40).

5.11.1.2. C6 glucose to C12 alkane

The C12 alkane production reaction follows the similar pathway till the production of HMF and after that two hydrogen molecules saturate the ring and form the component **C**. The reaction energies of **B** to **C** reaction in gas and water phases, respectively are -52.89 kcal/mol and -55.73 kcal/mol. The ΔE of aldol self-condensation reaction of **C** in gas and aqueous phases are -24.75 kcal/mol and -21.84 kcal/mol, respectively. This is followed by keto-enol tautomerisation reaction (**D**+H_2 → **E**) for which the energy differences are -19.55 kcal/mol and -24.93 kcal/mol for gas and water phases, respectively. Finally, hydrodeoxygenation of **D** which produces C12 alkane; the ΔE for gas and water phases are -180.96 kcal/mol and -214.68 kcal/mol, respectively. Here too, all reactions are favourable in both phases except aldol self-crossed condensation reaction at T=298 K and P=1 atm (see Tables 5.39 and 5.40).

Table 5.39: The thermodynamic properties (ΔG, ΔH, and K_{eq}) for each reaction pathway at various temperatures and P=1 atm in gas phase environment.

Reactions	Temperature (K)							
	298	300	400	500	600	700	800	900
	ΔG							
A→B+3H_2O	-38.69	-38.92	-51.00	-63.13	-75.22	-87.24	-99.17	-111.01
B+2H_2→C	-12.90	-12.79	-6.70	-0.38	6.06	12.58	19.14	25.72
C+C→D	30.14	30.24	35.32	40.36	45.34	50.28	55.17	60.03
D+H_2→E	-26.93	-26.89	-24.71	-22.48	-20.22	-17.96	-15.69	-13.42
E+8H_2→F+6H_2O	-156.72	-156.73	-156.93	-156.53	-155.63	-154.35	-152.77	-150.93
B+Acetone→C1	12.68	12.75	16.67	20.52	24.31	28.05	31.74	35.38
C1+3H_2→D1	-20.77	-20.60	-10.92	-0.92	9.27	19.58	29.94	40.33
D1+5H_2→E1+4H_2O	-93.51	-93.53	-94.39	-94.87	-95.04	-94.96	-94.67	-94.22
C1+HMF→D2	12.31	12.39	16.60	20.75	24.86	28.91	32.91	36.87
D2+5H_2→E2	-33.06	-32.78	-17.04	-0.77	15.81	32.58	49.46	66.38
E2+9H_2→F2+7H_2O	-174.35	-174.37	-175.33	-175.60	-175.32	-174.59	-173.51	-172.14
	ΔH							
A→B+3H_2O	-2.89	-2.87	-2.51	-2.53	-2.85	-3.39	-4.10	-4.93
B+2H_2→C	-30.61	-30.63	-31.60	-32.34	-32.87	-33.23	-33.44	-33.52
C+C→D	14.92	14.92	15.09	15.31	15.58	15.87	16.17	16.49
D+H_2→E	-33.31	-33.32	-33.55	-33.71	-33.80	-33.84	-33.84	-33.80
E+8H_2→F+6H_2O	-155.05	-155.09	-157.43	-159.86	-162.24	-164.47	-166.52	-168.37
B+Acetone→C1	0.94	0.94	1.13	1.40	1.72	2.07	2.42	2.79
C1+3H_2→D1	-48.93	-48.96	-50.39	-51.49	-52.28	-52.81	-53.12	-53.24
D1+5H_2→E1+4H_2O	-43.87	-43.54	-25.40	-6.48	13.16	33.45	54.35	75.83
C1+HMF→D2	-0.29	-0.29	-0.14	0.10	0.39	0.72	1.07	1.43
D2+5H_2→E2	-78.83	-78.88	-81.23	-83.05	-84.37	-85.25	-85.77	-85.97
E2+9H_2→F2+7H_2O	-170.30	-170.34	-172.95	-175.71	-178.44	-181.02	-183.41	-185.59
	K_{eq}							
A→B+3H_2O	2.40E+28	2.25E+28	7.35E+27	3.93E+27	2.52E+27	1.74E+27	1.24E+27	9.10E+26
B+2H_2→C	2.92E+09	2.10E+09	4.57E+03	1.47E+00	6.19E-03	1.18E-04	5.89E-06	5.67E-07
C+C→D	7.78E-23	9.32E-23	5.00E-20	2.28E-18	3.04E-17	2.00E-16	8.43E-16	2.64E-15
D+H_2→E	5.62E+19	3.88E+19	3.17E+13	6.71E+09	2.33E+07	4.04E+05	1.93E+04	1.82E+03
E+8H_2→F+6H_2O	8.88E+114	1.55E+114	5.63E+85	2.65E+68	4.94E+56	1.57E+48	5.47E+41	4.51E+36
B+Acetone→C1	5.00E-10	5.10E-10	7.82E-10	1.07E-09	1.39E-09	1.74E-09	2.13E-09	2.55E-09
C1+3H_2→D1	1.72E+15	1.01E+15	9.27E+05	2.52E+00	4.18E-04	7.71E-07	6.60E-09	1.60E-10
D1+5H_2→E1+4H_2O	3.83E+68	1.38E+68	3.77E+51	2.96E+41	4.17E+34	4.46E+29	7.33E+25	7.61E+22
C1+HMF→D2	9.38E-10	9.46E-10	8.55E-10	8.47E-10	8.80E-10	9.40E-10	1.02E-09	1.11E-09
D2+5H_2→E2	1.78E+24	7.60E+23	2.05E+09	2.18E+00	1.74E-06	6.70E-11	3.08E-14	7.59E-17
E2+9H_2→F2+7H_2O	7.48E+127	1.09E+127	6.33E+95	5.78E+76	7.31E+63	3.27E+54	2.54E+47	6.36E+41

Table 5.40: The thermodynamic properties (ΔG, ΔH, and K_{eq}) for each reaction pathway at various temperatures and P=1 atm in aqueous phase environment.

Reactions	Temperature (K)							
	298	300	400	500	600	700	800	900
				ΔG				
A→B+3H_2O	-51.37	-51.59	-63.53	-75.52	-87.47	-99.35	-111.14	-122.84
B+2H_2→C	-14.94	-2.24	4.09	10.64	17.32	24.08	30.88	37.70
C+C→D	29.71	28.11	32.66	37.15	41.60	46.00	50.37	54.69
D+H_2→E	-29.80	-27.31	-24.68	-22.01	-19.30	-16.59	-13.87	-11.15
E+8H_2→F+ 6H_2O	-197.56	-223.51	-224.11	-224.11	-223.64	-222.79	-221.64	-220.26
B+Acetone→ C1	13.87	13.95	18.19	22.37	26.49	30.56	34.57	38.54
C1+3H_2→D1	-26.94	-26.78	-17.51	-7.93	1.84	11.71	21.64	31.60
D1+5H_2→E1+ 4H_2O	-119.93	-119.95	-120.71	-121.06	-121.10	-120.88	-120.45	-119.86
C1+HMF→D2	14.04	14.12	18.54	22.92	27.24	31.51	35.73	39.91
D2+5H_2→E2	-48.42	-48.15	-32.99	-17.30	-1.32	14.85	31.12	47.44
E2+9H_2→F2+ 7H_2O	-215.03	-215.05	-216.02	-216.30	-216.02	-215.30	-214.23	-212.87
				ΔH				
A→B+3H_2O	-15.95	-15.94	-15.61	-15.64	-15.95	-16.47	-17.16	-17.97
B+2H_2→C	-32.95	-20.77	-21.74	-22.49	-23.03	-23.40	-23.62	-23.70
C+C→D	15.91	14.40	14.57	14.79	15.05	15.34	15.63	15.95
D+H_2→E	-37.51	-35.06	-35.30	-35.48	-35.58	-35.62	-35.62	-35.58
E+8H_2→F+ 6H_2O	-195.30	-220.71	-222.99	-225.37	-227.68	-229.85	-231.84	-233.63
B+Acetone→ C1	1.13	1.14	1.34	1.62	1.94	2.29	2.65	3.01
C1+3H_2→D1	-53.89	-53.92	-55.31	-56.38	-57.15	-57.66	-57.96	-58.07
D1+5H_2→E1+ 4H_2O	-116.98	-117.01	-118.52	-120.12	-121.71	-123.21	-124.60	-125.86
C1+HMF→D2	0.79	0.80	0.95	1.18	1.47	1.79	2.13	2.48
D2+5H_2→E2	-92.51	-92.55	-94.84	-96.61	-97.90	-98.76	-99.26	-99.46
E2+9H_2→F2+ 7H_2O	-210.91	-210.96	-213.62	-216.40	-219.12	-221.67	-224.02	-226.16
				K_{eq}				
A→B+3H_2O	4.74E+37	3.84E+37	5.19E+34	1.02E+33	7.28E+31	1.05E+31	2.32E+30	6.80E+29
B+2H_2→C	9.01E+10	4.27E+01	5.82E-03	2.23E-05	4.90E-07	3.03E-08	3.66E-09	7.00E-10
C+C→D	1.62E-22	3.30E-21	1.43E-18	5.73E-17	7.00E-16	4.32E-15	1.74E-14	5.23E-14
D+H_2→E	7.24E+21	7.84E+19	3.07E+13	4.17E+09	1.08E+07	1.51E+05	6.15E+03	5.10E+02
E+8H_2→F+ 6H_2O	7.93E+144	6.92E+162	2.87E+122	9.24E+97	2.93E+81	3.67E+69	3.59E+60	3.10E+53
B+Acetone→ C1	6.72E-11	6.89E-11	1.15E-10	1.66E-10	2.24E-10	2.88E-10	3.59E-10	4.37E-10
C1+3H_2→D1	5.79E+19	3.23E+19	3.70E+09	2.93E+03	2.14E-01	2.21E-04	1.22E-06	2.12E-08
D1+5H_2→E1+ 4H_2O	9.16E+87	2.45E+87	9.03E+65	8.34E+52	1.30E+44	5.55E+37	8.11E+32	1.28E+29
C1+HMF→D2	5.04E-11	5.14E-11	7.37E-11	9.59E-11	1.20E-10	1.45E-10	1.73E-10	2.03E-10
D2+5H_2→E2	3.27E+35	1.20E+35	1.06E+18	3.67E+07	3.02E+00	2.30E-05	3.14E-09	3.02E-12
E2+9H_2→F2+7 H_2O	5.13E+157	4.75E+156	1.09E+118	3.55E+94	4.92E+78	1.68E+67	3.38E+58	4.98E+51

5.11.1.3. C6 glucose to C15 alkane

The reaction pathway of production of C15 alkane from glucose is common with C9 alkane formation till the production of **C1** component. This further follows an aldol crossed-condensation reaction of **C1** with 5-HMF to produce **D2** for which the energy differences are -13.98 kcal/mol and -13.16 kcal/mol, respectively for gas and water phases. Similarly, the hydrogenation reaction of **D2** estimate the energy differences as -133.91 kcal/mol and -146.14 kcal/mol for gas and aqueous phases, respectively. Finally, hydrodeoxygenation reaction of **D2** produces C15 alkane; and the ΔE of this reaction step are -198.67 kcal/mol and -233.03 kcal/mol, respectively for gas and aqueous phases. Aldol crossed-condensation reactions of acetone and HMF are neither exothermic nor spontaneous in both phases otherwise all remaining reactions under this pathway are favourable in both phases at T=298 K and P=1 atm.

5.11.2. Thermochemistry

The thermochemical analyses of all reactions are carried out at various temperatures and 1 atm pressure. The thermodynamic parameters (ΔG, ΔH, and K_{eq}) in gas and aqueous phases are listed in Tables 5.39 and 5.40, respectively, with their corresponding temperature conditions. The graphs of ΔG *vs.* T and **ln K_{eq}** *vs.* **1/T** for C6 glucose to C9, C12, and C15 alkanes are shown in Figures 5.72, 5.73, and 5.74, respectively.

5.11.2.1. C6 Sugar to C9 alkane

The gas phase dehydration reaction of glucose into 5-HMF is spontaneous and it improves further with temperature. Similar trends can be seen in aqueous phase (see Figure 5.72), however, this reaction is 12.68 kcal/mol more spontaneous under aqueous phase at 298 K. Assary et al. [53] in their computational study, for the formation of 5-HMF from glucose, also calculated this reaction as a spontaneous in aqueous phase; however, they used implicit solvation model to create aqueous phase environment. The reaction enthalpy of this reaction

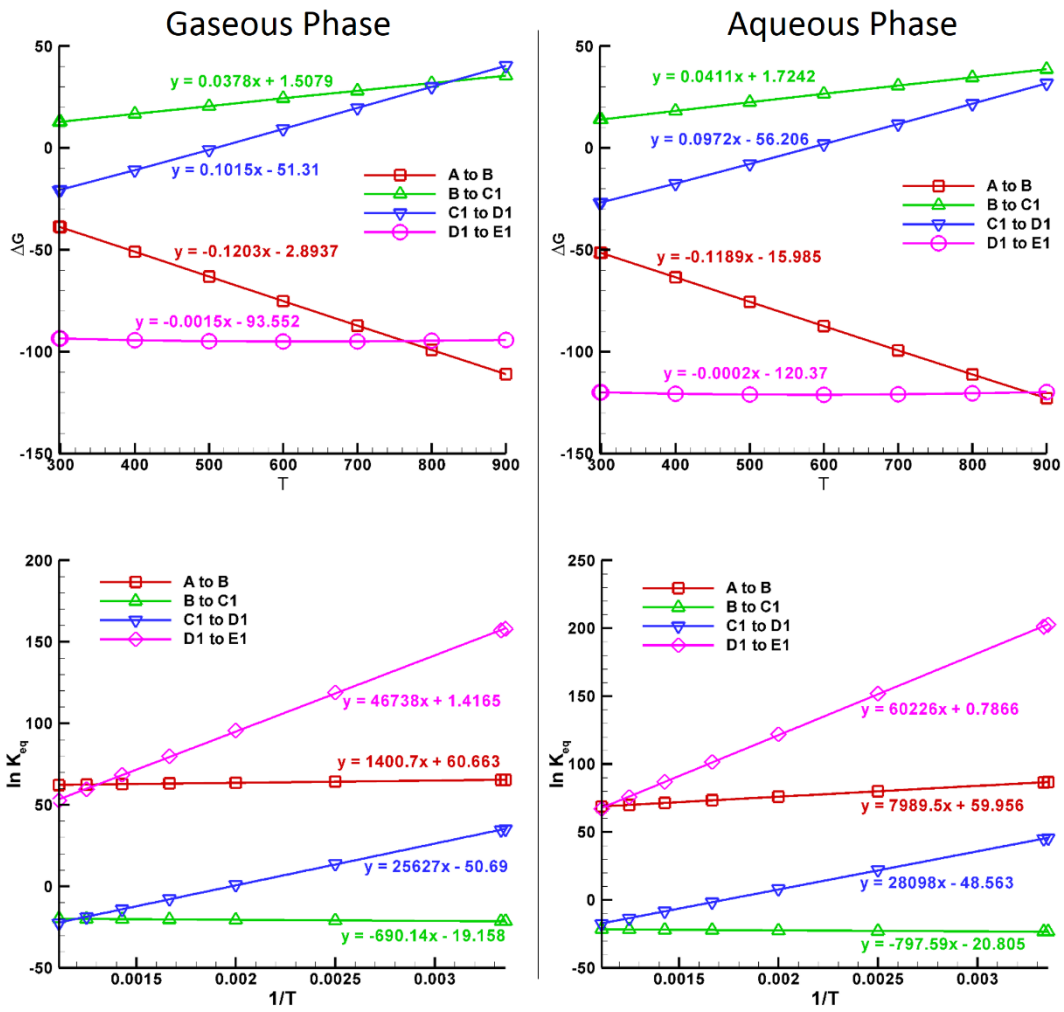

Figure 5.72: The ΔG vs. T and **ln Keq** vs. **1/T** graphs of C6 glucose to C9 alkanes.

does not show considerable temperature effect in both phases. The equilibrium constant values show that the equilibrium tends to shift towards the product for this reaction. On the other hand, the second reaction, aldol crossed-condensation with acetone, is neither spontaneous nor exothermic in both phases. Surprisingly, this reaction becomes even less favourable with increasing temperature in both phases. The hydrogenation reaction of **C1** which produces **D1** becomes less spontaneous with increasing temperature in both phases; however, it is exothermic at each temperature. The hydrodeoxygenation reaction of **D1** is favourable in aqueous phase. The reaction in gas phase is spontaneous too but not exothermic even with temperature increment. The equilibrium constant values of all reactions under this reaction pathway decrease with increasing temperature except for aldol crossed-condensation reaction.

5.11.2.2. C6 Sugar to C12 alkane

The dehydration reaction of glucose is common in this reaction and has already been discussed earlier. This follows the second reaction forward as it can be seen in Figure 5.69 that 5-HMF undergoes two molecular hydrogenation reactions to saturate the ring. The thermochemistry indicates that this reaction is not spontaneous in both phases; however, the reaction is exothermic in both phases at each temperature values. The equilibrium constant values for this reaction suggest that the equilibrium shifts towards the reactants with increasing temperature; however, the values are favourable till 400 K and 300 K in gas and aqueous phases, respectively.

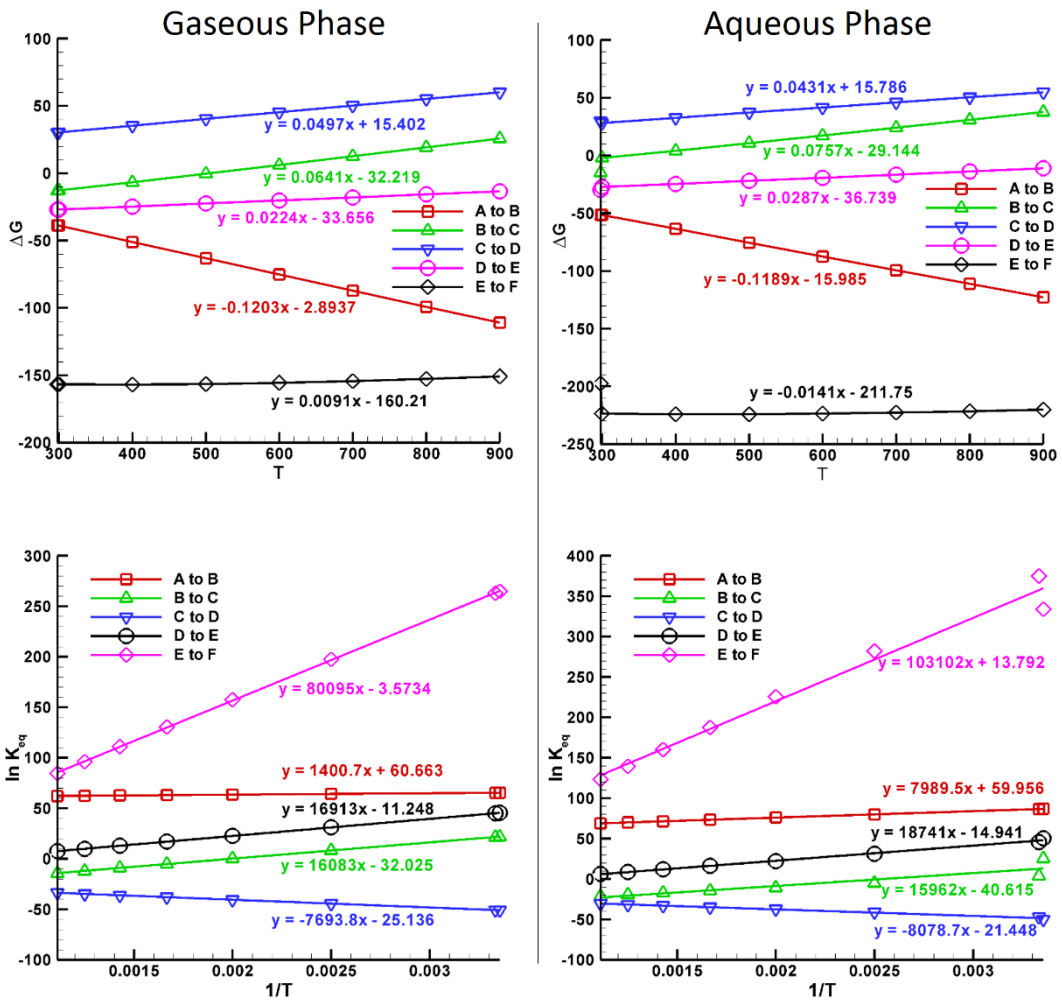

Figure 5.73: The ΔG vs. T and **ln Keq** vs. **1/T** graphs of C6 glucose to C12 alkanes.

Further, the reaction proceeds for self aldol-condensation of **C** which is not favourable at all temperature values. In fact, the temperature increment worsens the reaction free energies and reaction enthalpies in both phases. However, the hydrogenation reaction of intermediate **D** is favourable reaction but becomes slightly less spontaneous upon the temperature increment. The hydrodeoxygenation reaction of **E** to produce C12 alkane is calculated to be the most favourable reaction under this pathway in both gas and aqueous phases, though, the aqueous phase environment is much more favourable compared to the gas phase environment. The equilibrium constant values decrease with increasing temperature for all reactions except the self aldol-condensation reaction of **C** which explains the non-favourability of this reaction.

5.11.2.3. C6 Sugar to C15 alkane

The 'C6 to C15 alkane' reaction pathway shares two initial reactions with 'C6 to C9 alkane' reaction pathway, therefore, it is not discussed here again to avoid repetitions. The third reaction step is aldol crossed-condensation of 5-HMF with **C1** which is not favourable at all temperature values in both phases similar to previous aldol condensation reactions. However, this reaction is slightly endothermic at each temperature values in aqueous phase and becomes more endothermic with increasing temperature. The fourth reaction step, i.e., five molecular hydrogenation reactions to component **D2** to form **E2**, is spontaneous upto T=500 K for gas phase and upto T=600 K for aqueous phase but beyond these temperatures it becomes unspontaneous; however, this reaction is highly exothermic in both phases at each temperature value. Finally, the hydrodeoxygenation reaction of **E2** which produces $C_{15}H_{32}$ alkane is most favourable reaction in both phases amongst all reactions under this reaction pathway. Further temperature increment enhances its exothermicity but slightly decreases the reaction free energy values. The equilibrium constant values decrease with increasing temperature for all reactions except two aldol crossed-condensation reactions which slightly tend to shift the equilibrium towards reactants.

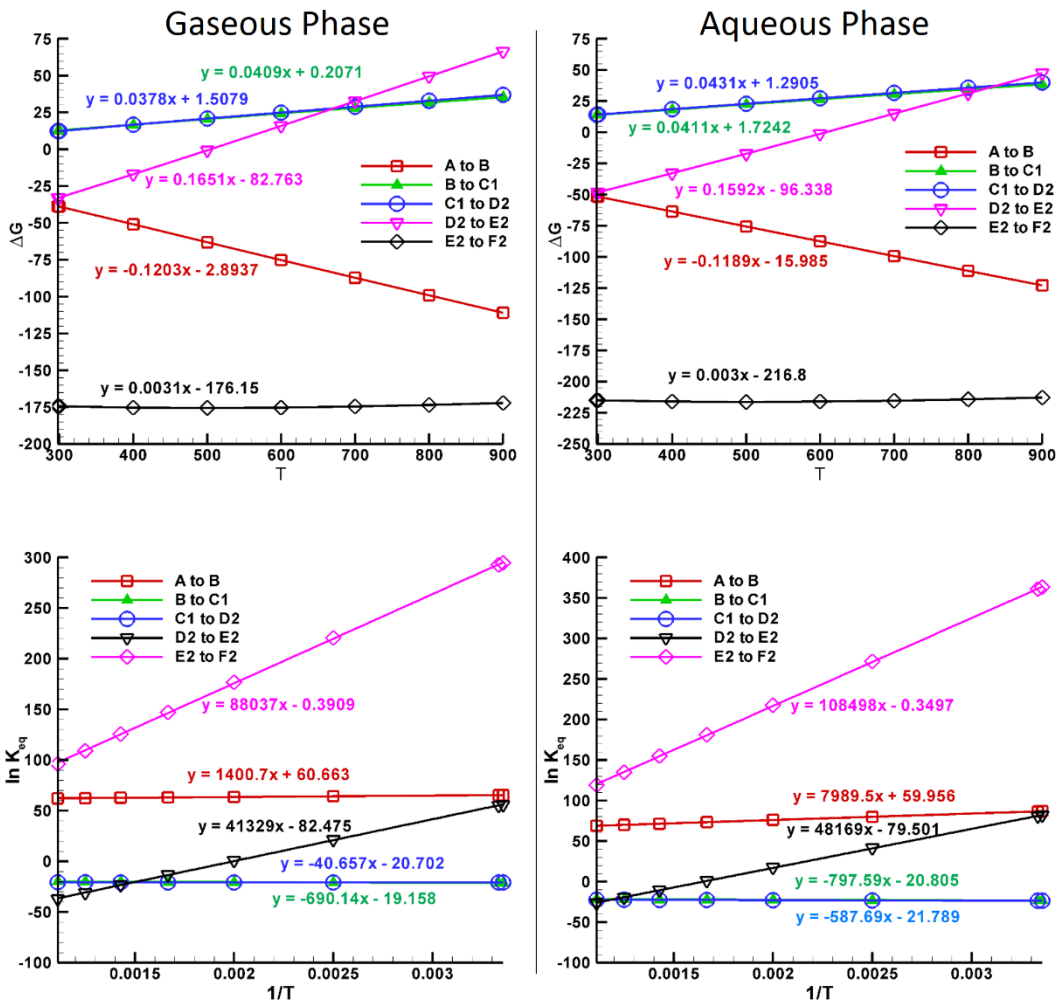

Figure 5.74: The ΔG vs. T and **ln Keq** vs. **1/T** graphs of C6 glucose to C15 alkanes.

Finally, summarizing all reactions under each reaction pathway, the aqueous phase environment proved to be more favourable for all hydrodeoxygenation reactions which is consistent with the experimental findings due to Huber et al. [57]. This is probably because of proton transfer from water compounds and enriched solvation due to the additional water compounds produced during the course of hydrodeoxygenation reactions. In the adopted model reactions of Huber et al. [57], the glucose molecule dehydrated into 5-HMF directly, however, a few researchers have argued the formation of fructose in the course of reaction [182, 54]. Although, the formation of 5-HMF from fructose has also been found as an exothermic and spontaneous reaction of similar energetics [182]. On the other hand, the aldol condensation reactions are found as unfavourable in each pathway, be it aldol crossed-condensation of HMF

or acetone or aldol self-condensation reaction but these reactions are very important for the formation of large organic compounds such as long alkane chains or platform chemicals [57]. The temperature increment has not shown any considerable effect for aldol condensation reactions but the pressure change along with temperature change may favour these reactions thermodynamically.

CONCLUSIONS AND FUTURE SCOPES

6.1. Conclusions

6.1.1. Molecular modelling approach to elucidate the thermal decomposition routes of vanillin

The vanillin component is considered as bio-oil model compound for its decomposition under density functional theory framework employing B3LYP/6-311+g(d,p) level of theory. The present study elucidates the formation of various pyrolytic products of vanillin found by experimental researchers. Further, it also presents the energy requirement using the potential energy surfaces for all considered reaction pathways theoretically. The dehydrogenations of hydroxyl and formyl functional groups of vanillin are competitive to each other in energetics and favourable compared to methoxy cleavage of vanillin. However, the single step hydrogenation reaction after methyl cleavage of vanillin makes reaction to reconsider the other pathways. The reaction pathway 3 which produces guaiacol required least activation energy, i.e., 10.13 kcal/mol only; and this reaction is reported to be favourable at each temperature condition. The reaction pathway 5 which produces benzene from vanillin is second most favourable reaction after reaction pathway 3 according to activation energy requirement. It is found that atomic hydrogen addition prior to the cleavage of oxy-functional is much more favourable compared to the cleavage of oxy-functional followed by atomic hydrogen addition.

6.1.2. Gas Phase Conversion of Eugenol into Various Hydrocarbons and Platform Chemicals

The conversion of eugenol, a bio-oil model component, using eight primary and four secondary reaction schemes is studied numerically under gas phase environment at B3LYP/6-311+g(d,p)

level of theory. The present study concludes that direct cleavages of functional groups of eugenol are not favourable. Instead, an atomic hydrogenation reaction prior to the cleavage of functional groups of eugenol makes reactions much more favourable. The activation energy for the production of guaiacol from eugenol under reaction scheme 2 is 10.53 kcal/mol only which is the least activation energy required amongst all activation energies corresponding to each reaction scheme. The activation energies of some of the reactions are high which cannot be carried out in the gas phase milieu, can be tried in the solution phase using various solvents to decrease the activation energy. The reaction scheme 5, i.e., the production of propylcyclohexane from eugenol, is most exothermic and spontaneous reaction at all temperature conditions.

6.1.3. Unravelling the Dissociation Mechanism of Ferulic Acid under Density Functional Theory Framework

The decomposition of ferulic acid into various end products such as ethylbenzene, cinnamic acid, eugenol, *cis*-isoeugenol, vanillin, 4-ethylguaiacol, guaiacol, and acetovanillone is performed in gas phase under density functional theory framework using B3LYP/6-311+g(d,p) level of theory. The methyl group cleavage from ferulic acid has been concluded as the lowest bond dissociation energy scission amongst other 14 bond scissions. In addition, the formation of ethylbenzene is investigated by various reaction approaches and the dominating reaction scheme initiates from demethoxylation of ferulic acid to produce 4-hydroxycinnamic acid followed by the production of cinnamic acid from dehydroxylation of 4-hydroxycinnamic acid; and, decarboxylation of cinnamic acid to produce vinylbenzene followed by production of ethylbenzene using hydrogenation of C=C chain double bond. Further, the productions of *cis*-isoeugenol, 4-ethylguaiacol, and acetovanillone are performed with a common important intermediate 4-vinylguaiacol which concurs the experimental findings. The production of 4-vinylguaiacol from ferulic acid has been upvoted by various researchers experimentally and

this numerical study incorporates its formation with 52.53 kcal/mol of activation energy which is achievable at pyrolysis temperature conditions.

6.1.4. DFT Analyses of Reaction Pathways on various Guaiacol Conversion Reactions in Gas Phase Environment

The conversion of guaiacol to many important products, e.g., phenol, anisole, cyclopentanone, cyclohexane, and cyclohexanone using various pathways is studied at B3LYP/6-311+g(d,p) level of theory under DFT framework. The reaction pathways 1 (and 3) and 2 which produce phenol and anisole, respectively are both exothermic and spontaneous over discussed temperature range with slight decrease in both thermodynamic properties with temperature increment. The reaction pathways 5 and 6 produce same desired product, i.e., cyclohexanone, and both reactions are exothermic and spontaneous at 398 K but with increasing temperature, the exothermicity and spontaneity of both reactions increases and decreases, respectively. However, pathway 6 dominates over pathway 5 in the terms of thermodynamic properties at each temperature.

6.1.5. Production of Benzene from 2-Hydroxybenzaldehyde by Various Reaction Paths using IRC Calculations within DFT framework

2-Hydroxybenzaldehyde (2-HB) is considered as a model bio-oil compound and carried out seven different reaction pathways at B3LYP/6-311+g(d,p) level of theory to find out the optimum reaction progress to produce benzene component. The optimum reaction progress undergo through a single step hydrogenation to the aromatic carbon atom of $C_{aromatic}$-CHO bond of 2-HB followed by formyl group elimination to produce phenol. Similarly, a single step hydrogenation to aromatic carbon atom of $C_{aromatic}$-OH bond followed by hydroxyl group elimination to produce benzene. The activation energy of the optimum reaction pathway has been reported as 13.19 kcal/mol. The decarbonylation reactions of 2-hydroxybenzaldehyde and

benzaldehyde require a large amount of activation energy thus these are not favourable reactions.

6.1.6. Quantum Chemical Study on Gas Phase Pyrolysis of *p*-Isopropenylphenol

The analyses of decomposition process of *p*-isopropenylphenol (*p*-IPP) are carried out theoretically within the perspective of density functional theory. The B3LYP/6-311+g(d,p) level of theory is applied for all quantum chemical calculations. The bond dissociation energies suggest that the dehydrogenation of hydroxyl functional of *p*-IPP is dominating bond cleavage with demethylation of *p*-IPP in competitive energetics. All eight primary reaction schemes led to the formations of various products, e.g., benzene, phenol, *cis* and *trans* 4-propenylphenol, *cis* and *trans* 4-propylcyclohexanone, indan-5-ol, 4-cyclopropylphenol, etc. The direct scissions of hydroxyl, isopropenyl, and methyl groups are high barrier height demanding, therefore, the addition reaction of hydrogen atom to the aromatic carbon is carried out prior to the functional cleavage. Using similar approach, reaction schemes 3 and 4 which produce benzene from *p*-IPP component employing different reaction pathways require significantly low activation barriers. On the other hand, the thermochemical study, which is performed in the range of 398 K – 898 K, suggests that all reaction schemes are favourable at each temperature condition except reaction scheme 8 which becomes non-spontaneous at T>598 K.

6.1.7. DFT Study on the Production of Toluene from Decomposition Reactions of 2-Hydroxy-6-methylbenzaldehyde

The gas phase decomposition of 2-hydroxy-6-methylbenzaldehyde (HMB) is carried out numerically in the framework of density functional theory. The bond dissociation energy analysis predicted dehydrogenation of methyl group of HMB as the least energy demanding

bond scission. The conversion of HMB component into toluene is performed by 8 different reaction possibilities along with the calculations of their potential energy surfaces. In addition, the production of 2-hydroxybenzaldehyde from HMB is also investigated. It has been observed that the optimum reaction progress for the conversion of HMB into toluene involves the hydrogenation at the aromatic carbon of $C_{aromatic}$-CHO bond of HMB followed by elimination of CHO functional group. This produces an intermediate product, *m*-cresol, which further undergoes hydrogenation at the aromatic carbon of $C_{aromatic}$-OH functional group followed by OH elimination reaction to produce toluene. The elimination of OH functional group from hydrogen atom inserted *m*-cresol component determines the overall reaction rate for which the activation energy is 12.26 kcal/mol. Furthermore, the thermochemical analysis revealed that the reaction is favourable even at 473 K; however, at further elevated temperature, the reaction free energy and reaction enthalpy have been seen even more favourable. On the other hand, the production of 2-hydroxybenzaldehyde from HMB is not endorsed compared to the production of toluene from optimum reaction progress.

6.1.8. Molecular Simulations of Palladium Catalysed Hydrodeoxygenation of 2-Hydroxybenzaldehyde using Density Functional Theory

The catalytic conversion of 2-hydroxybenzaldehyde over Pd(111) surface is performed numerically within the framework of density functional theory. It has been observed that present catalytic model showed a very good behaviour in the prediction of adsorption energies of a few aromatic compounds. Direct cleavages of CHO and OH functionals from 2-HB over Pd(111) surface are not thermodynamically beneficial because of difficult ring stabilization after cleavages which results into high kinetic barriers. The catalytic conversion of 2-hydroxybenzaldehyde over Pd(111) surface suggests the production of phenol using reaction scheme 1 which incorporated the dissociation of hydrogen from formyl group of 2-HB

followed by elimination of CO from $C_6H_4(OH)(CO)^*$ and association of hydrogen to 2-hydroxyphenyl. Since, reaction mechanisms involving the formation of benzaldehyde from 2-HB over Pd(111) surface are highly kinetic demanding, therefore, the production of benzaldehyde from 2-HB is highly dubious. In addition, the conversion of phenol into benzene using direct dehydroxylation over Pd(111) surface is not possible in the applied range of temperature because of very high activation energy; therefore, phenol component will be the major product from the conversion of 2-HB over Pd(111) catalyst surface in the applied reaction conditions.

6.1.9. Elucidation of Gas Phase Hydrodeoxygenation Mechanism of Guaiacol over Pd(111) Catalyst Surface: The DFT Framework

The hydrodeoxygenation of guaiacol over Pd(111) catalyst surface is numerically performed within the framework of density functional theory employing various reaction approaches and reported corresponding activation energies. It has been observed during the course of HDO of guaiacol that the reaction progresses involving eliminations of hydrogen atom from hydroxyl or methoxy groups are highly favourable. The most likely major product is catechol because further reduction of catechol is a high kinetic demanding process. The most dominating reaction approach for the production of catechol involved the elimination of hydrogen atom from methoxy group of guaiacol followed by scission and association of CH_2 group and H atom, respectively. The removal of CH_2 from $C_6H_4(OH)(OCH_2)^*$ controls the overall reaction rate and its activation energy is reported as 23.06 kcal/mol. The present observations are in line with the experimental findings; and, in addition, the Pd(111) catalyst surface resembles similar reaction progress for the HDO of guaiacol as of Pt(111) catalyst surface. The kinetic analysis of rate determining step suggests a favourable environment even at 473 K; and upon temperature increment to 673 K, the favourability further improves.

6.1.10. Pt- and Pd-doped Graphene Sheets as Catalysts for Upgrading Bio-oil Model Compounds: Chemisorption Study by DFT

The surface behaviours of Pd- and Pt-doped graphene sheets are studied within the framework of density functional theory (DFT) for adsorptions of gas phase phenolic species such as phenol, anisole, salicylaldehyde, guaiacol, and vanillin. The depositions of metals (Pd or Pt) onto the defect sites of graphene sheets are very high energy releasing processes; and these energies are in very good agreements with the literature findings. The adsorptions of phenol, anisole, and guaiacol are found most stable *via* phenyl ring interactions over both surfaces but salicylaldehyde and vanillin components act differently over each surface. While Pt-doped graphene surface showed better adsorption stability of salicylaldehyde *via* phenyl ring, Pd-doped surface advocated its most stable adsorption configuration *via* the interaction of hydroxyl group. On the other hand, vanillin component binds strongly to both catalytic surfaces *via* the interaction of oxygen atom of formyl group. The thermochemical analyses of all adsorption configurations of each model compound over both catalytic surfaces suggested a very high energy release due to adsorption of every phenolic species along with a high availability of free energy as well. Furthermore, the equilibrium constant values at each temperature suggested higher tendency of equilibrium shift towards the formation of adsorption complexes. Along with this, ln $\mathbf{K_{eq}}$ vs. **1/T** relations are proposed for each adsorption configuration with R^2 values ranging between 0.9712 and 0.9714.

6.1.11. Thermochemistry analyses for transformation of C6 glucose compound into C9, C12 and C15 alkanes using density functional theory

The reaction thermochemistry of conversion of glucose molecule into various long chain alkanes is carried out in both gas and aqueous phases at different temperature values using

B3LYP/6-31+g(d,p) level of theory under DFT perspective. The thermochemistry suggested the dominance of aqueous phase over gas phase environment for the hydrolysis of sugar into long chain alkanes. The aldol condensation reactions are not favourable reactions at any temperature values from 300-900 K with P=1 atm; however, these reactions are quite necessary to perform C-C coupling to form large organic compounds. The hydrodeoxygenation reactions under each reaction pathway are found as most favourable reactions in both phases, however, aqueous phase dominates over gas phase in all discussed thermodynamic parameters. The temperature variations have been quite useful for most cases but in some cases, the increment in temperature has not considerably affected the thermodynamic properties of reactions.

6.2. Future Scopes

- **Solvation Effects:** The gas phase decomposition often led to higher energetics, therefore, the solution phase environment can be stimulating in order to minimise the energy requirements. In addition, similar phenomena can be applicable to catalytic hydrodeoxygenation reactions as well.
- **Catalyst and Effect of Support:** The direct cleavages of hydroxyl groups on Pd(111) catalyst led to high activation barriers, therefore, other catalytic systems or incorporation of a catalyst support may be remarkable in order to stabilize the catalyst and reduce the kinetic barrier in numerical framework.
- **Bimetallic System:** The numerical framework of bimetallic catalyst systems in modelling of hydrodeoxygenation process of bio-oil is very limited thus two metal atoms as in the form of catalyst can be analysed to understand the energy differences.
- **Metal atom doping:** The doping of metal atoms other than Pd and Pt on the defected graphene sheets may result into different binding capability. Further, the deposition of metal atoms on double defected graphene sheet may have the potential to emerge as a novel catalytic system.

REFERENCES

1. Huber, G.W., Iborra, S., Corma, A.: Synthesis of transportation fuels from biomass: Chemistry, catalysts, and engineering. Chem. Rev. 106, 4044–4098 (2006).

2. World Population Prospects The 2015 Revision. (2015).

3. World Energy Scenario 2016. (2016).

4. Stöcker, M.: Biofuels and Biomass-To-Liquid Fuels in the Biorefinery: Catalytic Conversion of Lignocellulosic Biomass using Porous Materials. Angew. Chemie Int. Ed. 47, 9200–9211 (2008).

5. Ragauskas, A.J.: The Path Forward for Biofuels and Biomaterials. Science. 311, 484–489 (2006).

6. World Energy Resources: 2013 survey. (2013).

7. Wang, H., Male, J., Wang, Y.: Recent Advances in Hydrotreating of Pyrolysis Bio-Oil and Its Oxygen-Containing Model Compounds. ACS Catal. 3, 1047–1070 (2013).

8. Mu, W., Ben, H., Ragauskas, A., Deng, Y.: Lignin Pyrolysis Components and Upgrading—Technology Review. BioEnergy Res. 6, 1183–1204 (2013).

9. Kanaujia, P.K., Sharma, Y.K., Garg, M.O., Tripathi, D., Singh, R.: Review of analytical strategies in the production and upgrading of bio-oils derived from lignocellulosic biomass. J. Anal. Appl. Pyrolysis. 105, 55–74 (2014).

10. Huber, G.W., Cortright, R.D., Dumesic, J.A.: Renewable Alkanes by Aqueous-Phase Reforming of Biomass-Derived Oxygenates. Angew. Chemie Int. Ed. 43, 1549–1551

(2004).

11. Gollakota, A.R.K., Reddy, M., Subramanyam, M.D., Kishore, N.: A review on the upgradation techniques of pyrolysis oil. Renew. Sustain. Energy Rev. 58, 1543–1568 (2016).

12. Klass, D.L.: Biomass for Renewable Energy and Fuels. Encycl. Energy. 1, 193–212 (2004).

13. Sawin, J.L.., Sverrisson, F.: Renewables 2014 Global status Report. , Paris (2014).

14. Alonso, D.M., Bond, J.Q., Dumesic, J.A.: Catalytic conversion of biomass to biofuels. Green Chem. 12, 1493–1513 (2010).

15. Amidon, T.E., Liu, S.: Water-based woody biorefinery. Biotechnol. Adv. 27, 542–550 (2009).

16. Saidi, M., Samimi, F., Karimipourfard, D., Nimmanwudipong, T., Gates, B.C., Rahimpour, M.R.: Upgrading of lignin-derived bio-oils by catalytic hydrodeoxygenation. Energy Environ. Sci. 7, 103–129 (2014).

17. Towler, G.P., Oroskar, A.R., Smith, S.E.: Development of a sustainable liquid fuels infrastructure based on biomass. Environ. Prog. 23, 334–341 (2004).

18. Lynd, L.R., Wyman, C.E., Gerngross, T.U.: Biocommodity engineering. Biotechnol. Prog. 15, 777–793 (1999).

19. Dhyani, V., Bhaskar, T.: A comprehensive review on the pyrolysis of lignocellulosic biomass. Renew. Energy. (2017).

20. Mullen, C.A., Boateng, A.A.: Chemical Composition of Bio-oils Produced by Fast

Pyrolysis of Two Energy Crops. Energy & Fuels. 22, 2104–2109 (2008).

21. David, K., Ragauskas, A.J.: Switchgrass as an energy crop for biofuel production: A review of its ligno-cellulosic chemical properties. Energy Environ. Sci. 3, 1182 (2010).

22. Mohan, D., Pittman, C.U., Steele, P.H.: Pyrolysis of Wood / Biomass for Bio-oil : A Critical Review. Energy & Fuesl. 20, 848–889 (2006).

23. Pandey, M.P., Kim, C.S.: Lignin Depolymerization and Conversion: A Review of Thermochemical Methods. Chem. Eng. Technol. 34, 29–41 (2011).

24. Li, C., Zhao, X., Wang, A., Huber, G.W., Zhang, T.: Catalytic Transformation of Lignin for the Production of Chemicals and Fuels. Chem. Rev. 115, 11559–11624 (2015).

25. Liu, W., Jiang, H., Yu, H.: Thermochemical conversion of lignin to functional materials : a review and future directions. Green Chem. 17, 4888–4907 (2015).

26. Upton, B.M., Kasko, A.M.: Strategies for the Conversion of Lignin to High-Value Polymeric Materials : Review and Perspective. Chem. Rev. 116, 2275–2306 (2016).

27. Azadi, P., Inderwildi, O.R., Farnood, R., King, D.A.: Liquid fuels, hydrogen and chemicals from lignin: A critical review. Renew. Sustain. Energy Rev. 21, 506–523 (2013).

28. Kärkäs, M.D., Matsuura, B.S., Monos, T.M., Magallanes, G., Stephenson, C.R.J.: Transition-metal catalyzed valorization of lignin: the key to a sustainable carbon-neutral future. Org. Biomol. Chem. 14, 1853–1914 (2016).

29. Lin, Y.-C., Huber, G.W.: The critical role of heterogeneous catalysis in lignocellulosic biomass conversion. Energy Environ. Sci. 2, 68–80 (2009).

30. Hagglund, E., Bjorkman, C.: Lignin hydrochloride. Biochem. Z. 147, 74 (1924).

31. Spath, P.L., Dayton, D.C.: Preliminary Screening -- Technical and Economic Assessment of Synthesis Gas to Fuels and Chemicals with Emphasis on the Potential for Biomass-Derived Syngas. Nat. Ren. Ener. Lab. (2003).

32. Branca, C., Giudicianni, P., Di Blasi, C.: GC/MS characterization of liquids generated from low-temperature pyrolysis of wood. Ind. Eng. Chem. Res. 42, 3190–3202 (2003).

33. Diebold, J.P.: A Review of the Chemical and Physical Mechanisms of the Storage Stability of Fast Pyrolysis Bio-Oils. Nat. Ren. Ener. Lab. (2000).

34. Jiang, G., Nowakowski, D.J., Bridgwater, A. V.: Effect of the Temperature on the Composition of Lignin Pyrolysis Products. Energy & Fuels. 24, 4470–4475 (2010).

35. Czernik, S., Bridgwater, A.: Overview of applications of biomass fast pyrolysis oil. Energy & Fuels. 18, 590–598 (2004).

36. Bridgwater, A.: Fast pyrolysis processes for biomass. Renew. Sustain. Energy Rev. 4, 1–73 (2000).

37. Corma, A.: State of the art and future challenges of zeolites as catalysts. J. Catal. 216, 298–312 (2003).

38. Ikura, M., Stanciulescu, M., Hogan, E.: Emulsification of pyrolysis derived bio-oil in diesel fuel. Biomass and Bioenergy. 24, 221–232 (2003).

39. Chiaramonti, D., Bonini, M., Fratini, E., Tondi, G., Gartner, K., Bridgwater, A. V., Grimm, H.P., Soldaini, I., Webster, A., Baglioni, P.: Development of emulsions from biomass pyrolysis liquid and diesel and their use in engines - Part 1: Emulsion

production. Biomass and Bioenergy. 25, 85–99 (2003).

40. Chiaramonti, D., Bonini, M., Fratini, E., Tondi, G., Gartner, K., Bridgwater, A. V, Grimm, H.P., Soldaini, I., Webster, A., Baglioni, P.: Development of emulsions from biomass pyrolysis liquid and diesel and their use in engines — Part 2: tests in diesel engines. Biomass and Bioenergy. 25, 101–111 (2003).

41. Elliott, D.C., Schiefelbein, G.F.: Liquid hydrocarbon fuels from biomass. Am. Chem. Soc. Div. Fuel Chem. Prepr. 34, 1160–1166 (1989).

42. Jensen, F.: Introduction to Computational Chemistry. John Wiley & Sons Ltd. (2007).

43. Lewars, E.G.: Computitional Chemistry. Springer (2011).

44. Lu, J., Behtash, S., Mamun, O., Heyden, A.: Theoretical Investigation of the Reaction Mechanism of the Hydrodeoxygenation of Guaiacol over a Ru (0001) Model Surface. J. Catal. 321, 39–50 (2015).

45. Lu, J., Behtash, S., Mamun, O., Heyden, A.: Theoretical Investigation of the Reaction Mechanism of the Guaiacol Hydrogenation over a Pt(111) Catalyst. ACS Catal. 5, 2423–2435 (2015).

46. Lee, K., Gu, G.H., Mullen, C., Boateng, A., Vlachos, D.G.: Guaiacol hydrodeoxygenation mechanism on Pt(111): insights from density functional theory and linear free energy relations. ChemSusChem. 8, 315–22 (2015).

47. Chiu, C., Genest, A., Borgna, A., Rösch, N.: Hydrodeoxygenation of Guaiacol over Ru(0001): A DFT Study. ACS Catal. 4, 4178–4188 (2014).

48. Behtash, S., Lu, J., Williams, C.T., Monnier, J.R., Heyden, A.: Effect of palladium

surface structure on the hydrodeoxygenation of propanoic acid: Identification of active sites. J. Phys. Chem. C. 119, 1928–1942 (2015).

49. Vorotnikov, V., Mpourmpakis, G., Vlachos, D.G.: DFT Study of Furfural Conversion to Furan , Furfuryl Alcohol , and 2 - Methylfuran on Pd (111). ACS Catal. 2, 2496–2504 (2012).

50. Liu, C., Zhang, Y., Huang, X.: Study of guaiacol pyrolysis mechanism based on density function theory. Fuel Process. Technol. 123, 159–165 (2014).

51. Huang, J., Li, X., Wu, D., Tong, H., Li, W.: Theoretical studies on pyrolysis mechanism of guaiacol as lignin model compound. J. Renew. Sustain. Energy. 5, 043112–043117 (2013).

52. Wang, M., Liu, C., Xu, X., Li, Q.: Theoretical study of the pyrolysis of vanillin as a model of secondary lignin pyrolysis. Chem. Phys. Lett. 654, 41–45 (2016).

53. Assary, R.S., Redfern, P.C., Hammond, J.R., Greeley, J., Curtiss, L. a: Computational studies of the thermochemistry for conversion of glucose to levulinic acid. J. Phys. Chem. B. 114, 9002–9009 (2010).

54. Assary, R.S., Redfern, P.C., Greeley, J., Curtiss, L. a: Mechanistic insights into the decomposition of fructose to hydroxy methyl furfural in neutral and acidic environments using high-level quantum chemical methods. J. Phys. Chem. B. 115, 4341–4349 (2011).

55. Furimsky, E.: Chemistry of Catalytic Hydrodeoxygenation. Catal. Rev. 25, 421–458 (1983).

56. Furimsky, E.: Catalytic hydrodeoxygenation. Appl. Catal. A Gen. 199, 147–190 (2000).

57. Huber, G.W., Chheda, J.N., Barrett, C.J., Dumesic, J.A.: Production of Liquid Alkanes by Aqueous-Phase Processing of Biomass-Derived Carbohydrates. Science. 308, 1446–1450 (2005).

58. Schmidt, L.D., Dauenhauer, P.J.: Hybrid routes to biofuels. Nature. 447, 914–915 (2007).

59. Kunkes, E.L., Simonetti, D.A., West, R.M., Serrano-ruiz, J.C., Gärtner, C.A., Dumesic, J.A.: Catalytic Conversion of Biomass. Science. 322, 417–421 (2008).

60. Bond, J.Q., Alonso, D.M., Wang, D., West, R.M., Dumesic, J. a.: Integrated Catalytic Conversion of γ-Valerolactone to Liquid Alkenes for Transportation Fuels. Science. 327, 1110–1114 (2010).

61. Lange, J.P., Price, R., Ayoub, P.M., Louis, J., Petrus, L., Clarke, L., Gosselink, H.: Valeric biofuels: A platform of cellulosic transportation fuels. Angew. Chemie - Int. Ed. 49, 4479–4483 (2010).

62. Assary, R.S., Redfern, P.C., Hammond, J.R., Greeley, J., Curtiss, L. a.: Predicted thermochemistry for chemical conversions of 5-hydroxymethylfurfural. Chem. Phys. Lett. 497, 123–128 (2010).

63. Bu, Q., Lei, H., Zacher, A.H., Wang, L., Ren, S., Liang, J., Wei, Y., Liu, Y., Tang, J., Zhang, Q., Ruan, R.: A review of catalytic hydrodeoxygenation of lignin-derived phenols from biomass pyrolysis. Bioresour. Technol. 124, 470–477 (2012).

64. Davis, K.M., Rover, M., Brown, R.C., Bai, X., Wen, Z., Jarboe, L.R.: Recovery and utilization of lignin monomers as part of the biorefinery approach. Energies. 9, 1–28 (2016).

65. Nowakowski, D.J., Bridgwater, A. V., Elliott, D.C., Meier, D., de Wild, P.: Lignin fast pyrolysis: Results from an international collaboration. J. Anal. Appl. Pyrolysis. 88, 53–72 (2010).

66. Walton, N.J., Mayer, M.J., Narbad, A.: Vanillin. Phytochemistry. 63, 505–515 (2003).

67. Bindwal, A.B., Vaidya, P.D.: Reaction kinetics of vanillin hydrogenation in aqueous solutions using a Ru/C catalyst. Energy and Fuels. 28, 3357–3362 (2014).

68. Peng, J., Chen, P., Lou, H., Zheng, X.: Upgrading of bio-oil over aluminum silicate in supercritical ethanol. Energy and Fuels. 22, 3489–3492 (2008).

69. Shen, D.K., Gu, S., Luo, K.H., Wang, S.R., Fang, M.X.: The pyrolytic degradation of wood-derived lignin from pulping process. Bioresour. Technol. 101, 6136–6146 (2010).

70. Shin, E.J., Nimlos, M.R., Evans, R.J.: A study of the mechanisms of vanillin pyrolysis by mass spectrometry and multivariate analysis. Fuel. 80, 1689–1696 (2001).

71. Liu, C., Deng, Y., Wu, S., Mou, H., Liang, J., Lei, M.: Study on the pyrolysis mechanism of three guaiacyl-type lignin monomeric model compounds. J. Anal. Appl. Pyrolysis. 118, 123–129 (2016).

72. Horáček, J., Šťávová, G., Kelbichová, V., Kubička, D.: Zeolite-Beta-supported platinum catalysts for hydrogenation/hydrodeoxygenation of pyrolysis oil model compounds. Catal. Today. 204, 38–45 (2013).

73. Nimmanwudipong, T., Runnebaum, R.C., Ebeler, S.E., Block, D.E., Gates, B.C.: Upgrading of lignin-derived compounds: Reactions of eugenol catalyzed by HY zeolite and by Pt/γ-Al 2O 3. Catal. Letters. 142, 151–160 (2012).

74. Zhang, C., Xing, J., Song, L., Xin, H., Lin, S., Xing, L., Li, X.: Aqueous-phase hydrodeoxygenation of lignin monomer eugenol: Influence of Si/Al ratio of HZSM-5 on catalytic performances. Catal. Today. 234, 145–152 (2014).

75. Bykova, M. V., Ermakov, D.Y., Kaichev, V. V., Bulavchenko, O.A., Saraev, A.A., Lebedev, M.Y., Yakovlev, V.: Ni-based sol-gel catalysts as promising systems for crude bio-oil upgrading: Guaiacol hydrodeoxygenation study. Appl. Catal. B Environ. 113–114, 296–307 (2012).

76. Bykova, M. V., Bulavchenko, O., Ermakov, D.Y., Lebedev, M.Y., Yakovlev, V., Parmon, V.N.: Guaiacol hydrodeoxygenation in the presence of Ni-containing catalysts. Catal. Ind. 3, 15–22 (2011).

77. Mortensen, P.M., Grunwaldt, J., Jensen, P.A., Jensen, A.D.: Screening of Catalysts for Hydrodeoxygenation of Phenol as a Model Compound for Bio-oil. ACS Catal. 3, 1774–1785 (2013).

78. Chen, M.-Y., Huang, Y.-B., Pang, H., Liu, X.-X., Fu, Y.: Hydrodeoxygenation of lignin-derived phenols into alkanes over carbon nanotube supported Ru catalysts in biphasic systems. Green Chem. 17, 1710–1717 (2015).

79. Deepa, A.K., Dhepe, P.L.: Function of metals and supports on the hydrodeoxygenation of phenolic compounds. Chempluschem. 79, 1573–1583 (2014).

80. Ledesma, E.B., Hoang, J.N., Nguyen, Q., Hernandez, V., Nguyen, M.P., Batamo, S., Fortune, C.K.: Unimolecular decomposition pathway for the vapor-phase cracking of eugenol, a biomass tar compound. Energy and Fuels. 27, 6839–6846 (2013).

81. Toms, A., Wood, J.M.: The degradation of trans-ferulic acid. Biochemistry. 9, 337–343

(1970).

82. Karmakar, B., Vohra, R.M., Nandanwar, H., Sharma, P., Gupta, K.G., Sobti, R.C.: Rapid degradation of ferulic acid via 4-vinylguaiacol and vanillin by a newly isolated strain of Bacillus coagulans. J. Biotechnol. 80, 195–202 (2000).

83. Buranov, A.U., Mazza, G.: Extraction and purification of ferulic acid from flax shives, wheat and corn bran by alkaline hydrolysis and pressurised solvents. Food Chem. 115, 1542–1548 (2009).

84. Esparan, V., Krings, U., Struch, M., Berger, R.G.: A three-enzyme-system to degrade curcumin to natural vanillin. Molecules. 20, 6640–6653 (2015).

85. Lepifre, S., Baumberger, S., Pollet, B., Cazaux, F., Coqueret, X., Lapierre, C.: Reactivity of sulphur-free alkali lignins within starch films. Ind. Crops Prod. 20, 219–230 (2004).

86. Hasyierah, M.. N., Zulkali, M.M.D., Syahidah, K.I.K.: Ferulic acid from lignocellulosic biomass - review. In: Malaysian University Conferences on Engineering and Technology. 1–8 (2008).

87. Fiddler, W., Parker, W.E., Wasserman, a E., Doerr, R.C.: Thermal decomposition of ferulic acid. J. Agric. Food Chem. 15, 757–761 (1967).

88. Wit, M.K.-D., Frost, D.J., Ward, J.P.: Formation of p-vinylguaiacol oligomers in the thermal decarboxylation of ferulic acid. Recl. des Trav. Chim. des Pays-Bas. 90, 906–911 (1971).

89. Mathew, S., Abraham, T.E., Sudheesh, S.: Rapid conversion of ferulic acid to 4-vinyl guaiacol and vanillin metabolites by Debaryomyces hansenii. J. Mol. Catal. B Enzym. 44, 48–52 (2007).

90. Nimmanwudipong, T., Aydin, C., Lu, J., Runnebaum, R.C., Brodwater, K.C., Browning, N.D., Block, D.E., Gates, B.C.: Selective hydrodeoxygenation of guaiacol catalyzed by platinum supported on magnesium oxide. Catal. Letters. 142, 1190–1196 (2012).

91. Lee, C.R., Yoon, J.S., Suh, Y.-W., Choi, J.-W., Ha, J.-M., Suh, D.J., Park, Y.-K.: Catalytic roles of metals and supports on hydrodeoxygenation of lignin monomer guaiacol. Catal. Commun. 17, 54–58 (2012).

92. Gao, D., Schweitzer, C., Hwang, H.T., Varma, A.: Conversion of Guaiacol on Noble Metal Catalysts: Reaction Performance and Deactivation Studies. Ind. Eng. Chem. Res. 53, 18658–18667 (2014).

93. Sun, J., Karim, A.M., Zhang, H., Kovarik, L., Li, X.S., Hensley, A.J., McEwen, J.S., Wang, Y.: Carbon-supported bimetallic Pd-Fe catalysts for vapor-phase hydrodeoxygenation of guaiacol. J. Catal. 306, 47–57 (2013).

94. Mu, W., Ben, H., Du, X., Zhang, X., Hu, F., Liu, W., Ragauskas, A.J., Deng, Y.: Noble metal catalyzed aqueous phase hydrogenation and hydrodeoxygenation of lignin-derived pyrolysis oil and related model compounds. Bioresour. Technol. 173, 6–10 (2014).

95. Chang, J., Danuthai, T., Dewiyanti, S., Wang, C., Borgna, A.: Hydrodeoxygenation of guaiacol over carbon-supported metal catalysts. ChemCatChem. 5, 3041–3049 (2013).

96. Shafaghat, H., Sirous Rezaei, P., Daud, W.M.A.W.: Catalytic hydrogenation of phenol, cresol and guaiacol over physically mixed catalysts of Pd/C and zeolite solid acids. RSC Adv. 5, 33990–33998 (2015).

97. Boonyasuwat, S., Omotoso, T., Resasco, D.E., Crossley, S.P.: Conversion of guaiacol

over supported Ru catalysts. Catal. Letters. 143, 783–791 (2013).

98. Aqsha, A., Katta, L., Mahinpey, N.: Catalytic Hydrodeoxygenation of Guaiacol as Lignin Model Component Using Ni-Mo / TiO 2 and Ni-V / TiO 2 Catalysts. Catal. Letters. 145, 1351–1363 (2015).

99. Ma, R., Cui, K., Yang, L., Ma, X., Li, Y.: Selective catalytic conversion of guaiacol to phenols over a molybdenum carbide catalyst. Chem. Commun. 51, 10299–10301 (2015).

100. Bykova, M. V., Ermakov, D.Y., Kaichev, V. V., Bulavchenko, O.A., Saraev, A.A., Lebedev, M.Y., Yakovlev, V.: Ni-based sol-gel catalysts as promising systems for crude bio-oil upgrading: Guaiacol hydrodeoxygenation study. Appl. Catal. B Environ. 113–114, 296–307 (2012).

101. Hurff, S.J., Klein, M.T.: Reaction pathway analysis of thermal and catalytic lignin fragmentation by use of model compounds. Ind. Eng. Chem. Fundam. 22, 426–430 (1983).

102. Olcese, R.N., Bettahar, M., Petitjean, D., Malaman, B., Giovanella, F., Dufour, A.: Gas-phase hydrodeoxygenation of guaiacol over Fe/SiO2 catalyst. Appl. Catal. B Environ. 115–116, 63–73 (2012).

103. Gao, D., Xiao, Y., Varma, A.: Guaiacol Hydrodeoxygenation over Platinum Catalyst: Reaction Pathways and Kinetics. Ind. Eng. Chem. Res. 54, 10638–10644 (2015).

104. Robichaud, D.J., Scheer, A.M., Mukarakate, C., Ormond, T.K., Buckingham, G.T., Ellison, G.B., Nimlos, M.R.: Unimolecular thermal decomposition of dimethoxybenzenes. J. Chem. Phys. 140, 234302–234314 (2014).

105. Huang, J., He, C.: Pyrolysis mechanism of α-O-4 linkage lignin dimer: A theoretical study. J. Anal. Appl. Pyrolysis. 113, 655–664 (2015).

106. Zhang, J.J., Jiang, X.Y., Ye, X.N., Chen, L., Lu, Q., Wang, X.H., Dong, C.Q.: Pyrolysis mechanism of a β-O-4 type lignin dimer model compound: A joint theoretical and experimental study. J. Therm. Anal. Calorim. 123, 501–510 (2016).

107. Custodis, V.B.F., Hemberger, P., Ma, Z., Van Bokhoven, J.A.: Mechanism of fast pyrolysis of lignin: Studying model compounds. J. Phys. Chem. B. 118, 8524–8531 (2014).

108. McClymont, E.L., Bingham, E.M., Nott, C.J., Chambers, F.M., Pancost, R.D., Evershed, R.P.: Pyrolysis GC-MS as a rapid screening tool for determination of peat-forming plant composition in cores from ombrotrophic peat. Org. Geochem. 42, 1420–1435 (2011).

109. Hirano, T., Honda, Y., Watanabe, T., Kuwahara, M.: Degradation of Bisphenol A by the Lignin-Degrading Enzyme, Manganese Peroxidase, Produces by the White-rot Basidiomycete, Pleurotus ostreatus. Biosci. Biotechnol. Biochem. 64, 1958–1962 (2000).

110. Hunter, S.E., Savage, P.E.: Kinetics and mechanism of p-isopropenylphenol synthesis via hydrothermal cleavage of bisphenol A. J. Org. Chem. 69, 4724–4731 (2004).

111. Tagaya, H., Katoh, K., Kadokawa, J.I., Chiba, K.: Decomposition of polycarbonate in subcritical and supercritical water. Polym. Degrad. Stab. 64, 289–292 (1999).

112. Zhao, L., Xiao, X., Peng, L., Gu, F.L., Zhang, R.Q.: Visible-light photocatalytic mechanism of bisphenol-A on nano-Bi2O3: a combined DFT calculation and experimental study. RSC Adv. 4, 10343–10349 (2014).

113. Stas, M., Kubic, D., Chudoba, J., Posp, M.: Overview of Analytical Methods Used for Chemical Characterization of Pyrolysis Bio-oil. Energy & Fuels. 28, 385–402 (2014).

114. Loo, A.Y., Jain, K., Darah, I.: Food Chemistry Antioxidant activity of compounds isolated from the pyroligneous acid , Rhizophora apiculata. Food Chem. 107, 1151–1160 (2008).

115. Nowakowski, D.J., Jones, J.M.: Uncatalysed and potassium-catalysed pyrolysis of the cell-wall constituents of biomass and their model compounds. J. Anal. Appl. Pyrolysis. 83, 12–25 (2008).

116. Djokic, M.R., Dijkmans, T., Yildiz, G., Prins, W., Geem, K.M. Van: Quantitative analysis of crude and stabilized bio-oils by comprehensive two-dimensional gas-chromatography. J. Chromatogr. A. 1257, 131–140 (2012).

117. Parr, R.G., Weitao, Y.: Density-Functional Theory of Atoms and Molecules. Oxford University Press (1994).

118. Hohenberg, P., Kohn, W.: Inhomogeneous electron gas. Phys. Rev. 136, B864–B871 (1964).

119. Kohn, W., Sham, L.: Self-Consistent Equations Including Exchange and Correlation Effects. Phys. Rev. 385, A1133–A1138 (1965).

120. Becke, A.D.: Density-functional thermochemistry.III. The role of exact exchange. J. Chem. Phys. 98, 5648–5652 (1993).

121. March, N.H. (Norman H.: Self-consistent fields in atoms; Hartree and Thomas-Fermi atoms,. Pergamon Press (1975).

122. Thomas, L.H.: The calculation of atomic fields. Math. Proc. Cambridge Philos. Soc. 23, 542 (1927).

123. Kohn, W., Sham, L.: Self-Consistent Equations Including Exchange and Correlation Effects, (1965).

124. Simón, L., Goodman, J.M.: How reliable are DFT transition structures? Comparison of GGA, hybrid-meta-GGA and meta-GGA functionals. Org. Biomol. Chem. 9, 689–700 (2011).

125. Becke, A.D.: Density-functional exchange-energy approximation with correct asymptotic behavior. Phys. Rev. A. 38, 3098–3100 (1988).

126. Perdew, J.P., Wang, Y.: Accurate and simple analytic representation of the electron-gas correlation energy. Phys. Rev. B. 45, 13244–13249 (1992).

127. Hay, P.J., Wadt, W.R.: Ab initio effective core potentials for molecular calculations. Potentials for the transition metal atoms Sc to Hg. J. Chem. Phys. 82, 270 (1985).

128. McQuarrie, D.A., D., S.J.: Molecular thermodynamics. University Science Books, California (1999).

129. Eyring, H.: The Activated Complex in Chemical Reactions. J. Chem. Phys. 3, 107–115 (1935).

130. Carneiro, J. de M., Cruz, M.T. de M.: Density Functional Theory Study of the Adsorption of Formaldehyde on Pd 4 and on Pd 4 /γ-Al 2 O 3 Clusters †. J. Phys. Chem. A. 112, 8929–8937 (2008).

131. Velcheva, E.A., Stamboliyska, B.A.: IR spectral and structural changes caused by the

conversion of 3-methoxy-4-hydroxybenzaldehyde (vanillin) into the oxyanion. Spectrochim. Acta - Part A. 60, 2013–2019 (2004).

132. Egawa, T., Kameyama, A., Takeuchi, H.: Structural determination of vanillin, isovanillin and ethylvanillin by means of gas electron diffraction and theoretical calculations. J. Mol. Struct. 794, 92–102 (2006).

133. Balachandran, V., Parimala, K.: Vanillin and isovanillin: Comparative vibrational spectroscopic studies, conformational stability and NLO properties by density functional theory calculations. Spectrochim. Acta - Part A Mol. Biomol. Spectrosc. 95, 354–368 (2012).

134. Bui, V.N., Laurenti, D., Afanasiev, P., Geantet, C.: Hydrodeoxygenation of guaiacol with CoMo catalysts . Part I : Promoting effect of cobalt on HDO selectivity and activity. Appl. Catal. B, Environ. 101, 239–245 (2011).

135. Ghampson, I.T., Sepúlveda, C., Garcia, R., Fierro, J.L.G., Escalona, N., Desisto, W.J.: General Comparison of alumina- and SBA-15-supported molybdenum nitride catalysts for hydrodeoxygenation of guaiacol. "Applied Catal. A, Gen. 435–436, 51–60 (2012).

136. Olbert-majkut, A., Wierzejewska, M.: Conformational Study of Eugenol by Density Functional Theory Method and Matrix-Isolation Infrared Spectroscopy. J. Phys. Chem. A. 112, 5691–5699 (2008).

137. Rizzi, G.P., Boekley, L.J.: Observation of Ether-Linked Phenolic Products during Thermal Degradation of Ferulic Acid in the Presence of Alcohols. J. Agric. Food Chem. 40, 1666–1670 (1992).

138. Esatbeyoglu, T., Ulbrich, K., Rehberg, C., Rohn, S., Rimbach, G.: Thermal stability,

antioxidant, and anti-inflammatory activity of curcumin and its degradation product 4-vinyl guaiacol. Food Funct. 6, 887–893 (2015).

139. Koseki, T., Ito, Y., Furuse, S., Ito, K., Iwano, K.: Conversion of Ferulic acid into 4-vinylguaiacol vanillin and vanilliv acid in model solution of shochu. J. Ferment. Bioengeneering. 82, 46–50 (1996).

140. Li, X., Yang, J., Li, X., Gu, W., Huang, J., Zhang, K.Q.: The metabolism of ferulic acid via 4-vinylguaiacol to vanillin by Enterobacter sp. Px6-4 isolated from Vanilla root. Process Biochem. 43, 1132–1137 (2008).

141. Ghosh, S., Sachan, A., Mitra, A.: Degradation of ferulic acid by a white rot fungus Schizophyllum commune. World J. Microbiol. Biotechnol. 21, 385–388 (2005).

142. Yoon, S.-H., Li, C., Lee, Y.-M., Lee, S.-H., Kim, S.-H., Choi, M.-S., Seo, W.-T., Yang, J.-K., Kim, J.-Y., Kim, S.-W.: Production of vanillin from ferulic acid using recombinant strains of Escherichia coli. Biotechnol. Bioprocess Eng. 10, 378–384 (2005).

143. Brunati, M., Marinelli, F., Bertolini, C., Gandolfi, R., Daffonchio, D., Molinari, F.: Biotransformations of cinnamic and ferulic acid with actinomycetes. Enzyme Microb. Technol. 34, 3–9 (2004).

144. Bykova, M. V., Zavarukhin, S.G., Trusov, L.I., Yakovlev, V.A.: Guaiacol hydrodeoxygenation kinetics with catalyst deactivation taken into consideration. Kinet. Catal. 54, 40–48 (2013).

145. Moon, J.S., Kim, E.G., Lee, Y.K.: Active sites of Ni2P/SiO2 catalyst for hydrodeoxygenation of guaiacol: A joint XAFS and DFT study. J. Catal. 311, 144–152

(2014).

146. Saeys, M., Reyniers, M.F., Neurock, M., Marin, G.B.: Ab initio reaction path analysis of catalytic reactions: benzene hydrogenation and cyclohexane on Pt(111). J. Phys. Chem. B. 109, 2064–2073 (2005).

147. Saeys, M., Neurock, M., Marin, G.B., Hall, T., Charlottes, V.: Density Functional Theory Analysis of Benzene (De) hydrogenation on Pt (111): Addition and Removal of the First Two H-Atoms. J. Phys. Chem. B. 107, 3844–3855 (2003).

148. Kistiakowsky, G.B., Ruhoff, J.R., Smith, H.A., Vaughan, W.E., Smith, A., Vaughan, W.E.: Heats of Organic Reactions. IV. Hydrogenation of Some Dienes and of Benzene. J. Am. Chem. Soc. 58, 146–153 (1936).

149. Giuliano, B.M., Velino, B., Maris, A., Caminati, W.: Conformational landscape of indan-5-ol : A free-jet millimetre wave study. J. Mol. Spectrosc. 307, 6–9 (2015).

150. Zaveri, N.T., Journigan, V.B., Polgar, W.E.: Discovery of the First Small-Molecule Opioid Pan Antagonist with Nanomolar Affinity at Mu, Delta, Kappa, and Nociceptin Opioid Receptors. ACS Chem. Neurosci. 6, 646–657 (2015).

151. Chang, S.D., Mascarella, S.W., Spangler, S.M., Gurevich, V. V, Navarro, H. a, Carroll, F.I., Bruchas, M.R.: Quantitative Signaling and Structure-Activity Analyses Demonstrate Functional Selectivity at the Nociceptin/Orphanin FQ Opioid Receptor. Mol. Pharmacol. . 88, 502–511 (2015).

152. Felix, R.A.: United States Patent, (1977).

153. Carneiro, W.D.M., Aranda, D.A.G., Bu, M.: Density Functional Theory Study of Benzene Adsorption on Small Pd and Pt Clusters.pdf. J. Phys. Chem. C. 111, 11068–

11076 (2007).

154. Orita, H., Itoh, N.: Simulation of phenol formation from benzene with a Pd membrane reactor: Ab initio periodic density functional study. Appl. Catal. A Gen. 258, 17–23 (2004).

155. Li, G., Han, J., Wang, H., Zhu, X., Ge, Q.: Role of dissociation of phenol in its selective hydrogenation on Pt(111) and Pd(111). ACS Catal. 5, 2009–2016 (2015).

156. Rubeš, M., He, J., Nachtigall, P., Bludský, O.: Direct hydrodeoxygenation of phenol over carbon-supported Ru catalysts: A computational study. J. Mol. Catal. A Chem. 423, 300–307 (2016).

157. de Souza, P.M., Rabelo-Neto, R.C., Borges, L.E.P., Jacobs, G., Davis, B.H., Resasco, D.E., Noronha, F.B.: Hydrodeoxygenation of Phenol over Pd Catalysts. Effect of Support on Reaction Mechanism and Catalyst Deactivation. ACS Catal. 7, 2058–2073 (2017).

158. Julkapli, N.M., Bagheri, S.: Graphene supported heterogeneous catalysts: An overview. Int. J. Hydrogen Energy. 40, 948–979 (2015).

159. Lepró, X., Terrés, E., Vega-Cantú, Y., Rodríguez-Macías, F.J., Muramatsu, H., Kim, Y.A., Hayahsi, T., Endo, M., R., M.T., Terrones, M.: Efficient anchorage of Pt clusters on N-doped carbon nanotubes and their catalytic activity. Chem. Phys. Lett. 463, 124–129 (2008).

160. Bachiller-Baeza, B., Guerrero-Ruiz, A., Rodríguez-Ramos, I.: Role of the residual chlorides in platinum and ruthenium catalysts for the hydrogenation of α,β-unsaturated aldehydes. Appl. Catal. A, Gen. 192, 289–297 (2000).

161. Lam, E., Luong, J.H.T.: Carbon materials as catalyst supports and catalysts in the transformation of biomass to fuels and chemicals. ACS Catal. 4, 3393–3410 (2014).

162. Lee, C., Wei, X., Kysar, J.W., Hone, J.: Measurement of the Elastic Properties and Intrinsic Strength of Monolayer Graphene. Science. 321, 385–388 (2008).

163. Novoselov, K.S., Geim, A.K., Morozov, S. V, Jiang, D., Zhang, Y., Dubonos, S. V, Grigorieva, I. V, Firsov, A. A.: Electric Field Effect in Atomically Thin Carbon Films. Science. 306, 666–669 (2004).

164. Nair, R.R., Blake, P., Grigorenko, A.N., Novoselov, K.S., Booth, T.J., Stauber, T., Peres, N.M.R., Geim, A.K.: Fine Structure Constant Defines Visual Transparency of Graphene. Science. 320, 1308–1308 (2008).

165. Rao, C.N.R., Sood, A.K., Subrahmanyam, K.S., Govindaraj, A.: Graphene: The new two-dimensional nanomaterial. Angew. Chemie - Int. Ed. 48, 7752–7777 (2009).

166. Balandin, A. a, Ghosh, S., Bao, W., Calizo, I., Teweldebrhan, D., Miao, F., Lau, C.N.: Superior Thermal Conductivity of Single-Layer Graphene. Nano Lett. 8, 902–907 (2008).

167. Fan, X., Zhang, G., Zhang, F.: Multiple Roles of Graphene in Heterogeneous Catalysis. Chem. Soc. Rev. 44, 3023–3035 (2015).

168. Xu, D., Zhao, J., Wang, X.: A density functional theory study of the adsorption of bimetallic Fe n Pt m clusters on defective graphene: Structural, electronic, and magnetic properties. J. Nanoparticle Res. 15, 1590–1603 (2013).

169. Wanno, B., Tabtimsai, C.: A DFT investigation of CO adsorption on VIIIB transition metal-doped graphene sheets. Superlattices Microstruct. 67, 110–117 (2014).

170. Wu, L., Song, J., Zhou, B., Wu, T., Jiang, T., Han, B.: Preparation of Ru/Graphene using Glucose as Carbon Source and Hydrogenation of Levulinic Acid to γ-Valerolactone. Chem. - An Asian J. 11, 2792–2796 (2016).

171. Shi, J., Zhao, M., Wang, Y., Fu, J., Lu, X., Hou, Z.: Upgrading of aromatic compounds in bio-oil over ultrathin graphene encapsulated Ru nanoparticles. J. Mater. Chem. A. 4, 5842–5848 (2016).

172. Wang, Y., Rong, Z., Wang, Y., Wang, T., Du, Q., Wang, Y., Qu, J.: Graphene-based metal/acid bifunctional catalyst for the conversion of levulinic acid to γ-valerolactone. ACS Sustain. Chem. Eng. 5, 1538–1548 (2017).

173. Fellah, M.F.: Direct decarbonylation of furfural to furan: A density functional theory study on Pt-graphene. Appl. Surf. Sci. 405, 395–404 (2017).

174. Ferrante, F., Prestianni, A., Cortese, R., Schimmenti, R., Duca, D.: Density Functional Theory Investigation on the Nucleation of Homo- and Heteronuclear Metal Clusters on Defective Graphene. J. Phys. Chem. C. 120, 12022–12031 (2016).

175. McLean, A.D., Chandler, G.S.: Contracted Gaussian basis sets for molecular calculations. I. Second row atoms, Z=11–18. J. Chem. Phys. 72, 5639–5648 (1980).

176. López, M.J., Cabria, I., Alonso, J.A.: Palladium clusters anchored on graphene vacancies and their effect on the reversible adsorption of hydrogen. J. Phys. Chem. C. 118, 5081–5090 (2014).

177. Tang, Y., Yang, Z., Dai, X.: Trapping of metal atoms in the defects on graphene. J. Chem. Phys. 135, 1–7 (2011).

178. Liu, C., Assary, R.S., Curtiss, L. a: Investigation of thermochemistry associated with the

carbon-carbon coupling reactions of furan and furfural using ab initio methods. J. Phys. Chem. A. 118, 4392–404 (2014).

179. Alonso, D.M., Wettstein, S.G., Dumesic, J. a.: Bimetallic catalysts for upgrading of biomass to fuels and chemicals. Chem. Soc. Rev. 41, 8075 (2012).

180. Gallezot, P.: Conversion of biomass to selected chemical products. Chem. Soc. Rev. 41, 1538–1558 (2012).

181. Serrano-Ruiz, J.C., Dumesic, J. a.: Catalytic routes for the conversion of biomass into liquid hydrocarbon transportation fuels. Energy Environ. Sci. 4, 83–99 (2011).

182. Assary, R.S., Kim, T., Low, J.J., Greeley, J., Curtiss, L.A.: Glucose and fructose to platform chemicals: understanding the thermodynamic landscapes of acid-catalysed reactions using high-level ab initio methods. Phys. Chem. Chem. Phys. 14, 16603–16611 (2012).

183. Assary, R.S., Curtiss, L. a: Comparison of Sugar Molecule Decomposition Through Glucose and Fructose : A High level Quantum Chemical Study. Energy & Fuels. 26, 1–6 (2012).

184. Marenich, A. V., Cramer, C.J., Truhlar, D.G.: Universal solvation model based on solute electron density and on a continuum model of the solvent defined by the bulk dielectric constant and atomic surface tensions. J. Phys. Chem. B. 113, 6378–6396 (2009).

RESEARCH OUTPUT

International Refereed Journals:

- **Anand M. Verma** and Nanda Kishore, "DFT Study on Gas Phase Hydrodeoxygenation of Guaiacol by Various Reaction Schemes", *Molecular Simulation*, 43, 141-153, 2017.
- **Anand M. Verma** and Nanda Kishore, "DFT Analyses of Reaction Pathways and Temperature Effects on various Guaiacol Conversion Reactions in Gas Phase Environment", *Chemistry Select*, 1, 6196-6205, 2016.
- **Anand M. Verma** and Nanda Kishore, "Gas Phase Conversion of Eugenol into Various Hydrocarbons and Platform Chemicals", *RSC Advances*, 7, 2527-2543, 2017.
- **Anand M. Verma** and Nanda Kishore, "Production of Benzene from 2-Hydroxybenzaldehyde by Various Reaction Paths using IRC Calculations within a DFT framework", *ChemistrySelect*, 2, 1556-1564, 2017.
- **Anand M. Verma** and Nanda Kishore, "Molecular Modelling Approach to Elucidate the Thermal Decomposition Routes of Vanillin", *New Journal of Chemistry*, 41, 8845-8859, 2017.
- **Anand M. Verma** and Nanda Kishore, "Molecular Simulations of Palladium Catalysed Hydrodeoxygenation of 2-Hydroxybenzaldehyde using Density Functional Theory", *Physical Chemistry Chemical Physics*, 19, 25582-25597, 2017.
- **Anand M. Verma** and Nanda Kishore, "Thermochemistry Analyses for the transformation of C6 Glucose compound into C9, C12, and C15 Alkanes using Density Functional Theory", *Molecular Physics*, 115, 413-423, 2017.

- **Anand M. Verma**, Harshal D. Kawale, Kushagra Agrawal, and Nanda Kishore, "Quantum Chemical Study on Gas Phase Pyrolysis of *p*-Isopropenylphenol", *Journal of Molecular Graphics and Modelling*, 81, 134-145, 2018.

- **Anand M. Verma,** Kushagra Agrawal, Harshal D. Kawale, and Nanda Kishore, "Quantum chemical study on gas phase decomposition of ferulic acid", *Molecular Physics*, 116, 1895-1907, 2018.

- **Anand M. Verma,** Kushagra Agrawal, Harshal D. Kawale, and Nanda Kishore, "Production of Toluene by Decomposition of 2-Hydroxy-6-methylbenzaldehyde: A DFT Study", *ChemistrySelect*, 3, 12279-12288, 2018.

- **Anand M. Verma**, Kushagra Agrawal, and Nanda Kishore, "Binding of Phenolic Model Compounds with Noble Metal Doped Graphene Sheets", *Computational and Theoretical Chemistry*, 1134, 37-46, 2018.

- **Anand M. Verma** and Nanda Kishore, "Kinetic Analysis of Gas Phase Hydrodeoxygenation of Guaiacol over Pd(111) Catalyst Surface within the Framework of Density Functional Theory" (under review).

Book Chapters:

- **Anand M. Verma** and Nanda Kishore, "A Succinct Review on the Upgradation of Lignin Derived Bio-Oil Model Components", *Sustainable Energy – A Transformational Journey*, Vol. 1, Springer, 2018.

- **Anand M. Verma** and Nanda Kishore, "Current Advances in Bio-oil Upgrading: A Brief Discussion", *Sustainable Energy – A Transformational Journey*, Vol. 1, Springer, 2018.

Conferences/Proceedings/Workshops:

- **Anand M. Verma**, Kushagra Agrawal, and Nanda Kishore, "Gas Phase Kinetic Investigations of Decomposition of Salicylaldehyde over Pd(111) Catalyst Surface", *REFLUX*, March 2018, IIT Guwahati, India. (Secured 1st position).

- Kushagra Agrawal, **Anand M. Verma**, and Nanda Kishore, "Elucidating the Production of Vanillin from Ferulic Acid using DFT", *Research Conclave*, March 2018, IIT Guwahati, India.

- **Anand M. Verma**, "A Workshop on Gaussian 09 Software Package", December 2014, Pune, India.

Table 1: Cartesian coordinates of vanillin, eugenol, ferulic acid, guaiacol, 2-hydroxybenzaldehyde (2-HB), *p*-isopropenylphenol, and 2-hydroxy-6-methylbenzaldehyde along with their electronic energy and zero point vibrational energy (ZPVE).

S. No.	Structure Notation	Structure	x-y-z coordinates	Electronic Energy with ZPVE	ZPVEs	Spin Multiplicities
1.	Vanillin	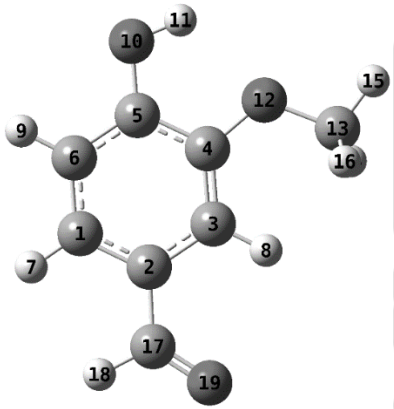	Tag Symbol X Y Z 1 C -1.13951 -1.67326 -2.7E-05 2 C -1.47317 -0.31746 -0.00002 3 C -0.45809 0.657554 -4.2E-05 4 C 0.865263 0.263767 -0.00007 5 C 1.197604 -1.11223 0.000009 6 C 0.194096 -2.07286 -2E-06 7 H -1.92672 -2.41977 -0.00003 8 H -0.74942 1.699845 0.000036 9 H 0.475389 -3.11869 0.000024 10 O 2.497041 -1.49085 0.000071 11 H 3.042058 -0.6908 -1.9E-05 12 O 1.958248 1.088416 -5.7E-05 13 C 1.743875 2.498861 0.000025 14 H 1.19681 2.810193 0.894819 15 H 2.733528 2.951429 -0.00014 16 H 1.196334 2.810215 -0.89448 17 C -2.88669 0.09134 0.000017 18 H -3.60893 -0.75226 0.000028 19 O -3.28271 1.239377 0.000039	-535.332805	0.146324	1

2.	**Eugenol**	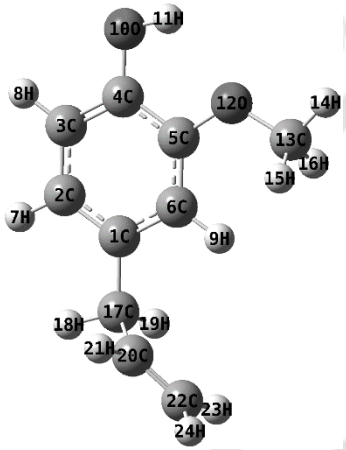	Tag	Symbol	X	Y	Z	-538.658834	0.197726	1
			1	C	0.921847	-0.81144	-0.25298			
			2	C	0.22401	-2.00746	-0.10414			
			3	C	-1.16244	-2.01827	0.071398			
			4	C	-1.86729	-0.82617	0.10102			
			5	C	-1.17351	0.38958	-0.04542			
			6	C	0.204067	0.39514	-0.21805			
			7	H	0.76134	-2.94949	-0.12717			
			8	H	-1.70675	-2.94789	0.187748			
			9	H	0.739077	1.331006	-0.31993			
			10	O	-3.22034	-0.8299	0.273338			
			11	H	-3.52022	0.088975	0.264996			
			12	O	-1.98317	1.498768	0.00469			
			13	C	-1.38858	2.783784	-0.13284			
			14	H	-2.20475	3.501092	-0.06471			
			15	H	-0.66801	2.972635	0.669312			
			16	H	-0.8922	2.886499	-1.10326			
			17	C	2.42711	-0.79683	-0.46703			
			18	H	2.790206	-1.82936	-0.40995			
			19	H	2.660078	-0.44086	-1.47759			
			20	C	3.1732	0.042306	0.537084			
			21	H	3.021549	-0.22728	1.5809			
			22	C	3.97571	1.061797	0.237507			
			23	H	4.15119	1.364179	-0.79109			
			24	H	4.491758	1.6249	1.007203			

3. Ferulic Acid

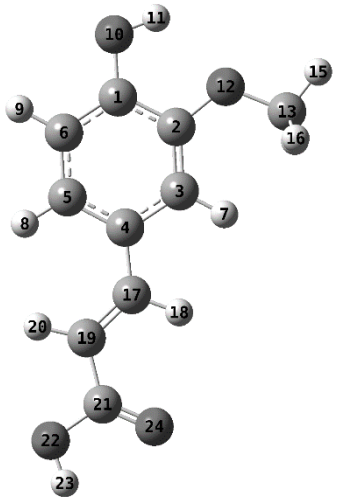

Tag	Symbol	X	Y	Z
1	C	2.500479	-1.08385	0.000015
2	C	2.199585	0.291195	0.00007
3	C	0.879222	0.711921	0.00005
4	C	-0.1761	-0.2244	-0.00001
5	C	0.144025	-1.59054	-5.5E-05
6	C	1.466276	-2.01449	-4.7E-05
7	H	0.641608	1.768058	0.000092
8	H	-0.64376	-2.3333	-9.9E-05
9	H	1.718875	-3.06788	-9.6E-05
10	O	3.790375	-1.50308	0.000017
11	H	4.359355	-0.72055	0.000024
12	O	3.307058	1.099647	0.000138
13	C	3.121956	2.512244	-0.00014
14	H	2.582832	2.837388	0.895042
15	H	4.120575	2.944889	-0.00033
16	H	2.582637	2.837007	-0.89534
17	C	-1.54255	0.280582	0.000005
18	H	-1.64928	1.363102	0.000015
19	C	-2.68821	-0.425	-1.2E-05
20	H	-2.71808	-1.50716	-1.8E-05
21	C	-3.98225	0.269735	0.000004
22	O	-5.01977	-0.61444	-1.3E-05
23	H	-5.83311	-0.08889	0.000017
24	O	-4.1647	1.468243	0.000034

-687.993570 | 0.185178 | 1

4. Guaiacol

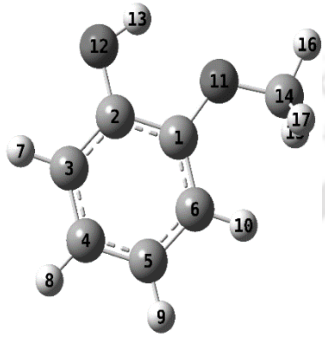

Tag	Symbol	X	Y	Z
1	C	-0.43936	-0.08047	-0.00009
2	C	0.477492	0.98703	0.00002
3	C	1.840317	0.725771	0.00014
4	C	2.298133	-0.59356	0.000107
5	C	1.392694	-1.6483	-5.7E-05
6	C	0.016782	-1.39363	-0.00019
7	H	2.528173	1.5629	0.000262
8	H	3.363894	-0.78929	0.000214
9	H	1.743868	-2.67323	-9.3E-05
10	H	-0.68295	-2.2192	-0.00036
11	O	-1.75494	0.317596	-0.00041
12	O	0.029334	2.274592	0.000033
13	H	-0.93705	2.250544	-0.00043
14	C	-2.76768	-0.68096	0.000362
15	H	-2.70186	-1.30856	0.895039
16	H	-3.71653	-0.14722	0.000897
17	H	-2.70301	-1.30879	-0.89424

-421.979936 | 0.136975 | 1

5. 2-hydroxy-benzaldehyde

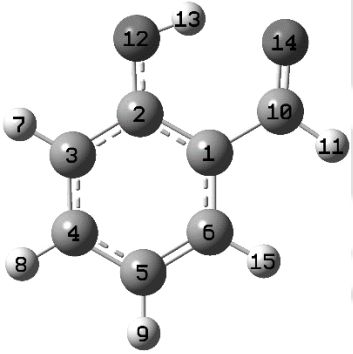

Tag	Symbol	X	Y	Z
1	C	-0.33365	-0.55124	-7.4E-05
2	C	-0.06361	0.841539	-8.2E-05
3	C	1.26544	1.282711	-7E-06
4	C	2.299746	0.359284	0.000085
5	C	2.04784	-1.02142	0.000105
6	C	0.737919	-1.46352	-9E-06
7	H	1.457495	2.348646	-7E-06
8	H	3.32412	0.715461	0.000158
9	H	2.869124	-1.72707	0.000186
10	C	-1.70424	-1.03386	-0.00027
11	H	-1.83134	-2.13233	-0.00103
12	O	-1.04604	1.753412	-0.00019
13	H	-1.9049	1.272911	0.000436
14	O	-2.69481	-0.30746	0.000419
15	H	0.515591	-2.52621	-4.1E-05

-420.813738 | 0.114481 | 1

6. ***p*-isopropenyl-phenol**

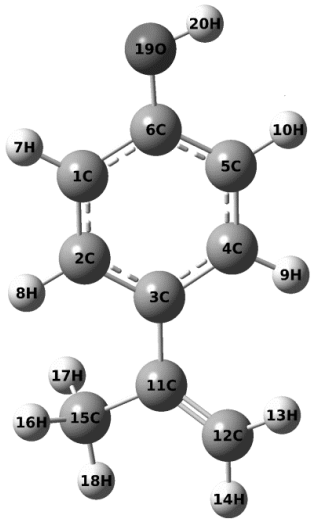

Tag	Symbol	X	Y	Z
1	C	1.421131	-1.20065	-0.22487
2	C	0.032513	-1.14563	-0.21944
3	C	-0.66126	0.058066	-0.0118
4	C	0.108935	1.207111	0.222953
5	C	1.498665	1.166453	0.223494
6	C	2.161746	-0.04041	-0.00561
7	H	1.943174	-2.13425	-0.39665
8	H	-0.51759	-2.06168	-0.39672
9	H	-0.38624	2.14777	0.432103
10	H	2.067135	2.071657	0.417793
11	C	-2.14688	0.112382	-0.03287
12	C	-2.81043	1.208104	-0.42728
13	H	-2.30118	2.092194	-0.79213
14	H	-3.89382	1.242754	-0.41169
15	C	-2.89883	-1.12417	0.403191
16	H	-2.74066	-1.95599	-0.29113
17	H	-2.56717	-1.46307	1.389608
18	H	-3.97175	-0.93051	0.444328
19	O	3.526648	-0.14662	-0.0138
20	H	3.921345	0.716542	0.148212

-424.139212 | 0.164799 | 1

7. **2-hydroxy-6-methylbenza-ldehyde**

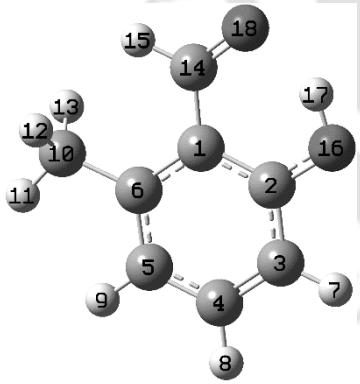

Tag	Symbol	X	Y	Z
1	C	0.277108	0.345345	0.000002
2	C	0.548346	-1.05153	0.000008
3	C	-0.50691	-1.97216	-0.00002
4	C	-1.8089	-1.50809	-3.8E-05
5	C	-2.09319	-0.13463	-1.6E-05
6	C	-1.07055	0.802402	0
7	H	-0.27409	-3.0296	-1.9E-05
8	H	-2.62727	-2.21991	-6.2E-05
9	H	-3.12442	0.198881	-1.3E-05
10	C	-1.41275	2.27564	0.000051
11	H	-2.4954	2.407361	0.000404
12	H	-1.01744	2.788123	0.881791
13	H	-1.01804	2.788039	-0.882
14	C	1.393722	1.275386	-3.8E-05
15	H	1.151505	2.349442	-6.7E-05

-460.111091 | 0.142078 | 1

16	O	1.799137	-1.52918	0.000086
17	H	2.416235	-0.75864	0.000011
18	O	2.579323	0.939451	-5.3E-05

Table 2: Cartesian coordinates of guaiacol, 2-hydroxybenzaldehyde (2-HB), catechol, phenol, and benzene along with corresponding electronic energy and zero point vibrational energy (ZPVE).

Species	Structure	xyz-coordinate				Electronic Energy	ZPVE
Guaiacol Config. 1	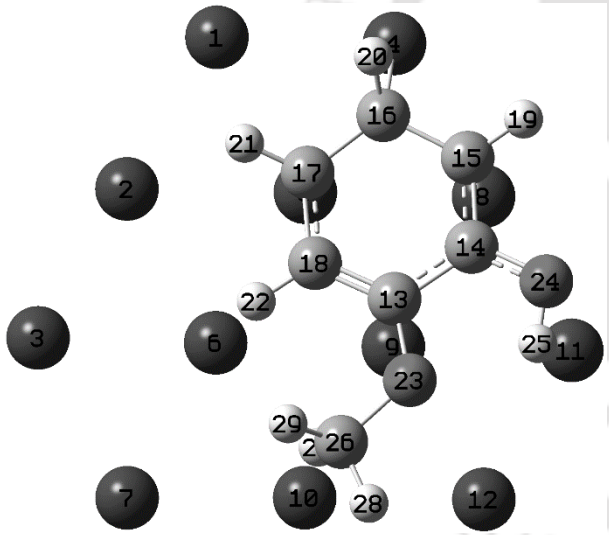	Tag	Symbol	X	Y	Z	-1943.543229	0.136568
		1	Pd	0.538909	4.168532	-0.23735		
		2	Pd	-1.84218	2.768753	-0.05964		
		3	Pd	-4.18727	1.397776	0.115687		
		4	Pd	2.897311	2.773396	-0.48107		
		5	Pd	0.549221	1.406177	-0.30545		
		6	Pd	-1.81999	0.018781	-0.12793		
		7	Pd	-4.20834	-1.43712	0.048913		
		8	Pd	2.931095	0.035962	-0.5504		
		9	Pd	0.557832	-1.34402	-0.37285		
		10	Pd	-1.80149	-2.74687	-0.19712		
		11	Pd	2.94443	-2.71322	-0.61837		
		12	Pd	0.611724	-4.09249	-0.44421		
		13	C	1.652095	-0.48347	2.384837		
		14	C	3.019641	-0.36781	1.963339		
		15	C	3.515645	0.833036	1.419579		
		16	C	2.670567	2.027404	1.408215		
		17	C	1.237343	1.81183	1.656547		
		18	C	0.782406	0.570608	2.217125		
		19	H	4.595133	0.955096	1.424312		
		20	H	3.103079	2.939108	1.846075		
		21	H	0.660652	2.694168	1.935754		
		22	H	-0.25033	0.498191	2.534038		
		23	O	1.393025	-1.65416	2.999085		
		24	O	3.868405	-1.35757	2.266213		
		25	H	3.336182	-2.12098	2.540892		
		26	C	0.034154	-1.97444	3.292876		
		27	H	-0.56339	-1.95173	2.373586		
		28	H	0.049951	-2.98268	3.702388		
		29	H	-0.37138	-1.28059	4.036169		

2-HB

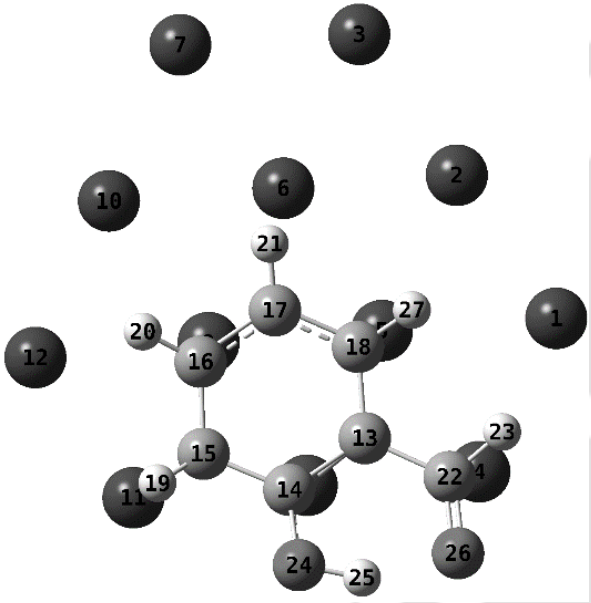

Tag	Symbol	X	Y	Z		
1	Pd	-1.00372	-4.03346	-0.28625		
2	Pd	1.539698	-2.96736	-0.05119		
3	Pd	4.043627	-1.92468	0.179914		
4	Pd	-3.15401	-2.33158	-0.50442		
5	Pd	-0.64725	-1.29299	-0.27487		
6	Pd	1.881587	-0.23741	-0.03938		
7	Pd	4.44012	0.882888	0.196058		
8	Pd	-2.82421	0.386693	-0.4951		
9	Pd	-0.29259	1.434376	-0.26231		
10	Pd	2.231101	2.506774	-0.02788		
11	Pd	-2.47291	3.114164	-0.48227		
12	Pd	0.019472	4.166802	-0.25202		
13	C	-2.65761	-0.46641	1.461393	-1942.37	0.112424
14	C	-3.24326	0.884177	1.488171		
15	C	-2.39355	2.083324	1.464608		
16	C	-0.96321	1.832272	1.673412		
17	C	-0.41114	0.515967	1.81365		
18	C	-1.21923	-0.66183	1.637084		
19	H	-2.81871	2.954005	1.970315		
20	H	-0.37969	2.662399	2.064174		
21	H	0.572675	0.41318	2.256149		
22	C	-3.56021	-1.63547	1.550729		
23	H	-3.08831	-2.5629	1.929672		
24	O	-4.53007	1.028502	1.770296		
25	H	-4.92406	0.092242	1.737987		
26	O	-4.81549	-1.49094	1.621122		
27	H	-0.91057	-1.56625	2.162763		

Catechol

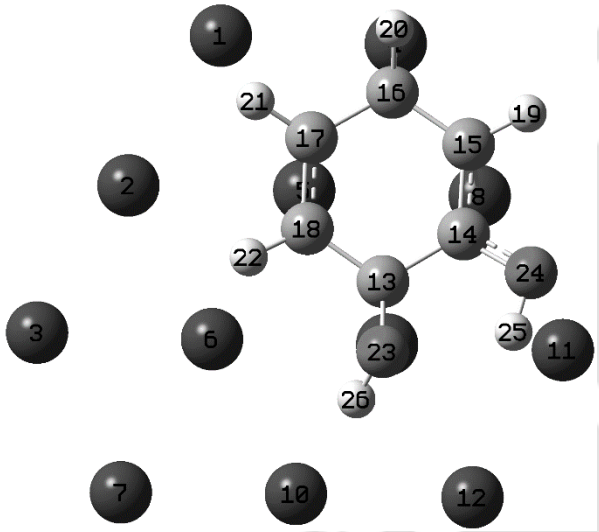

Tag	Symbol	X	Y	Z		
1	Pd	0.5803	4.145202	-0.23607		
2	Pd	-1.80383	2.747863	-0.08274		
3	Pd	-4.15198	1.37925	0.068385		
4	Pd	2.943733	2.747	-0.40106		
5	Pd	0.592619	1.382156	-0.24975		
6	Pd	-1.77977	-0.0029	-0.09668		
7	Pd	-4.17119	-1.45642	0.056698		
8	Pd	2.979399	0.008658	-0.41608		
9	Pd	0.602985	-1.36887	-0.26312		
10	Pd	-1.75937	-2.76937	-0.11131		
11	Pd	2.994579	-2.74127	-0.42987		
12	Pd	0.658843	-4.11819	-0.27949	-1904.273234	0.107334
13	C	1.073491	-0.5872	1.761568		
14	C	2.544371	-0.53078	1.765689		
15	C	3.271899	0.685374	1.598205		
16	C	2.595437	1.975475	1.550106		
17	C	1.143552	1.937939	1.711579		
18	C	0.417965	0.702566	1.81868		
19	H	4.324115	0.657334	1.864083		
20	H	3.113337	2.811621	2.029294		
21	H	0.649494	2.840791	2.060998		
22	H	-0.59349	0.718486	2.210018		
23	O	0.575411	-1.60758	2.561517		
24	O	3.209084	-1.5967	2.239487		
25	H	2.532865	-2.29526	2.402393		
26	H	-0.15349	-2.04275	2.080268		

Phenol

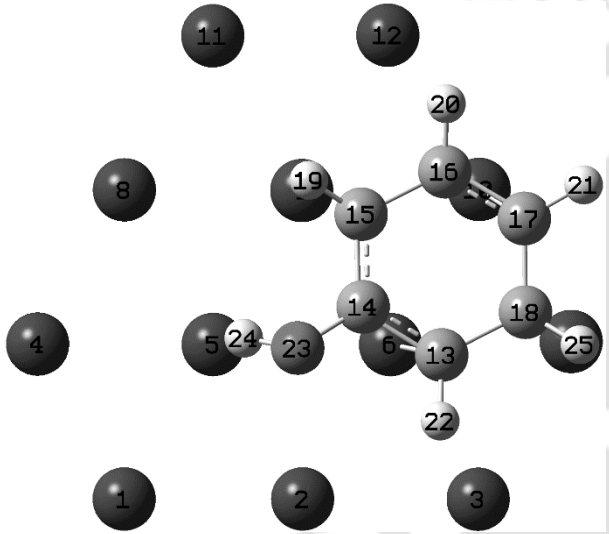

Tag	Symbol	X	Y	Z		
1	Pd	-3.53584	-2.50171	-0.02855		
2	Pd	-0.83623	-3.09929	-0.15977		
3	Pd	1.81747	-3.69255	-0.29549		
4	Pd	-4.32439	0.127801	0.03069		
5	Pd	-1.67115	-0.4669	-0.10453		
6	Pd	1.010161	-1.06266	-0.24006		
7	Pd	3.753768	-1.62245	-0.37594		
8	Pd	-2.49425	2.166086	-0.04467		
9	Pd	0.185942	1.560867	-0.18016		
10	Pd	2.872055	0.982623	-0.31379		
11	Pd	-0.6407	4.196255	-0.12078	-1829.049662	0.102996
12	Pd	2.009373	3.618527	-0.25314		
13	C	1.782508	-1.44629	1.732895		
14	C	0.759891	-0.4603	1.946811		
15	C	1.037723	0.94916	1.806445		
16	C	2.447045	1.311722	1.742119		
17	C	3.490324	0.337479	1.662247		
18	C	3.192111	-1.07845	1.587258		
19	H	0.371435	1.624695	2.337812		
20	H	2.702628	2.323065	2.046657		
21	H	4.505781	0.639894	1.895009		
22	H	1.544576	-2.44748	2.080767		
23	O	-0.35897	-0.87775	2.575046		
24	H	-1.15029	-0.53489	2.099226		
25	H	3.914249	-1.76644	2.03806		

Benzene

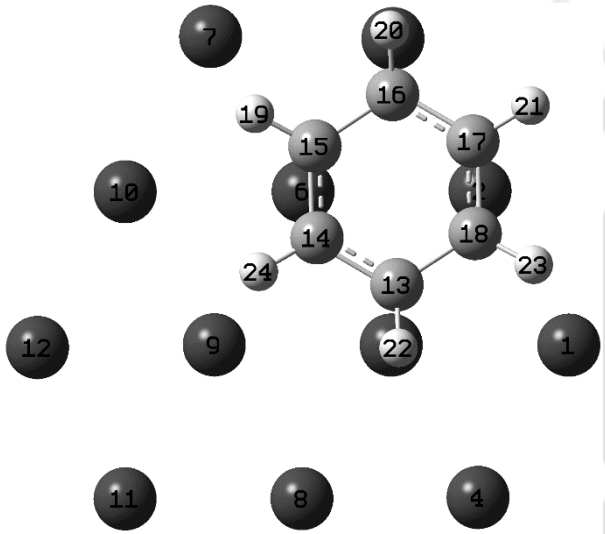

Tag	Symbol	X	Y	Z		
1	Pd	-2.20661	3.494186	-0.25589		
2	Pd	-2.91974	0.821196	-0.29775		
3	Pd	-3.62704	-1.80711	-0.33727		
4	Pd	0.457724	4.170487	-0.12151		
5	Pd	-0.25537	1.541409	-0.1621		
6	Pd	-0.96828	-1.115	-0.19923		
7	Pd	-1.64714	-3.83445	-0.23744		
8	Pd	2.405834	2.248599	-0.01947		
9	Pd	1.686439	-0.40528	-0.06089		
10	Pd	0.990934	-3.06651	-0.10046		
11	Pd	4.351722	0.30727	0.076843	-1753.838258	0.099492
12	Pd	3.658833	-2.31836	0.037754		
13	C	-1.0884	1.026034	1.823188		
14	C	-0.72925	-0.36391	1.928575		
15	C	-1.70509	-1.39585	1.834528		
16	C	-3.12079	-1.11311	1.681667		
17	C	-3.49458	0.283272	1.702748		
18	C	-2.5096	1.322797	1.760503		
19	H	-1.4172	-2.39705	2.139323		
20	H	-3.82115	-1.83489	2.108329		
21	H	-4.52969	0.537694	1.909138		
22	H	-0.44079	1.757272	2.301361		
23	H	-2.8274	2.323044	2.039962		
24	H	0.266522	-0.6172	2.275775		

Table 3. Cartesian coordinates of graphene, Pd- and Pt-doped graphene sheets along with ZPVE corrected electronic energy (E_{corr}) and ZPVE in hartree units.

S. No.	Structure	Cartesian Coordinates	E_{corr}	ZPVE

1. Graphene

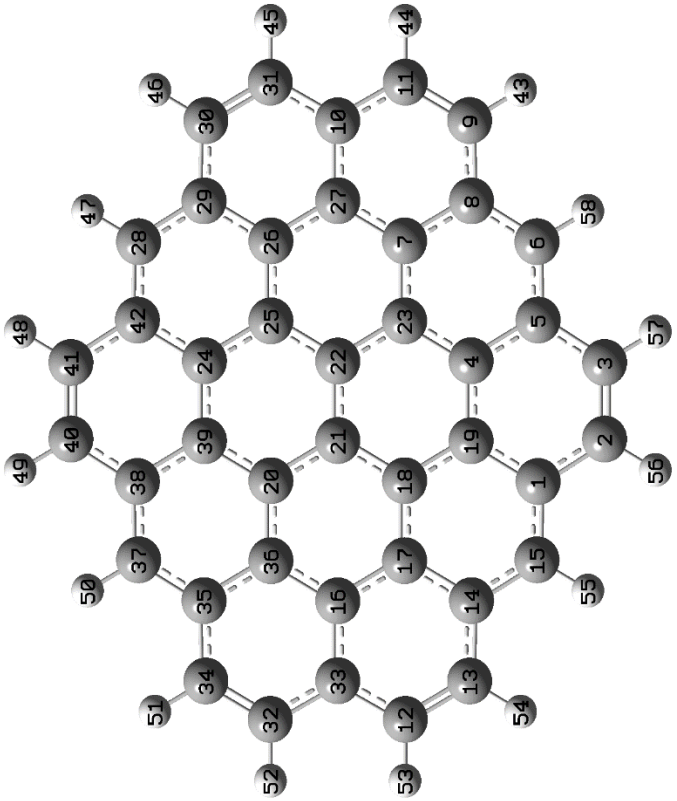

Tag	Symbol	X	Y	Z
1	C	-1.42967	-3.69337	0.00094
2	C	-0.67773	-4.91868	0.000304
3	C	0.677782	-4.91868	-0.00026
4	C	0.708456	-2.45794	0.00362
5	C	1.42972	-3.69337	-0.00092
6	C	2.817637	-3.67214	-0.00078
7	C	2.832784	-1.23197	0.004396
8	C	3.541678	-2.4657	-0.00046
9	C	4.964892	-2.43086	-4.8E-05
10	C	4.959821	0.000026	0.000678
11	C	5.644809	-1.24498	0.000349
12	C	-5.64478	-1.24505	-0.00039
13	C	-4.96485	-2.43091	0.000018
14	C	-3.54163	-2.46573	0.000439
15	C	-2.81758	-3.67215	0.00079
16	C	-3.54442	-1.5E-05	0.00314
17	C	-2.83276	-1.23198	-0.00412
18	C	-1.4161	-1.23278	0.005412
19	C	-0.70841	-2.45794	-0.00365
20	C	-1.41614	1.23278	0.005464
21	C	-0.70384	-1.2E-05	-0.00537
22	C	0.703824	-4E-06	0.005231
23	C	1.416127	-1.2328	-0.00544
24	C	0.70841	2.457953	0.003598

-1609.632115 | 0.437023

25	C	1.416095	1.232781	-0.00528
26	C	2.832767	1.231991	0.004297
27	C	3.544429	0.000016	-0.00331
28	C	2.817591	3.672165	-0.00078
29	C	3.541648	2.465733	-0.00045
30	C	4.964864	2.430909	-4.9E-05
31	C	5.6448	1.245039	0.00035
32	C	-5.64481	1.244967	-0.00039
33	C	-4.95981	-3.4E-05	-0.0007
34	C	-4.9649	2.430846	0.000018
35	C	-3.54168	2.465695	0.000459
36	C	-2.83279	1.231962	-0.00434
37	C	-2.81765	3.672132	0.000789
38	C	-1.42973	3.693366	0.000958
39	C	-0.70846	2.457943	-0.00359
40	C	-0.6778	4.918691	0.000299
41	C	0.677725	4.918702	-0.00028
42	C	1.429666	3.693387	-0.00093
43	H	5.508174	-3.37101	-0.00088
44	H	6.730795	-1.24065	0.000907
45	H	6.730779	1.240737	0.000906
46	H	5.508112	3.371078	-0.00087
47	H	3.363168	4.611908	-0.00274
48	H	1.224697	5.856827	-0.00098
49	H	-1.22476	5.856823	0.000985
50	H	-3.36323	4.611884	0.002771
51	H	-5.50818	3.370999	0.000836
52	H	-6.73079	1.240635	-0.00093
53	H	-6.73076	-1.24075	-0.00092
54	H	-5.50809	-3.37108	0.000788
55	H	-3.36315	-4.61189	0.002743
56	H	-1.2247	-5.8568	0.001004

		57	H	1.224736	-5.85682	-0.00094	
		58	H	3.363212	-4.61189	-0.00278	
		Tag	Symbol	X	Y	Z	
2.	Pd-doped Graphene 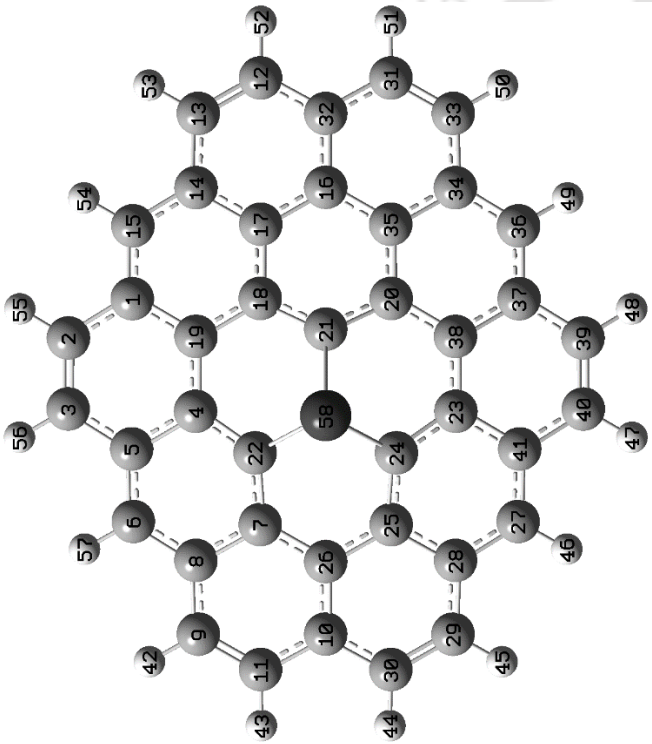	1	C	1.536638	3.686813	-0.1826	-1698.152466 0.424659
		2	C	0.788794	4.904931	-0.35093	
		3	C	-0.56449	4.910608	-0.41203	
		4	C	-0.60895	2.481416	-0.00697	
		5	C	-1.32566	3.698241	-0.28273	
		6	C	-2.70926	3.667296	-0.42152	
		7	C	-2.76866	1.24837	-0.07699	
		8	C	-3.45054	2.474458	-0.36256	
		9	C	-4.85609	2.428127	-0.59096	
		10	C	-4.85438	0.000416	-0.43235	
		11	C	-5.5309	1.242152	-0.60916	
		12	C	5.744903	1.242434	-0.40972	
		13	C	5.068665	2.430028	-0.38	
		14	C	3.652624	2.47189	-0.23473	
		15	C	2.925953	3.674892	-0.2628	
		16	C	3.65895	-0.00029	-0.13533	
		17	C	2.955616	1.238533	-0.08199	
		18	C	1.542393	1.247705	0.120102	
		19	C	0.819463	2.473188	0.015397	
		20	C	1.542071	-1.24787	0.119891	
		21	C	0.957298	-2.4E-05	0.37779	
		22	C	-1.4009	1.347741	0.190903	
		23	C	-0.60953	-2.48136	-0.00659	
		24	C	-1.40136	-1.34766	0.191783	
		25	C	-2.76908	-1.248	-0.0764	
		26	C	-3.47474	0.000281	-0.14943	
		27	C	-2.71012	-3.66694	-0.42069	
		28	C	-3.45121	-2.47398	-0.36177	
		29	C	-4.85675	-2.42737	-0.59016	
		30	C	-5.53123	-1.2412	-0.6087	

		31	C	5.744614	-1.24341	-0.41014		
		32	C	5.066995	-0.00042	-0.31151		
		33	C	5.06808	-2.43085	-0.38075		
		34	C	3.652033	-2.47241	-0.23539		
		35	C	2.955289	-1.23894	-0.08231		
		36	C	2.925134	-3.67526	-0.26362		
		37	C	1.535835	-3.68694	-0.18308		
		38	C	0.818906	-2.47325	0.015326		
		39	C	0.787794	-4.90495	-0.35136		
		40	C	-0.56551	-4.91048	-0.41201		
		41	C	-1.32648	-3.69804	-0.28229		
		42	H	-5.3824	3.360782	-0.7703		
		43	H	-6.59892	1.225844	-0.80352		
		44	H	-6.59926	-1.22466	-0.80306		
		45	H	-5.38332	-3.35993	-0.76927		
		46	H	-3.23624	-4.59598	-0.62154		
		47	H	-1.10462	-5.83856	-0.57711		
		48	H	1.342249	-5.83141	-0.46735		
		49	H	3.457703	-4.61143	-0.40184		
		50	H	5.606239	-3.36867	-0.47966		
		51	H	6.824051	-1.23683	-0.5311		
		52	H	6.824343	1.235624	-0.53065		
		53	H	5.607062	3.367751	-0.47863		
		54	H	3.458724	4.610992	-0.40073		
		55	H	1.343382	5.831354	-0.4666		
		56	H	-1.10345	5.838776	-0.57715		
		57	H	-3.23523	4.596401	-0.62248		
		58	Pd	-0.68943	0.000016	1.418939		
3.	Pt doped graphene	Tag	Symbol	X	Y	Z	-1690.596226	0.426067
		1	C	-1.5997	-3.68416	-0.29667		
		2	C	-0.85878	-4.90293	-0.49262		
		3	C	0.493204	-4.91501	-0.5715		
		4	C	0.553268	-2.50039	-0.09488		

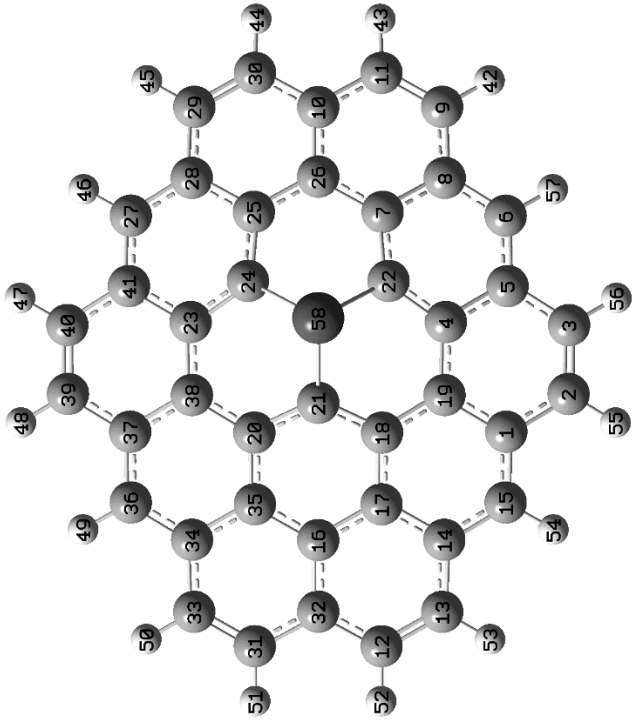

5	C	1.258642	-3.7078	-0.42489
6	C	2.638787	-3.67136	-0.60047
7	C	2.71577	-1.26091	-0.20151
8	C	3.382699	-2.47851	-0.54506
9	C	4.776176	-2.42791	-0.83574
10	C	4.772266	-0.00023	-0.65418
11	C	5.443657	-1.23888	-0.87019
12	C	-5.80892	-1.24188	-0.53871
13	C	-5.13371	-2.42986	-0.50988
14	C	-3.71951	-2.47116	-0.34943
15	C	-2.98895	-3.67084	-0.38489
16	C	-3.72573	0.00031	-0.23234
17	C	-3.02365	-1.24068	-0.17654
18	C	-1.61643	-1.25198	0.047177
19	C	-0.88012	-2.47421	-0.07196
20	C	-1.61606	1.252171	0.047026
21	C	-1.03153	0.000014	0.31715
22	C	1.360138	-1.37786	0.13903
23	C	0.553779	2.500365	-0.0944
24	C	1.360675	1.377953	0.140267
25	C	2.716148	1.260741	-0.20091
26	C	3.40709	-0.00011	-0.30067
27	C	2.639452	3.671141	-0.59995
28	C	3.383275	2.478163	-0.54451
29	C	4.776709	2.42741	-0.83531
30	C	5.444005	1.238269	-0.86995
31	C	-5.80865	1.24287	-0.5389
32	C	-5.13085	0.000441	-0.42776
33	C	-5.13314	2.430705	-0.51021
34	C	-3.71895	2.471704	-0.34974

35	C	-3.02333	1.241117	-0.17671
36	C	-2.98815	3.671283	-0.38531
37	C	-1.59894	3.684376	-0.2969
38	C	-0.87953	2.474333	-0.07194
39	C	-0.85792	4.903108	-0.49285
40	C	0.494074	4.915003	-0.57146
41	C	1.259291	3.707682	-0.42451
42	H	5.296649	-3.35609	-1.05127
43	H	6.501449	-1.21535	-1.11384
44	H	6.501788	1.214549	-1.11362
45	H	5.297276	3.355553	-1.05078
46	H	3.15899	4.594254	-0.84122
47	H	1.026159	5.841454	-0.76551
48	H	-1.41936	5.823595	-0.62201
49	H	-3.51744	4.60669	-0.54111
50	H	-5.66983	3.367624	-0.62427
51	H	-6.88645	1.234492	-0.6731
52	H	-6.88672	-1.23327	-0.67291
53	H	-5.67062	-3.36667	-0.62383
54	H	-3.51843	-4.60617	-0.54052
55	H	-1.42029	-5.82341	-0.62157
56	H	1.025072	-5.84159	-0.76551
57	H	3.15826	-4.59452	-0.84167
58	Pt	0.632104	-0.00021	1.302301

Table 4. Spin state analysis of all adsorbed configurations of phenolic species over Pd- and Pt-doped graphene sheets. E_{Rel} is relative energy in kcal/mol and SM is spin multiplicity.

Species	Configurations	SM	PdGr	PtGr
			E_{Rel} (kcal/mol)	
Phenol	1	1	0.00	0.00
		3	21.13	23.30
		5	67.89	67.68
		7	129.40	130.00
		9	196.87	196.81
	2	1	0.00	0.00
		3	22.23	21.71
		5	68.52	67.59
		7	128.15	128.99
		9	195.97	196.40
2-HB	1	1	0.00	0.00
		3	19.71	21.48
		5	66.30	66.05
		7	126.03	128.01
		9	193.82	195.12
	2	1	0.00	0.00
		3	18.62	14.08
		5	65.94	63.75
		7	121.76	120.22
		9	191.21	187.64
	3	1	0.00	0.00
		3	19.41	15.26
		5	65.91	62.05
		7	128.24	123.05
		9	192.62	189.87
Anisole	1	1	0.00	0.00
		3	22.92	22.92
		5	69.84	68.77
		7	131.64	130.58
		9	197.88	198.55
	2	1	0.00	0.00
		3	20.01	21.92
		5	66.89	66.73
		7	127.26	129.28
		9	195.17	196.21
Guaiacol	1	1	0.00	0.00
		3	22.85	22.37
		5	69.83	69.41

		7	130.17	131.49
		9	197.83	198.20
	2	**1**	0.00	0.00
		3	19.91	21.68
		5	66.66	66.49
		7	127.64	129.00
		9	195.42	195.86
	3	**1**	0.00	0.00
		3	21.05	22.92
		5	67.62	67.30
		7	129.02	129.68
		9	196.67	196.60
Vanillin	**1**	**1**	0.00	0.00
		3	19.39	23.03
		5	66.21	67.53
		7	126.37	130.11
		9	201.48	197.07
	2	**1**	0.00	0.00
		3	19.72	21.76
		5	66.54	66.43
		7	126.99	128.94
		9	194.79	195.85
	3	**1**	0.00	0.00
		3	21.89	21.18
		5	68.27	67.10
		7	129.39	129.33
		9	197.07	195.97
	4	**1**	0.00	0.00
		3	23.37	20.81
		5	70.58	66.79
		7	132.05	126.89
		9	207.92	194.45

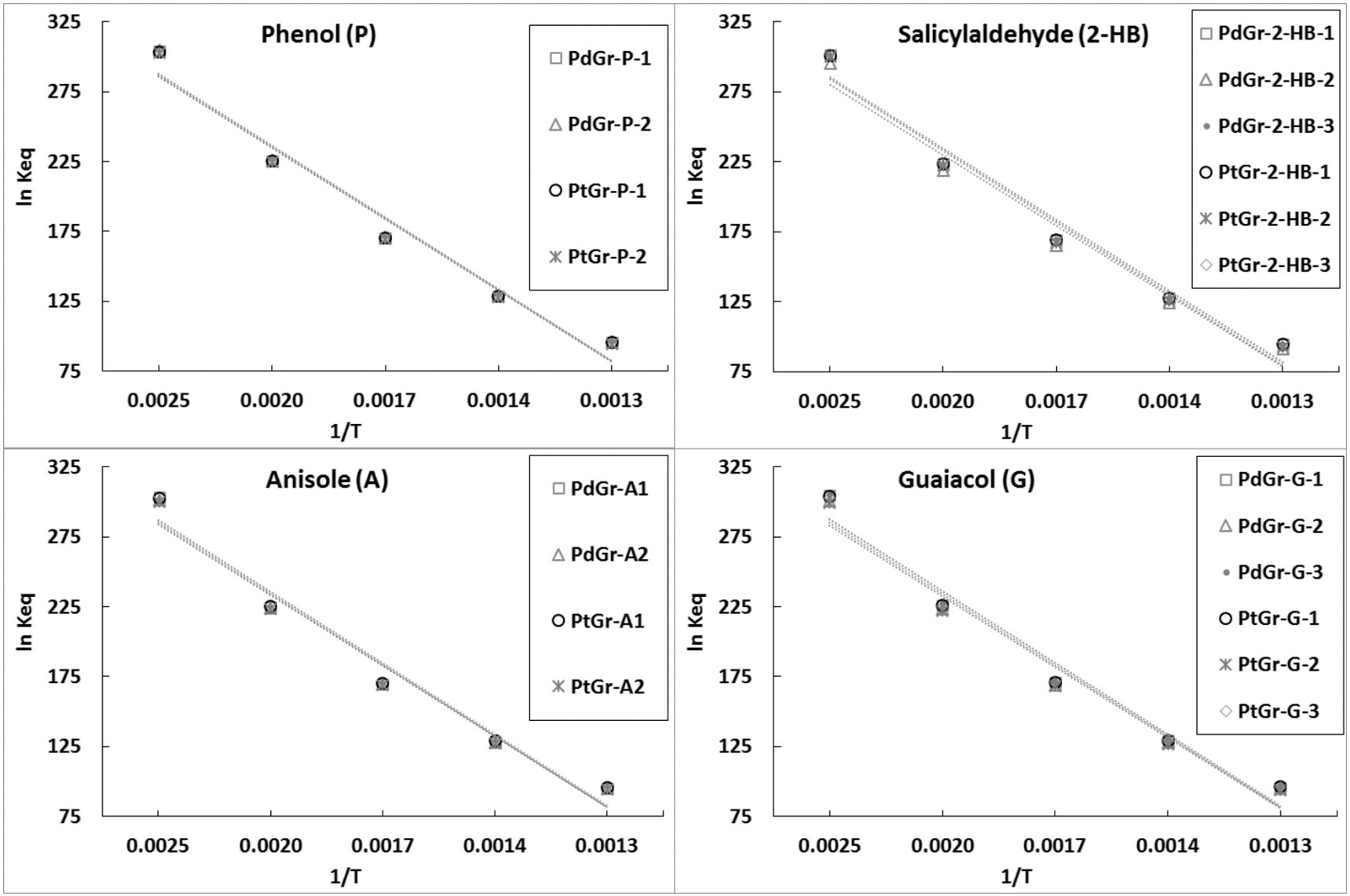

Figure 1. ln $\mathbf{K_{eq}}$ vs. **1/T** relations for the adsorptions of phenol, anisole, guaiacol, and 2-HB over Pd- and Pt-doped metal graphene sheets.

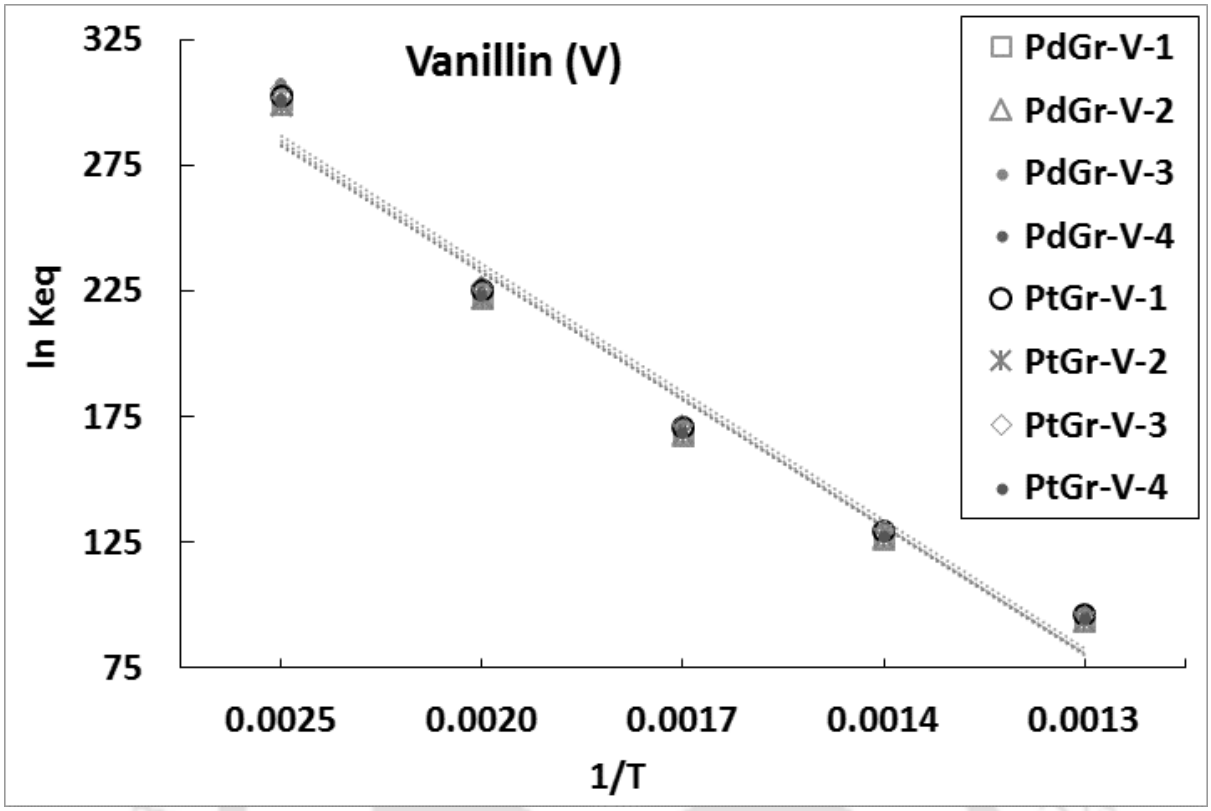

Figure 2. ln $\mathbf{K_{eq}}$ vs. **1/T** relations for the adsorption of vanillin over both doped metal graphene sheets.